Anisotropic Properties and Critical Behavior of High-Temperature Superconductors

Dissertation

zur
Erlangung der naturwissenschaftlichen Doktorwürde
(Dr. sc. nat.)

vorgelegt der
Mathematisch-naturwissenschaftlichen Fakultät der
Universität Zürich

von

Stephen Michael Weyeneth
aus Lüterkofen-Ichertswil (SO)

Zürich, 2009

Promotionskomitee:

Prof. Dr. Hugo Keller, Universität Zürich (Vorsitz und Leitung der Dissertation)
Prof. Dr. Roman Puzniak, Polnische Wissenschaftsakademie Warschau
Prof. Dr. Toni Schneider, Universität Zürich
Prof. Dr. Andreas Schilling, Universität Zürich

Die vorliegende Arbeit wurde von der Mathematisch-naturwissenschaftlichen Fakultät der Universität Zürich auf Antrag von Prof. Dr. Hugo Keller als Dissertation angenommen.

dedicated to Nicole

Fundamental physical constants used in this thesis were updated from:
http://physics.nist.gov/cuu/Constants/index.html

Symbol	Definition	Numerical value
k_{B}	Boltzmann constant	$1.3806504 \cdot 10^{-23}$ JK^{-1}
$\hbar$	Planck constant	$6.62606896 \cdot 10^{-34}$ Js
μ_0	magnetic constant	$4\pi \cdot 10^{-7}$ NA^{-2}
e	elementary charge	$1.602176487 \cdot 10^{-19}$ C
m_{e}	electron mass	$9.10938215 \cdot 10^{-31}$ kg

Abstract

Since the discovery of the cuprate high-temperature superconductors in 1986 by Bednorz and Müller, the understanding of the mechanisms responsible for the high transition temperature T_c has remained one of the major unsolved problems in condensed matter physics. Extensive scientific research uncovered in 23 years several additional high-T_c compounds, classified as the cuprates, the diborides (MgB_2 and its doped relatives), and the iron-pnictides. Although promising theoretical explanations have been attempted, still no rigid framework exists that consistently explains all the experimentally observed peculiarities associated with superconductivity at "high" temperatures.

The efforts to explain high-temperature superconductivity, in particular to understand the microscopic pairing mechanism, profit from knowledge about similarities in the behavior of the three classes of high-temperature superconductors. Interestingly enough, transition temperatures above 30 K have been accomplished only in layered systems so far.

In this thesis focus is put on anisotropic thermodynamical properties of various high-temperature superconductors, in particular by means of a detailed experimental study of the effective-mass anisotropy parameter γ. Magnetic measurements have the potential to uncover anisotropic bulk properties of the superconducting state. Two complementary techniques, SQUID and torque magnetometry, were used. Thanks to the high sensitivity of the self-designed experimental equipment, even the smallest available single crystals may be investigated for their magnetic properties. The magnetization data presented reveal new insights into the critical behavior and the anisotropic properties of high-temperature superconductors.

Critical fluctuations are especially pronounced in high-temperature superconductors, first of all due to the high T_c, secondly because of the highly anisotropic superconducting properties. Magnetization data of single crystals of MgB_2, $YBa_2Cu_4O_8$, and $Bi_2Sr_2CaCu_2O_{8+\delta}$ reveal so-called universality related to 3D-xy critical behavior close to T_c. By applying a magnetic field, the critical behavior at T_c is known to be perturbed due to the presence of vortices, leading to pronounced magnetic-field-induced finite size effects. Within the 3D-xy universality class, describing the fluctuation behavior in type II superconductors close to T_c, strong evidence is found in this work for such finite size effects and a break down of mean-field behavior. As a result, the upper critical field H_{c2}, is confirmed to be an artifact of the mean-field description. Instead, a 3D to 1D crossover prevails, where superconductivity close to T_c is confined to one-dimensional cylinders with diameters on the nanometer scale. In addition, vortex-lattice melting is observed in the studied systems and found to be consistent with 3D-xy behavior.

The recent discovery of superconductivity in iron-pnictide superconductors stimulated hope to reach an understanding of high-temperature superconductivity. Since anisotropic properties are a generic feature among the known high-temperature superconductors, a careful investigation is needed in order to clarify their role in the microscopic pairing mechanism.

Anisotropic properties of iron-pnictides were studied for single crystals of $SmFeAsO_{1-x}F_x$, $NdFeAsO_{1-x}F_x$, and $Rb_{1-x}Ba_xFe_2As_2$, revealing strong temperature dependent peculiarities of the anisotropy parameter. In the superconducting phase the magnetic penetration depth anisotropy γ_λ is found to increase with decreasing temperature, in contrast to the upper critical field anisotropy γ_H, which steadily decreases. The existence of two distinct anisotropy parameters is unusual and cannot be explanained within Ginzburg-Landau theory. A tentative explanation for the characteristic temperature dependencies could be an anisotropic pairing mechanism involving multiple energy gaps. Since all known high-temperature superconductors show pronounced anisotropic properties and indications for multi-band superconductivity, a unified theoretical description of high-temperature superconductivity must not disregard these facts.

When Bednorz and Müller discovered high-temperature superconductivity in the cuprates, they were guided by the notion that Jahn-Teller polaron formation, as an unconventional electron-lattice interaction, might favor a high T_c. Recent theoretical and experimental work further support a polaronic two-band scenario for superconductivity in highly anisotropic high-T_c compounds. Although no complete theory for high-temperature superconductivity on the base of polaron formation has yet been found, these aspects appear to be very promising.

Zusammenfassung

Seit die Hochtemperatur-Supraleitung in den Kuprat-Supraleitern durch Bednorz und Müller 1986 entdeckt wurde, wird das Ergründen der physikalischen Ursache der unkonventionell hohen Übergangstemperaturen als eines der grössten ungelösten Probleme der Wissenschaft betrachtet. Nach 23 Jahren intensiver experimenteller Forschung sind bislang folgende drei Hauptklassen an Hochtemperatur Supraleitern bekannt: Die Kuprate, die Diboride (MgB_2 und verwandte Dotierte) und die Eisen-Pniktide. Auch wenn bereits vielversprechende theoretische Erklärungsansätze existieren, besteht bis heute kein zusammenhängendes Theoriegerüst, welches die Hochtemperatur-Supraleitung einheitlich erklären könnte.

Um den mikroskopischen Paarungsmechanismus der Hochtemperatur-Supraleitung vollumfänglich zu verstehen, sind Gemeinsamkeiten der drei Klassen von Hochtemperatur-Supraleitern von essentieller Bedeutung. Ein wesentlicher Fakt in diesem Zusammenhang ist, dass Hochtemperatur-Supraleitung bislang nur in geschichteten Systemen gefunden wurde.

In der vorliegenden Dissertation werden die anisotropen Eigenschaften verschiedener Hochtemperatur-Supraleiter untersucht, oftmals durch den effektive-Masse Anisotropie-Parameter γ charakterisiert. Magnetometrische Messmethoden erlauben es, richtungsabhängige Materialeigenschaften im supraleitenden Zustand zu untersuchen. Besonderes Augenmerk wurde hier auf zwei sich ergänzende Messprinzipien gelegt: SQUID und Torque Magnetometrie. Dank der spezifischen Sensitivität der selbst entwickelten Apparaturen, können sogar kleinste Einkristalle auf ihre magnetischen Eigenschaften in der supraleitenden Phase vermessen werden. Aus den hier gezeigten Magnetisierungsdaten sind neue Erkenntnisse über das kritische Verhalten, als auch über anisotrope Eigenschaften von Hochtemperatur-Supraleitern, hervorgegangen.

Kritische Fluktuationseffekte sind besonders in Hochtemperatur-Supraleiteren stark ausgeprägt, einerseits durch die hohe Übergangstemperatur T_c, andererseits durch die hohe Anisotropie. Messergebnisse der Magnetisierung von MgB_2, $YBa_2Cu_4O_8$ und $Bi_2Sr_2CaCu_2O_{8+\delta}$ Einkristallen zeigen ein universelles Verhalten nahe T_c auf, in Bezug auf ein 3D-xy kritisches Verhalten. Die Präsenz eines äusseren Magnetfeldes führt wegen der Bildung von Flussschläuchen zu starken feldinduzierten "Finite-Size"-Effekten und stört somit das kritische Verhalten nahe T_c. Innerhalb der 3D-xy Universalitätsklasse, welche das Fluktuationsverhalten eines Typ-II Supraleiters nahe T_c zu beschreiben vermag, wurde hier die Existenz solcher "Finite-Size"-Effekte nachgewiesen, was ein Zusammenbruch der Ginzburg-Landau Annahme eines räumlich homogenen supraleitenden Zustands (Mean-Field Annahme) mit sich bringt. Das Gesamtresultat beweist, dass der Parameter H_{c2} (oberes kritisches Feld), als ein Artefakt einer "Mean-Field" Näherung aufgefasst werden muss. An seiner Stelle findet in Supraleitern an der Phasengrenze ein 3D zu 1D Crossover statt, bei welchem die eigentlich dreidimensionale Phase der Supraleitung nahe T_c in eindimensionale Nano-Zylinder eingesperrt wird. Ebenso konnte, konsistent innerhalb der 3D-xy Fluktuationstheorie, ein

Flussschlauch-Gitter Schmelzen aufgelöst werden.

Die kürzliche Entdeckung der Hochtemperatur-Supraleitung in den Eisen-Pniktiden liess die Hoffnung wieder aufleben, ein endgültiges Verständnis für die Ursache der Hochtemperatur-Supraleitung zu finden. Da anisotrope Eigenschaften generisch in allen heutzutage bekannten Hochtemperatur-Supraleitern vorhanden sind, ist es zwingend notwendig deren Rolle im Mechanismus der Paarbildung zu erforschen. Aus diesem Grund sind in dieser Arbeit die anisotropen Eigenschaften der Eisen-Pniktide an $SmFeAsO_{1-x}F_x$, $NdFeAsO_{1-x}F_x$ und $Rb_{1-x}Ba_xFe_2As_2$ Einkristallen untersucht worden, mit dem Resultat, dass die Anisotropie-Parameter eine starke Temperaturabhängigkeit zeigen. In der supraleitenden Phase steigt die Anisotropie der magnetischen Eindringtiefen γ_λ immer höher, je weiter die Temperatur reduziert wird, im Gegensatz zur Anisotropie des oberen kritischen Feldes γ_H, welche kontinuierlich abnimmt. Dieses unkonventionelle Resultat ist inkonsistent mit der traditionellen Ginzburg-Landau Theorie. Eine Erklärung der erwähnten Temperaturabhängigkeit wäre eine richtungsabhängige Paarbildung der Elektronen in Kombination mit mehreren Energiebändern, die zur Paarbildung beitragen. Alle bekannten Hochtemperatur-Supraleiter weisen markante anisotropische Eigenschaften auf, und in allen liegen Indizien vor, dass mehrere Energiebänder in der Supraleitung involviert sind. Darum liegt die Schlussfolgerung nahe, dass ein gesamtheitliches theoretisches Modell der Hochtemperatur-Supraleitung diese fundamentalen Fakten nicht ausser Acht lassen darf.

Als Bednorz und Müller die Hochtemperatur-Supraleitung in den Kupraten entdeckten, waren sie der Ansicht, dass dynamisch geformte Jahn-Teller Polaronen ein ungewöhnlich hohes T_c begüngstigen könnten. Neuere theoretische und experimentelle Ergebnisse unterstützen vermehrt ein polaronisches Zweiband-Szenario in hoch anisotropen Hochtemperatur-Supraleitern. Obschon noch keine vollständige Theorie der Hochtemperatur-Supraleitung in dieser Richtung formuliert ist, erscheinen all diese Ansätze äusserst vielversprechend.

Contents

1 Introduction

In 1908 Kamerlingh Onnes successfully liquefied the inert gas helium in his laboratory in Leiden [1]. While giving access to temperatures well below 5 K, this pioneering achievement opened new research domains, allowing material properties to be studied at low temperatures. Subsequent investigations in Leiden on highly pure mercury revealed an unexpected sudden drop in the resistivity at 4.2 K to immeasurable small values [2]. The conclusion was reached, that the electrical current flowed without dissipation of energy [3, 4, 5], since below the transition temperature $T_c \sim 4.2$ K mercury enters the so-called superconducting state. It turns out, that in a large number of compounds a superconducting state is attained below a material specific temperature T_c. Among the elements, niobium exhibits the highest $T_c \sim 9$ K [6].

In the first 20 years after the discovery of superconductivity, the widespread belief prevailed, that if a magnetic field is applied to a superconductor, zero resistance should lead to persisting, irreversibly induced currents. This would render a thermodynamic treatment of superconductivity rather questionable. However, it was shown in 1933 by Meissner and Ochsenfeld, that the transition to the superconducting state is indeed reversible and independent on the actual history of the magnetic field [7]. Furthermore, any magnetic field applied to a superconductor is completely expelled from the bulk, thus leading to ideal diamagnetism.

In 1935 London and London succeeded in deriving a basic electromagnetic description of the macroscopic properties of superconductivity [8, 9], which was generalized in the work of Ginzburg and Landau in 1950, who developed the arguably still most successful phenomenological description of superconductivity, the Ginzburg-Landau theory [10]. This theory is able to describe the thermodynamics of fundamental properties of superconductors as a function of temperature and field without any microscopic implications.

The understanding of the microscopic mechanism of superconductivity was enhanced, when in 1950 the observation of an isotope effect on T_c in mercury was made by Reynolds *et al.* [11] and Maxwell [12]. The observed shift in T_c for different isotopes was in the same year theoretically comprehended by Fröhlich, who assumed that the electrons interact through phonons [13, 14]. Combining the experimentally proven existence of a superconducting energy gap of the order of $k_B T_c$ [15], with phonon-mediated interaction between electrons, Bardeen, Cooper and Schrieffer derived a microscopic theory for superconductivity [16, 17], identifying paired electrons, so-called *Cooper pairs* [18], as charge carriers in the superconducting state.

Undeterred by the advances in theory, scientists were searching for superconductors with ever higher T_c. Still in 1985, superconductivity was thought to be restricted to rather low temperatures, the maximum observed T_c at that time being around 23 K, as found in the binary compound Nb_3Ge [19, 20]. The era of high-temperature (high-T_c) superconductivity started with the discovery of superconductivity around 30 K in the Ba-La-Cu-O system in

1986 by Bednorz and Müller [21]. This system belongs to the class of copper oxide superconductors (cuprates), with transition temperatures (at ambient pressure) so far up to 138 K [22] in the mercury based cuprate system Hg-Ba-Ca-Cu-O, in which transition temperatures above 130 K were first observed 1993 by Schilling *et al.* [23]. Tremendous work has been done in order to identify the still unresolved mechanism of high-T_c superconductivity in the cuprates, accompanied by a restless search for new systems with high transition temperatures. Thus, sudden excitement was roused, when in 2001 superconductivity was found at 39 K in the binary compound MgB_2 by Nagamatsu *et al.* [24], and again in 2008, when superconductivity at 28 K was observed in the iron-pnictide $LaFeAsO_{1-x}F_y$ by Kamihara *et al.* [25]. Within a short period of time, even higher transition temperatures for iron-pnictides up to $T_c \sim 56$ K were found. So far three classes of high-T_c superconductors are known: the cuprates, the diborides (MgB_2 and its doped relatives), and the iron-pnictides.

Although the microscopic mechanism of high-T_c superconductivity has not yet been consistently explained, the various materials belonging to the three classes of high-T_c superconductors show generic similarities that may serve this purpose. An important issue is that all the high-T_c superconductors have layered structures with pronounced anisotropic physical properties [26, 27, 28, 29, 30]. Additionally, in diverse high-T_c compounds of all three classes, superconductivity was found to involve multiple energy gaps, a scenario named multi-gap superconductivity [29, 31, 32, 33, 34, 35, 36, 37]. This important fact is interpreted to be responsible for the high T_c [38], in relation with the anisotropy of the system since a pairing mechanism on the base of polaron formation was suggested [39, 40, 41, 42]. It is hence worthwhile to compare the anisotropic properties of different high-T_c superconductors, and to explore common features and differences among them.

Magnetization measurements are well suited for the investigation of macroscopic bulk properties of superconductors. Not only do they allow the determination of fundamental thermodynamical parameters, but also the study of critical behavior and inhomogeneity effects. In Chapter 2 a derivation of some phenomenological parameters of superconductivity is presented, forming the basis for a subsequent discussion of experimental techniques. In Chapter 3 the occurrence of critical phenomena in high-T_c superconductors close to the transition temperature is discussed, and experimental investigations of critical phenomena in the three high-T_c superconductors MgB_2, $YBa_2Cu_4O_8$, and $Bi_2Sr_2CaCu_2O_{8+\delta}$ are presented. The scaling analysis of the data, reproduces anisotropic properties of the samples, and reveals crossover phenomena at the phase boundary, where critical fluctuations are dominating. In Chapter 4 anisotropic properties of diverse novel iron-pnictide superconductors, as determined by magnetization measurements, are discussed. As shown, a combination of SQUID and torque investigations reveals unconventional behavior of the anisotropy parameter in these compounds, presumably reflecting multiple gaps involved in the superconducting mechanism.

2 Magnetic properties of high-T_c superconductors

This chapter starts with a summary of the main electro- and thermodynamical concepts within the framework of Ginzburg-Landau theory. A phenomenological expression for the magnetization of anisotropic type II superconductors is subsequently derived. Two experimental techniques, SQUID and torque magnetometry, are introduced which both are well suited for investigating the magnetic properties of superconductors.

2.1 The characteristics of superconductivity

According to thermodynamics, a phase transition takes place, if the total free energy f of a system can be reduced by entering a new phase [43]. For superconductors the laws of thermodynamics can be applied, and the free energy per unit volume f is a well defined quantity, solely dependent on external parameters such as the magnetic field[1] $\vec{H}$. It was proposed by Ginzburg and Landau, that in the superconducting state $f(\vec{H})$ may be written in the form [10]

$$f(\vec{H}) = f_{\mathrm{n}}(0) + \alpha|\psi|^2 + \frac{\beta}{2}|\psi|^4 + \frac{1}{2m_e^*}\left|\left(\frac{\hbar}{i}\vec{\nabla} - e^*\vec{A}\right)\psi\right|^2 + \frac{\mu_0\vec{H}^2}{2}, \tag{2.1}$$

where m_e^* denotes the effective mass and e^* the charge of the superfluid carriers, $f_{\mathrm{n}}(0)$ the normal state free energy density, $\psi = |\psi|\mathrm{e}^{i\phi}$ the complex, macroscopic order parameter of the superconducting phase, and α and β the expansion coefficients from the Landau theory of phase transitions [43]. The vector potential $\vec{A}$ of the magnetic field is defined[2] as a solution of the equations

$$\vec{\nabla} \times \vec{A} = \vec{B}, \tag{2.2}$$

$$\frac{\partial}{\partial t}\vec{A} = -\vec{E} - \vec{\nabla}\Gamma, \tag{2.3}$$

$$\vec{\nabla} \cdot \vec{A} = 0. \tag{2.4}$$

Here $\vec{E}$ is the electric field strength and Γ the electrostatic potential. The magnetic induction[3] $\vec{B}$ is related to $\vec{H}$ and the magnetization $\vec{M}$ of the material through

$$\vec{B} = \frac{\partial f}{\partial H} = \mu_0\left(\vec{H} + \vec{M}\right). \tag{2.5}$$

[1] The magnetic field $\vec{H}$, usually referred to the magnetic field strength, is measured in units of A/m.
[2] In this derivation the London gauge [Eq. (2.4)] is assumed.
[3] The magnetic induction $\vec{B}$ is measured in units of T=kgA^{-1}s^{-2} (Tesla).

By standard variational methods the two Ginzburg-Landau equations are derived from Eq. (2.1) as

$$0 = \alpha|\psi| + \beta|\psi|^2\psi + \frac{1}{2m_e^*}\left(\frac{\hbar}{i}\vec{\nabla} - e^*\vec{A}\right)^2\psi, \tag{2.6}$$

$$\vec{j}_s = \frac{e^*}{m_e^*}|\psi|^2\left(\hbar\vec{\nabla}\phi - e^*\vec{A}\right) = e^* n_s^* \vec{v}_s. \tag{2.7}$$

Here $|\psi|^2 = n_s^*$ denotes the density of the superfluid carriers[4], $\vec{v}_s$ the average carrier velocity, and $\vec{j}_s$ the density of the circulating supercurrents. Equation (2.6) describes implicitly the spatial variation of ψ, in terms of a natural length scale

$$\xi_{GL} = \sqrt{\frac{\hbar^2}{2m_e^*|\alpha|}}. \tag{2.8}$$

This length is identified as the coherence length of the superconducting state. Additionally, if the gradient of the phase $\vec{\nabla}\phi$ can be neglected, the fundamental London equation [9] is derived from Eq. (2.7) as

$$\vec{j}_s = -\frac{n_s^* e^{*2}}{m_e^*}\vec{A} \qquad \text{or equivalently} \qquad \frac{\vec{A}}{\mu_0\lambda_L^2} = -\vec{j}_s, \tag{2.9}$$

where

$$\lambda_L = \sqrt{\frac{m_e^*}{\mu_0 n_s^* e^{*2}}} \tag{2.10}$$

is known as the London magnetic penetration depth. The combination of Eqs. (2.2), (2.3), and (2.9), results in the two electromagnetic fields

$$\frac{\vec{E}}{\mu_0\lambda_L^2} = \frac{\partial}{\partial t}\vec{j}_s - \vec{\nabla}\Gamma, \tag{2.11}$$

$$\frac{\vec{B}}{\mu_0\lambda_L^2} = -\vec{\nabla}\times\vec{j}_s. \tag{2.12}$$

In conclusion, this derivation establishes λ_L and ξ_{GL}, as important length scales of a superconductor. The observable parameters in an experiment are denoted as the magnetic penetration depth λ and the coherence length ξ. Both length scales are associated with fundamental energy scales: The length ξ is coupled to the domain wall energy of the superconducting phase, whereas λ is related to the energy involved in the suppression of superconductivity due to the presence of a magnetic field. A detailed analysis [44] yields, that the ratio

$$\kappa = \frac{\lambda}{\xi} \tag{2.13}$$

allows two different types of superconductors to be identified:

[4]Since in the superconducting state the electrons form Cooper pairs [16, 17, 18], the usual conventions $e^* = 2e$, $m^* = 2m_e$, and $n_s^* = n_s/2$ are justified

- For $\kappa < 1/\sqrt{2}$ the material is a type I superconductor, for which a magnetic field induces perfect diamagnetism up to the thermodynamic critical field H_c, where superconductivity is fully suppressed. The ideal diamagnetism of a type I superconductor is known as the *Meissner-Ochsenfeld-effect*.

- For $\kappa > 1/\sqrt{2}$ the material is a type II superconductor. Here the magnetic field penetrates the superconductor above a certain field H_{c1} (lower critical field) in form of quantized flux lines (vortices), each containing a single flux quantum $\Phi_0 = \pi\hbar/e$. Since the field now penetrates the material partially, superconductivity is limited by the upper critical field H_{c2}, which is much higher than H_c in a type I superconductor. For fields H between H_{c1} and H_{c2} a superconductor is in the so-called mixed state, whereas for $H < H_{c1}$ the phase is known as the Meissner state.

In type II superconductors λ and ξ are directly related to H_{c1} and H_{c2} according to [44]

$$H_{c1} = \frac{\Phi_0}{2\pi\mu_0\lambda^2}\ln(\sqrt{\kappa}), \tag{2.14}$$

$$H_{c2} = \frac{\Phi_0}{2\pi\mu_0\xi^2}. \tag{2.15}$$

2.2 The magnetization of type II superconductors in the mixed state

The total free energy density of a type II superconductor in the mixed state may be calculated [44] using Eq. (2.1), resulting in

$$f(H) = \frac{\mu_0 H^2}{2} - \frac{\Phi_0 H}{8\pi\lambda^2}\ln\left(\frac{\upsilon H_{c2}}{H}\right), \tag{2.16}$$

where υ is a numerical constant, which takes into account the vortex-lattice symmetry and the uncertainty in defining the vortex-core size [45, 46, 47, 48]. The first term in Eq. (2.16) denotes the energy available in the normal state. The second part stems from the reduction of this normal state energy due to the creation of vortices. Invoking Eq. (2.5) and taking the derivative of Eq. (2.16), the magnetic moment

$$m = VM = V\left(\frac{B}{\mu_0} - H\right) = \frac{V}{\mu_0}\frac{\partial f}{\partial H} - VH = -\frac{V\Phi_0}{8\pi\mu_0\lambda^2}\ln\left(\frac{\eta H_{c2}}{H}\right) \tag{2.17}$$

is derived, where V is the volume of the sample, and $\eta = \upsilon/\mathrm{e} \sim 1$ is a numerical constant.

Equations (2.16) and (2.17) are valid for an isotropic type II superconductor. Since the crystal structure of a superconductor, however, may be anisotropic, this picture needs to be generalized in order to describe anisotropic (layered) superconductors. The crystal structure of layered superconductors often has uniaxial crystal symmetry, with the crystallographic c-axis perpendicular to the conducting layers in the ab-plane. Physical properties within the ab-plane are generally isotropic, as compared with those along the c-axis. In Ginzburg-Landau theory the anisotropic behavior of a layered superconductor can be characterized by

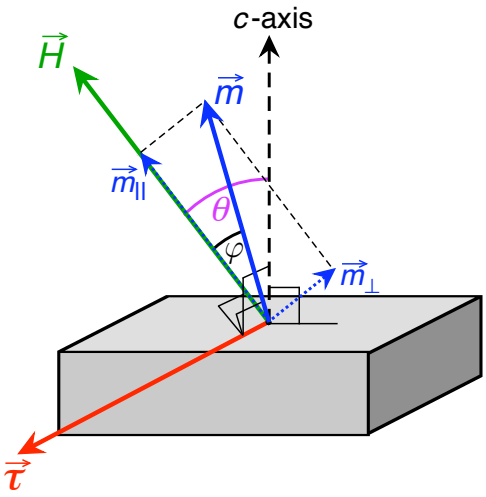

Figure 2.1: Definition of the magnetic torque $\vec{\tau}$ following Eq. (2.24). The angle θ is measured between the direction of the applied magnetic field $\vec{H}$ and the c-axis of the crystal, whereas φ denotes the angle between $\vec{H}$ and the magnetic moment $\vec{m}$. The components of the magnetic moment are $\vec{m}_{\perp}$ and $\vec{m}_{||}$.

the anisotropy parameter γ according to [44, 49]

$$\gamma = \sqrt{\frac{m_c^*}{m_{ab}^*}} = \frac{\lambda_c}{\lambda_{ab}} = \frac{H_{c2}^{||ab}}{H_{c2}^{||c}} = \frac{\xi_{ab}}{\xi_c}. \tag{2.18}$$

Here m_{ab}^* and m_c^* are the effective carrier mass components[5] related to supercurrents flowing in the ab-planes and along the c-axis, respectively, λ_{ab} and λ_c the corresponding magnetic penetration depth components, $H_{c2}^{||ab}$ and $H_{c2}^{||c}$ the upper critical field components, and ξ_{ab} and ξ_c the components of the coherence length. In this framework, known as the anisotropic Ginzburg Landau theory (AGLT), Eq. (2.15) is generalized in the form

$$H_{c2}^{||c} = \frac{\Phi_0}{2\pi\mu_0\xi_{ab}^2}, \tag{2.19}$$

$$H_{c2}^{||ab} = \frac{\Phi_0}{2\pi\mu_0\xi_{ab}\xi_c}. \tag{2.20}$$

Due to this anisotropic behavior, the free energy F is consequently a function of the angle θ between the direction of the applied magnetic field and the c-axis. For an uniaxial crystal structure, the angular scaling function [50]

$$\epsilon(\theta) = \sqrt{\cos^2(\theta) + \frac{1}{\gamma^2}\sin^2(\theta)}, \tag{2.21}$$

thus, enters the free energy [51]

$$F(\theta) = \frac{\mu_0 V H^2}{2} - \frac{V\Phi_0\epsilon(\theta)H}{8\pi\lambda_{ab}^2}\ln\left(\frac{\upsilon H_{c2}^{||c}}{\epsilon(\theta)H}\right). \tag{2.22}$$

[5] In general, the effective mass and related parameters are tensors. Hence, individual parameters derived for different orientations of a physical quantity are denoted as components.

Since $F(\theta)$ is clearly anisotropic, a superconducting crystal will exhibit a magnetic torque $\tau(\theta)$ when a field is applied along an arbitrary orientation θ according to

$$\tau(\theta) = -\frac{\partial F}{\partial \theta} = -\frac{V\Phi_0 H}{16\pi\lambda_{ab}^2}\left(1-\frac{1}{\gamma^2}\right)\frac{\sin(2\theta)}{\epsilon(\theta)}\ln\left(\frac{\eta H_{c2}^{||c}}{\epsilon(\theta)H}\right). \tag{2.23}$$

Using the general relation between the magnetic moment[6] and the torque

$$\vec{\tau} = \mu_0\left(\vec{m}\times\vec{H}\right) \qquad \text{or} \qquad \tau(\theta) = \mu_0 m(\theta) H\sin(\varphi) = \mu_0 m_\perp(\theta) H, \tag{2.24}$$

where φ denotes the angle between $\vec{m}$ and $\vec{H}$ (see Fig. 2.1), the expression for the magnetic moment in a layered superconductor is obtained as

$$m(\theta) = -\frac{V\Phi_0\epsilon(\theta)}{8\pi\mu_0\lambda_{ab}^2}\ln\left(\frac{\eta H_{c2}^{||c}}{\epsilon(\theta)H}\right). \tag{2.25}$$

In conclusion, fundamental parameters of a superconductor, such as λ_{ab}, γ, and $H_{c2}^{||c}$ can be derived by studying the angular dependence of the magnetic moment $m(\theta)$.

2.3 SQUID magnetometry

Inductive techniques are well suited to measure the magnetic moment of a sample. The magnetic moment m is determined from the voltage U induced by a magnetic flux change of a moving sample in a pick-up coil system. In the centre of a single loop with radius R, the magnetic flux Φ, related to a point-dipole magnetic moment m at a distance z along the symmetry axis is

$$\Phi = \mu_0 m\frac{R^2}{2\left(z^2+R^2\right)^{3/2}}. \tag{2.26}$$

By moving the sample, the voltage $\sim \partial\Phi/\partial t$ can be recorded and analyzed as a function of the sample position z. A widely used commercial realization of this method is the SQUID (Superconducting QUantum Interference Device) magnetometer by *Quantum Design* [52]. In this instrument, the detection loops are wound in a so-called second derivative configuration (see Fig. 2.2a). Two N-turn outer coils are located at a relative distance $d = 1.5$ cm from a sandwiched $2N$-turn oppositely wound inner coil.

A magnetic moment moving on the symmetry axis z within the above described pick-up coil system generates due to the flux change a characteristic output voltage U_{SQUID}, measured by using a SQUID-sensor [53]

$$U_{\mathrm{SQUID}}(z) = C\left(\frac{2}{\left(z^2+R^2\right)^{3/2}} - \frac{1}{\left((z+d)^2+R^2\right)^{3/2}} - \frac{1}{\left((z-d)^2+R^2\right)^{3/2}}\right). \tag{2.27}$$

Here the central coil is assumed to be at $z = 0$ while the two outer coils are at $z = -d$ and $z = +d$ (see Fig. 2.2a) and C is a calibration factor, depending on the electronic amplification layout. During data acquisition, the measured voltage $U_{\mathrm{SQUID}}(z)$ is fitted to Eq. (2.27), from which the magnetic moment is calculated. As an example, a measurement of the diamagnetic response of superconducting tantalum (Ta) is shown in Fig. 2.2b.

[6] Here $\vec{m}_\perp$ is the perpendicular component of $\vec{m}$ with respect to the magnetic field $\vec{H}$.

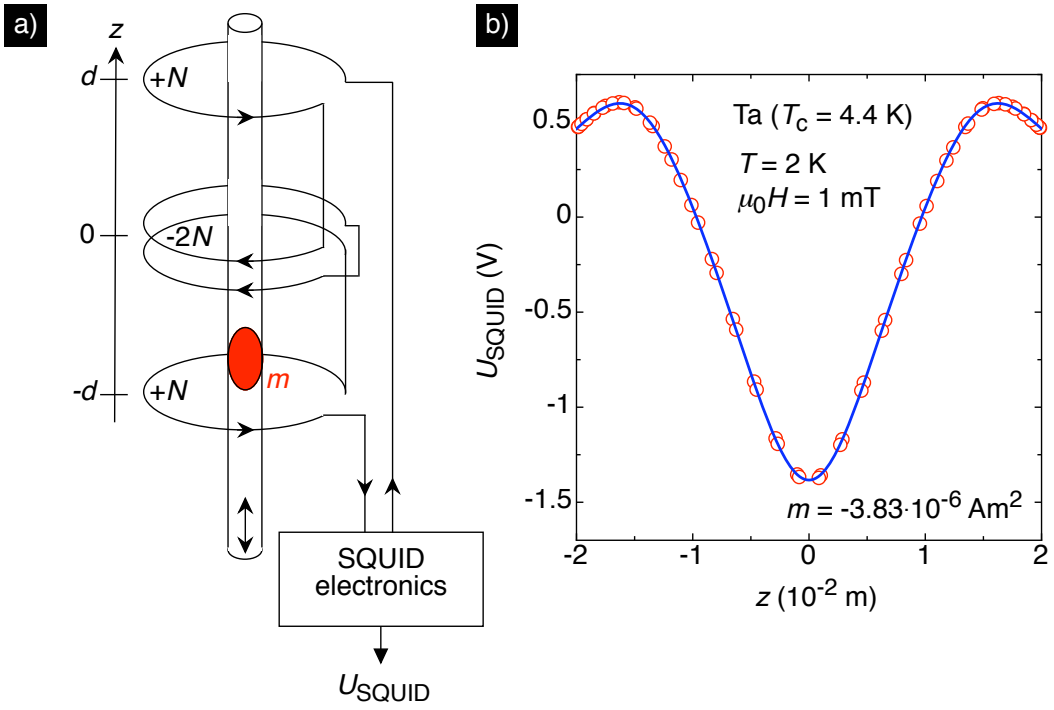

Figure 2.2: a) Diagram showing the second derivative pick-up coil configuration used in a SQUID magnetometer as explained in the text. The SQUID electronics measures the amplified signal U_{SQUID}. b) Example of a measurement of the voltage U_{SQUID} as a function of position z for a tantalum (Ta) sample at 2 K in a 1 mT field. The data were fitted to Eq. (2.27), from which the magnetic moment m was calculated.

2.4 Torque magnetometry

The magnetic torque as defined in Eq. (2.24) is directly related to the magnetic moment of a sample and the applied magnetic field strenght. Torque measurements are usually done using optical, capacitive or piezoresistive devices[7]. Recently, significant progress was made in producing piezoresistive torque sensors [26, 27, 28, 29, 30, 54, 55, 56, 57]. Depending on the actual sensor geometry, even very small single crystals ($\leq$ 100 ng) can be studied owing to the high sensitivity of piezoresistive elements. Doped silicon is generally piezoresistive, allowing highly sensitive torque sensors to be made on the micrometer scale by aid of advanced semiconductor technologies. The piezoresistive sensor elements (piezoresistive paths) are placed on silicon legs, connected with a sample platform (see Fig. 2.3). The change in resistance allows detection of a torque acting on a sample, because of the deflection of the platform in a magnetic field.

The torque sensors used in this work are based on a custom-made design (see Fig. 2.3). The sample platform is symmetrically connected by two piezoresistive legs to the frame of the sensor [57]. The central beam along the axis of rotation contains solely metallic paths, forming a current loop on the edge of the sample platform, which may be used for absolute calibration of the Wheatstone bridge [55, 57]. The piezoresistors of two sensors are connected in a Wheatstone bridge configuration, such that small resistance changes in the piezoresistors can be measured with high accuracy (see Fig. 2.4). The two sensitive legs

[7] A piezoresistive torque sensor is based on a resistance change because of internal mechanical stress.

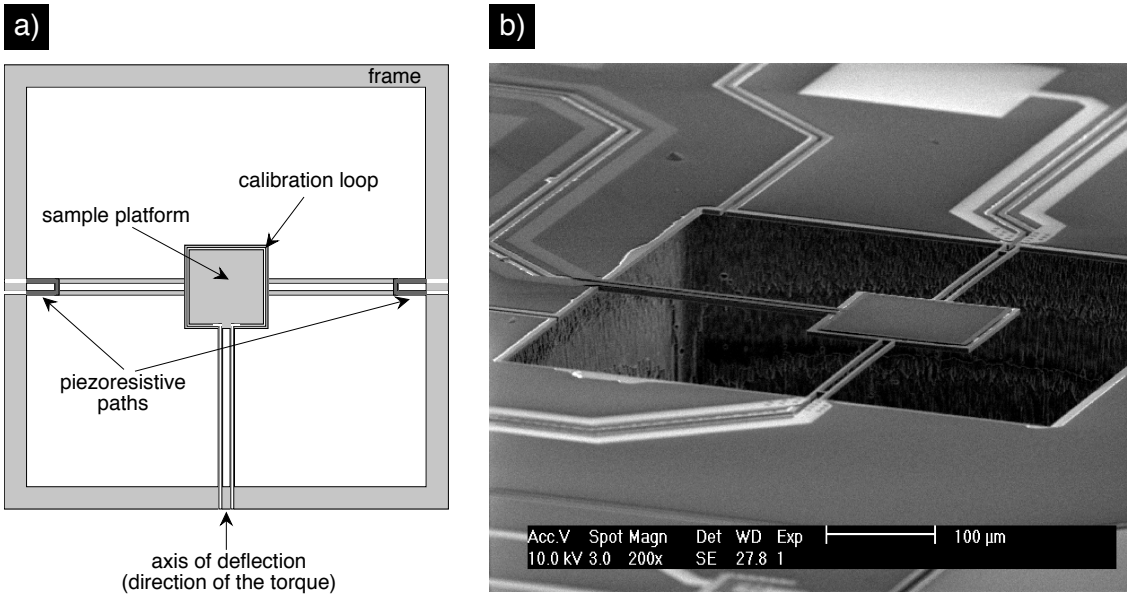

Figure 2.3: a) Schematic design of a piezoresistive torque sensor as described in the text. The main components of the sensor are indicated. b) Scanning electron microscope image of an actual piezoresistive torque sensor as used in this work. After [57].

of the *active* sensor counteract when the sensor platform deflects, and form, together with the two non-deflecting resistors of a completely separate *dummy* sensor, the Wheatstone bridge. A typical Wheatstone bridge configuration is sketched in Fig. 2.4 where the resistors of the active sensor are labeled by R_1 and R_2, and the resistance changes ΔR_1 and ΔR_2, respectively. The two resistors of the dummy sensor, R_3 and R_4, are connected as shown. When the voltage U_0 is applied over the bridge, a voltage U_{torque} can be measured across to it. Although the resistors R_1, R_2, R_3, and R_4 never match in reality, their relative change is assumed to be unique according to [55, 57]

$$\frac{\Delta R_1}{R_1} = \frac{\Delta R_2}{R_2} = \frac{\Delta R}{R} = G\tau. \tag{2.28}$$

Thus the ratio $\Delta R/R$ is proportional to the torque τ, with G as an empirical gain factor. Calculating the voltage U_{torque}, in the limit $\Delta R \ll R$ leads to

$$\begin{aligned} U_{\text{torque}} &\simeq U_0 \cdot \left[\frac{R_1R_3 - R_2R_4}{(R_1+R_4)(R_2+R_3)} + \frac{R_1R_3 + R_2R_4}{(R_1+R_4)(R_2+R_3)} \frac{\Delta R}{R} \right] \\ &= U_{\text{offset}} + U_{\text{gain}} \frac{\Delta R}{R}. \end{aligned} \tag{2.29}$$

Obviously, the measured voltage U_{torque} includes an offset term U_{offset} due to the diversity of the four involved resistors. Since U_{offset} only adds as a constant to the measured Wheatstone bridge voltage it is often disregarded. The second term in Eq. (2.29) is much more important because of its proportionality to the torque of the sample. In the ideal case when all four resistors match, Eq. (2.29) has the simple form

$$U_{\text{torque}} = \frac{U_0}{2} \frac{\Delta R}{R}. \tag{2.30}$$

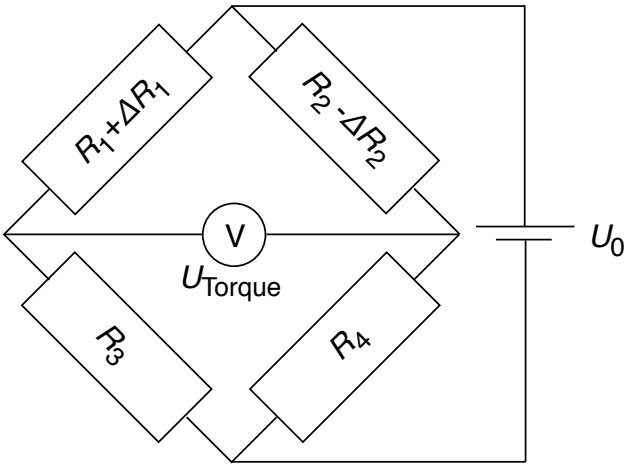

Figure 2.4: Electrical circuit of a typical Wheatstone bridge used for torque measurements, consisting of two resistors from an active sensor (R_1 and R_2) and two resistors from a dummy sensor (R_3 and R_4) as explained in the text.

Concluding, by measuring in an experiment the voltage U_{torque}, the magnetic torque of a magnetized sample can be accurately probed.

Torque magnetometry is a technique supplementary to SQUID magnetometry. While a SQUID magnetometer, as described in Sec. 2.3, measures in general the component of m parallel to the applied magnetic field $m_{||}$, a torque measurement is, according to Eq. (2.24) sensitive to the component of the magnetic moment perpendicular to the field $m_{\perp}$. Especially, in high magnetic fields torque magnetometry is a widely used technique, since due to the proportionality $\tau \sim H$ large torque signals are observed. Furthermore commercially available SQUID-magnetometers loose sensitivity at magnetic fields above 1 T. It is usually advantageous to combine SQUID and torque magnetometry in order to get complementary information on the magnetic properties of an anisotropic material.

3 Dimensional crossover in the critical regime of high-T_c superconductors

This chapter covers recent experimental results focussing on fluctuation effects in high-T_c superconductors. First, a basic overview of the theory of critical phenomena in superconductors is given. Then, experimental magnetization data of various high-T_c superconductors and their interpretation in terms of critical fluctuations are presented. In particular, the observation of 3D-xy critical phenomena in the two-band superconductor MgB_2 and the cuprate superconductors $YBa_2Cu_4O_8$ and $Bi_2Sr_2CaCu_2O_{8+\delta}$ will be discussed.

3.1 A brief introduction to critical phenomena

When in the superconducting state T_c is approached, the London approximation discussed in Sec. 2.1 breaks down, since fluctuations of the order parameter ψ are not taken into account. Conventional low-T_c superconductors, for which fluctuation effects are usually negligible, are well described by the London mean-field approach. In high-T_c superconductors, however, T_c is about an order of magnitude higher, what enhances fluctuations considerably. A deeper understanding of fluctuations, universality, and critical phenomena in general can be gained, within the renormalization group theory of Wilson [58]. In general terms, any thermodynamic system which undergoes a phase transition shows *universal behavior* close to the critical point T_c [58, 59]. The concept of *scaling laws* between *critical exponents*, and related *universal scaling functions* is of vital importance to the modern theory of criticality [60, 61].

Continuous second-order phase transitions in a thermodynamic system are characterized by a continuous change of state from a disordered to an ordered phase, and consequently lead to a reduction in symmetry of the system at T_c [58, 59]. It is convenient to define the reduced temperature t as

$$t = \frac{T}{T_c} - 1. \tag{3.1}$$

Near T_c (where $|t| \to 0$), there are observable physical quantities, denoted as $\mathcal{P}$, which exhibit, if subjected to fluctuations, a characteristic temperature dependence as

$$\mathcal{P} = \mathcal{P}^{\pm} |t|^{\alpha_{\mathcal{P}}}, \tag{3.2}$$

evincing singular behavior at T_c [58, 59, 60, 61]. Here $\alpha_{\mathcal{P}}$ and $\mathcal{P}^{\pm}$ are known as the critical exponent and the critical amplitude of $\mathcal{P}$, respectively, where

$$\pm = \mathrm{sign}(t) \tag{3.3}$$

distinguishes wheater the transition is approached from above (+) or from below (-) T_c.

The broken symmetry below T_c can be connected to an order parameter, a concept

first introduced by Landau [43]. For a continuous transition, the order parameter has its maximum value at zero temperature, decreases with increasing temperature, and vanishes at and above T_c [61]. The correlation length ξ_i, where the index i denotes some crystallographic orientation within an uniaxial system[1], describes the spatial extent over which fluctuations of the order parameter are relevant. In different words, the length scale ξ_i defines the size of the domains, within which the order parameter is correlated[2] [58, 59, 60, 61]. These domains are expected to become very large close to T_c and diverge at T_c, according to

$$\xi_i = \xi_{i0}^{\pm}|t|^{-\nu}, \tag{3.4}$$

where ν is the critical exponent and $\xi_{i0}^{\pm}$ are the critical amplitudes of the correlation length [61]. In this context, fluctuations of the order parameter are dominant at T_c. The critical exponent ν is the same above and below T_c, whereas the critical amplitude ξ_{i0}^{+} is different from ξ_{i0}^{-}.

The singular behavior of the normalized specific heat c, derived from the total specific heat[3] C, is characterized by the critical exponent α according to

$$c = \frac{C}{V k_B} = -\frac{T}{k_B}\frac{\partial^2 f}{\partial T^2} = \frac{\mathcal{A}^{\pm}}{\alpha}|t|^{-\alpha}. \tag{3.5}$$

Here $\mathcal{A}^{\pm}$ denote the critical amplitudes of the specific heat singularity [61]. Furthermore, ν and α are not independent on each other, but related by the Josephson scaling law in three dimensions (D=3) [61]

$$\alpha = 2 - D\nu = 2 - 3\nu. \tag{3.6}$$

The renormalization group theory predicts that due to symmetry reasons only a finite set of configurations for the critical exponents and amplitude ratios are possible, forming so-called universality classes. Within a given universality class the full set of critical exponents and certain critical amplitude ratios are well-defined and universal among all the systems of this class [61]. Thus, systems belonging to the same universality class will show the same critical behavior. A certain universality class is uniquely defined by the dimension D of a system and the number of components N of the order parameter [28, 61]. For example, the 3D-xy universality class corresponds to $D = 3$ and $N = 2$. Well known representatives of the 3D-xy universality class are the λ-transition at T_λ in superfluid ^{4}He, the magnetic transition at T_c (Curie temperature) of a three dimensional easy-plane ferromagnet, and the superconducting transition at T_c in superconductors as it will be discussed in Sec. 3.2. Although the microscopical details of all these systems are completely different, universality for all the critical exponents is granted by renormalization group theory [58].

[1] Within an uniaxial system, the index i is either $i = c$ for the properties along the c-axis, or $i = ab$ for the properties in the ab-plane. This definition is equivalent with the one in Sec. 2.2.

[2] Since the correlation length, defined within the concepts of critical phenomena, is somewhat related to the mean-field coherence length in Eq. (2.8), both physical quantities are labeled with the same variable ξ_i.

[3] The total specific heat C is defined by the free energy density f of the system since $C = -VT\partial^2 f/\partial T^2$.

3.2 3D-xy critical phenomena in type II superconductors

The order parameter of a superconductor is represented by a two-component vector ψ, as defined along with Eq. (2.1)

$$\psi = |\psi| \mathrm{e}^{i\phi}. \tag{3.7}$$

Since the order parameter ψ is fully determined by the two independent components $|\psi|$ and ϕ, superconductors are systems with $N = 2$. Superconductors are three dimensional systems ($D = 3$), in particular close to T_c, and thus belong to the 3D-xy universality class. Accordingly, when thermal fluctuations dominate, a bulk type II superconductor is expected to exhibit 3D-xy critical behavior sufficiently close to T_c [61, 62]. This needs to be reconsidered if additional fluctuations of the vector potential $\vec{A}$ are taken into account [28, 63]. Nevertheless, for extreme type-II superconductors, such as the high-T_c superconductors, the coupling to vector potential fluctuations is weak [61]. Consequently, there is a temperature range close to T_c, in which vector potential fluctuations can be neglected, so that type II superconductors indeed belong to the 3D-xy universality class [61, 62]. The deviation from mean-field behavior for high-T_c superconductors can be understood by noting that thermal fluctuations are much stronger than in conventional superconductors, which is because their free energy density multiplied by the correlation volume is comparable to the thermal energy in a wide temperature range around T_c [64]. Since the Ginzburg-Landau functional in Eq. (2.1) only weakly depends on the phase ϕ, already a small thermal energy can give rise to large phase fluctuations, causing a loss in coherence of the macroscopic phase and a breakdown of superconductivity. In contrast, thermal fluctuations in $|\psi|$ are mostly negligible [28, 61]. Enhanced fluctuations in the high-T_c superconductors, thus, lead to a suppression of superconductivity due to lack of phase coherence, much more than due to pair breaking and a suppression of the superfluid density $n_\mathrm{s}^* = |\psi|^2$ [28, 61, 65].

Though extreme type II superconductors belong to the 3D-xy universality class, a rigid fluctuation based analysis is desired in order to get insight into the critical phenomena related to superconductivity. The predictions of renormalization group theory [58, 61] imply, that the singular part of the free energy density of an extreme type II superconductor adopts the scaling form

$$f_\mathrm{s} = \frac{\mathcal{Q}^{\pm} \gamma k_\mathrm{B} T}{\xi_{ab}^3} \mathcal{G}^{\pm}(z). \tag{3.8}$$

Approaching T_c, the correlation lengths [see Eq. (3.4)] diverge as

$$\xi_{ab,c} = \xi_{ab0,c0}^{\pm} \, |t|^{-\nu} \qquad \text{with} \qquad t = \frac{T}{T_\mathrm{c}} - 1 \tag{3.9}$$

and the anisotropy is given by

$$\gamma = \frac{\xi_{ab}}{\xi_c} = \frac{\xi_{ab0}^{\pm}}{\xi_{c0}^{\pm}}. \tag{3.10}$$

In this case the magnetization per unit volume, $M = m/V$, of an uniaxial superconductor in a magnetic field H_c applied along the c-axis[4] fulfills the scaling form [61, 63, 66, 67]

$$\frac{M}{TH_c^{1/2}} = -\frac{\mathcal{Q}^{\pm}\gamma k_{\mathrm{B}}\mu_0^{1/2}}{\Phi_0^{3/2}}\mathcal{F}^{\pm}(z)\,, \tag{3.11}$$

where

$$\mathcal{F}^{\pm}(z) = z^{-1/2}\frac{d\mathcal{G}^{\pm}}{dz}, \tag{3.12}$$

$$z = x^{-1/2\nu} = \frac{(\xi_{ab0}^{\pm})^2\,|t|^{-2\nu}\,\mu_0 H_c}{\Phi_0}. \tag{3.13}$$

In this relation $\mathcal{F}^{\pm}(z)$ and $\mathcal{G}^{\pm}(z)$ are universal scaling functions with $\mathcal{G}^{\pm}(z=0) = 1$ where x and z are the associated scaling variables.

Supposing that fluctuations dominate, the critical exponents [see Eq. (3.6)] in the 3D-xy universality class are given by [68]

$$\nu \simeq 0.671 \simeq 2/3 \qquad \text{and} \qquad \alpha = 2 - 3\nu \simeq -0.013. \tag{3.14}$$

Additionally, the universal critical amplitude relations are [61, 63, 66, 67, 68]

$$\frac{\xi_{ab0}^{-}}{\xi_{ab0}^{+}} = \frac{\xi_{c0}^{-}}{\xi_{c0}^{+}} \simeq 2.21, \qquad \frac{\mathcal{Q}^{-}}{\mathcal{Q}^{+}} \simeq 11.5, \qquad \frac{\mathcal{A}^{+}}{\mathcal{A}^{-}} = 1.07, \tag{3.15}$$

and

$$\mathcal{A}^{-}\xi_{a0}^{-}\xi_{b0}^{-}\xi_{c0}^{-} \simeq \mathcal{A}^{-}(\xi_{ab0}^{-})^2\xi_{c0}^{-} = \frac{\mathcal{A}^{-}(\xi_{ab0}^{-})^3}{\gamma} = (\mathcal{R}^{-})^3, \qquad \mathcal{R}^{-} \simeq 0.815. \tag{3.16}$$

Furthermore, the transition temperature T_c, the critical amplitude of the correlation length ξ_{c0}^{-}, and the critical amplitude of the in-plane magnetic penetration depth λ_{ab0}, are not independent within the 3D-xy universality class, but related through the universal relation [61, 63, 66, 67]

$$k_{\mathrm{B}}T_c = \frac{\Phi_0^2}{4\pi^2\mu_0}\frac{\xi_{c0}^{-}}{\lambda_{ab0}^2} = \frac{\Phi_0^2}{4\pi^2\mu_0}\frac{\xi_{ab0}^{-}}{\gamma\lambda_{ab0}^2}. \tag{3.17}$$

The existence of a magnetization at T_c, of a magnetic penetration depth below T_c, and of a magnetic susceptibility above T_c implies the following asymptotic forms of the scaling function [61, 63, 66, 67]

$$\begin{aligned}
\mathcal{Q}^{\pm}\,\frac{1}{\sqrt{z}}\frac{d\mathcal{G}^{\pm}}{dz}\bigg|_{z\to\infty} &= \mathcal{Q}^{\pm}c_{\infty}^{\pm}, \\
\mathcal{Q}^{-}\,\frac{d\mathcal{G}^{-}}{dz}\bigg|_{z\to 0} &= \mathcal{Q}^{-}c_0^{-}\,(\ln z + c_1)\,, \\
\mathcal{Q}^{+}\,\frac{1}{z}\frac{d\mathcal{G}^{+}}{dz}\bigg|_{z\to 0} &= \mathcal{Q}^{+}c_0^{+},
\end{aligned} \tag{3.18}$$

[4] For simplicity, and allowing an easier comparison between theory and experiment, this derivation assumes the magnetic field H_i to be applied along the c-axis ($i = c$). In general, all of the calculations can be done with an arbitrary orientation of the magnetic field.

with the universal coefficients

$$\mathcal{Q}^- c_0^- \simeq -0.7, \qquad \mathcal{Q}^+ c_0^+ \simeq 0.9, \qquad \mathcal{Q}^\pm c_\infty^\pm \simeq 0.5, \qquad c_1 \simeq 1.76. \tag{3.19}$$

For extreme type II superconductors there is considerable experimental evidence for 3D-xy critical behavior close to T_c [61, 62, 63, 64, 65, 66, 67, 69, 70, 71, 72, 73, 74, 75, 76, 77, 78, 79, 80, 81, 82, 83, 84, 85]. Critical behavior is, however, not readily observed in experiments because of the presence of disorder and inhomogeneities. As far as disorder is concerned, there is the Harris criterion [86], which states that disorder is irrelevant at the unperturbed critical point, provided that the specific heat critical exponent α is negative. Since, according to Eq. (3.14), α is negative in the 3D-xy universality class, disorder is not expected to play an essential role. But if inhomogeneity is involved, superconductivity is restricted to homogeneous domains of finite spatial extent, denoted $L_{ab,c}$. Therefore, the global system is inhomogeneous and the transition appears characteristically rounded[5], uncovering a finite size effect (FSE) [87, 88] since the correlation lengths $\xi_{ab,c}$, defined in Eq. (3.9), cannot grow beyond the extent of the homogenous domains $L_{ab,c}$. Hence, as long as $\xi_{ab,c} < L_{ab,c}$ the critical properties of the fictitious homogeneous system can be explored.

A magnetic field H_c applied to a type II superconductor, additionally acts as an external perturbation due to vortex-formation. The correlation length will not be able to grow beyond a limiting length which must be related to the distance of neighboring vortex lines. Therefore, in type II superconductors exposed to a magnetic field H_c, there is an additional limiting length scale [78, 79]

$$L_{H_c} = \sqrt{\frac{\Phi_0}{a\mu_0 H_c}}. \tag{3.20}$$

Here $a \simeq 3.12$ is a geometrical factor related to the average distance between vortex lines [63, 65, 78, 79]. Thus, the higher the magnetic field H_c, the smaller becomes L_{H_c}, confining superconductivity into cylinders of diameter L_{H_c}. Since the density of vortex lines becomes larger with increasing magnetic field, a limiting field $H_{\rm pc}(T)$ is approximately attained when the vortex cores overlap. Here a crossover is expected to occur, since superconductivity, expected to behave three-dimensional far below T_c, is spacially confined into quasi one-dimensional cylinders at the field $H_{\rm pc}(T)$.

In summary, due to the FSE's, the correlation lengths cannot grow beyond the limiting length scales [79]

$$L_{ab,c} = \xi_{ab,c}(t_{\rm p}) = \xi^\pm_{ab0,c0}|t_{\rm p}|^{-\nu}, \tag{3.21}$$

$$L_{H_c} = \xi_{ab}(t_{\rm p}) = \xi^\pm_{ab0}|t_{\rm p}|^{-\nu} = \sqrt{\frac{\Phi_0}{a\mu_0 H_c}}. \tag{3.22}$$

This scenario is somewhat different from the mean-field expectation Eq. (2.15), having instead of a reputed singularity at $H_{c2}(T)$ now a rounded transition due to inhomogeneities and due to the perturbing magnetic field H_c. From Eq. (3.22) the crossover lines $H_{\rm pc}(T)$,

[5] The word *rounded* denotes the fact, that by inclusion of the discussed effects, the sharp phase transition, expected to occur at T_c, smears effectively out and any sharp feature at the transition appears rounded; as for instance within a magnetization experiment.

which replace the mean-field estimate $H_{c2}(T)$, are derived to be

$$\begin{aligned} H_{\rm pc}(T<T_{\rm c}) &= \frac{\Phi_0}{a\mu_0(\xi^-_{ab0})^2}(1-T/T_{\rm c})^{4/3}, \\ H_{\rm pc}(T>T_{\rm c}) &= \frac{\Phi_0}{a\mu_0(\xi^+_{ab0})^2}(T/T_{\rm c}-1)^{4/3}. \end{aligned} \tag{3.23}$$

The mean-field parameter $H_{c2}(T)$, thus, is completely masked by the FSE's. As far as the magnetization is concerned, the inhomogeneity induced FSE is expected to set in close to $T_{\rm c}$ when $\xi_{ab,c}$ approaches $L_{ab,c}$, while for a field applied along the c-axis, the magnetic field induced FSE dominates when $L_{H_c} \lesssim L_{ab}$. Accordingly, magnetization measurements are not only expected to provide estimates for the critical properties of the associated fictitious homogeneous system, but in addition have the potential to uncover inhomogeneities that give rise to a FSE. As a unique size of the homogeneous domains is unlikely, the smallest extent will determine the scale where the increase of the respective correlation length starts to deviate from the critical behavior of a fictitious homogenous system.

In conclusion, close to $T_{\rm c}$ the correlation lengths are confined within their limiting length scales $L_{ab,c}$ and L_{H_c}. The magnetic field induced FSE drives the system to a 3D to 1D crossover. The system behaves three-dimensional far away from $T_{\rm c}$, but the confinement of the diverging correlation length at the phase boundary leads to spatially separated, quasi one-dimensional superconducting cylinders, and a rounded transition at the temperature $T_{\rm p}(H_c)$ according to:

	Inhomogeneity induced FSE	Magnetic field induced FSE
$T<T_{\rm c}$	$T_{\rm p}=T_{\rm c}\left[1-\left(\xi^-_{i0}/L_c\right)^{3/2}\right]$	$T_{\rm p}(H_c)=T_{\rm c}\left[1-\left(a\mu_0 H_c\left(\xi^-_{ab0}\right)^2/\Phi_0\right)^{3/4}\right]$
$T>T_{\rm c}$	$T_{\rm p}=T_{\rm c}\left[1+\left(\xi^+_{i0}/L_c\right)^{3/2}\right]$	$T_{\rm p}(H_c)=T_{\rm c}\left[1+\left(a\mu_0 H_c\left(\xi^+_{ab0}\right)^2/\Phi_0\right)^{3/4}\right]$

The presence of a FSE prevents the occurrence of a continuous phase transition in the (H_c,T)-plane along $H_{c2}(T)$-lines as predicted by the mean-field approach [89, 90] and instead, the superconducting system will behave quasi one dimensional close to $T_{\rm c}$ [66, 82, 83, 84]. The effect of this discussion is demonstrated, if the magnetization is related to the specific heat in terms of the Maxwell relation

$$\frac{1}{V}\frac{\partial\,(C/T)}{\partial H_c}\bigg|_T = \mu_0\,\frac{\partial^2 M}{\partial T^2}\bigg|_{H_c}. \tag{3.24}$$

Extending the scaling form for the specific heat [Eq. (3.5)], to include an applied magnetic field H_c, according to [61]

$$c=-\frac{T}{k_{\rm B}}\frac{\partial^2 f_{\rm s}}{\partial T^2}=\frac{\mathcal{A}^-}{\alpha}\,|t|^{-\alpha}\,\mathcal{H}(x) \qquad \text{with} \qquad x=\frac{t}{H_c^{1/2\nu}}, \tag{3.25}$$

the scaling form

$$T\mu_0 H_c \frac{\partial^2 M}{\partial T^2} = k_B T H_c \frac{\partial (c/T)}{\partial H_c} = -\frac{k_B \mathcal{A}^-}{2\alpha\nu} H_c^{-\alpha/2\nu} x^{1-\alpha} \frac{\partial}{\partial x} \mathcal{H}(x) \tag{3.26}$$

is obtained, describing the shape of a dip-like function. The FSE thus replaces the singularity at the upper critical field $H_{c2}(T)$ obtained in the Gaussian mean-field approximation [90], where $\partial^2 M/\partial T^2|_{T\approx T_c} = 0$. From Eq. (3.14), where the critical exponents are given as $\alpha \simeq -0.013 \approx 0$ and $1/2\nu \approx 3/4$, magnetization data plotted as $TH_c\, \partial^2 M/\partial T^2$ versus $tH_c^{-3/4}$ are expected to collapse onto a single curve according to Eq. (3.26). Even more, the scaling in Eq. (3.26) will reveal any additional phase transition within the fluctuation regime close to T_c. It is widely accepted, that in extreme type II superconductors a vortex-lattice melting transition occurs at the melting line $H_m(T)$, being first microscopically observed by means of μSR by Lee *et al.* [91] and found to be a first-order phase transition [92, 93]. Such a first-order phase transition is expected to be visible in the scaling form Eq. (3.26) as a pronounced peak in the dip-like function, obtained from the magnetic field induced FSE [66, 80].

3.3 Observation of a finite size effect and 3D-xy critical behavior in single crystal MgB_2

In conventional low-T_c superconductors, the observation of thermal fluctuation effects is limited because the large correlation volume makes these effects small, thus favoring a macroscopic mean-field behavior. By contrast, the high transition temperature T_c and small correlation volume in a variety of cuprate superconductors lead to significant fluctuation effects [61, 63]. In MgB_2, where superconductivity was discovered in 2001 [24], the correlation volume and T_c lie between these extremes, suggesting that fluctuation effects should be observable. Indeed, excess magneto-conductance [94], fluctuation effects in the specific heat [95], and fluctuating diamagnetic magnetization [96] were observed in powder samples.

In order to explore the importance of critical fluctuations in MgB_2, the reversible magnetization of a high quality MgB_2 single crystal ($V \simeq 1.4 \times 10^{-11}$ m^3) was studied in the vicinity of the zero field transition temperature $T_c \simeq 38.83$ K for several magnetic fields up to 30 mT, applied along the crystallographic c-axis. The nearly rectangular shaped MgB_2 single crystal investigated here was grown by high-pressure synthesis [97]. The magnetic moment m was measured by a commercial *Quantum Design* DC-SQUID magnetometer MPMS XL. Zero-field cooled and field cooled magnetization curves were compared in order to determine the reversible part of the magnetization and to suppress unwanted contributions from irreversible magnetization. Figure 3.1 shows the measured reversible magnetic moment as a function of temperature close to T_c. Although there appears to be an almost constant negative shift in the curves with increasing magnetic field, similar to what would be expected for mean-field behavior, critical fluctuations are qualitatively evident in the pronounced rounding of the magnetization curve near T_c, which is attributable to FSE's occurring at the phase transition.

Though MgB_2 is a two-gap superconductor the scaling analysis uncovers below T_c remarkable consistency with 3D-xy critical behavior. To explore the evidence for an inhomogeneity induced FSE, attributable to a system consisting of homogeneous domains of

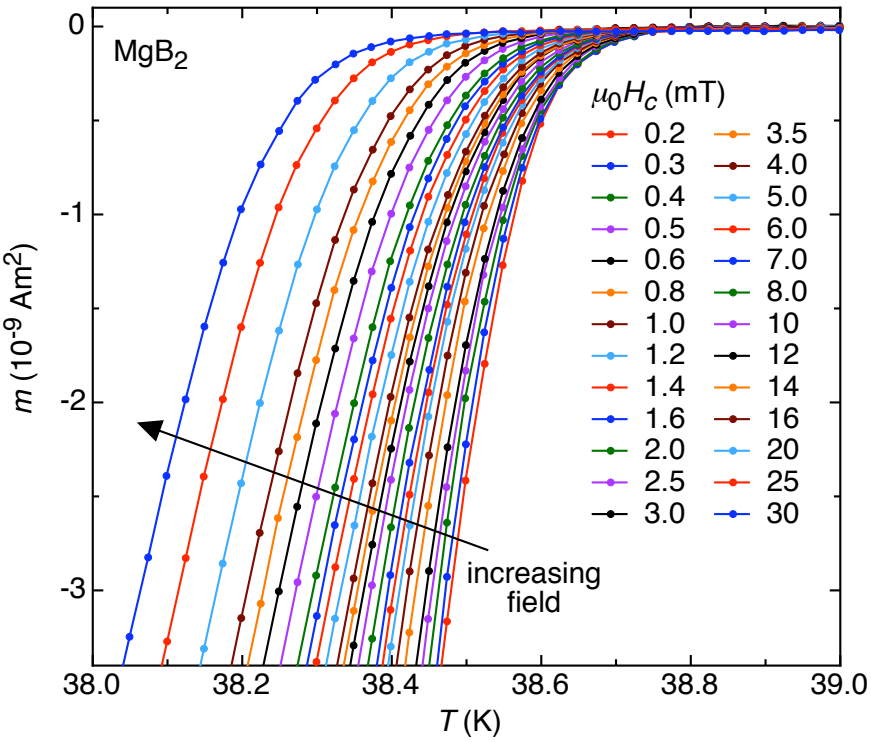

Figure 3.1: Temperature dependence of the magnetic moment m of the MgB_2 single crystal in the vicinity of T_c for various magnetic fields H_c applied along the c-axis. The lines are guides to the eye. After [83].

finite extent only, the scaling form Eq. (3.11) is rewritten with aid of Eq. (3.18), resulting in

$$\frac{M}{T} = -\frac{k_B}{\Phi_0 \xi_c} \mathcal{Q}^- \frac{d\mathcal{G}^-}{dz} = -|t|^{2/3} \frac{k_B}{\Phi_0 \xi_{c0}} \mathcal{Q}^- \frac{d\mathcal{G}^-}{dz}\bigg|_{z=H_c L_{ab}^2/\Phi_0} . \tag{3.27}$$

Sufficiently close to T_c, however, the correlation length ξ_c approaches L_c, the extent of the homogeneous domains along the c-axis, and the scaling form reduces to a constant value

$$\frac{M}{T} = -\frac{k_B}{\Phi_0 L_c} \mathcal{Q}^- \frac{d\mathcal{G}^-}{dz}\bigg|_{z=H_c L_{ab}^2/\Phi_0} . \tag{3.28}$$

In Fig. 3.2 the scaling of $|t|^{-2/3}|m|/(VT)$ versus $|t| = 1 - T/T_c$ is presented for $T < T_c$. Below $|t_p(L_c)| \simeq 3 \cdot 10^{-4}$ apparently a limiting behavior of the magnetization data is obtained because of the inhomogeneity induced FSE. The analysis leads to a remarkable estimate of the extent of homogeneous domains in MgB_2 along the respective crystallographic axes

$$L_{ab} \approx L_c \geqslant 5 \times 10^{-7} \text{ m}, \tag{3.29}$$

suggesting that MgB_2 is rather homogeneous compared to the cuprates, for which much lower values of $L_{ab,c} \sim 10^{-9} - 10^{-8}$ m are observed [79, 81].

Obviously a magnetic field induced FSE is involved at the phase boundary. The result is summarized in Fig. 3.3 in terms of the (H_c, T)-phase diagram. Several dimensional crossover lines are associated with limits for the correlation lengths due to the overlapping of

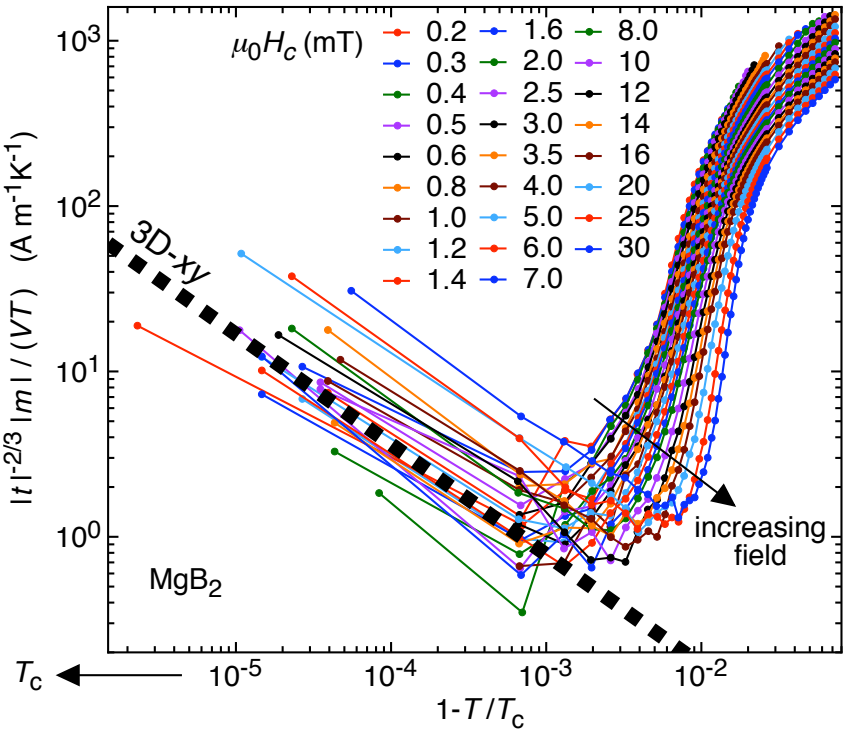

Figure 3.2: Scaling plot for $T < T_c$ of $|t|^{-2/3}|m|/(VT)$ versus $1 - T/T_c$ for single crystal MgB_2. Below $|t_p(L_c)| \simeq 3 \cdot 10^{-4}$, a limiting behavior of the magnetization data is obtained, dictated by the inhomogeneity induced finite size effect. The solid lines are guides to the eye and the dotted line denotes the limiting behavior $|t|^{-2/3}|m|/(VT) \sim -|t|^{-2/3}$. After [83].

vortex cores. An analysis leads to the estimates for the critical amplitudes of the correlation lengths

$$\xi^-_{ab0} = 5.2 \times 10^{-9} \text{ m}, \qquad \text{and} \qquad \xi^+_{ab0} = 2.4 \times 10^{-9} \text{ m}. \tag{3.30}$$

It implies that in type II superconductors, such as MgB_2, in a magnetic field H_c superconductivity is confined into cylinders with diameter L_{H_c}, as given in Eq. (3.22). Thus, for a magnetic field applied along the c-axis, there is below T_c a 3D to 1D crossover line

$$H_{pc}(T) = \frac{\Phi_0}{a\mu_0(\xi^-_{ab0})^2}(1 - T/T_c)^{4/3}. \tag{3.31}$$

Accordingly, below T_c there is no continuous phase transition in the (H_c, T)-plane along the H_{c2}-lines as predicted by the mean-field approach. Nevertheless, the magnetic field induced FSE is not restricted to the superconducting phase ($T < T_c$) and indeed, above T_c a line

$$H_{pc}(T) = \frac{\Phi_0}{a\mu_0(\xi^+_{ab0})^2}(T/T_c - 1)^{4/3} \tag{3.32}$$

is present, where the 3D to 1D crossover occurs and uncondensed pairs are confined into cylinders. The crossover lines are presented in Fig. 3.3, by making use of Eq. (3.30). Additionally, the vortex-lattice melting transition line $H_{mc}(T)$ is shown in Fig. 3.3, as estimated from magnetization data [96]. Within the 3D-xy model $H_{mc}(T)$ follows the same temperature dependence as $H_{pc}(T)$ below T_c[see Eq. (3.31)].

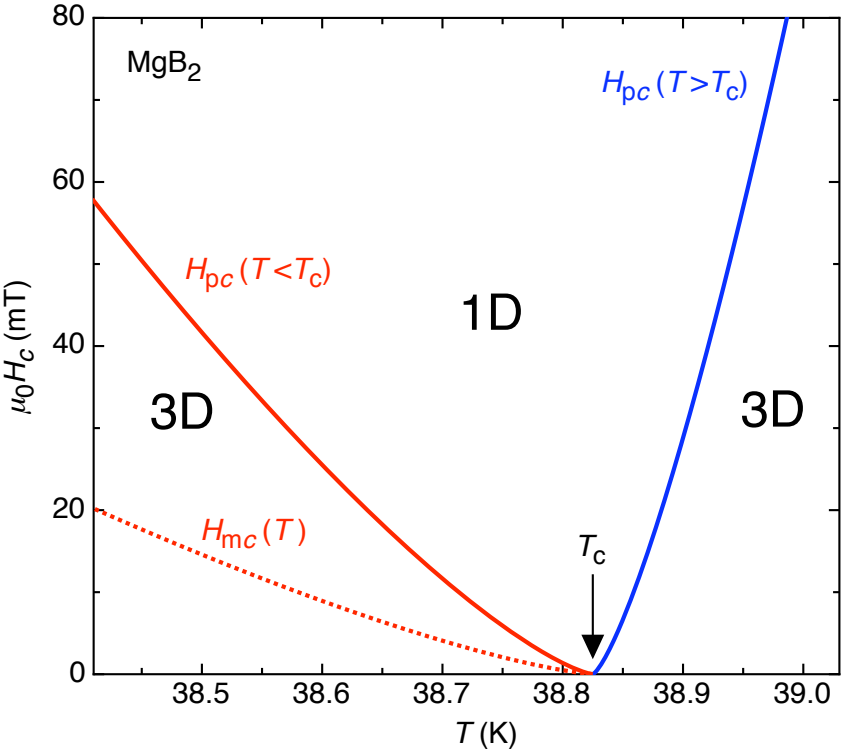

Figure 3.3: Dimensional crossover lines $H_{pc}(T)$, stemming from the magnetic field induced FSE in single crystal MgB_2. Below T_c a 3D to 1D crossover takes place, where superconductivity is confined into cylinders with diameter L_{H_c}, as given in Eq. (3.23). Consistently, there is above T_c a 3D to 1D crossover, where uncondensed pairs are confined into cylinders. The dotted line denotes the location of the vortex-lattice melting transition line $H_{mc}(T)$. After [83].

3.4 Magnetic field induced 3D to 1D crossover in stoichiometric $YBa_2Cu_4O_8$

Fluctuation effects are known to be strongly enhanced in high-T_c cuprate superconductors due to their anisotropic structure and high zero-field transition temperature T_c [61, 98]. For $YBa_2Cu_4O_8$ and related compounds various studies indicate the importance of critical fluctuations [99, 100, 101, 102]. The cuprate $YBa_2Cu_4O_8$ has a stoichiometric structure and is available as high quality single crystals [103, 104]. This, in particular, allows the magnetic field induced FSE to be probed, since the additional rounding of the transition because of inhomogeneities is reduced.

The $YBa_2Cu_4O_8$ single crystal investigated in this work was grown by a high-pressure synthesis method [104]. The volume of the sample was estimated to be 3.9×10^{-10} m^3. The magnetic moment m was measured with a commercial *Quantum Design* DC-SQUID magnetometer MPMS XL. For these investigations the applied magnetic field was oriented along the c-axis of the crystal. Temperature dependent magnetization curves were measured for different magnitudes of the field, and the zero-field cooled and field cooled data were compared in order to access the reversible magnetization. The superconducting susceptibility was finally obtained by correcting the measured data for the normal state and sample holder contributions. In Fig. 3.4 some of the measured magnetization data m versus T are shown

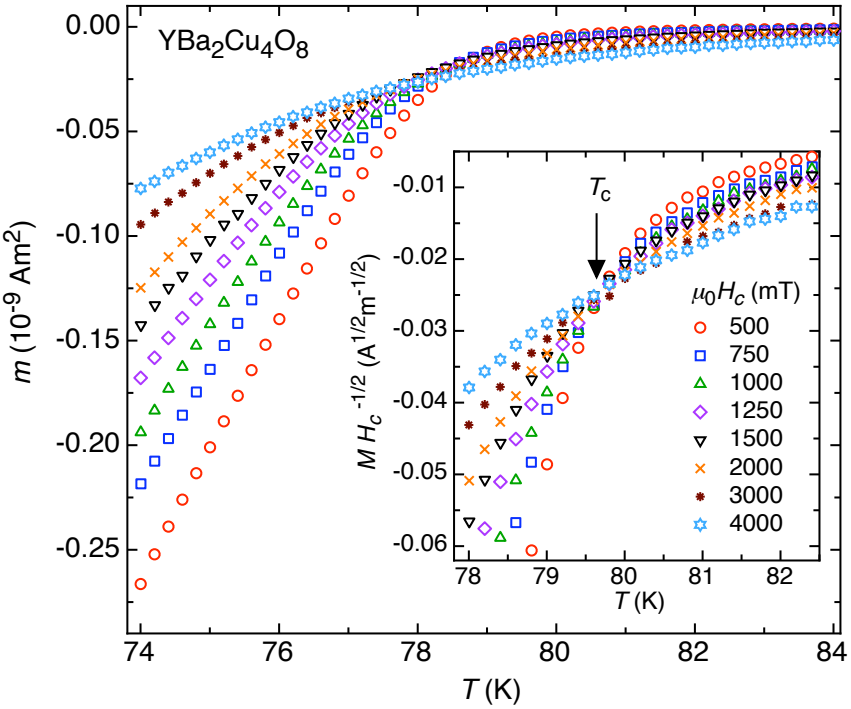

Figure 3.4: Temperature dependent magnetic moment m of the studied $YBa_2Cu_4O_8$ single crystal for various magnetic fields H_c applied along the c-axis in the vicinity of T_c. The inset demonstrates the scaling plot $MH_c^{-1/2}$ versus T from which $T_c \simeq 79.6$ K is estimated. After [84].

for magnetic fields H_c applied along the c-axis. The inset to the Fig. 3.4 demonstrates how $T_c \simeq 79.6$ K was estimated: According to Eqs. (3.11), (3.18), and (3.19), a plot of $MH_c^{-1/2}$ versus T should exhibit a crossing point at T_c, where a field independent value

$$\left.\frac{M}{H_c^{1/2}}\right|_{T_c} = -0.5 k_B T_c \gamma \mu_0^{1/2} \Phi_0^{-3/2} \tag{3.33}$$

is expected. The anisotropy parameter is estimated as

$$\gamma \simeq 8.3. \tag{3.34}$$

In Fig. 3.5 the scaling $TH_c\,\partial^2 M/\partial T^2$ versus $x = tH_c^{-3/4}$ is presented[6] for various fields H_c. Apparently, the data collapse reasonably well onto a single curve. The peak marked by the dashed arrow at the position x_m denotes the vortex-lattice melting transition. Furthermore, the 3D to 1D crossover due to the magnetic field induced FSE takes place at x_p as indicated by the solid arrow. The appearance of these characteristic points differ clearly from mean-field behavior for which $\partial^2 M/\partial T^2|_{T\approx T_c} = 0$. Note that both the peak and the dip are hardly visible in the raw magnetization shown in Fig. 3.4. The location of the dip determines the line

$$x_p = t_p H_c^{-3/4} \simeq -1.07 \times 10^{-6}\ \mathrm{m^{3/4} A^{-3/4}}, \tag{3.35}$$

in the (H_c, T)-plane, where the 3D to 1D crossover is found. The 3D to 1D crossover field H_{pc} is accordingly calculated to follow the line

$$\mu_0 H_{pc}(T) \simeq 115\ \mathrm{T} \cdot (1 - T/T_c)^{4/3}. \tag{3.36}$$

[6]The variable x is introduced in Eq. (3.13).

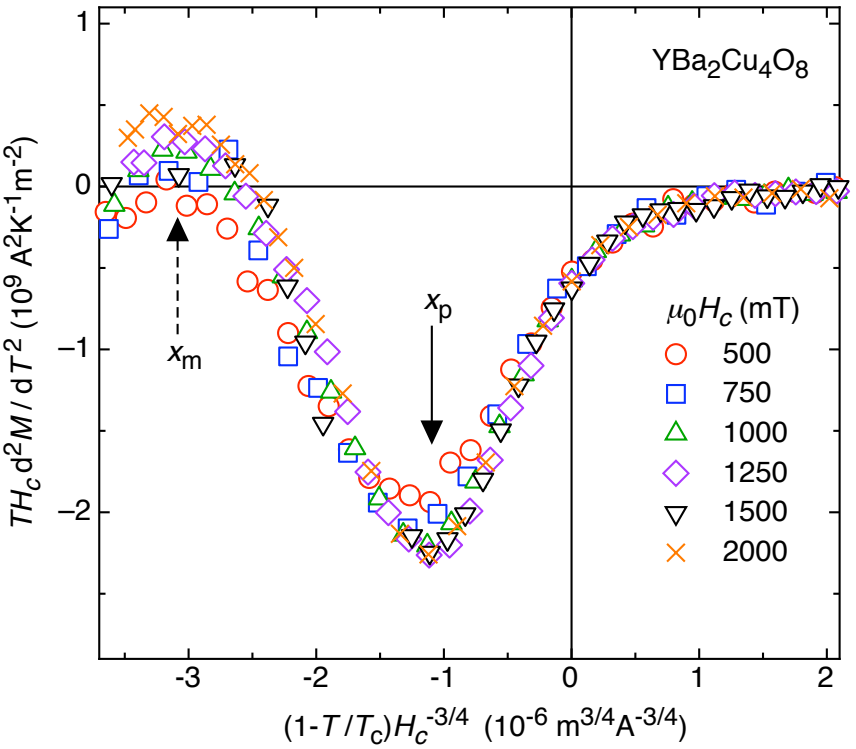

Figure 3.5: Scaling plot of $TH_c\,\partial^2 M/\partial T^2$ versus $tH_c^{-3/4}$ for single crystal $YBa_2Cu_4O_8$. The data collapse well onto a single curve. The peak marked by x_m, corresponds to the vortex-lattice melting transition. The dip marked by x_p, shows the position of the 3D to 1D crossover due to the magnetic field induced FSE. After [84].

In addition, there is a pronounced peak at

$$x_m = t_m H_c^{-3/4} \simeq -3.13 \times 10^{-6}\ \mathrm{m}^{3/4}\mathrm{A}^{-3/4}, \tag{3.37}$$

corresponding to the vortex-lattice melting transition. Rewritten, the melting line H_{mc} is obtained in the form

$$\mu_0 H_{mc}(T) \simeq 27\ \mathrm{T} \cdot (1 - T/T_c)^{4/3}. \tag{3.38}$$

Accordingly, the universal ratio of the reduced temperatures for the melting line H_{mc} and the 3D to 1D crossover line H_{pc} is obtained as

$$\frac{t_p\,(H_c)}{t_m\,(H_c)} \simeq 0.34, \tag{3.39}$$

This value agrees well with the estimates $t_p\,(H_c)\,/t_m\,(H_c) \simeq 0.3$ for an $NdBa_2Cu_3O_{7-\delta}$ single crystal [80] and $t_p\,(H_c)\,/t_m\,(H_c) \simeq 0.35$ for a $YBa_2Cu_3O_{6.97}$ single crystal [76] derived from data in the references shown. The vortex-lattice melting transition line H_{mc} follows the same temperature dependence as the 3D to 1D crossover line H_{pc}, hence, both are well described within the 3D-xy universality class.

3.5 Evidence for Kosterlitz-Thouless and 3D-xy critical behavior in single crystal $Bi_2Sr_2CaCu_2O_{8+\delta}$

In the previous discussion, the effect on 3D-xy critical phenomena was discussed for high-T_c type II superconductors, for correlation lengths confined within domains of finite dimensions; either due to inhomogeneities or due to the perturbation of an external magnetic field. In highly anisotropic type II superconductors, two-dimensionality is expected to contribute significantly, since the pronounced layering confines superconductivity within the CuO_2 layers. While noting that $Bi_2Sr_2CaCu_2O_{8+\delta}$ is highly anisotropic ($\gamma >> 1$) 2D-xy behavior is anticipated far from T_c as for a (Berezinskii)-Kosterlitz-Thouless transition at a temperature T_{KT} well below T_c [105, 106]. Sufficiently below the Kosterlitz-Thouless transition temperature T_{KT} the magnetization is given by [107]

$$M = \left(\frac{k_B T}{d\Phi_0} - \frac{\Phi_0}{8\pi\mu_0\lambda_{ab}^2(T)} \right) \ln\left(\frac{\Phi_0}{\mu_0 H_c a_0^2 \gamma_3} \right) \tag{3.40}$$

where ρ_s is the 2D superfluid density, related to the in-plane magnetic penetration depth λ_{ab} through

$$\rho_s(T) = \frac{d\Phi_0^2}{4\pi^2\mu_0\lambda_{ab}^2(T)}. \tag{3.41}$$

Here d is the thickness of the independent superconducting sheets, γ_3 a parameter that vanishes as T approaches T_{KT}, and a_0 the microscopic short-distance cutoff length, corre-

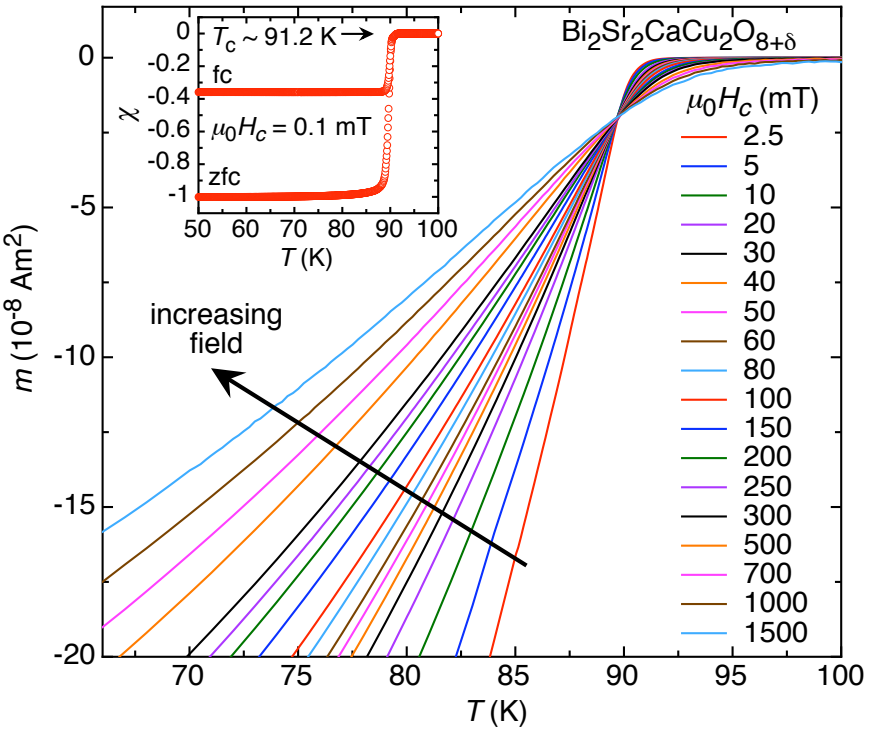

Figure 3.6: Temperature dependence of the reversible magnetic moment m at various fields applied along the c-axis of a $Bi_2Sr_2CaCu_2O_{8+\delta}$ single crystal. The inset shows a low field susceptibility measurement at 0.1 mT with an estimated $T_c \sim 91.2$ K. The rather sharp transition into the Meissner state indicates a high quality of the crystal. After [85].

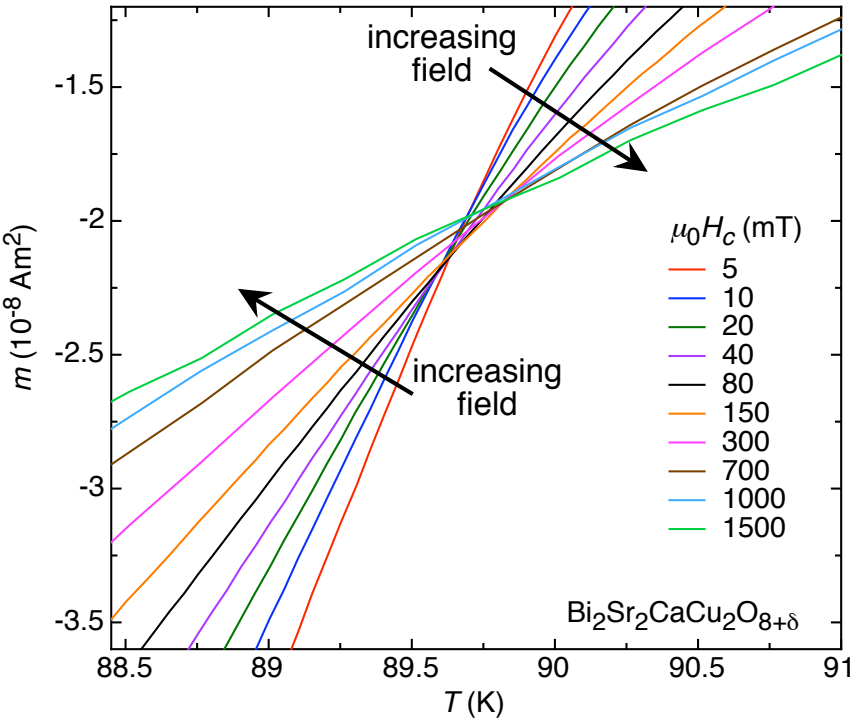

Figure 3.7: Magnetic moment m versus T at various magnetic fields for single crystal $Bi_2Sr_2CaCu_2O_{8+\delta}$, exhibiting a crossing anomaly, as it shifts from higher temperatures towards $T_{KT} \simeq 89.5$ K for decreasing fields. After [85].

sponding essentially to the diameter of the vortex cores.

The studied $Bi_2Sr_2CaCu_2O_{8+\delta}$ single crystal with a volume of $V \simeq 4.6 \times 10^{-11}$ m^3 was selected for its sharp low-field Meissner transition from a batch of several high quality single crystals [108]. The magnetization was measured in a *Quantum Design* DC-SQUID magnetometer MPMS XL. Figure 3.6 summarizes the measured temperature dependence of the magnetic moment in fields ranging from 2.5 mT to 1500 mT, applied along the c-axis. The reversible superconducting diamagnetic magnetic moment m was obtained by comparing field cooled and zero-field cooled data. Due to a substantial pinning contribution at low magnetic fields, data below 2.5 mT were omitted. During analysis, a temperature dependent normal state paramagnetic background was subtracted.

A characteristic feature of a 2D superconductor is the crossing phenomenon occurring at fixed magnetic fields and above T_{KT} in the plot M versus T [61, 107]. A glance at Fig. 3.7 reveals that this phenomenon is well confirmed above $T = 89.5$ K $\simeq T_{KT}$. Indeed, there is a downward shift of the crossing point towards T_{KT} from above as the field decreases. The same behavior was also found in highly anisotropic $TlBa_2Ca_2Cu_3O_{9+\delta}$, $Bi_2Sr_2CuO_{6+\delta}$ and underdoped $La_{2-x}Sr_xCuO_4$ single crystals [61, 109, 110, 111]

In order to estimate the bulk T_c, Eqs. (3.11), (3.18), and (3.19) are invoked, revealing that the plot $mH_c^{-1/2}$ versus T should exhibit a crossing point at T_c, where Eq. (3.33) is expected to hold. According to Fig. 3.8, which shows $mH_c^{-1/2}$ versus T, there is a crossing point at $T_c \simeq 91.21$ K, where

$$\frac{m}{H_c^{1/2}} \simeq -2.39 \times 10^{-11} \text{ A}^{1/2}\text{m}^{5/2}. \tag{3.42}$$

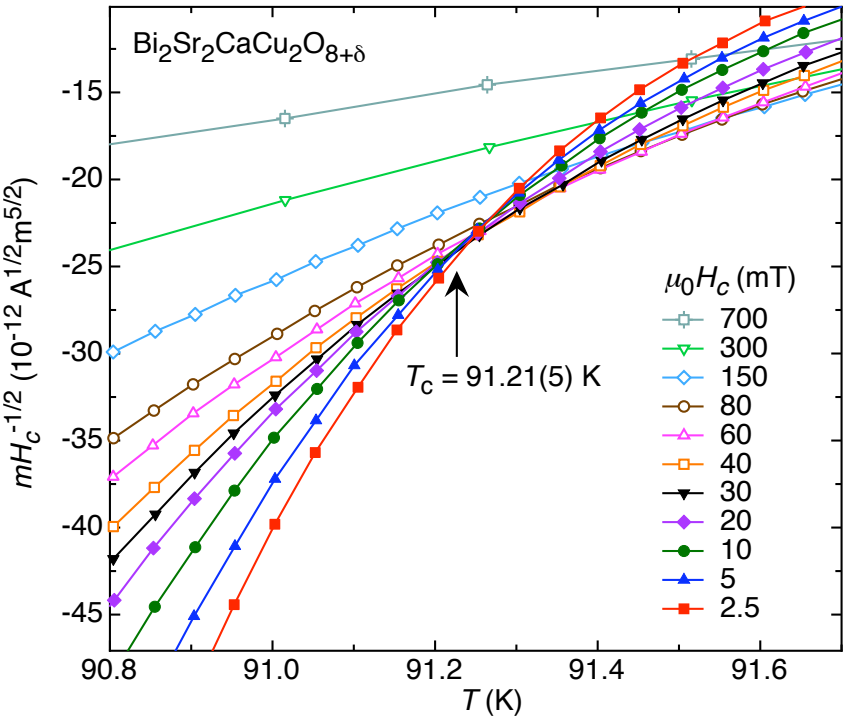

Figure 3.8: Scaling plot of $m/H_c^{1/2}$ versus T yielding the estimated $T_c \simeq 91.21$ K at the crossing point. From the quantitative measure $mH_c^{-1/2}$ the anisotropy parameter for the $Bi_2Sr_2CaCu_2O_{8+\delta}$ single crystal is estimated to be $\gamma \simeq 69$. After [85].

With $V \simeq 4.6 \times 10^{-11}$ m^3 this yields with Eq. (3.33) for the anisotropy parameter $\gamma \simeq 69$. Given this rather large anisotropy, the 2D-xy to 3D-xy crossover should occur rather close to the bulk T_c.

Another property in which KT-behavior should be observable is the magnetic field dependence of the specific heat peak. Instead of a "simple" 3D-xy behavior, as observed for MgB_2 in Sec. 3.3 and for $YBa_2Cu_4O_8$ in Sec. 3.4, here an additional 2D-xy to 3D-xy crossover is expected. Indeed, in $Bi_2Sr_2CaCu_2O_{8+\delta}$ the specific heat peak was found to shift [112] in contradiction to the expected generic behavior [see Eq. (3.23)] as observed for less anisotropic high-T_c superconductors (see for instance Figs. 3.3 and 3.5) [66, 83, 84]. Given the Maxwell relation in Eq. (3.24), which relates magnetization and specific heat, this anomalous shift should also be observable in terms of the magnetization. In Fig. 3.9 the plot of $\partial^2 m/\partial T^2|_{H_c}$ versus T for various magnetic fields reveals a consistent anomalous shift of the specific heat peak, as the average dip position shifts with increasing field towards higher temperatures. Noting that this shift occurs slightly above $T_{KT} \simeq 89.5$ K, this peculiarity is evident to be induced by 2D-xy behavior, whereas 3D-xy behavior is expected to set in close to $T_c \simeq 91.21$ K. Between T_{KT} and T_c, thus, a 2D to 3D crossover takes place, leading to a more complex crossover region where the confinement of the corellation lengths is dominating. As observed for less anisotropic superconductors like MgB_2 in Sec. 3.3 and $YBa_2Cu_4O_8$ in Sec. 3.4, the mean-field parameter H_{c2} is completely masked by the FSE.

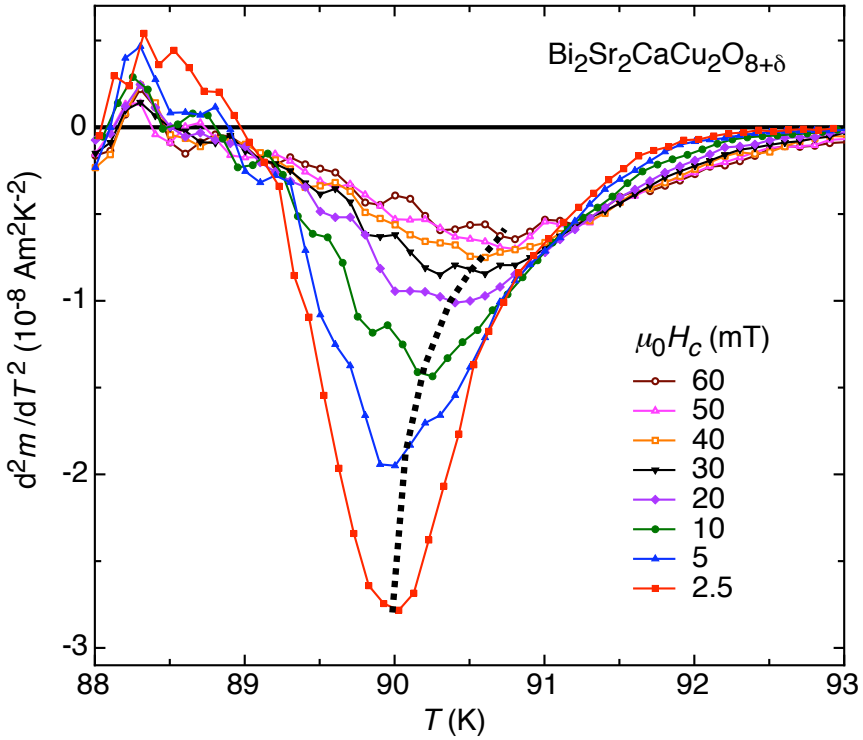

Figure 3.9: Scaling plot of $\partial^2 m/\partial T^2\big|_{H_c}$ versus T according to Eq. (32) for single crystal $Bi_2Sr_2CaCu_2O_{8+\delta}$. The dotted line indicates the locations of the respective minima $T_p(H_c)$. After [85].

3.6 Publications related to Chapter 3

- *Probing superconductivity in MgB_2 confined to magnetic field tuned cylinders by means of critical fluctuations*
  S. Weyeneth, T. Schneider, N. D. Zhigadlo, J. Karpinski, and H. Keller
  J. Phys.: Condens. Matter **20**, 135208 (2008).

- *3D-xy critical properties of $YBa_2Cu_4O_8$ and magnetic-field-induced 3D to 1D crossover*
  S. Weyeneth, T. Schneider, Z. Bukowski, J. Karpinski, and H. Keller
  J. Phys.: Condens. Matter **20**, 345210 (2008).

- *Evidence for Kosterlitz-Thouless and three-dimensional XY critical behavior in $Bi_2Sr_2CaCu_2O_{8+\delta}$*
  S. Weyeneth, T. Schneider, and E. Giannini
  Phys. Rev. B **79**, 214504 (2009).

3.6.1 Publication I: Probing superconductivity in MgB_2 confined to magnetic field tuned cylinders by means of critical fluctuations

S. Weyeneth, T. Schneider, N. D. Zhigadlo, J. Karpinski, and H. Keller
J. Phys.: Condens. Matter **20**, 135208 (2008).

Abstract
We report and analyze reversible magnetization measurements on a high quality MgB_2 single crystal in the vicinity of the zero-field transition temperature, $T_c \simeq 38.83$ K, at several magnetic fields up to 30 mT, applied along the c-axis. Though MgB_2 is a two gap superconductor, our scaling analysis uncovers remarkable consistency with 3D-xy critical behavior, revealing that close to criticality the order parameter is a single complex scalar as in ^{4}He. This opens up the window onto the exploration of the magnetic field induced finite size effect, whereupon the correlation length transverse to the applied magnetic field H_i applied along the i-axis cannot grow beyond the limiting magnetic length $L_{H_i} = (\Phi_0/(a\mu_0 H_i))^{1/2}$ with $a \simeq 3.12$, related to the average distance between vortex lines. We find unambiguous evidence for this finite size effect. It implies that in type II superconductors, such as MgB_2, there is the 3D to 1D crossover line $H_{pi}(T) = (\Phi_0/(a\mu_0 \xi^-_{j0}\xi^-_{k0}))(1 - T/T_c)^{4/3}$ with $i \neq j \neq k$ and $\xi^{\pm}_{i0,j0,k0}$ denotes the critical amplitudes of the correlation lengths above (+) and below (−) T_c along the respective axis. Consequently, above $H_{pi}(T)$ and $T < T_c$ superconductivity is confined to cylinders with diameter L_{H_i} (1D). In contrast, above T_c and $H_{pi}(T) = (\Phi_0/(a\mu_0 \xi^+_{j0}\xi^+_{k0}))(T/T_c - 1)^{4/3}$ the uncondensed pairs are confined to cylinders. Accordingly, there is no continuous phase transition in the (H_c, T) -plane along the H_{c2}-lines as predicted by the mean-field treatment.

DOI: 10.1088/0953-8984/20/13/135208
PACS numbers: 74.40.+k, 74.25.Ha, 74.70.Ad, 74.25.Qt

The original publication is electronically available at:
http://www.iop.org/EJ/abstract/0953-8984/20/13/135208

Open access repositories:
http://www.zora.uzh.ch/10513
http://arxiv.org/abs/0705.3775

At completion of this thesis, according to the Thomson Reuters ISI Web of Knowledge database, this article has been cited at least 2 times.

IOP Publishing Journal of Physics: Condensed Matter
J. Phys.: Condens. Matter **20** (2008) 135208 (8pp) doi:10.1088/0953-8984/20/13/135208

Probing superconductivity in MgB_2 confined to magnetic field tuned cylinders by means of critical fluctuations

S Weyeneth[1], T Schneider[1], N D Zhigadlo[2], J Karpinski[2] and H Keller[1]

[1] Physik-Institut der Universität Zürich, Winterthurerstrasse 190, CH-8057 Zürich, Switzerland
[2] Laboratory for Solid State Physics, ETH Zürich, CH-8093 Zürich, Switzerland

E-mail: wstephen@physik.uzh.ch

Received 23 November 2007, in final form 13 February 2008
Published 7 March 2008
Online at stacks.iop.org/JPhysCM/20/135208

Abstract
We report and analyze reversible magnetization measurements on a high quality MgB_2 single crystal in the vicinity of the zero-field transition temperature, $T_c \simeq 38.83$ K, at several magnetic fields up to 300 Oe, applied along the c-axis. Although MgB_2 is a two-gap superconductor our scaling analysis uncovers remarkable consistency with 3D-xy critical behavior, revealing that close to criticality the order parameter is a single complex scalar as in ^{4}He. This opens up the window onto the exploration of the magnetic field induced finite size effect, whereupon the correlation length transverse to the applied magnetic field H_i applied along the i-axis cannot grow beyond the limiting magnetic length $L_{H_i} = (\Phi_0/(aH_i))^{1/2}$ with $a \simeq 3.12$, related to the average distance between vortex lines. We find unambiguous evidence for this finite size effect. It implies that in type II superconductors, such as MgB_2, there is a 3D–1D crossover line $H_{pi}(T) = (\Phi_0/(a\xi^-_{j0}\xi^-_{k0}))(1 - T/T_c)^{4/3}$ with $i \neq j \neq k$ and $\xi^{\pm}_{i0,j0,k0}$ denotes the critical amplitudes of the correlation lengths above $(+)$ and below $(-)$ T_c along the respective axis. Consequently, above $H_{pi}(T)$ and $T < T_c$ superconductivity is confined to cylinders with diameter L_{H_i} (1D). In contrast, above T_c and $H_{pi}(T) = (\Phi_0/(a\xi^+_{j0}\xi^+_{k0}))(T/T_c - 1)^{4/3}$ the uncondensed pairs are confined to cylinders. Accordingly, there is no continuous phase transition in the (H, T)-plane along the H_{c2}-lines as predicted by the mean-field treatment.

(Some figures in this article are in colour only in the electronic version)

1. Introduction

Since the discovery of superconductivity in MgB_2 [1] many important properties have already been measured, particularly outside the regime where thermal fluctuations dominate. The observation of thermal fluctuation effects have been limited in conventional low-T_c superconductors because the large correlation volume makes these effects very small compared to the mean-field behavior. By contrast, the high transition temperature T_c and small correlation volume in a variety of cuprate superconductors lead to significant fluctuation effects [2, 3]. In MgB_2 the correlation volume and T_c lie between these extremes, suggesting that fluctuation effects will be observable. Indeed, excess magnetoconductance [4], fluctuation effects in the specific heat [5], and fluctuating diamagnetic magnetization [6] were observed recently in powder samples. Here we report and analyze reversible magnetization data of a high quality MgB_2 single crystal in the vicinity of the zero-field transition temperature, $T_c \simeq 38.83$ K, at several magnetic fields up to 300 Oe, applied along the c-axis. Though MgB_2 is a two-gap superconductor our scaling analysis uncovers below T_c remarkable consistency with 3D-xy critical behavior, revealing that the order parameter is a single complex scalar as in ^{4}He. The high quality of the single crystal made it possible to enter this regime. For this reason the magnetic field induced finite size effect, whereupon the correlation length transverse to the applied magnetic field cannot grow beyond the limiting magnetic

length $L_{H_i} = (\Phi_0/(aH_i))^{1/2}$, with the magnetic field H_i applied along the i-axis and $a \simeq 3.12$, could be verified and studied in detail. L_{H_i} is related to the average distance between vortex lines. Indeed, as the magnetic field increases, the density of vortex lines becomes greater, but this cannot continue indefinitely; the limit is roughly set on the proximity of vortex lines by the overlapping of their cores. This finite size effect implies that in type II superconductors superconductivity in a magnetic field is confined to cylinders with diameter L_{H_i}. Accordingly, there is below T_c a 3D–1D crossover line $H_{pi}(T) = (\Phi_0/(a\xi^-_{j0}\xi^-_{k0}))(1 - T/T_c)^{4/3}$ with $i \neq j \neq k$. $\xi^{\pm}_{i0,j0,k0}$ denotes the critical amplitudes of the correlation lengths above (+) and below (−) T_c along the respective axis. It circumvents the occurrence of the continuous phase transition in the (H, T)-plane along the H_{c2}-lines predicted by the mean-field treatment. Furthermore, our analysis of the magnetization data of Lascialfari *et al* [6] taken on a MgB_2 powder sample also confirms that there is a magnetic field induced finite size effect above T_c as well. It leads to the line $H_{pi}(T) = (\Phi_0/(a\xi^+_{j0}\xi^+_{k0}))(T/T_c - 1)^{4/3}$, where the 3D–1D crossover occurs and the uncondensed pairs are forced to be confined in cylinders.

The paper is organized as follows: next we sketch the scaling theory appropriate for a neutral type II superconductor with a single complex scalar order parameter falling in the absence of a magnetic field into the 3D-xy universality class. The following section is devoted to experimental details, the presentation of our magnetization data for $T \lesssim T_c$, their analysis by means of the scaling theory and the analysis of the magnetization data of Lascialfari *et al* [6] taken on a MgB_2 powder sample for $T \gtrsim T_c$.

Though MgB_2 is a two-gap superconductor, an effective one-gap description appears to apply sufficiently close to T_c [7]. As we concentrate on the effects of thermal fluctuations in the presence of comparatively low magnetic fields we adopt this effective one-gap description. Accordingly, the order parameter is assumed to be a single complex scalar. To derive the scaling form of the magnetization in the fluctuation dominated regime we note that the scaling of the magnetic field is in terms of the number of flux quanta per correlation area. Thus, when the thermal fluctuations of the order parameter dominate, the singular part of the free energy per unit volume of a homogeneous system scales as [2, 3, 8–13]

$$f_s = \frac{Q^{\pm} k_B T}{\xi_{ab}^2 \xi_c} G^{\pm}(z) = \frac{Q^{\pm} k_B T \gamma}{\xi_{ab}^3} G^{\pm}(z), \qquad z = \frac{H_c \xi_{ab}^2}{\Phi_0}. \tag{1}$$

$Q^{\pm}$ is a universal constant and $G^{\pm}(z)$ a universal scaling function of its argument, with $G^{\pm}(z = 0) = 1$. $\gamma = \xi_{ab}/\xi_c$ denotes the anisotropy, ξ_{ab} the zero-field in-plane correlation length and H_c the magnetic field applied along the c-axis. Approaching T_c, the in-plane correlation length diverges as

$$\xi_{ab} = \xi^{\pm}_{ab0} |t|^{-\nu}, \qquad t = T/T_c - 1, \qquad \pm = \mathrm{sgn}(t). \tag{2}$$

Supposing that 3D-xy fluctuations dominate, the critical exponents are given by [14]

$$\nu \simeq 0.671 \simeq 2/3, \qquad \alpha = 2\nu - 3 \simeq -0.013, \tag{3}$$

and there are the universal critical amplitude relations [2, 3, 9–11, 14]

$$\frac{\xi^-_{ab0}}{\xi^+_{ab0}} = \frac{\xi^-_{c0}}{\xi^+_{c0}} \simeq 2.21, \qquad \frac{Q^-}{Q^+} \simeq 11.5, \qquad \frac{A^+}{A^-} = 1.07, \tag{4}$$

and

$$A^- \xi^-_{a0}\xi^-_{b0}\xi^-_{c0} \simeq A^- \left(\xi^-_{ab0}\right)^2 \xi^-_{c0} = \frac{A^- \left(\xi^-_{ab0}\right)^3}{\gamma} = \left(R^-\right)^3 \qquad R^- \simeq 0.815, \tag{5}$$

where $A^{\pm}$ is the critical amplitude of the specific heat singularity, defined as

$$c = \left(A^{\pm}/\alpha\right) |t|^{-\alpha} + B. \tag{6}$$

Furthermore, in the 3D-xy universality class T_c, ξ^-_{c0} and the critical amplitude of the in-plane penetration depth λ_{ab0} are not independent but related by the universal relation [2, 3, 9–11, 14],

$$k_B T_c = \frac{\Phi_0^2}{16\pi^3} \frac{\xi^-_{c0}}{\lambda^2_{ab0}} = \frac{\Phi_0^2}{16\pi^3} \frac{\xi^-_{ab0}}{\gamma \lambda^2_{ab0}}. \tag{7}$$

From the singular part of the free energy per unit volume given by (1) we derive for the magnetization per unit volume $m = M/V = -\partial f_s/\partial H$ the scaling form

$$\frac{m}{T H_c^{1/2}} = -\frac{Q^{\pm} k_B \xi_{ab}}{\Phi_0^{3/2} \xi_c} F^{\pm}(z), \qquad F^{\pm}(z) = z^{-1/2} \frac{\mathrm{d}G^{\pm}}{\mathrm{d}z}, \qquad z = x^{-1/2\nu} = \frac{\left(\xi^{\pm}_{ab0}\right)^2 |t|^{-2\nu} H_c}{\Phi_0}. \tag{8}$$

In terms of the variable x this scaling form is similar to Prange's [15] result for Gaussian fluctuations. More generally, the existence of the magnetization at T_c, of the penetration depth below T_c and of the magnetic susceptibility above T_c imply the following asymptotic forms of the scaling function [2, 3, 8, 12, 13]

$$\begin{aligned} Q^{\pm} \frac{1}{\sqrt{z}} \frac{\mathrm{d}G^{\pm}}{\mathrm{d}z}\bigg|_{z\to\infty} &= Q^{\pm} c^{\pm}_{\infty}, \\ Q^- \frac{\mathrm{d}G^-}{\mathrm{d}z}\bigg|_{z\to 0} &= Q^- c^-_0 (\ln(z) + c_1), \\ Q^+ \frac{1}{z} \frac{\mathrm{d}G^+}{\mathrm{d}z}\bigg|_{z\to 0} &= Q^+ c^+_0, \end{aligned} \tag{9}$$

with the universal coefficients [2, 8]

$$Q^- c^-_0 \simeq -0.7, \qquad Q^+ c^+_0 \simeq 0.9, \qquad q = Q^{\pm} c^{\pm}_{\infty} \simeq 0.5. \tag{10}$$

The scaling form (8) with the limits (9), together with the critical exponents (3) and the universal relations (4) and (7), are characteristic critical properties of an extreme type II superconductor. They provide the basis to extract from experimental data the doping dependence of the non-universal critical properties, including the transition temperature T_c, the

critical amplitudes of correlation lengths $\xi^{\pm}_{ab0,c0}$, the anisotropy γ etc, while the universal relations are independent of the doping level.

In practice, however, there are limitations set by the presence of disorder, inhomogeneities and the magnetic field induced finite size effect. Nevertheless, as far as cuprate superconductors are concerned there is considerable evidence for 3D-xy critical behavior, except for a rounded transition close to T_c [2, 3, 10–13, 16–24]. As far as disorder is concerned there is the Harris criterion [25], which states that short range correlated and uncorrelated disorder is irrelevant at the unperturbed critical point, provided that the specific heat exponent α is negative. Since in the 3D-xy universality class α is negative (3), disorder is not expected to play an essential role. However, when superconductivity is restricted to homogeneous domains of finite spatial extent $L_{ab,c}$, the system is inhomogeneous and the resulting rounded transition uncovers a finite size effect [26, 27] because the correlation lengths $\xi_{ab,c} = \xi^{\pm}_{ab0,c0}|t|^{-\nu}$ cannot grow beyond $L_{ab,c}$, the respective extent of the homogeneous domains. Hence, as long as $\xi_{ab,c} < L_{ab,c}$ the critical properties of the fictitious homogeneous system can be explored. There is considerable evidence that this scenario accounts for the rounded transition seen in the specific heat [2] and the magnetic penetration depths [28]. In type II superconductors, exposed to a magnetic field H_i, there is an additional limiting length scale $L_{H_i} = \sqrt{\Phi_0/(aH_i)}$ with $a \simeq 3.12$ [29], related to the average distance between vortex lines [3, 29–31]. Indeed, as the density of vortex lines becomes greater with increasing magnetic field, this cannot continue indefinitely. The limit is roughly set on the proximity of vortex lines by the overlapping of their cores. Due to these limiting lengths the correlation lengths cannot grow beyond [29]

$$\xi_i\left(t_p\right) = \xi^{\pm}_{0i}\left|t_p\right|^{-\nu} = L_i,$$
$$\sqrt{\xi_i\left(t_p\right)\xi_j\left(t_p\right)} = \sqrt{\xi^{\pm}_{0i}\xi^{\pm}_{0j}}\left|t_p\right|^{-\nu} = \sqrt{\Phi_0/\left(aH_k\right)} = L_{H_k}, \tag{11}$$

where $i \neq j \neq k$. As far as the magnetization is concerned the inhomogeneity induced finite size effect is expected to set in close to T_c, where $\xi_{ab,c}$ approaches $L_{ab,c}$, while for a field applied along the c-axis, the magnetic finite size effect dominates when $L_{H_c} = \sqrt{\Phi_0/(aH_c)} \lesssim L_{ab}$. Accordingly, sufficiently extended magnetization measurements are not expected to provide estimates for the critical properties of the associated fictitious homogeneous system only, but do have the potential to uncover inhomogeneities giving rise to a finite size effect as well. As a unique size of the homogeneous domains is unlikely, the smallest extent will set the scale where the growth of the respective correlation length starts to deviate from the critical behavior of the homogeneous counterpart.

To recognize the implications of the magnetic field induced finite size effect, it is instructive to note that the scaling form of the singular part of the free energy per unit volume, (1), is formally equivalent to an uncharged superfluid, such as ^{4}He, constrained to a cylinder of diameter $L_{H_c} = (\Phi_0/(aH_c))^{1/2}$. Indeed, the finite size scaling theory predicts that, in a system confined to a barlike geometry, $L \cdot L \cdot H$, with $H \to \infty$, an observable $O(t, L)$ scales as [26, 27, 32]

$$\frac{O\left(t, L\right)}{O\left(t, \infty\right)} = f_O\left(y\right), \qquad y = \xi\left(t\right)/L, \tag{12}$$

where $f(y)$ is the finite size scaling function. As in the confined system a 3D–1D crossover occurs, there is a rounded transition only. Indeed, because the correlation length $\xi(t)$ cannot grow beyond L there is a rounded transition at

$$\begin{aligned} T_p &= T_c\left(1 - \left(\frac{\xi_0^-}{L}\right)^{1/\nu}\right) \qquad : T < T_c. \\ T_p &= T_c\left(1 + \left(\frac{\xi_0^+}{L}\right)^{1/\nu}\right) \qquad : T > T_c. \end{aligned} \tag{13}$$

The resulting rounding of the specific heat singularity and the shift of the smeared peak from T_c to T_p is well confirmed in ^{4}He [33, 34]. In superconductors the specific heat adopts with (6) and (12) the finite size scaling form

$$c\left(t, L_{H_c}\right) = \frac{A^-}{\alpha}\left|t\right|^{-\alpha} f_c\left(tL_{H_c}^{1/\nu}\right), \qquad \nu \simeq 2/3, \tag{14}$$

where

$$f_c\left(tL_{H_c}^{1/\nu}\right) = \begin{cases} 1 & : tL_{H_c}^{1/\nu} = 0 \quad : t \leqslant 0 \\ c_\infty^-\left(tL_{H_c}^{1/\nu}\right)^{\alpha} & : L_{H_c}^{1/\nu} \to \infty \quad : t < 0 \end{cases} \tag{15}$$

Invoking (13) in the form $|t_p| = (\xi^-_{ab0}/L_{Hc})^{1/2\nu}$, the height of the rounded specific heat peak at T_p vanishes then as

$$\begin{aligned} c\left(T_p\right) &= \frac{A^-}{\alpha}\left|t_p\right|^{-\alpha} f_c\left(\left(\xi^-_{ab0}\right)^{1/\nu}\right) \\ &= \frac{A^-}{\alpha}\left(\frac{\left(\xi^-_{ab0}\right)^2 a}{\Phi_0}\right)^{-\alpha/2\nu} f_c\left(\left(\xi^-_{ab0}\right)^{1/\nu}\right) H_c^{-\alpha/2\nu}, \end{aligned} \tag{16}$$

because $\alpha < 0$ (3). The resulting shift and reduction of the rounded specific heat peak with increasing magnetic field is in a variety of type II superconductors [29], including MgB_2 [35, 5], qualitatively well confirmed.

Furthermore, (14) yields with Maxwell's relation

$$\left.\frac{\partial(C/T)}{\partial H_c}\right|_T = \left.\frac{\partial^2 M}{\partial T^2}\right|_{H_c} \tag{17}$$

the scaling form

$$\frac{\partial(c/T)}{\partial H_c} = \frac{\partial^2 m}{\partial T^2} = -\frac{k_B A^{\pm}}{2\alpha\nu T} H_c^{-1-\alpha/2\nu}|x|^{1-\alpha}\frac{\partial f_c^{\pm}}{\partial x}. \tag{18}$$

2. Experiment, results and analysis

The nearly rectangular shaped MgB_2 single crystal investigated here was fabricated by high-pressure synthesis described in detail elsewhere [36]. Its calculated volume is 1.4×10^{-5} cm^3 and agrees with susceptibility measurements in the Meissner state with the calculated shape factor 0.81. The magnetic moment was measured by a commercial Quantum Design DC-SQUID magnetometer MPMS XL, allowing us to

J. Phys.: Condens. Matter **20** (2008) 135208 S Weyeneth *et al*

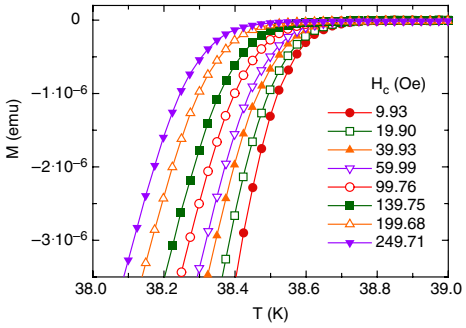

Figure 1. Measured magnetic moment of the studied MgB_2 single crystals for different magnetic fields applied along the crystals' c-axis. The lines are guides to the eye. For clarity not all measured fields are shown.

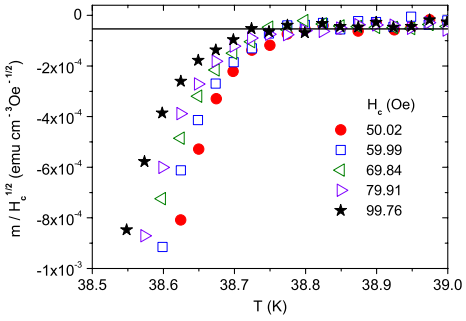

Figure 2. $m/H_c^{1/2}$ versus T for a MgB_2 single crystal with the magnetic field H_c applied along the c-axis. The solid line is $m/(T_c H_c^{1/2}) \approx -1.4 \times 10^{-6}$ (emu cm^{-3} K^{-1} Oe$^{-1/2}$) with $T_c = 38.83$ K.

achieve a temperature resolution up to 0.01 K. The installed reciprocating sample option (RSO) allows us to measure magnetic moments down to 10^{-8} emu. In our sample this allows us to detect the magnetic moment near T_c down to 25 Oe. The applied magnetic field was oriented along the c-axis of the sample. After applying the magnetic field well below T_c it was kept constant and the magnetic moment of the sample was measured at a stabilized temperature by moving the sample with a frequency of 0.5 Hz through a set of detection coils. The diamagnetic magnetization, $M = mV$, was then obtained by subtracting $M_b = 5 \times 10^{-8} H$ emu, the temperature independent paramagnetic and sample holder contributions. Zero-field cooled (ZFC) magnetization curves have been compared to field cooled (FC) data, obtained by cooling to a given temperature in the presence of different fields. Here we concentrate on the reversible regime (figure 1) close to T_c. Due to the small volume of the sample its magnetic moment can be reliably detected only below and slightly above T_c. For this reason we concentrate on the fluctuation effects below and at T_c.

To estimate T_c from the magnetization data $m(T, H_c)$ we invoke the limit $z \to \infty$. Here the scaling form (8) reduces with (9) and (10) to

$$\frac{m}{H_c^{1/2}} = -\frac{k_B q}{\Phi_0^{3/2}} \frac{\xi_{ab}}{\xi_c} T, \qquad q = Q^{\pm} c_\infty^{\pm} \simeq 0.5. \tag{19}$$

$Q^+ c_\infty^+ = Q^- c_\infty^-$ follows from the fact that $m/H_c^{1/2}$ adopts at the zero-field transition temperature T_c a unique value. Here the curves $m/H_c^{1/2}$ versus T taken at different fields H_c should cross and $m/H_c^{1/2} \gamma T_c$ adopts the universal value

$$\frac{m\xi_c(T_c)}{H_c^{1/2} T_c \xi_{ab}(T_c)} = -\frac{k_B q}{\Phi_0^{3/2}}. \tag{20}$$

Accordingly, the location of a crossing point in $m/H_c^{1/2}$ versus T provides an estimate for the 3D transition temperature and the factor of proportionality in m/T_c versus $H_c^{1/2}$ probes the anisotropy $\gamma = \xi_{ab}(T_c)/\xi_c(T_c)$. From figure 2 showing

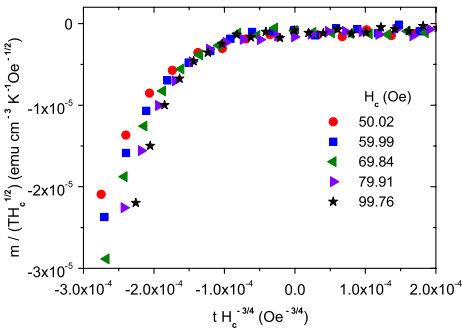

Figure 3. Scaling plot $m/(T H^{1/2})$ versus $t H_c^{-3/4}$.

$m/H_c^{1/2}$ versus T we derive the estimate $T_c \simeq 38.83$ K and (20) yields with $m/(T_c H_c^{1/2}) \approx 1.4 \times 10^{-6}$ (emu cm^{-3} K^{-1} Oe$^{-1/2}$) for the anisotropy the value

$$\xi_{ab}(T_c)/\xi_c(T_c) \approx 1.9. \tag{21}$$

In a homogeneous system where the correlation lengths diverge at T_c as $\xi_{ab,c} = \xi_{ab0,c0}^{\pm} |t|^{-\nu}$ with $\nu \simeq 2/3$, whereupon $\xi_{ab}(T_c)/\xi_c(T_c)$ corresponds to the anisotropy $\gamma = \xi_{ab0}^{\pm}/\xi_{c0}^{\pm}$. In contrast, in an inhomogeneous system, consisting of homogeneous domains of spatial extent $L_{ab,c}$ this ratio probes $\xi_{ab}(T_c)/\xi_c(T_c) = L_{ab}/L_c$, because the correlation lengths cannot exceed the homogeneous domains. Nevertheless, $\xi_{ab}(T_c)/\xi_c(T_c) \approx 1.9$ is close to $\gamma \simeq 2$, the estimate obtained near T_c with torque magnetometry [37].

According to the scaling form (8), consistency with critical behavior also requires that for low fields the data plotted as $m/(T H_c^{1/2})$ versus $t H_c^{-3/4}$ should collapse near $t H_c^{-3/4} \to 0$ on a single curve. Evidence for this collapse emerges from figure 3.

Because the limiting magnetic length, $L_{H_c} = \sqrt{\Phi_0/(a H_c)}$, decreases with increasing field, this scaling behavior no longer applies at higher fields. Indeed, with increasing field $L_{H_c} =$

J. Phys.: Condens. Matter **20** (2008) 135208 S Weyeneth *et al*

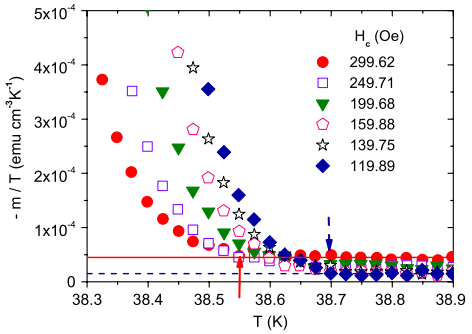

Figure 4. $-m/T$ versus T for various applied magnetic fields. The solid line indicates $-m/T_{\rm p} = 4.5 \times 10^{-5}$ (emu cm^{-3} K^{-1}) at $H_c = 299.2$ Oe, where $T_{\rm p} \simeq 38.55$ K and the dashed one $-m/T_{\rm p} = 1.5 \times 10^{-5}$ (emu cm^{-3} K^{-1}) at $H_c = 119.9$ Oe, where $T_{\rm p} \simeq 38.7$ K. The arrows mark the respective $T_{\rm p}$ values.

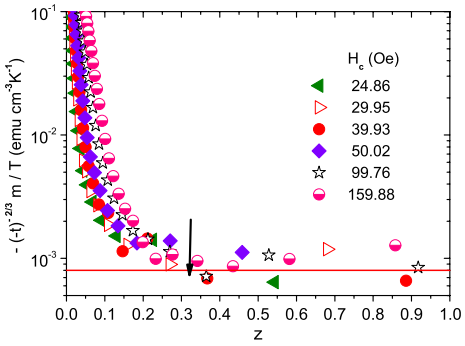

Figure 5. $|t|^{-2/3} m/T$ versus z for various fields. The solid line is $|t|^{-2/3} m/T = 8 \times 10^{-4}$ (emu cm^{-3} K^{-1}) and the arrow marks $z = 1/a \simeq 0.32$.

$\sqrt{\Phi_0/(aH_c)}$ approaches ξ_{ab}, and when $\xi_{ab}(T_{\rm p}) = L_{H_c}$ the scaling form (19) reduces to

$$\frac{m}{T_{\rm p}} \simeq -0.5 \frac{k_{\rm B}}{\Phi_0^{3/2}} \frac{\xi_{ab}\left(T_{\rm p}\right)}{\xi_{\rm c}\left(T_{\rm p}\right)} H_c^{1/2} = -0.5 \frac{k_{\rm B}}{\Phi_0 a^{1/2}} \frac{1}{\xi_{\rm c}\left(T_{\rm p}\right)}, \quad (22)$$

where

$$T_{\rm p} = T_{\rm c}\left(1 - \left(\frac{aH_c\left(\xi^-_{ab0}\right)^2}{\Phi_0}\right)^{3/4}\right) = T_{\rm c}\left(1 - \left(\frac{\xi^-_{ab0}}{L_{H_c}}\right)^{3/2}\right), \quad (23)$$

in analogy to (13), the expression for ^{4}He constrained below $T_{\rm c}$ to cylinders of diameter L. Accordingly, in sufficiently high fields the magnetic field induced finite size effect is predicted to eliminate the characteristic critical field dependence, $-m/T_{\rm c} \propto H_c^{1/2}$, emerging from figure 2, because the in-plane correlation length ξ_{ab} cannot grow beyond L_{H_c}. A glance at figure 4, showing $-m/T$ versus T for various applied magnetic fields in the range from 120 to 300 Oe, reveals that this prediction is well confirmed in this field range. Indeed, $-m/T$ levels off above $T = T_{\rm p}$ and the magnitude of $-m/T_{\rm p}$ is controlled by $\xi_{\rm c}(T_{\rm p})$.

Using equation (23), $T_{\rm p}(H_c = 299.2\ {\rm Oe}) \simeq 38.55$ K and $T_{\rm p}(H_c = 119.9\ {\rm Oe}) \simeq 38.7$ K, we obtain for the critical amplitude of the in-plane correlation length the estimate

$$\xi^-_{ab0} \simeq 52\ {\rm Å}. \quad (24)$$

On this basis the dependence of $m/(TH_c^{1/2})$ on the scaling variable $z = (\xi^-_{ab0})^2 |t|^{-4/3} H_c/\Phi_0$ is then readily calculated. When the magnetic field induced finite size effect scenario holds true, the effective range of the scaling variable is restricted to

$$z \leqslant 1/a \simeq 0.32, \quad (25)$$

because the correlation length cannot exceed $\xi_{ab} = L_{H_c}$. As a consequence, (8) reduces for $z \gtrsim 0.32$ to

$$|t|^{-2/3} \frac{m}{T} = -\frac{k_{\rm B}}{\Phi_0 \xi^-_{c0}} Q^- \left.\frac{{\rm d}G^-}{{\rm d}z}\right|_{z=1/a}. \quad (26)$$

Accordingly, in the plot $|t|^{-2/3} m/T$ versus z the data should collapse and level off for $z \gtrsim 0.32$. From figure 5, showing this scaling plot, it is seen that this behavior is well confirmed down to $H_c = 24.86$ Oe, whereupon we obtain for L_{ab}, the spatial extent of the homogeneous domains in the ab-plane, the lower bound

$$L_{ab} = \left(\frac{\Phi_0}{aH_c}\right)^{1/2} \geqslant 5.2 \times 10^{-5}{\rm cm}, \quad (27)$$

revealing the high quality of the sample.

To check the estimates for the critical amplitudes of the correlation lengths, we invoke, using (8), (9) and (10), the limiting behavior

$$\frac{{\rm d}m}{{\rm d}\ln\left(H_c\right)} = 0.7 \frac{k_{\rm B} T}{\Phi_0 \xi_{\rm c}}, \quad (28)$$

applicable for $z \to 0$. From the plot ${\rm d}m/{\rm d}\ln(H_c)$ versus H_c at $T = 38.7$ K, shown in figure 6 and ${\rm d}m/{\rm d}\ln(H_c) = 1.2 \times 10^{-3}$ (emu cm^{-3} ln(Oe)$^{-1}$) we obtain for the critical amplitude of the c-axis correlation length the estimate

$$\xi^-_{c0} \simeq 33\ {\rm Å}, \quad (29)$$

in reasonable agreement with $\xi^-_{abo}/\gamma \simeq 52\ {\rm Å}/1.9 \simeq 27$ Å. Note that at this temperature and $\xi^-_{abo} \simeq 52$ Å the limit $z \to 0$ is attained because $z = 2.74 \times 10^{-3} H_c$, with H_c in Oe. Together with the universal relation (7), $\xi^-_{c0} \simeq 33$ Å yields for the critical amplitude of the in-plane penetration depth, λ_{ab0}, and the Ginzburg parameter, κ_{ab0}, the estimates

$$\lambda_{ab0} \simeq 7.3 \times 10^{-5}{\rm cm}, \qquad \kappa_{ab0} = \lambda_{ab0}/\xi^-_{ab0} \simeq 140, \quad (30)$$

which apply very close to $T_{\rm c}$. Unfortunately, the available magnetic penetration depth data does not enter this regime [38, 39].

To explore the evidence for an inhomogeneity induced finite size effect, attributable to a system consisting of

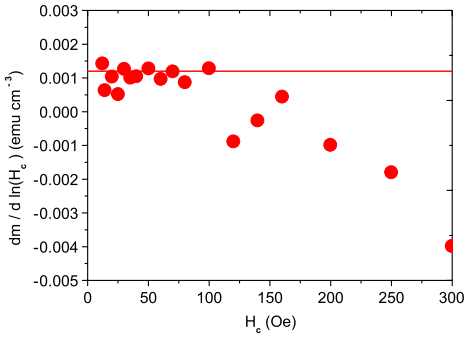

Figure 6. $\mathrm{d}m/\mathrm{d}\ln(H_c)$ versus H_c at $T = 38.7$ K. The solid line is $\mathrm{d}m/\mathrm{d}\ln(H_c) = 1.2 \times 10^{-3}$ (emu cm^{-3} ln(Oe)$^{-1}$).

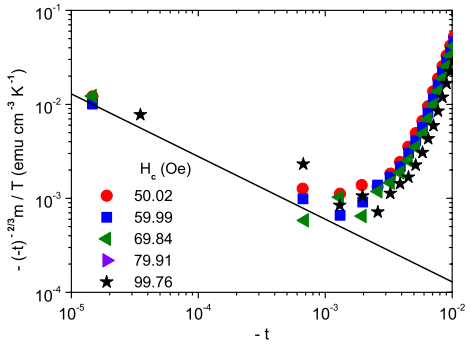

Figure 7. $-|t|^{-2/3}m/T$ versus $-t$. The solid line is $-|t|^{-2/3}m/T = 6 \times 10^{-6}(-t)^{-2/3}$ (emu cm^{-3} K^{-1}).

homogeneous domains of finite extent, we rewrite the scaling form (8) with the aid of (9) in the form

$$\frac{m}{T} = -\frac{k_\mathrm{B}}{\Phi_0 \xi_\mathrm{c}} Q^- \frac{\mathrm{d}G^-}{\mathrm{d}z} = -|t|^{2/3} \frac{k_\mathrm{B}}{\Phi_0 \xi_{c0}} Q^- \frac{\mathrm{d}G^-}{\mathrm{d}z}\bigg|_{z=H_c L_{ab}^2/\Phi_0}, \tag{31}$$

because ξ_{ab} cannot grow beyond L_{ab}, the extent of the homogeneous domains in the ab-plane. However, sufficiently close to T_c, ξ_c approaches L_c, the extent of the homogeneous domains along the c-axis. Here this scaling form reduces to

$$\frac{m}{T} = -f_0(H_c), \qquad f_0(H_c) = \frac{k_\mathrm{B}}{\Phi_0 L_\mathrm{c}} Q^- \frac{\mathrm{d}G^-}{\mathrm{d}z}\bigg|_{z=H_c L_{ab}^2/\Phi_0}. \tag{32}$$

In figure 7 we depict $-|t|^{-2/3}m/T$ versus $-t$. Apparently, this limiting behavior is attained roughly below $-t = -t_{pL_c} = 3 \times 10^{-4}$, where

$$\xi_\mathrm{c}(t) = \xi_{c0}^- \left|t_{pL_c}\right|^{-2/3} = L_\mathrm{c}. \tag{33}$$

With $\xi_{c0}^- = \xi_{ab0}^-/\gamma \simeq 52$ Å$/1.9$ we obtain for L_c, the c-axis extent of the homogeneous domains, the estimate

$$L_\mathrm{c} \approx 6 \times 10^{-5} \text{ cm}, \tag{34}$$

which is comparable to the lower bound $L_{ab} \geqslant 5.2 \times 10^{-5}$ cm (27), revealing again the high quality of the sample.

We have seen that the attainable critical regime is limited by both the magnetic field and inhomogeneity induced finite size effects. The former leads according to (23) in the (H, T)-plane to the line

$$H_\mathrm{cp}(T) = \frac{\Phi_0}{a\left(\xi_{ab0}^-\right)^2}\left(1 - \frac{T}{T_\mathrm{c}}\right)^{4/3} \quad : T < T_\mathrm{c}, \qquad H_\mathrm{cp}(T) = \frac{\Phi_0}{a\left(\xi_{ab0}^-\right)^2}\left(\frac{T}{T_\mathrm{c}} - 1\right)^{4/3} \quad : T > T_\mathrm{c}, \tag{35}$$

depicted in figure 8. It is a crossover line because for a fixed temperature, e.g. below T_c, the limiting length $L_{H_c} = (\Phi_0/(aH_c))^{1/2}$ decreases with increasing magnetic field and matches at H_cp the in-plane correlation length ξ_{ab}. Here and above H_cp, superconductivity is then confined to cylinders of diameter L_{H_cp} in the ab-plane and height L_c along the c-axis. Hence in a homogeneous system where $L_c = L_{ab} = \infty$ a 3D–1D crossover takes place. Even in the presence of inhomogeneities, corresponding to homogeneous domains of extent $L_{ab,c}$, this holds true when $H_c > \Phi_0/(aL_{ab}^2)$ and $-t = 1 - T/T_\mathrm{c} > (\xi_{c0}^-/L_\mathrm{c})^{3/2}$ because the magnetic field induced finite size effect dominates when $L_{H_c} < L_{ab}$ and $\xi_\mathrm{c} < L_\mathrm{c}$. Indeed, below $H_c = \Phi_0/(aL_{ab}^2)$ and $-t = 1 - T/T_\mathrm{c} = (\xi_{c0}^-/L_\mathrm{c})^{3/2}$ superconductivity occurs in finite boxes with extent $L_{ab}^2 L_\mathrm{c}$ and above superconductivity is again confined to cylinders and their finite height L_c is not detected because $\xi_\mathrm{c} < L_\mathrm{c}$. Noting then that in the present case of MgB_2 $L_{ab} \geqslant 5.2 \times 10^{-5}$ cm (27), the 3D–1D crossover scenario applies down to fields smaller than 25 Oe, while the finite extent of the homogeneous domains along the c-axis requires that $1 - T/T_\mathrm{c} \gtrsim 3 \times 10^{-4}$

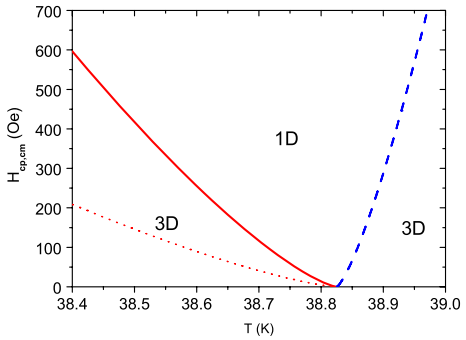

Figure 8. Crossover lines H_cp and vortex melting line H_{cm} versus T. The 3D–1D and the 1D–3D crossover lines H_cp follow from (35) for $\xi_{ab0}^- = 52$ Å (24), $\xi_{ab0}^+ = 52$ Å$/2.21 \simeq 23.62$ Å (4) and $T_\mathrm{c} = 38.83$ K. The solid line applies below T_c and the dashed line above T_c. The dotted vortex melting line H_{cm} follows from (38) and lies at temperatures below the crossover lines H_cp.

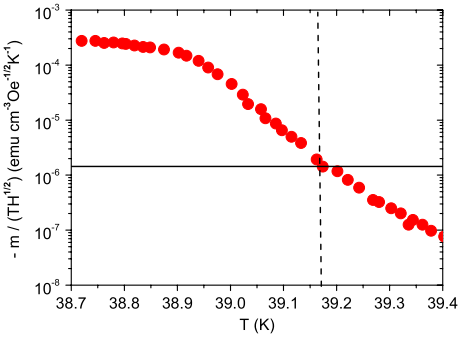

Figure 9. $m/(T\,H^{1/2})$ versus T at $H = 1$ Oe for the MgB_2 powder sample of Lascialfari *et al* [6]. The horizontal line is $m/(T_c H^{1/2}) \simeq -1.44 \times 10^{-6}$ (emu cm^{-3} K^{-1} Oe$^{-1/2}$) and the vertical one marks $T_c \simeq 39.17$ K.

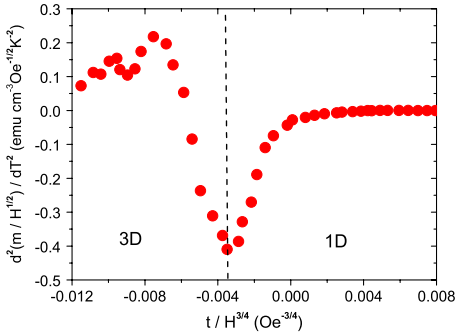

Figure 10. $\mathrm{d}^2(m/H^{1/2})/\mathrm{d}T^2$ versus $t/H^{3/4}$ for $H = 1$ Oe derived from the data of Lascialfari *et al* [6]. The minimum at $t_p H^{-3/4} \simeq -3.4 \times 10^{-3}$ Oe$^{-3/4}$ locates the 3D–1D crossover line, while the peak at $t_m H^{-3/4} \simeq -7.5 \times 10^{-3}$ Oe$^{-3/4}$ signals the vortex melting transition.

(see figure 6), excluding a very narrow temperature range below T_c.

Finally, we show that this scenario is also consistent with the measurements of Lascialfari *et al* [6] performed on powder samples at $T \gtrsim T_c$. The rather large volume of the sample made it possible to explore the critical regime above T_c as well. To demonstrate the consistency with our analysis we reproduced some data in figure 9 in terms of $m/(T\,H^{1/2})$ versus T. For a powder sample we obtain from (8), (9) and (10) at T_c the value

$$\frac{m}{T_c H^{1/2}} = -0.5 \frac{k_B \gamma}{\Phi_0^{3/2}} \left\langle \epsilon\,(\delta)^3 \right\rangle, \qquad \gamma = \frac{\xi_{ab}}{\xi_c}, \tag{36}$$

where

$$\epsilon\,(\delta) = \left(\cos\,(\delta)^2 + \frac{1}{\gamma^2} \sin\,(\delta)^2 \right)^{1/2}. \tag{37}$$

δ denotes the random orientation of the applied magnetic field with respect to the c-axis and $\langle \epsilon(\delta)^3 \rangle$ is the corresponding average. For $\gamma = 1.9$ we obtain $\langle \epsilon(\delta)^3 \rangle \simeq 0.541$ and with this $m/(T_c H^{1/2}) \simeq -1.44 \times 10^{-6}$ (emu cm^{-3} K^{-1} Oe$^{-1/2}$). Perfect agreement with our analysis emerges from figure 9 for $T_c \simeq 39.17$ K, consistent with the observation of Lascialfari *et al* [6] that in this sample T_c is near 39.1 K. To explore the occurrence of the vortex melting transition and the 3D to 1D crossover we displayed in figure 10 the data of Lascialfari *et al* [6] according to the scaling form (18). The minimum at $t_p H^{-3/4} \simeq -3.4 \times 10^{-3}$ Oe$^{-3/4}$ locates the 3D–1D crossover line, while the peak at $t_m H^{-3/4} \simeq -7.5 \times 10^{-3}$ Oe$^{-3/4}$ signals the vortex melting transition. For the ratio of the universal values of the scaling variable z at the melting and the 1D to 3D crossover line we obtain the estimate

$$z_m/z_p = \left(t_p\,(H)\,/t_m\,(H) \right)^{4/3} \simeq 0.35, \tag{38}$$

in reasonable agreement with $z_m/z_p \simeq 0.25$, the value emerging from the specific heat data of Roulin *et al* [23] for $YBa_2Cu_3O_{6.97}$. The resulting vortex melting line is included in figure 8.

At higher fields and fixed temperature, however, a crossover from $m/T \propto H$ to $m/T = $ const. is expected to occur. Indeed, approaching the limit $z \to 0$, the scaling form

$$\frac{m}{T} = -0.9 \frac{k_B \xi_{ab}^2}{\Phi_0^2 \xi_c} \left\langle \epsilon\,(\delta)^2 \right\rangle H, \tag{39}$$

applies according to (8), (9) and (10). As the scaling variable z increases with rising magnetic field it approaches the value $z = 1/a$, where the magnetic field induced finite size effect sets in. Here the scaling expression (8) applies in the form

$$\frac{m}{T} = -\frac{k_B}{\Phi_0 \xi_c} \langle \epsilon\,(\delta) \rangle\, Q^+ \left. \frac{\mathrm{d}G^+}{\mathrm{d}z} \right|_{z=1/a,} \tag{40}$$

for $z \geqslant 1/a$, where

$$z = \frac{H \xi_{ab}^2}{\Phi_0} \epsilon\,(\delta)\,. \tag{41}$$

From figure 11, showing m/T versus H at $T = 39.3$ K for the MgB_2 powder sample of Lascialfari *et al* [6], it is seen that this behavior, including the saturation due to the magnetic field induced finite size effect, is well confirmed. Therefore, in analogy to the situation below T_c, there is a magnetic field induced finite size effect above T_c as well. However, there is no long range order in this regime so that uncondensed pairs are forced to be confined above $H_{cp}(T)$ (see figure 8) in cylinders of diameter $L_{H_{cp}}$.

3. Summary

To summarize, our scaling analysis of reversible magnetization data of a MgB_2 single crystal with the magnetic field applied along the c-axis provided considerable evidence that even in this type II superconductor the 3D-xy critical regime is experimentally accessible, provided that the sample is

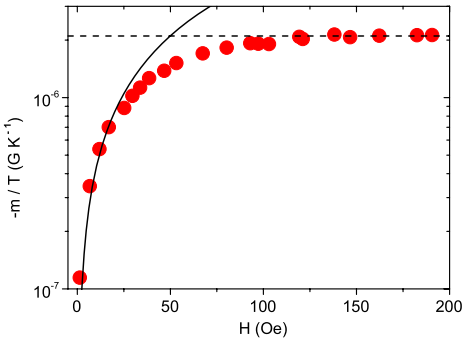

Figure 11. m/T versus H at $T = 39.3$ K for the MgB_2 powder sample of Lascialfari *et al* [6]. The solid line is $m/T = -4.2 \times 10^{-8} H$ (G K^{-1}) and the dashed one $m/T = -2.1 \times 10^{-6}$ (G K^{-1}), marking the saturation due to the magnetic field induced finite size effect.

sufficiently homogeneous. The high quality of our sample allowed us to explore the occurrence of the magnetic field induced finite size effect down to rather low magnetic fields where 3D-xy fluctuations still dominate. In this regime we were able to provide fairly unambiguous evidence for this finite size effect. This implies that in type II superconductors, such as MgB_2, exposed to a magnetic field superconductivity is confined to cylinders. Their diameter is given by the limiting magnetic length $L_{H_i} = (\Phi_0/(aH_i))^{1/2}$, whereupon for a magnetic field applied parallel to the i-axis there is a line $H_{pi}(T) = (\Phi_0/(a\xi^-_{j0}\xi^-_{k0}))(1 - T/T_c)^{4/3}$ with $i \neq j \neq k$, where below T_c a 3D–1D crossover takes place. $\xi^-_{i0,j0,k0}$ denote the critical amplitudes of the correlation length below T_c along the respective axis. Accordingly, there is below T_c no continuous phase transition in the (H, T)-plane along the H_{c2}-lines as predicted by the mean-field treatment. Our scaling analysis of the magnetization data of Lascialfari *et al* [6] also confirmed that the magnetic field induced finite size effect is not restricted to the superconducting phase ($T < T_c$). Indeed, above T_c there is a line $H_{pi}(T) = (\Phi_0/(a\xi^+_{j0}\xi^+_{k0}))(T/T_c - 1)^{4/3}$ where the 3D to 1D crossover occurs and uncondensed pairs are forced to be confined in cylinders. Furthermore, we have shown that the scaling analysis of magnetization data also opens a door onto the ascertainment of the homogeneity of the sample in terms of the finite size effect arising from the limited extent of the homogeneous domains.

Acknowledgments

The authors are grateful to J Roos for helping to prepare the manuscript and useful comments. This work was supported by the Swiss National Science Foundation and in part by the NCCR program MaNEP.

References

[1] Nagamatsu J, Nakagawa N, Maranaka T, Zenitani Y and Akimitsu J 2001 *Nature* **410** 63
[2] Schneider T and Singer J M 2000 *Phase Transition Approach To High Temperature Superconductivity* (London: Imperial College Press)
[3] Schneider T 2004 *The Physics of Superconductors* ed K Bennemann and J B Ketterson (Berlin: Springer) p 111
[4] Kang W N *et al* 2002 *J. Korean Phys. Soc.* **40** 949
[5] Park T, Salamon M B, Jung C U, Park M-S, Kim K and Lee S-I 2002 *Phys. Rev.* B **66** 134515
[6] Lascialfari A, Mishonov T, Rigamonti A, Tedesco P and Varlamov A 2002 *Phys. Rev.* B **65** 180501(R)
[7] Dao V H and Zhitomirski M E 2005 *Eur. Phys. J.* B **44** 183
[8] Hofer J, Schneider T, Singer J M, Willemin M, Keller H, Sasagawa T, Kishio K, Conder K and Karpinski J 2000 *Phys. Rev.* B **62** 631
[9] Fisher D S, Fisher M P A and Huse D A 1991 *Phys. Rev.* B **43** 130
[10] Schneider T and Ariosa D 1992 *Z. Phys.* B **89** 267
[11] Schneider T and Keller H 1993 *Int. J. Mod. Phys.* B **8** 487
[12] Schneider T, Hofer J, Willemin M, Singer J M and Keller H 1998 *Eur. Phys. J.* B **3** 413
[13] Hofer J, Schneider T, Singer J M, Willemin M, Keller H, Rossel C and Karpinski J 1999 *Phys. Rev.* B **60** 1332
[14] Pelissetto A and Vicari E 2002 *Phy. Rep.* **368** 549
[15] Prange R E 1970 *Phys. Rev.* B **1** 2349
[16] Hubbard M A, Salamon B and Veal B W 1996 *Physica* C **259** 309
[17] Babíc D, Cooper J R, Hodby J W and Changkang Chen 1999 *Phys. Rev.* B **60** 698
[18] Overend N, Howson M A and Lawrie I D 1994 *Phys. Rev. Lett.* **72** 3238
[19] Kamal S, Bonn D A, Goldenfeld N, Hirschfeld P J, Liang R and Hardy W N 1994 *Phys. Rev. Lett.* **73** 1845
[20] Jaccard Y, Schneider T, Looquet J P, Williams E J, Martinoli P and Fischer Ø 1996 *Europhys. Lett.* **34** 281
[21] Kamal S, Liang R, Hosseini A, Bonn D A and Hardy W N 1998 *Phys. Rev.* B **58** R8933
[22] Pasler V, Schweiss P, Meingast Ch, Obst B, Wühl H, Rykov A I and Tajima S 1998 *Phys. Rev. Lett.* **81** 1094
[23] Roulin M, Junod A and Walker E 1998 *Physica* C **296** 137
[24] Schneider T 2007 *Phys. Rev.* B **75** 174517
[25] Harris A B 1974 *J. Phys. C: Solid State Phys.* **7** 1671
[26] Cardy J L (ed) 1988 *Finite-Size Scaling* (Amsterdam: North-Holland)
[27] Privman V 1990 *Finite Size Scaling and Numerical Simulations of Statistical Systems* (Singapore: World Scientific)
[28] Schneider T and Di Castro D 2004 *Phys. Rev.* B **69** 024502
[29] Schneider T 2004 *J. Supercond.* **17** 41
[30] Haussmann R 1999 *Phys. Rev.* B **60** 12373
[31] Lortz R, Meingast C, Rykov A I and Tajima S 2003 *Phys. Rev. Lett.* **91** 207001
[32] Nho K and Manousakis E 2001 *Phys. Rev.* B **64** 144513
[33] Coleman M and Lipa J A 1995 *Phys. Rev. Lett.* **74** 286
[34] Gasparini F M, Kimball M O and Mooney K P 2001 *J. Phys.: Condens. Matter* **13** 4871
[35] Lyard L *et al* 2002 *Phys. Rev.* B **66** 180502(R)
[36] Karpinski J *et al* 2003 *Supercond. Sci. Technol.* **16** 221
[37] Angst M, Puzniak R, Wisniewski A, Jun J, Kazakov S M, Karpinski J, Roos J and Keller H 2002 *Phys. Rev. Lett.* **88** 167004
[38] Panagopoulos C, Rainford B D, Xiang T, Scott C A, Kambara M and Inoue I H 2001 *Phys. Rev.* B **64** 094514
[39] Di Castro D, Khasanov R, Grimaldi C, Karpinski J, Kazakov S M, Brütsch R and Keller H 2005 *Phys. Rev.* B **72** 094504

3.6.2 Publication II: 3D-xy critical properties of $YBa_2Cu_4O_8$ and magnetic-field-induced 3D to 1D crossover

S. Weyeneth, T. Schneider, Z. Bukowski, J. Karpinski, and H. Keller
J. Phys.: Condens. Matter **20**, 345210 (2008).

Abstract
We present reversible magnetization data of a $YBa_2Cu_4O_8$ single crystal and analyze the evidence for 3D-xy critical behavior and a magnetic field induced 3D to 1D crossover. Remarkable consistency with these phenomena is observed in agreement with a magnetic field induced finite size effect, whereupon the correlation length transverse to the applied magnetic field cannot grow beyond the limiting magnetic length scale $L_H = (\Phi_0/(a\mu_0 H))^{1/2}$. By applying the appropriate scaling form we obtain the zero-field critical temperature, the 3D to 1D crossover, the vortex melting line and the universal ratios of the related scaling variables. Accordingly, there is no continuous phase transition in the (H_c, T)-plane along the H_{c2}-lines as predicted by the mean-field treatment.

DOI: 10.1088/0953-8984/20/34/345210
PACS numbers: 74.25.Ha, 74.25.Op, 74.25.Dw, 74.25.Bk, 74.25.Qt, 74.40.+k

The original publication is electronically available at:
http://www.iop.org/EJ/abstract/0953-8984/20/34/345210

Open access repositories:
http://www.zora.uzh.ch/10573
http://arxiv.org/abs/0803.1384

At completion of this thesis, according to the Thomson Reuters ISI Web of Knowledge database, this article has been cited at least 2 times.

IOP Publishing Journal of Physics: Condensed Matter
J. Phys.: Condens. Matter **20** (2008) 345210 (4pp) doi:10.1088/0953-8984/20/34/345210

3D-xy critical properties of $YBa_2Cu_4O_8$ and magnetic-field-induced 3D to 1D crossover

S Weyeneth[1], T Schneider[1], Z Bukowski[2], J Karpinski[2] and H Keller[1]

[1] Physik-Institut der Universität Zürich, Winterthurerstrasse 190, CH-8057 Zürich, Switzerland
[2] Laboratory for Solid State Physics, ETH Zürich, CH-8093 Zürich, Switzerland

E-mail: wstephen@physik.uzh.ch

Received 23 April 2008, in final form 27 June 2008
Published 1 August 2008
Online at stacks.iop.org/JPhysCM/20/345210

Abstract
We present reversible magnetization data of a $YBa_2Cu_4O_8$ single crystal and analyze the evidence for 3D-xy critical behavior and a magnetic-field-induced 3D to 1D crossover. Remarkable consistency with these phenomena is observed in agreement with a magnetic-field-induced finite size effect, whereupon the correlation length transverse to the applied magnetic field cannot grow beyond the limiting magnetic length scale $L_H = (\Phi_0/(aH))^{1/2}$. By applying the appropriate scaling form we obtain the zero-field critical temperature, the 3D to 1D crossover, the vortex melting line and the universal ratios of the related scaling variables. Accordingly there is no continuous phase transition in the (H, T) plane along the H_{c2} lines as predicted by the mean-field treatment.

(Some figures in this article are in colour only in the electronic version)

1. Introduction

Fluctuation effects are known to be strongly enhanced in high temperature cuprate superconductors due to their anisotropic behavior and their high zero-field transition temperature T_c [1, 2]. For $YBa_2Cu_4O_8$ and related compounds several studies point to the importance of critical fluctuations [3–6]. To circumvent the smearing of the phase transition due to inhomogeneities $YBa_2Cu_4O_8$ is an exquisite candidate due to its nearly stoichiometric structure and the availability of excellent single crystals [7, 8]. As $YBa_2Cu_4O_8$ is intrinsically doped there is no anomalous precursor diamagnetism expected, as reported for example in aluminum-doped MgB_2 [6].

In this study we present reversible magnetization data of a $YBa_2Cu_4O_8$ single crystal and analyze the evidence for 3D-xy critical behavior and a magnetic-field-induced 3D to 1D crossover. We observe remarkable consistency with these phenomena. Since near-T_c thermal fluctuations are expected to dominate [1, 9–12], Gaussian fluctuations point to a magnetic-field-induced 3D to 1D crossover [13]. Whereby the effect of fluctuations is enhanced, it appears inevitable to take thermal fluctuations into account. Indeed, invoking the scaling theory of critical phenomena we show that the data are inconsistent with the traditional mean-field interpretation. In contrast, we observe agreement with a magnetic-field-induced finite size effect, whereupon the correlation length transverse to the magnetic field H_i, applied along the i axis, cannot grow beyond the limiting magnetic length

$$L_{H_i} = (\Phi_0/(aH_i))^{1/2}, \tag{1}$$

with $a \simeq 3.12$ [14]. L_{H_i} is related to the average distance between vortex lines. Indeed, as the magnetic field increases, the density of vortex lines becomes greater, but this cannot continue indefinitely. The limit is roughly set on the proximity of vortex lines by the overlapping of their cores. This finite size effect implies that, in type II superconductors, superconductivity in a magnetic field is confined to cylinders with diameter L_{H_i} [12, 15]. Accordingly, below T_c there is the 3D to 1D crossover line

$$H_{pi}(T) = (\Phi_0/(a\xi^-_{j0}\xi^-_{k0}))(1 - T/T_c)^{4/3}, \tag{2}$$

with $i \neq j \neq k$. $\xi^-_{i0,j0,k0}$ denotes the critical amplitudes of the correlation lengths below T_c along the respective axes.

It circumvents the occurrence of the continuous phase transition in the (H_c, T) plane along the H_{c2} lines predicted by the mean-field treatment [16]. Indeed, the relevance of thermal fluctuations emerges already from the reversible magnetization data shown in figure 1. As a matter of fact, the typical mean-field behavior [16], whereby the magnetization scales below T_c linearly with the magnetic field, does not emerge.

2. Experiment and analysis

The $YBa_2Cu_4O_8$ single crystal investigated in this work was fabricated by a high-pressure synthesis method described in detail elsewhere [7, 8]. The volume of the nearly rectangular shaped sample is estimated to be 3.9×10^{-4} cm^3. The magnetic moment was measured by a commercial Quantum Design DC-SQUID magnetometer MPMS XL with installed RSO option, allowing us to achieve a resolution of 10^{-8} emu. For this experiment the applied magnetic field was oriented along the c axis of the crystal. For different magnitudes of the field, temperature-dependent magnetization curves were measured. The zero-field-cooled (ZFC) and field-cooled (FC) data have been compared in order to probe the reversible magnetization only. The superconducting susceptibility was finally obtained by correcting the measured data for the normal state and sample holder contributions. In figure 1 we depicted some of the measured magnetization curves m versus T for magnetic fields H_c applied along the c axis. At a first glance the data fall on rather smooth curves, revealing that the extraction of critical and crossover behavior requires a rather detailed analysis. When thermal fluctuations dominate and the coupling to the charge is negligible the magnetization per unit volume, $m = M/V$, adopts the scaling form [1, 9–11]

$$\frac{m}{TH^{1/2}} = -\frac{Q^{\pm}k_B\xi_{ab}}{\Phi_0^{3/2}\xi_c}F^{\pm}(z),$$
$$F^{\pm}(z) = z^{-1/2}\frac{dG^{\pm}}{dz}, \qquad (3)$$
$$z = x^{-1/2\nu} = \frac{\left(\xi^{\pm}_{ab0}\right)^2|t|^{-2\nu}H_c}{\Phi_0}.$$

$Q^{\pm}$ is a universal constant and $G^{\pm}(z)$ is a universal scaling function of its argument, with $G^{\pm}(z=0)=1$. $\gamma = \xi_{ab}/\xi_c$ denotes the anisotropy, ξ_{ab} the zero-field in-plane correlation length and H_c the magnetic field applied along the c axis. In terms of the variable x the scaling form (3) is similar to Prange's [17] result for Gaussian fluctuations. Approaching T_c the in-plane correlation length diverges as

$$\xi_{ab} = \xi^{\pm}_{ab0}|t|^{-\nu}, \qquad t = T/T_c - 1, \qquad \pm = \mathrm{sgn}(t). \quad (4)$$

Supposing that 3D-xy fluctuations dominate, the critical exponents are given by [18]

$$\nu \simeq 0.671 \simeq 2/3, \qquad \alpha = 2\nu - 3 \simeq -0.013, \quad (5)$$

and there are the universal critical amplitude relations [1, 9–12, 18]

$$\frac{\xi^-_{ab0}}{\xi^+_{ab0}} = \frac{\xi^-_{c0}}{\xi^+_{c0}} \simeq 2.21, \qquad \frac{Q^-}{Q^+} \simeq 11.5, \qquad \frac{A^+}{A^-} = 1.07, \quad (6)$$

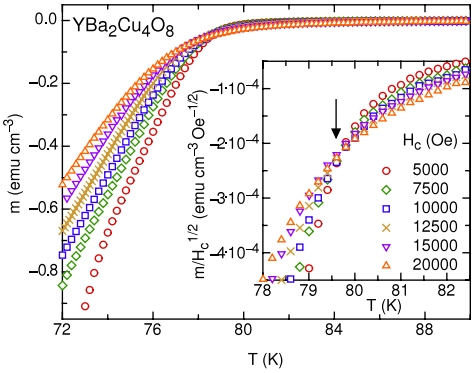

Figure 1. Reversible magnetization m versus T of a $YBa_2Cu_4O_8$ single crystal for magnetic fields H_c applied along the c axis. The inset shows $m/H_c^{1/2}$ versus T. The arrow indicates the crossing point which yields the estimate $T_c \simeq 79.6$ K.

and

$$A^-\xi^-_{a0}\xi^-_{b0}\xi^-_{c0} \simeq A^-\left(\xi^-_{ab0}\right)^2\xi^-_{c0} = \frac{A^-\left(\xi^-_{ab0}\right)^3}{\gamma}$$
$$= \left(R^-\right)^3, \qquad R^- \simeq 0.815. \qquad (7)$$

$A^{\pm}$ is the critical amplitude of the specific heat singularity, defined as

$$c = \frac{C}{Vk_B} = \frac{A^{\pm}}{\alpha}|t|^{-\alpha} + B, \qquad (8)$$

where B denotes the background. Furthermore, in the 3D-xy universality class T_c, ξ^-_{c0} and the critical amplitude of the in-plane magnetic field penetration depth λ_{ab0} are not independent, but related by the universal relation [1, 9–11, 18]

$$k_BT_c = \frac{\Phi_0^2}{16\pi^3}\frac{\xi^-_{c0}}{\lambda^2_{ab0}} = \frac{\Phi_0^2}{16\pi^3}\frac{\xi^-_{ab0}}{\gamma\lambda^2_{ab0}}. \qquad (9)$$

Furthermore, the existence of the magnetization at T_c of the penetration depth below T_c and of the magnetic susceptibility above T_c imply the following asymptotic forms of the scaling function [1, 9–12]:

$$Q^{\pm}\frac{1}{\sqrt{z}}\frac{dG^{\pm}}{dz}\bigg|_{z\to\infty} = Q^{\pm}c^{\pm}_{\infty},$$
$$Q^-\frac{dG^-}{dz}\bigg|_{z\to0} = Q^-c^-_0(\ln z + c_1), \qquad (10)$$
$$Q^+\frac{1}{z}\frac{dG^+}{dz}\bigg|_{z\to0} = Q^+c^+_0,$$

with the universal coefficients

$$Q^-c^-_0 \simeq -0.7, \qquad Q^+c^+_0 \simeq 0.9, \qquad Q^{\pm}c^{\pm}_{\infty} \simeq 0.5, \quad (11)$$
$$c_1 \simeq 1.76. \quad (12)$$

We are now prepared to analyze the magnetization data. To estimate T_c we note that, according to equations (3), (10)

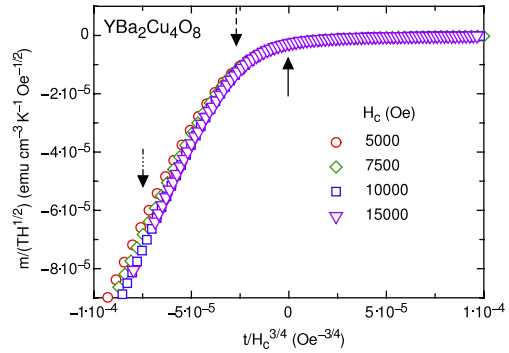

Figure 2. $m/(T H_c^{1/2})$ versus $t/H^{3/4}$ for a $YBa_2Cu_4O_8$ single crystal with $T_c = 79.6$ K. The full arrow marks the zero-field critical temperature T_c, the dashed arrow the 3D to 1D crossover and the dotted arrow the vortex melting line.

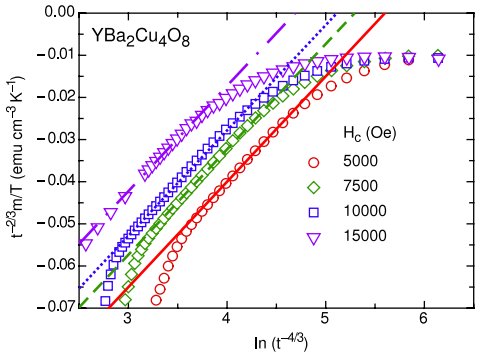

Figure 3. $|t|^{-2/3} m/T$ versus $\ln(|t|^{-4/3})$ for a $YBa_2Cu_4O_8$ single crystal according to equation (14). The lines are fits to the rescaled magnetization data. Here $\xi_{ab0}^2 |t_p|^{-4/3} = \Phi_0/aH_c$.

and (12), the plot $m/H_c^{1/2}$ versus T should exhibit a crossing point at T_c because $m/TH_c^{1/2}$ tends to the value $m/T_c H_c^{1/2} = -0.5 k_B \gamma \Phi_0^{-3/2}$. The inset in figure 1 reveals that there is a crossing point near $T_c \simeq 79.6$ K. Given this estimate, consistency with 3D-xy critical behavior then requires according to the scaling form (3) that the data plotted as $m/(TH_c^{1/2})$ versus $tH_c^{-1/2\nu} \simeq tH_c^{-3/4}$ should collapse near $tH_c^{-3/4} \to 0$ on a single curve. Evidence for this collapse emerges from figure 2 with $T_c \simeq 79.6$ K. Considering the limit $z \to 0$ below T_c the appropriate scaling form is

$$\frac{m}{T} = -\frac{Q^- c_0^- k_B}{\Phi_0 \xi_c^-} \left(\ln\left(\frac{H_c (\xi_{ab})^2}{\Phi_0} \right) + c_1 \right), \qquad (13)$$

according to equations (3), (10) and (12). Thus, given the magnetization data of a homogeneous system, attaining the limit $z = H_c(\xi_{ab0}^{\pm})^2 |t|^{-2\nu}/\Phi_0 \ll 1$, the growth of ξ_{ab} and ξ_c is unlimited and estimates for ξ_{c0}^- and ξ_{ab0}^- can be deduced from

$$|t|^{-2/3} \frac{m}{T} = -\frac{Q^- c_0^- k_B}{\Phi_0 \xi_{c0}^-} \left(\ln\left(\frac{H_c \left(\xi_{ab0}^-\right)^2 |t|^{-4/3}}{\Phi_0} \right) + c_1 \right). \qquad (14)$$

In figure 3 we depicted $|t|^{-2/3} m/T$ versus $\ln(|t|^{-4/3})$. From the straight lines we obtain

$$-\frac{Q^- c_0^- k_B}{\Phi_0 \xi_{c0}^-} \simeq 0.025, \qquad (15)$$

and with that

$$\xi_{c0}^- \simeq 1.87 \text{ Å}. \qquad (16)$$

Furthermore, from $\ln(H_c(\xi_{ab0}^-)^2/\Phi_0)$ versus $\ln(H_c)$ we deduce

$$\xi_{ab0}^- \simeq 15.6 \text{ Å}. \qquad (17)$$

For the anisotropy we obtain then the estimate

$$\gamma = \frac{\xi_{ab0}^-}{\xi_{c0}^-} \simeq 8.34, \qquad (18)$$

compared to $\gamma \simeq 13.4$, $\gamma \simeq 14.7$ [19] and $\gamma \simeq 12.3$ [20].

To explore the magnetic-field-induced 3D to 1D crossover further and to probe the vortex melting line directly we invoke Maxwell's relation

$$\left. \frac{\partial (C/T)}{\partial H_c} \right|_T = \left. \frac{\partial^2 M}{\partial T^2} \right|_{H_c}, \qquad (19)$$

uncovering the vortex melting transition in terms of a singularity, while the magnetic-field-induced finite size effect leads to a dip. These features seem to differ drastically from the nearly smooth behavior of the magnetization. Together with the scaling form of the specific heat (equation (8)), extended to the presence of a magnetic field:

$$c = \frac{A^-}{\alpha} |t|^{-\alpha} f(x), \qquad x = \frac{t}{H_c^{1/2\nu}}, \qquad (20)$$

we obtain the scaling form

$$T H_c^{1+\alpha/2\nu} \frac{\partial (c/T)}{\partial H_c} = -\frac{k_B A^-}{2\alpha\nu} x^{1-\alpha} \frac{\partial f}{\partial x} = T H_c^{1+\alpha/2\nu} \frac{\partial^2 m}{\partial T^2}. \qquad (21)$$

In figure 4 we depicted $T H_c \, d^2m/dT^2$ versus x for various magnetic fields H_c. Apparently, the data collapses reasonably well on a single curve. There is a peak and a dip marked by an arrow and a vertical line, respectively. Their occurrence differ clearly from the traditional mean-field behavior where $\partial^2 m/\partial T^2 = 0$. The finite depth of the dip is controlled by the magnetic-field-induced finite size effect. It replaces the reputed singularity at the upper critical field obtained in the Gaussian approximation [17]. Note that both the peak and the dip are hardly visible in the magnetization shown in figure 2. There we marked the location of the peak, the dip and T_c in terms of dashed and solid arrows. The location of the dip determines the line

$$x_p = t_p H_c^{-3/4} \simeq -2.85 \times 10^{-5} \text{ Oe}^{-3/4}, \qquad (22)$$

in the (H_c, T) plane where the 3D to 1D crossover occurs. Along this line, rewritten in the form $H_{pc}(T) = \Phi_0/(a(\xi_{ab0}^-)^2)(1 - T/T_c)^{4/3}$, the in-plane correlation length is

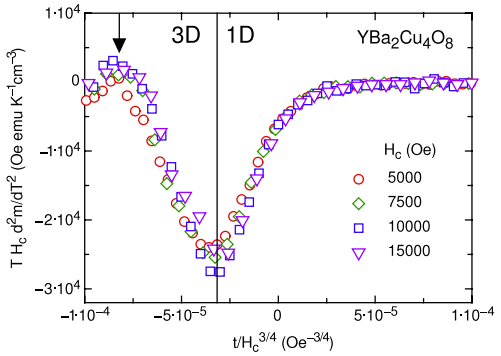

Figure 4. $T H_c d^2m/dT^2$ versus $x = t/H_c^{3/4}$ for a $YBa_2Cu_4O_8$ single crystal. The arrow marks the vortex melting line $x_m \simeq -8.35 \times 10^{-5}$ ($Oe^{-3/4}$) and the vertical line $x_p \simeq -2.85 \times 10^{-5}$ ($Oe^{-3/4}$) the 3D to 1D crossover line.

limited by L_{H_c} (equation (1)). In addition there is a peak at

$$x_m = t_m H_c^{-3/4} \simeq -8.35 \times 10^{-5}\ \mathrm{Oe}^{-3/4}, \qquad (23)$$

corresponding to the vortex melting transition. Rewritten, the vortex melting line follows in the form $H_{mc} \simeq 2.7 \times 10^5 \mathrm{Oe} \cdot (1 - T_m/T_c)^{4/3}$ which agrees very well with the previous estimate $H_{mc} \simeq 1.8 \times 10^5\ \mathrm{Oe} \cdot (1 - T_m/T_c)^{4/3}$ obtained by Katayama *et al* [21] as far as the temperature dependence is concerned. Accordingly, we obtain the universal ratios of the scaling variables of the reduced temperatures for the vortex melting line and the 3D to 1D crossover line as

$$\frac{z_m}{z_p} = \left(\frac{t_p(H_c)}{t_m(H_c)}\right)^{2\nu} \simeq 0.24, \qquad t_p(H_c)/t_m(H_c) \simeq 0.34. \qquad (24)$$

These values agree well with the estimates $t_p(H_c)/t_m(H_c) \simeq 0.3$ for an $NdBa_2Cu_3O_{7-\delta}$ single crystal [22] and $t_p(H_c)/t_m(H_c) \simeq 0.35$ for a $YBa_2Cu_3O_{6.97}$ single crystal [23] derived from the respective references.

Finally, invoking the universal relation (9) we obtain with $T_c = 79.6$ K and $\xi_{c0}^- \simeq 1.87$ Å(equation (16)) for the critical amplitude of the in-plane magnetic field penetration depth the value $\lambda_{ab0} \simeq 1.37 \times 10^{-5}$ cm, in reasonable agreement with the estimate $\lambda_{ab0} \simeq 1.7 \times 10^{-5}$ cm obtained from magnetization data of polycrystalline $YBa_2Cu_4O_8$ samples [24].

3. Summary

We have shown that the analysis of reversible magnetization data of a $YBa_2Cu_4O_8$ single crystal provides considerable insight into the effect of thermal fluctuations and the magnetic-field-induced 3D to 1D crossover. In particular we demonstrated that the fluctuation-dominated regime is experimentally accessible and uncovers remarkable consistency with 3D-xy critical behavior. Furthermore there is, however, the magnetic-field-induced finite size effect. It implies that the correlation length transverse to the magnetic field H_i, applied along the i axis, cannot grow beyond the limiting magnetic length $L_{H_i} = (\Phi_0/(aH_i))^{1/2}$, related to the average distance between vortex lines. Invoking the scaling theory of critical phenomena, clear evidence for this finite size effect has been provided. In type II superconductors it comprises the 3D to 1D crossover line $H_{pi}(T) = (\Phi_0/(a\xi_{j0}^-\xi_{k0}^-))(1 - T/T_c)^{4/3}$ with $i \neq j \neq k$ and $\xi_{i0,j0,k0}^-$ denoting the critical amplitude of the correlation length below T_c. As a result, below T_c and above $H_{pi}(T)$ superconductivity is confined to cylinders with diameter L_{H_i} (1D). Accordingly, there is no continuous phase transition in the (H_c, T) plane along the H_{c2} lines as predicted by the mean-field treatment. In addition, we confirmed the universal relationship between the 3D to 1D crossover and vortex melting line. The universal relation (9) and Maxwell's relation (19) also imply that the effects of isotope exchange and pressure on T_c, in-plane magnetic field penetration depth, correlation lengths, specific heat and magnetization are not independent.

Acknowledgments

This work was supported by the Swiss National Science Foundation and in part by the NCCR program MaNEP.

References

[1] Schneider T and Singer J M 2000 *Phase Transition Approach to High Temperature Superconductivity* (London: Imperial College Press)
[2] Larkin A and Varlamov A 2005 *Theory of Fluctuations in Superconductors* (Oxford: Oxford University Press)
[3] Lascialfari A, Tedesco P and Zucca I 2003 *Int. J. Mod. Phys.* B **17** 805
[4] Baraduc C, Buzdin A, Henry J-Y, Brison J-P and Puech L 1995 *Physica* C **248** 138
[5] Rosenstein B, Shapiro B Ya, Prozorov R, Shaulov A and Yeshurun Y 2001 *Phys. Rev.* B **63** 134501
[6] Rigamonti A, Lascialfari A, Romanò L, Varlamov A and Zucca I 2005 *J. Supercond.* **18** 763
[7] Karpinski J 1988 *Nature* **336** 660
[8] Karpinski J 1999 *Supercond. Sci. Technol.* **12** R153
[9] Hofer J, Schneider T, Singer J M, Willemin M and Keller H 1999 *Phys. Rev.* B **60** 1332
[10] Schneider T 2004 *The Physics of Superconductors* ed K Bennemann and J B Ketterson (Berlin: Springer) p 111
[11] Schneider T 2007 *Phys. Rev.* B **75** 174517
[12] Schneider T 2007 *Europhys. Lett.* **79** 57005
[13] Lee P A and Shenoy S R 1972 *Phys. Rev. Lett.* **28** 1025
[14] Schneider T 2004 *J. Supercond.* **17** 41
[15] Weyeneth S, Schneider T, Zhigadlo N D, Karpinski J and Keller H 2008 *J. Phys.: Condens. Matter* **20** 135208
[16] Abrikosov A 1957 *JETP* **5** 1174
[17] Prange R E 1970 *Phys. Rev.* B **1** 2349
[18] Pelissetto A and Vicari E 2002 *Phys. Rep.* **368** 549
[19] Kagawa N, Ishida T, Okuda K, Adachi S and Tajima S 2001 *Physica* C **357–360** 302
[20] Zech D, Rossel C, Lesne L, Keller H, Lee S L and Karpinski J 1996 *Phys. Rev.* B **54** 12535
[21] Katayama K, Ishida T, Adachi S and Tajima S 2003 *Physica* C **388/389** 741
[22] Plackowski T, Wang Y, Lortz R, Junod A and Wolf Th 2005 *J. Phys.: Condens. Matter* **17** 6871
[23] Roulin M, Junod A and Walker E 1998 *Physica* C **296** 137
[24] Khasanov R, Schneider T and Keller H 2005 *Phys. Rev.* B **72** 014524

3.6.3 Publication III: Evidence for Kosterlitz-Thouless and three-dimensional XY critical behavior in $Bi_2Sr_2CaCu_2O_{8+\delta}$

S. Weyeneth, T. Schneider, and E. Giannini
Phys. Rev. B **79**, 214504 (2009).

Abstract
We present reversible magnetization data of a high quality $Bi_2Sr_2CaCu_2O_{8+\delta}$ single crystal and explore the occurrence of 3D-xy critical behavior close to the bulk transition temperature T_c and of Kosterlitz-Thouless (KT) behavior. Below and above the presumed Kosterlitz-Thouless transition temperature T_{KT} we observe the characteristic 2D-xy behavior: a downward shift of the crossing point phenomenon towards T_{KT} as the field is decreased and sufficiently below T_{KT} the characteristic 2D-xy relationship between the magnetization and the in-plane magnetic penetration depth λ_{ab}. In contrast, the measured temperature dependence of the superfluid density does not exhibit the characteristic KT-behavior around the presumed T_{KT}. The absence of this feature is traced back to the 2D- to 3D-xy crossover setting in around and above T_{KT}. Invoking the Maxwell relation, the anomalous field dependence of the specific heat peak is also traced back to the intermediate 2D-xy behavior. However, close to T_c we observe consistency with 3D-xy critical behavior, in agreement with measurements of λ_{ab}.

DOI: 10.1103/PhysRevB.79.214504
PACS numbers: 74.72.−h, 74.25.Bt, 74.25.Dw

The original publication is electronically available at:
http://link.aps.org/doi/10.1103/PhysRevB.79.214504
http://www.vjsuper.org (Virtual Journal of Applications of Superconductivity)

Open access repositories:
http://www.zora.uzh.ch/20072
http://arxiv.org/abs/0902.1086

At completion of this thesis, according to the Thomson Reuters ISI Web of Knowledge database, this article has been cited at least 3 times.

PHYSICAL REVIEW B **79**, 214504 (2009)

Evidence for Kosterlitz-Thouless and three-dimensional *XY* critical behavior in $Bi_2Sr_2CaCu_2O_{8+\delta}$

S. Weyeneth* and T. Schneider
Physik-Institut der Universität Zürich, Winterthurerstrasse 190, CH-8057 Zürich, Switzerland

E. Giannini
DPMC, University of Geneva, 24 Quai Ernest-Ansermet, CH-1211 Geneva 4, Switzerland
(Received 6 February 2009; revised manuscript received 17 April 2009; published 4 June 2009)

We present reversible magnetization data of a high-quality $Bi_2Sr_2CaCu_2O_{8+\delta}$ single crystal and explore the occurrence of three-dimensional (3D)-*xy* critical behavior close to the bulk-transition temperature T_c and of Kosterlitz-Thouless (KT) behavior. Below and above the presumed Kosterlitz-Thouless transition temperature T_{KT} we observe the characteristic two-dimensional (2D)-*xy* behavior: a downward shift in the crossing point phenomenon toward T_{KT} as the field is decreased and sufficiently below T_{KT} the characteristic 2D-*xy* relationship between the magnetization and the in-plane magnetic penetration depth λ_{ab}. In contrast, the measured temperature dependence of the superfluid density does not exhibit the characteristic KT behavior around the presumed T_{KT}. The absence of this feature is traced back to the 2D- to 3D-*xy* crossover setting in around and above T_{KT}. Invoking the Maxwell relation, the anomalous field dependence of the specific-heat peak is also traced back to the intermediate 2D-*xy* behavior. However, close to T_c we observe consistency with 3D-*xy* critical behavior in agreement with measurements of λ_{ab}.

DOI: 10.1103/PhysRevB.79.214504 PACS number(s): 74.72.−h, 74.25.Bt, 74.25.Dw

I. INTRODUCTION

The study of thermal fluctuations received a considerable impetus from the discovery of the cuprate superconductors.[1–6] It was realized that in these materials the critical regime where thermal fluctuations dominate can be attained and that some of them are in addition quasi-two-dimensional (2D).[7] Furthermore, the systematics of the superconducting properties uncovered that the anisotropy is further enhanced with underdoping.[2,7] In this quasi-2D limit one expects the thermodynamic properties to be close to those of a two-dimensional superconductor, or more precisely of a stack of decoupled two-dimensional superconducting sheets. Although approximate treatments have been invoked to describe the thermodynamic properties of such materials, the essential ingredient, the Kosterlitz-Thouless (KT) behavior of the associated zero-field transition,[8] has mostly not been taken into account.[9–11] Only recently, this behavior was incorporated by combining Kosterlitz-Thouless renormalization group flows and explicit computations for plasmas.[12] On this basis the field and temperature dependences of the magnetization density, $m(H_c,T)$, for temperatures T near to and below the KT transition temperature T_{KT} were determined for magnetic fields H_c applied perpendicular to the superconducting sheet. These results are interesting on three immediate fronts. First, the resulting trends in the magnetization appear to emerge from the recent $Bi_2Sr_2CaCu_2O_{8+\delta}$ data of Li *et al.*[13] for underdoped and optimally doped samples. Second, by contrast evidence for smeared three-dimensional (3D)-*xy* behavior stems from the measured temperature dependence of the in-plane magnetic penetration depth λ_{ab}.[14–17] Third, the magnetic field dependence of the specific-heat peak exhibits, opposite to the generic behavior,[4,6] a shift to higher temperatures with increasing field strength.[18]

In this study we present reversible magnetization data of a $Bi_2Sr_2CaCu_2O_{8+\delta}$ single crystal and explore the evidence for intermediate KT-(2D-*xy*) and 3D-*xy* critical behavior. Below $T=89.5$ K$\simeq T_{KT}$ we observe consistency with the KT behavior in terms of the characteristic $m\propto\ln(H_c)$ dependence at fixed temperature. Furthermore, invoking the Maxwell relation $\partial^2 M/\partial T^2|_{H_c}=\partial(C/T)/\partial H_c|_T$ the anomalous field dependence of the specific heat peak is also traced back to 2D-*xy* behavior. However, close to the bulk-transition temperature $T_c\simeq 91.21$ K we observe consistency with 3D-*xy* critical behavior, consistent with previous measurements of the in-plane magnetic penetration depth λ_{ab}.[14,16,17] In Sec. II we sketch the theoretical background including the scaling relations for 2D- and 3D-*xy* critical behavior. Section III is devoted to the experimental details, and in Sec. IV we present the analysis of the data uncovering the evidence for 2D-*xy* and 3D-*xy* critical behavior in the respective temperature regimes. We close with a brief summary and some discussion.

II. THEORETICAL BACKGROUND

When thermal fluctuations dominate and the coupling to the charge is negligible a bulk superconductor is expected to exhibit sufficiently close to T_c 3D-*xy* critical behavior. In this case the magnetization per unit volume, $m=M/V$, adopts the scaling form[2–6,19]

$$\frac{m}{TH_c^{1/2}}=-\frac{Q^{\pm}k_B\xi_{ab}}{\Phi_0^{3/2}\xi_c}F^{\pm}(z),\quad F^{\pm}(z)=z^{-1/2}\frac{dG^{\pm}}{dz},$$

$$z=x^{-1/2\nu}=\frac{(\xi_{ab0}^{\pm})^2|t|^{-2\nu}H_c}{\Phi_0}. \tag{1}$$

In this form $Q^{\pm}$ is a universal constant and $G^{\pm}(z)$ is a universal scaling function of its argument, with $G^{\pm}(z=0)=1$. In addition $\gamma=\xi_{ab}/\xi_c$ denotes the anisotropy, ξ_{ab} the zero-field in-plane correlation length, and H_c the magnetic field applied along the c axis. In terms of the variable x the scaling form

[Eq. (1)] is similar to Prange's result for Gaussian fluctuations.[20] Approaching T_c the correlation lengths diverges as

$$\xi_{ab,c} = \xi^{\pm}_{ab0,c0}|t|^{-\nu}, \quad t = T/T_c - 1, \quad \pm = \mathrm{sgn}(t). \tag{2}$$

Supposing that 3D-xy fluctuations dominate the critical exponents are given by[21]

$$\nu \simeq 0.671 \simeq 2/3, \quad \alpha = 2 - 3\nu \simeq -0.013, \tag{3}$$

and there are the universal critical amplitude relations[2–4,19,21]

$$\frac{\xi^{-}_{ab0}}{\xi^{+}_{ab0}} = \frac{\xi^{-}_{c0}}{\xi^{+}_{c0}} \simeq 2.21, \quad \frac{Q^{-}}{Q^{+}} \simeq 11.5, \quad \frac{A^{+}}{A^{-}} = 1.07, \tag{4}$$

and

$$A^{-}\xi^{-}_{a0}\xi^{-}_{b0}\xi^{-}_{c0} \simeq A^{-}(\xi^{-}_{ab0})^2\xi^{-}_{c0} = \frac{A^{-}(\xi^{-}_{ab0})^3}{\gamma} = (R^{-})^3,$$
$$R^{-} \simeq 0.815, \tag{5}$$

where $A^{\pm}$ is the critical amplitude of the specific-heat singularity, defined as

$$c = \frac{C}{Vk_B} = \frac{A^{\pm}}{\alpha}|t|^{-\alpha} + B, \tag{6}$$

where B denotes the background. The anisotropy is then characterized in terms of

$$\gamma = \frac{\xi_{ab}}{\xi_c} = \frac{\xi^{\pm}_{ab0}}{\xi^{\pm}_{c0}}. \tag{7}$$

Furthermore, in the 3D-xy universality class T_c, ξ^{-}_{c0} and the critical amplitude of the in-plane magnetic penetration depth λ_{ab0} are not independent but are related by the universal relation,[2–4,19]

$$k_B T_c = \frac{\Phi_0^2}{16\pi^3}\frac{\xi^{-}_{c0}}{\lambda^2_{ab0}} = \frac{\Phi_0^2}{16\pi^3}\frac{\xi^{-}_{ab0}}{\gamma\lambda^2_{ab0}}. \tag{8}$$

The existence of the magnetization at T_c of the magnetic penetration depth below T_c and of the magnetic susceptibility above T_c implies the following asymptotic forms of the scaling function,[2–4,19]

$$Q^{\pm}\frac{1}{\sqrt{z}}\left.\frac{dG^{\pm}}{dz}\right|_{z\to\infty} = Q^{\pm}c^{\pm}_{\infty},$$
$$Q^{-}\left.\frac{dG^{-}}{dz}\right|_{z\to 0} = Q^{-}c^{-}_0(\ln z + c_1),$$
$$Q^{+}\frac{1}{z}\left.\frac{dG^{+}}{dz}\right|_{z\to 0} = Q^{+}c^{+}_0, \tag{9}$$

with the universal coefficients

$$Q^{-}c^{-}_0 \simeq -0.7, \quad Q^{+}c^{+}_0 \simeq 0.9, \quad Q^{\pm}c^{\pm}_{\infty} \simeq 0.5, \quad c_1 \simeq 1.76. \tag{10}$$

Noting that $Bi_2Sr_2CaCu_2O_{8+\delta}$ is highly anisotropic ($\gamma \gg 1$),[22] the system is expected to exhibit away from T_c 2D-xy behavior. A characteristic property of 2D-superconductors emerges from the magnetic field dependence of the magnetization. Sufficiently below the Kosterlitz-Thouless transition temperature T_{KT} the magnetization is given by[12]

$$m = -\frac{\pi\rho_s(T)}{2d\Phi_0}\left(1 - \frac{k_BT}{\pi\rho_s(T)}\right)\ln\left(\frac{\Phi_0}{4\pi H_c a_0^2\gamma_3}\right)$$
$$= -\left(\frac{\Phi_0}{32\pi^2\lambda^2_{ab}(T)} - \frac{k_BT}{d\Phi_0}\right)\ln\left(\frac{\Phi_0}{4\pi H_c a_0^2\gamma_3}\right), \tag{11}$$

where ρ_s is the 2D superfluid density, related to the in-plane magnetic penetration depth λ_{ab} via

$$\rho_s(T) = \frac{d\Phi_0^2}{16\pi^3\lambda^2_{ab}(T)}. \tag{12}$$

Here d is the thickness of the independent superconducting sheets, γ_3 is a parameter that vanishes as T approaches T_{KT}, and a_0 is the microscopic short-distance cutoff length. Moreover, $\rho_s(T_{\mathrm{KT}})$ and T_{KT} are related by

$$\rho_s(T_{\mathrm{KT}}) = \frac{2}{\pi}k_BT_{\mathrm{KT}}, \tag{13}$$

while $\rho_s(T)=0$ above T_{KT}. Below this universal Nelson-Kosterlitz jump $1/\lambda^2_{ab}(T)$ increases as[23,24]

$$\lambda^2_{ab}(T_{\mathrm{KT}})/\lambda^2_{ab}(T) = \frac{T}{T_{\mathrm{KT}}}[1 + \hat{b}(T_{\mathrm{KT}} - T)^{1/2}]. \tag{14}$$

Note that Eq. (11) gives a simple relation between the superfluid density and the derivative of the magnetization, namely,

$$\frac{dm}{d\ln(H_c)} = g(T) = \frac{\Phi_0}{32\pi^2\lambda^2_{ab}(T)} - \frac{k_BT}{d\Phi_0}. \tag{15}$$

Furthermore, at criticality m depends on H in terms of[12]

$$m = -\frac{k_BT_{\mathrm{KT}}}{d\Phi_0}\ln\left(\gamma_1 \ln\frac{\Phi_0}{4\pi H_c a_0^2\gamma_2}\right), \tag{16}$$

where γ_1 and γ_2 are constants. Correspondingly, plots of M vs T at different fields should then exhibit a systematic drift of the "crossing phenomenon." Above T_{KT} and for asymptotically small fields the magnetization is given by[12,30,31]

$$m \simeq -\frac{k_BT}{2d\Phi_0^2}\xi^2_{ab}H_c, \quad \xi_{ab} = \xi_{ab0}\exp\left(\frac{\tilde{b}}{(T/T_{\mathrm{KT}} - 1)^{1/2}}\right), \tag{17}$$

where ξ_{ab} is the Kosterlitz-Thouless correlation length.[8] The parameters $\tilde{b}$ and $\hat{b}$, determining the temperature dependence of the magnetic penetration depth below the jump [Eq. (14)], are related by[24]

$$\tilde{b}\hat{b} = \pi/(2T^{1/2}_{\mathrm{KT}}) \simeq 0.17 \ \mathrm{K}^{-1/2}. \tag{18}$$

III. EXPERIMENTAL DETAILS

Single crystals of $Bi_2Sr_2CaCu_2O_{8+\delta}$ were grown with the floating zone (FZ) method, from direct crystallization from

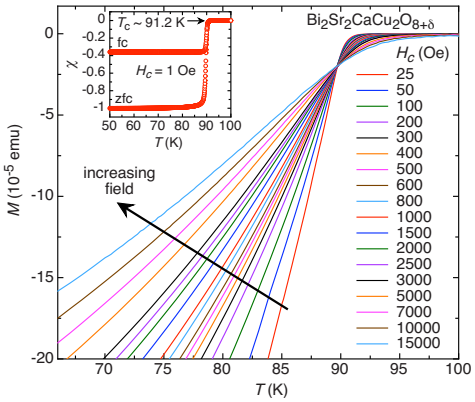

FIG. 1. (Color online) Temperature dependence of the measured reversible magnetic moment of the studied $Bi_2Sr_2CaCu_2O_{8+\delta}$ single crystal at various magnetic fields applied along the c axis. The inset depicts susceptibility measurements in 1 Oe in the ZFC and FC mode. The sharp onset of superconductivity points to a transition temperature close to $T_c \simeq 91.2$ K.

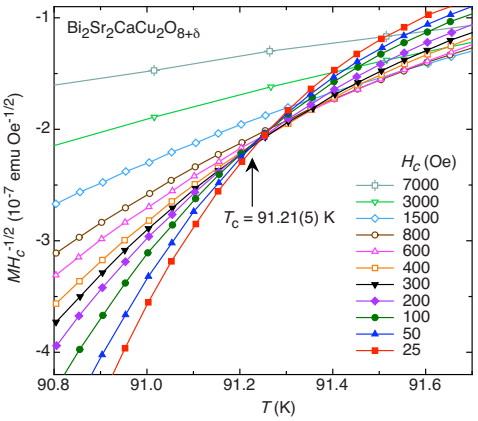

FIG. 2. (Color online) $M/H_c^{1/2}$ vs T yielding the estimate $T_c \simeq 91.21$ K in terms of the crossing point at $M/H_c^{1/2} \simeq -2.13 \times 10^{-7}$ emuOe$^{-1/2}$.

the melt (no solvent used). The feed rod was obtained from a commercial $Bi_2Sr_2CaCu_2O_{8+\delta}$ powder after pressing and sintering to a shape of 7 cm in length and about 7 mm in diameter. The seed rod was made with a previously crystallized rod. After a first fast FZ melting at a rate of 24 mm/h in Ar, the crystal growth was performed at a slow rate of 0.2 mm/h in a 7% O_2–93% Ar atmosphere, while both rods were counter-rotating at 18 rpm. The FZ growth was performed in a commercial two-mirror vertical furnace (from Cyberstar), equipped with two 1000 W halogen lamps. The growth conditions at the flat zone interface were kept stable for several days. A review of the growth technique can be found elsewhere.[25] The as-grown crystals were easily cleaved from the crystallized boule and annealed at $T = 500$ °C for 50 h in 0.1% O_2–99.9% Ar in order to tune and homogenize the oxygen content corresponding to the optimal doping level. Crystals with typical size of 1–5 mm and thickness of 0.05–0.1 mm could be extracted. The good crystalline quality of the samples was checked by x-ray diffraction and magnetic susceptibility measurements.

The $Bi_2Sr_2CaCu_2O_{8+\delta}$ sample used in this work, a $V \simeq 4.6 \times 10^{-5}$ cm^3 single crystal, was chosen by its sharp low-field Meissner transition from several high-quality single crystals. The magnetization was measured in a magnetic property measurement system (MPMS) XL from Quantum Design, equipped with a reciprocating sample option. The inset in Fig. 1 shows the measured susceptibility at $H_c = 1$ Oe applied along the c axis. It reveals a rather sharp transition at $T_c \simeq 91.2$ K and a well-saturated Meissner state, pointing to excellent quality. The volume of the sample was estimated by susceptibility measurements below T_c in the Meissner state with a magnetic field applied along the ab plane to minimize demagnetization effects. The extracted volume of $V \simeq 4.6 \times 10^{-5}$ cm^3 compares well with that estimated with an optical microscope. Figure 1 summarizes the measured temperature dependence of the magnetic moment at fields ranging from 25–15 000 Oe applied along the c axis. After applying the magnetic field, well below T_c it was kept constant and the magnetic moment of the single crystal was measured at a stabilized temperature by moving the sample with a frequency of 0.5 Hz through a set of detection coils. The reversible superconducting diamagnetic magnetization, $M = mV$, was then obtained by comparing field-cooled (FC) and zero-field-cooled (ZFC) data. Due to a substantial pinning contribution at low magnetic field we omitted data below 25 Oe. A temperature-dependent normal-state paramagnetic background was subtracted.

IV. DATA ANALYSIS

We are now prepared to analyze the magnetization data. To estimate the bulk T_c we invoke Eqs. (1), (9), and (10), revealing that the plot $m/H_c^{1/2}$ vs T should exhibit a crossing point at T_c. Here $m/(TH_c^{1/2})$ adopts with Eq. (7) the value $m/(T_c H_c^{1/2}) = -0.5 k_B \gamma \Phi_0^{-3/2}$. According to Fig. 2, showing $M/H_c^{1/2}$ vs T there is a crossing point at $T_c \simeq 91.21$ K where $M/H_c^{1/2} \simeq -2.13 \times 10^{-7}$ emuOe$^{-1/2}$. With $V \simeq 4.6 \times 10^{-5}$ cm^3, where $m = M/V$, it yields for the anisotropy [Eq. (7)] the estimate,

$$\gamma = \bar{\xi}_{ab0}/\bar{\xi}_{c0} \simeq 69, \tag{19}$$

compared to $\gamma \simeq 133$ for an underdoped sample with $T_c \simeq 84.2$ K and in reasonable agreement with earlier estimates for optimally doped samples.[22,26] Given this rather large anisotropy the 2D- to 3D-xy crossover is expected to occur rather close to the bulk T_c.

A characteristic feature of a 2D superconductor is the crossing phenomenon occurring at fixed magnetic fields and above T_{KT} in the plot M vs T.[2,12] A glance at Fig. 3 reveals that this phenomenon is well confirmed above $T = 89.5$ K $\simeq T_{KT}$. Indeed, there is as predicted a downward shift in the

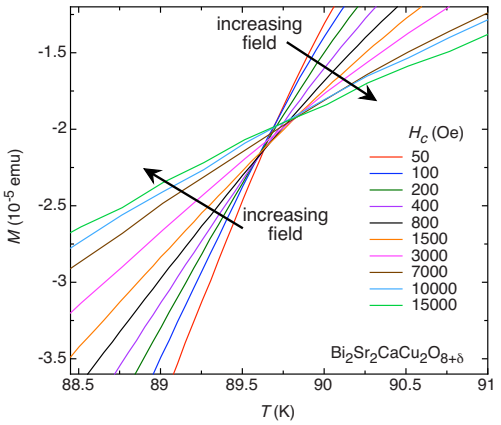

FIG. 3. (Color online) M vs T at various magnetic fields exhibiting a crossing phenomenon shifting toward $T_{KT} \simeq 89.5$ K from above as the field is decreased.

"crossing point" toward T_{KT} from above as the field is decreased.[12] The same behavior was also observed in the highly anisotropic Tl-1223, Bi-2201, and underdoped $La_{2-x}Sr_xCuO_4$ single crystals.[2,27–29]

To substantiate 2D-xy behavior further we invoke Eq. (11) in terms of the plot M vs H_c shown in Fig. 4. The solid lines in Fig. 4(a) indicate that sufficiently below $T_{KT} \simeq 89.5$ K the 2D relation [Eq. (15)] between the superfluid density and the derivative of the magnetization with respect to the logarithm of the field is for small fields well obeyed, so in this temperature regime the system indeed behaves as a stack of essentially decoupled two-dimensional Kosterlitz-Thouless films with $T_{KT} \simeq 89.5$ K. However, close to the bulk $T_c \simeq 91.21$ K one expects 3D-xy critical behavior. In this case and in the magnetic field range considered here the limit $z \to \infty$ is then approached. Here Eqs. (1), (9), and (10) imply the limiting behavior

$$m = -\frac{Q^+ c_\infty^+ k_B \xi_{ab} T}{\Phi_0^{3/2} \xi_c} H_c^{1/2} \simeq -\frac{0.5 k_B \xi_{ab0}^+ T}{2\Phi_0^{3/2} \xi_{c0}^+} H_c^{1/2}. \quad (20)$$

Figure 4(b), depicting M vs H_c close to $T_c \simeq 91.21$ K at $T=91$, 91.25, and 91.5 K, shows that this expectation is well confirmed. According to this, approaching T_c the system undergoes a 2D- to 3D-xy crossover. It implies that the characteristic 2D-xy critical behavior, including the jump of the superfluid density at T_{KT} [Eqs. (13) and (14)], is removed.

To clarify this point we invoke Eq. (11) to determine the temperature dependence of $1/\lambda_{ab}^2$ sufficiently below T_{KT}. Setting $M(H_c,T) = f(T) + g(T) \cdot \ln(H_c)$, $g(T)$ is then given by Eq. (15) and follows from plots as shown in Fig. 4(a) in terms of the slope of the straight lines. For $d=30$ Å we obtain for $1/\lambda_{ab}^2(T)$ the data points shown in Fig. 5. For comparison we included the ab-plane microwave surface impedance data of Lee *et al.*[15] for a high-quality $Bi_2Sr_2CaCu_2O_8$ single crystal, plotted in terms of the superfluid density, assuming $\lambda_{ab}(0) = 1350$ Å. Sufficiently below

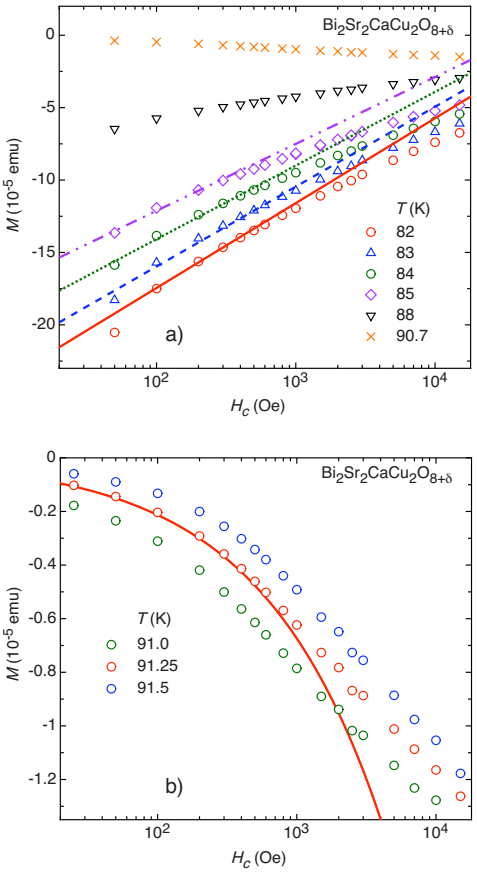

FIG. 4. (Color online) M vs H_c at various fixed temperatures. (a) From $T=82$ to 90.7 K. The straight lines indicate the characteristic 2D relation between the superfluid density and the derivative of the magnetization with respect to the logarithm of the field [Eq. (15)], valid in the low-field regime as long as pinning contributions are negligible. (b) M vs H_c at $T=91$, 91.25, and 91.5 K. The solid line is $M = -2.13 \times 10^{-7} \cdot H_c^{1/2}$ emu indicating the characteristic 3D-xy behavior at T_c in terms of Eq. (20).

T_{KT} we observe reasonable agreement with the 2D-xy prediction (●) and the measured $1/\lambda_{ab}^2(T)$ (■). Accordingly, in this regime the expulsion of vortices from the KT phase dominates. Here we also observe consistency with the characteristic KT behavior indicted by the dash-dot-dot line [Eq. (14)]. However, around T_{KT}, indicated by the horizontal and KT lines, the measured $1/\lambda_{ab}^2(T)$ does not exhibit any evidence for the characteristic jump from $1/\lambda_{ab}^2(T_{KT})$ to zero for $T > T_{KT}$. In contrast agreement with the leading 3D-xy critical behavior is observed (solid line), revealing the removal of the characteristic jump in $1/\lambda_{ab}^2(T)$ at T_{KT} due to the 2D- to 3D-xy crossover. To explore the effect of the 3D-xy fluctuations further, we use the critical amplitude, $1/\lambda_{ab0}^2 = 5$

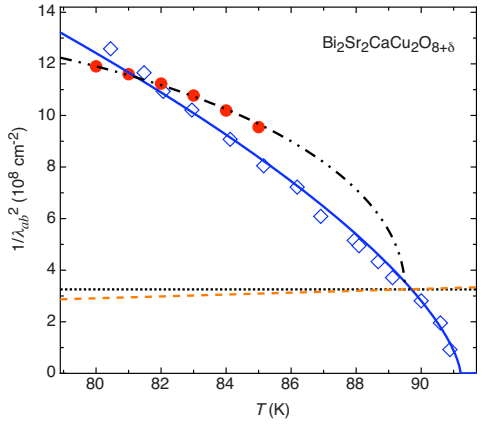

FIG. 5. (Color online) $1/\lambda_{ab}^2(T)$ vs T. ●: derived from the magnetization with the aid of Eq. (11) rewritten as $M(H_c,T)=f(T)+g(T)\cdot\ln(H_c)$ and $d=30$ Å; ■: experimental data derived from Lee *et al.* (Ref. 15) with $\lambda_{ab}(T=0)=1350$ Å. The solid line is $1/\lambda_{ab}^2(T)=1/\lambda_{ab0}^2(1-T/T_c)^{2/3}$ with $1/\lambda_{ab0}^2=5\times10^9$ cm^{-2} and $T_c=91.21$ K indicating 3D-xy critical behavior. The dashed line is the KT-line $1/\lambda_{ab}^2(T)=3.64\times10^6\cdot T$ cm^{-2} [Eq. (13)], the dotted one $1/\lambda_{ab}^2(T_{KT})=3.26\times10^8$ cm^{-2} with $T_{KT}=89.5$ K, and the dash-dot-dot one is Eq. (14) with $\hat{b}\simeq1$ K$^{-1/2}$.

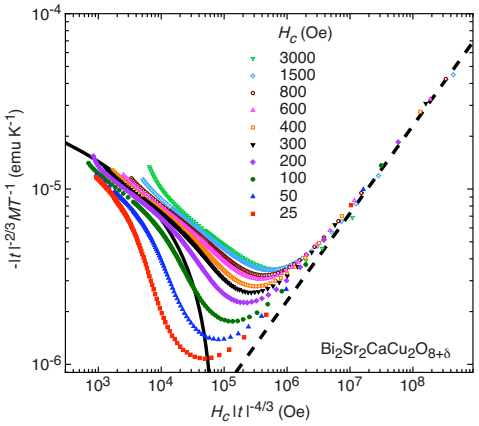

FIG. 6. (Color online) $-|t|^{-2/3}M/T$ vs $H_c|t|^{-4/3}$ for $T<T_c$ at various applied magnetic fields. The solid line is Eq. (25) and the dashed one Eq. (26).

$\times10^9$ cm^{-2} and $T_c=91.21$ K to obtain from the universal relation [Eq. (8)] the estimate

$$\xi_{c0}^- \simeq 2.9 \text{ Å} \tag{21}$$

for the amplitude of the c-axis correlation length. The occurrence of 3D-xy critical behavior then requires that $\xi_c(T)=\xi_{c0}^-|t|^{-2/3}$ exceeds d considerably, yielding with $d=30$ Å and $T_c=91.21$ K for the onset of 3D fluctuations the lower bound $T>90.24$ K. Furthermore, around and above $T=91$ K the 3D-xy critical regime is attained [see Fig. 4(b)]. So the occurrence of KT behavior in $1/\lambda_{ab}^2(T)$ is restricted to temperatures below $T_{KT}\simeq89.5$ K.

On the other hand, the small amplitude of the c-axis correlation length leads with $\gamma=69$ [Eq. (19)] to a rather large amplitude of the in-plane correlation length, $\xi_{ab0}^-=\gamma\xi_{c0}^-\simeq200$ Å and with the universal relation [Eq. (5)] to a very small amplitude of the specific-heat singularity,

$$A^- = \frac{0.815^3}{\gamma^2(\xi_{c0}^-)^3} \simeq 4.7\times10^{-6} \text{ Å}^{-3}, \tag{22}$$

in comparison with $A^-\simeq6.8\times10^{-4}$ Å^{-3} in optimally doped $YBa_2Cu_3O_{7-\delta}$ and 1.7×10^{-3} Å^{-3} in ^{4}He.[2] This small critical amplitude renders it difficult to observe 3D-xy critical behavior in the specific heat of $Bi_2Sr_2CaCu_2O_{8+\delta}$.[18]

Considering Eqs. (1), (9), and (10) consistency with 3D-xy critical behavior also requires that the data scale below T_c as

$$|t|^{-2/3}\frac{m}{T} = -\frac{Q^-c_0^-k_B}{\Phi_0\xi_{c0}^-}\left[\ln\left(\frac{(\xi_{ab0}^-)^2}{\Phi_0}H_c|t|^{-4/3}\right)+c_1\right], \quad z\to0, \tag{23}$$

and

$$|t|^{-2/3}\frac{m}{T} = -\frac{Q^-c_\infty^-k_B\xi_{ab0}^-}{\Phi_0^{3/2}\xi_{c0}^-}(H_c|t|^{-4/3})^{1/2}, \quad z\to\infty, \tag{24}$$

respectively. In Fig. 6 we plot $-|t|^{-2/3}M/T$ vs $H_c|t|^{-4/3}$ for $T<T_c$ at various applied magnetic fields. The solid line is Eq. (23) in terms of

$$-|t|^{-2/3}\frac{M}{T} = -3.32\times10^{-6}[\ln(H_c|t|^{-4/3})-11.23] \text{ (emuK}^{-1}), \tag{25}$$

and the dashed one

$$-|t|^{-2/3}\frac{M}{T} = 2.3\times10^{-9}(H_c|t|^{-4/3})^{1/2} \text{ (emuK}^{-1}) \tag{26}$$

corresponds to the limit [Eq. (24)]. While the $H_c|t|^{-4/3}\propto z\to\infty$ limiting behavior (dashed curve) is well confirmed we observe with decreasing z substantial deviations from the data collapse on a single curve.

From Eq. (26) we derive with $V=4.6\times10^{-5}$ cm^3, where $m=M/V$, the estimate

$$\gamma=\xi_{ab0}^-/\xi_{c0}^-\simeq68, \tag{27}$$

in reasonable agreement with $\gamma=\xi_{ab0}^-/\xi_{c0}^-\simeq69$ [Eq. (19)], derived from the crossing point in $M/H_c^{1/2}$ vs T shown in Fig. 2. The apparent failure of 3D-xy scaling outside the limit $H_c|t|^{-4/3}\propto z\to\infty$ is then attributable to the 3D- to 2D-xy crossover. In particular, very small magnetic fields would be required to attain the limit $H_c|t|^{-4/3}\propto z\to0$ with reduced temperatures t in the range where 3D-xy fluctuations dominate.

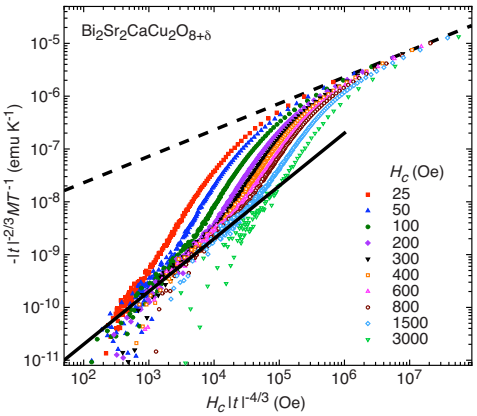

FIG. 7. (Color online) $-|t|^{-2/3}M/T$ vs $H_c|t|^{-4/3}$ for $T>T_c$ at various applied magnetic fields. The solid line is Eq. (30) and the dashed one Eq. (31).

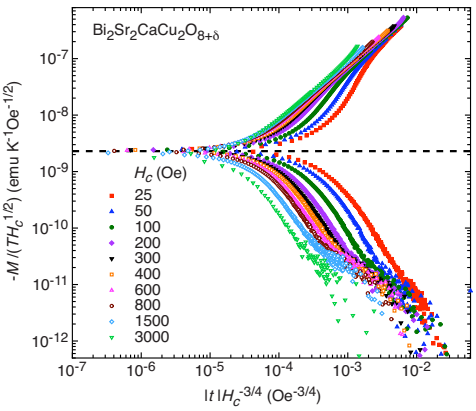

FIG. 8. (Color online) $-M/(TH_c^{1/2})$ vs $|t|H_c^{-3/4}$ at various applied magnetic fields. The dashed line is Eq. (31).

Indeed, given our evidence for 2D-xy behavior above $T_{KT} \simeq 89.5$ K in terms of the crossing phenomenon (Fig. 3) and 3D-xy critical behavior above $T=91$ K [Fig. 4(b)], transforming to $H_c|t|^{-4/3}=2\times10^6$ Oe for $H_c=600$ Oe. Figure 6 reveals that below this value pronounced deviations from the expected data collapse occur, so in this regime 3D-xy scaling fails because 3D fluctuations no longer dominate. Nevertheless, at much lower fields the limit $H_c|t|^{-4/3} \propto z \to 0$ should be attainable, leading to the asymptotic behavior indicated by the solid line [Eq. (25)] in Fig. 6.

Noting again that the occurrence of 3D behavior requires that the c-axis correlation length $\xi_c = \xi_{c0}^{\pm}|t|^{-2/3}$ exceeds the interlayer spacing d it is clear that the 3D- to 2D-xy crossover is not restricted to temperatures below T_c. Given the universal ratio $\xi_{c0}^{+} \simeq \xi_{c0}^{-}/2.21$ [Eq. (4)] it even follows that above T_c the 3D-xy critical regime is even much narrower. Considering then the limits $H_c|t|^{-4/3} \propto z \to 0$ and $z \to \infty$ above T_c, Eqs. (1), (9), and (10) yield the scaling forms

$$|t|^{-2/3}\frac{m}{T} = -\frac{Q^{+}c_0^{+}k_B(\xi_{ab0}^{-})^2}{\Phi_0^2 \xi_{c0}^{-}} H_c|t|^{-4/3}, \quad z \to 0 \qquad (28)$$

and

$$|t|^{-2/3}\frac{m}{T} = -\frac{Q^{+}c_\infty^{+}k_B\xi_{ab0}^{+}}{\Phi_0^{3/2}\xi_{c0}^{+}} (H_c|t|^{-4/3})^{1/2}, \quad z \to \infty. \qquad (29)$$

In Fig. 7 we depicted $-|t|^{-2/3}M/T$ vs $H_c|t|^{-4/3}$ for $T>T_c$ at various applied magnetic fields. The solid line is Eq. (28) in terms of

$$-|t|^{-2/3}M/T = 2\times10^{-13}H_c|t|^{-4/3}\ (\mathrm{emuK^{-1}}) \qquad (30)$$

and the dashed one

$$-|t|^{-2/3}M/T = 2.3\times10^{-9}(H_c|t|^{-4/3})^{1/2}\ (\mathrm{emuK^{-1}}), \qquad (31)$$

corresponding to the limit [Eq. (29)]. Note that Eqs. (26) and (31) fully agree with each other and with that confirm $Q^{+}c_\infty^{+} = Q^{-}c_\infty^{-}$ [Eq. (10)]. In analogy to Fig. 6 we observe that the $z \to \infty$ limiting behavior is well confirmed, while substantial deviations from a data collapse on a single curve set in for $H_c|t|^{-4/3} \lesssim 2\times10^6$ Oe. Here the crossover to 2D-xy behavior sets in and 3D-xy scaling fails. Nevertheless, in the limit $H_c \to 0$ and reduced temperatures t in the range where 3D-xy fluctuations dominate, the limit $H_c|t|^{-4/3} \propto z \to 0$ should be attainable. It is indicated by the solid line [Eq. (30)] in Fig. 7.

According to Eq. (1) one expects that the data plotted as $M/(TH_c^{1/2})$ vs $|t|H_c^{-3/4}$ should fall on two branches. An upper branch corresponding to $T>T_c$ and a lower one for $T<T_c$. A glance at Fig. 8, depicting this plot clearly reveals the flow to 3D-xy critical behavior by approaching T_c ($|t|=0$) and in particular consistency with the leading 3D-xy critical behavior below $|t|H_c^{-3/4}=10^{-5}$ $\mathrm{Oe}^{-3/4}$.

Another property where KT behavior in terms of the 2D- to 3D-xy crossover should be observable is the magnetic field dependence of the specific peak. Indeed, in $Bi_2Sr_2CaCu_2O_{8+\delta}$ this peak shifts[18] opposite to the generic behavior.[4,6] Given the Maxwell relation,

$$\left.\frac{\partial^2 M}{\partial T^2}\right|_{H_c} = \frac{\partial}{\partial H_c}(C/T)|_T, \qquad (32)$$

relating magnetization and specific heat, this abnormality should also be observable in $\partial^2 M/\partial^2 T|_{H_c}$. A glance at Fig. 9 depicting $\partial^2 M/\partial T^2|_{H_c}$ vs T for various magnetic fields reveals consistency with the anomalous shift in the specific-heat peak. Indeed the dip shifts toward higher temperatures.

Noting that the anomalous shift occurs slightly above $T_{KT} \simeq 89.5$ K, it is indeed expected to reflect 2D-xy behavior. To check this conjecture we invoke expression (17) for

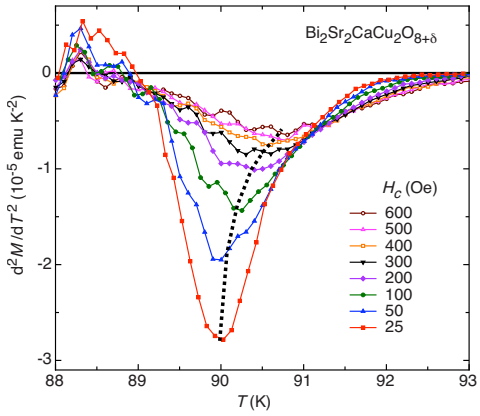

FIG. 9. (Color online) $\partial^2 M/\partial T^2|_{H_c}$ vs T at various H_c according to Eq. (32). The dotted line indicates the locations of the respective minima $T_p(H_c)$.

the magnetization valid above T_{KT} in the limit $H_c \to 0$. Although this limit is not attained in the field range considered here, m is expected to scale as $m \simeq -[k_B T/(2d\Phi_0^2)]\xi_{ab}^2 f(H_c)$ with $f(H_c)=H_c$ for $H_c \to 0$.[32] Accordingly, $\partial^2 M/\partial T^2|_{H_c}$ diverges at T_{KT}. However, there is the magnetic field induced finite-size effect preventing the correlation length ξ_{ab} to grow beyond the limiting magnetic length $L_{H_c}=[\Phi_0/(aH_c)]^{1/2}$ where $a \simeq 3.12$.[3–6] As a consequence, in finite fields the divergence is removed by a dip. Its minimum occurs at T_p given by

$$\xi_{ab}(T_p) = L_{H_c} = [\Phi_0/(aH_c)]^{1/2}. \tag{33}$$

In Fig. 10 we show T_p vs H derived from the data depicted in Fig. 9. For comparison we included

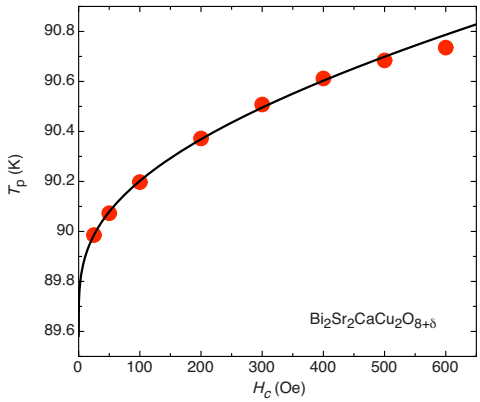

FIG. 10. (Color online) T_p vs H_c determined from the data depicted in Fig. 9. The solid line is Eq. (34) with $T_{KT}=89.5$ K, $\tilde{b} \simeq 0.3$, $a=3.12$, and $\xi_{ab0}=84$ Å.

$$T_p(H_c) = T_{KT}\left\{1 + \left[2\tilde{b}/\ln\left(\frac{\Phi_0}{a\xi_{ab0}^2 H_c}\right)\right]^2\right\}, \tag{34}$$

resulting from Eqs. (17) and (33), for a realistic set of parameters. Apparently, the characteristic shift toward higher temperatures and the $\ln(H_c)$ behavior are well confirmed and the values for $\tilde{b}$ [Eq. (17)] and $\hat{b}$ [Eq. (14)] are reasonably consistent with the relation $\tilde{b}\hat{b}=\pi/(2T_{KT}^{1/2}) \simeq 0.17$ K$^{-1/2}$ [Eq. (18)]. Furthermore, the observed H_c dependence of T_p down to 25 Oe also implies that the lateral extent L_{ab} of the homogenous regions exceeds $L_{H_c} \simeq 3640$ Å. Indeed, in the opposite case ($L_{ab} < L_{H_c}$) T_p would be independent of H_c. Thus, $L_{ab} > 3640$ Å uncovers a remarkable sample homogeneity. Nevertheless it appears to be unlikely that the asymptotic $H_c \to 0$ is experimentally attainable. Here $T_p(H_c)$ follows from $\xi_{ab}=\xi_{ab0}^-|T_p|^{-2/3}=L_{H_c}$ so

$$T_p = T_c\left[1 - \left(\frac{aH_c(\xi_{ab0}^-)^2}{\Phi_0}\right)^{3/4}\right], \tag{35}$$

whereupon T_p shifts with increasing field to lower temperatures, as observed in a variety of less anisotropic cuprates.[4,6]

V. SUMMARY AND DISCUSSION

Even though the mechanism of superconductivity in the cuprates remains a mystery the associated phase-transition properties can be understood as consequences of thermal fluctuations within the framework of the theory of critical phenomena. In this work we presented and analyzed reversible magnetization data of the highly anisotropic $Bi_2Sr_2CaCu_2O_{8+\delta}$ for magnetic fields applied along the c axis of the high-quality single crystal. We examined the occurrence of 3D-xy critical behavior close to the bulk-transition temperature T_c and of Kosterlitz-Thouless behavior. Below T_c and above the presumed Kosterlitz-Thouless transition temperature T_{KT} we observed, in agreement with the theoretical prediction,[12] a downward shift in the "crossing point" toward T_{KT} from above as the field is decreased. Sufficiently below T_{KT} we verified the characteristic 2D-xy relationship between the magnetization and the in-plane magnetic penetration depth.[12] In contrast, we have seen that the measured temperature dependence of the superfluid density does not exhibit the characteristic KT behavior (Nelson-Kosterlitz jump) around the presumed T_{KT}. The absence of this feature was traced back to the 2D- to 3D-xy crossover setting in around and above T_{KT}. Indeed, in the limit $H_c|t|^{-4/3} \to \infty$ we established clear evidence for 3D-xy critical behavior above and below T_c, while in the opposite limit ($H_c|t|^{-4/3} \to 0$) its failure was attributed to the dimensional crossover. Invoking the Maxwell relation $\partial^2 M/\partial^2 T|_H = \partial(C/T)/\partial H_c|_T$ the anomalous field dependence of the specific-heat peak was also traced back to the intermediate 2D-xy behavior.[18] Implications include: first, sufficiently below T_{KT} the isotope and pressure effects on $dm/d\ln(H_c)$ at fixed temperature T and the in-plane magnetic penetration depth $\lambda_{ab}(T)$ are not independent but related by Eq. (15). Second, the bulk-transition

temperature T_c and the critical amplitudes of the c-axis correlation length and in-plane magnetic penetration depth are related by the universal relation [Eq. (8)], so the isotope and pressure effects on these properties are related.[33]

ACKNOWLEDGMENTS

This work was partially supported by the Swiss National Science Foundation and the EU Project CoMePhS.

*wstephen@physik.uzh.ch

[1] G. Blatter, M. V. Feigel'man, V. B. Geshkenbein, A. I. Larkin, and V. M. Vinokur, Rev. Mod. Phys. **66**, 1125 (1994).
[2] T. Schneider and J. M. Singer, *Phase Transition Approach to High Temperature Superconductivity* (Imperial College Press, London, 2000).
[3] T. Schneider, in *The Physics of Superconductors*, edited by K. Bennemann and J. B. Ketterson (Springer, Berlin, 2004), p. 111.
[4] T. Schneider, J. Phys.: Condens. Matter **20**, 423201 (2008).
[5] S. Weyeneth, T. Schneider, N. D. Zhigadlo, J. Karpinski, and H. Keller, J. Phys.: Condens. Matter **20**, 135208 (2008).
[6] S. Weyeneth, T. Schneider, Z. Bukowski, J. Karpinski, and H. Keller, J. Phys.: Condens. Matter **20**, 345210 (2008).
[7] T. Schneider, Physica B **326**, 289 (2003).
[8] J. M. Kosterlitz, J. Phys. C **7**, 1046 (1974).
[9] L. N. Bulaevskii, M. Ledvij, and V. G. Kogan, Phys. Rev. Lett. **68**, 3773 (1992).
[10] J. Mosqueira, L. Cabo, and F. Vidal, Phys. Rev. B **76**, 064521 (2007).
[11] J. Mosqueira and F. Vidal, Phys. Rev. B **77**, 052507 (2008).
[12] V. Oganesyan, D. A. Huse, and S. L. Sondhi, Phys. Rev. B **73**, 094503 (2006).
[13] L. Li, Y. Wang, M. J. Naughton, S. Ono, Y. Ando, and N. P. Ong, Europhys. Lett. **72**, 451 (2005).
[14] T. Jacobs, S. Sridhar, Q. Li, G. D. Gu, and N. Koshizuka, Phys. Rev. Lett. **75**, 4516 (1995).
[15] Shih-Fu Lee, D. C. Morgan, R. J. Ormeno, D. Broun, R. A. Doyle, J. R. Waldram, and K. Kadowaki, Phys. Rev. Lett. **77**, 735 (1996).
[16] K. D. Osborn, D. J. Van Harlingen, Vivek Aji, N. Goldenfeld, S. Oh, and J. N. Eckstein, Phys. Rev. B **68**, 144516 (2003).
[17] T. Schneider and D. Di Castro, Phys. Rev. B **69**, 024502 (2004).
[18] A. Junod, A. Erb, and C. Renner, Physica C **317-318**, 333 (1999).
[19] J. Hofer, T. Schneider, J. M. Singer, M. Willemin, H. Keller, C. Rossel, and J. Karpinski, Phys. Rev. B **60**, 1332 (1999).
[20] R. E. Prange, Phys. Rev. B **1**, 2349 (1970).
[21] A. Pelissetto and E. Vicari, Phys. Rep. **368**, 549 (2002).
[22] S. Watauchi, H. Ikuta, H. Kobayashi, J. Shimoyama, and K. Kishio, Phys. Rev. B **64**, 064520 (2001).
[23] D. R. Nelson and J. M. Kosterlitz, Phys. Rev. Lett. **39**, 1201 (1977).
[24] V. Ambegaokar, B. I. Halperin, D. R. Nelson, and E. D. Siggia, Phys. Rev. B **21**, 1806 (1980).
[25] A. Revcolevschi and J. Jegoudez, Prog. Mater. Sci. **42**, 321 (1997).
[26] A. Piriou, Y. Fasano, E. Giannini, and O. Fischer, Phys. Rev. B **77**, 184508 (2008).
[27] G. Triscone, A. Junod, and R. E. Gladyshevskii, Physica C **264**, 233 (1996).
[28] G. Triscone, M. S. Chae, M. C. de Andrade, and M. B. Maple, Physica C **290**, 188 (1997).
[29] H. Iwasaki, F. Matsuoka, and K. Tanigawa, Phys. Rev. B **59**, 14624 (1999).
[30] T. Schneider, Phys. Rev. B **75**, 174517 (2007).
[31] B. I. Halperin and D. R. Nelson, J. Low Temp. Phys. **36**, 599 (1979).
[32] T. Schneider, EPL **79**, 57005 (2007).
[33] T. Schneider, Phys. Rev. B **67**, 134514 (2003).

4 Anisotropic superconducting properties of iron-pnictide high-T_c superconductors

This chapter focusses on results obtained for the novel iron-pnictide superconductors. In the first section the recent discovery of iron-pnictide superconductors is briefly summarized. Next the method of growing single crystals is described, followed by investigations of the anisotropic properties of several of these compounds.

4.1 High-T_c superconductivity in the iron-pnictide compounds

Already in the last century[1], the synthesis of iron-pnictide compounds with the ZrCuSiAs-type structure[2] was studied by Jeitschko *et al.* [113, 114, 115, 116]. In 1995 the first successful synthesis of the iron-pnictide LaFePO was announced [115]. Although a careful structural analysis was presented, the electronic and magnetic properties were not reported. It was not until 2006, that superconductivity in $LaFePO_{1-x}$ was found by Kamihara *et al.* [117] with a transition temperature $T_c \sim 5$ K. Already at that time, various transition-metal oxide families were known to exhibit superconductivity with similar low transition temperatures, including Sr_2RuO_4 [118], KOs_2O_6 [119], $Na_{0.33}V_2O_5$ [120], and $Na_{0.35}CoO_2 \cdot 1.3\ H_2O$ [121]. In contrast, the known copper-oxide high-T_c superconductors (cuprates) show superconductivity far above 30 K [21]. For this reason the above mentioned discovery by Kamihara *et al.* [117] did not attract much attention in the scientific community. Even the fact that iron-based materials may exhibit superconductivity is not particularly noteworthy, since superconductors containing iron, like U_6Fe [122], Th_7Fe [123], $R_2Fe_3Si_5$ (R = Sc, Y, Lu, and Tm) [124, 125], and the so-called skutterudites XFe_4P_{12} (X = La, Y) [126, 127] with transition temperatures in the range up to 7 K were already known for many years.

In January 2008, the field of superconductivity was stimulated by another achievement of Kamihara *et al.* who reported a $T_c \sim 26$ K in the closely related system $LaFeAsO_{1-x}F_x$ [25]. Within a very short time this discovery initiated an intensive quest for uncovering a whole class of novel high-T_c superconducting compounds with transition temperatures up to 56 K, called the class of iron-pnictide high-temperature superconductors (iron-pnictides).

Directly related with the compound discovered by Kamihara *et al.* [25, 117] are the superconductors belonging to the 1111-family with the general formula $LFePnO_{1-x}F_x$ (Pn = P, As; L = La, Ce, Pr, Nd, Sm, Gd, Tb, Dy, Ho, and Y) [25, 128, 129, 130, 131, 132, 133, 134,

[1] The *last* century refers to the latter half of the 20$^{\text{th}}$ century.
[2] At that time, the ZrCuSiAs-type structure was known as the PbFCl-type structure.

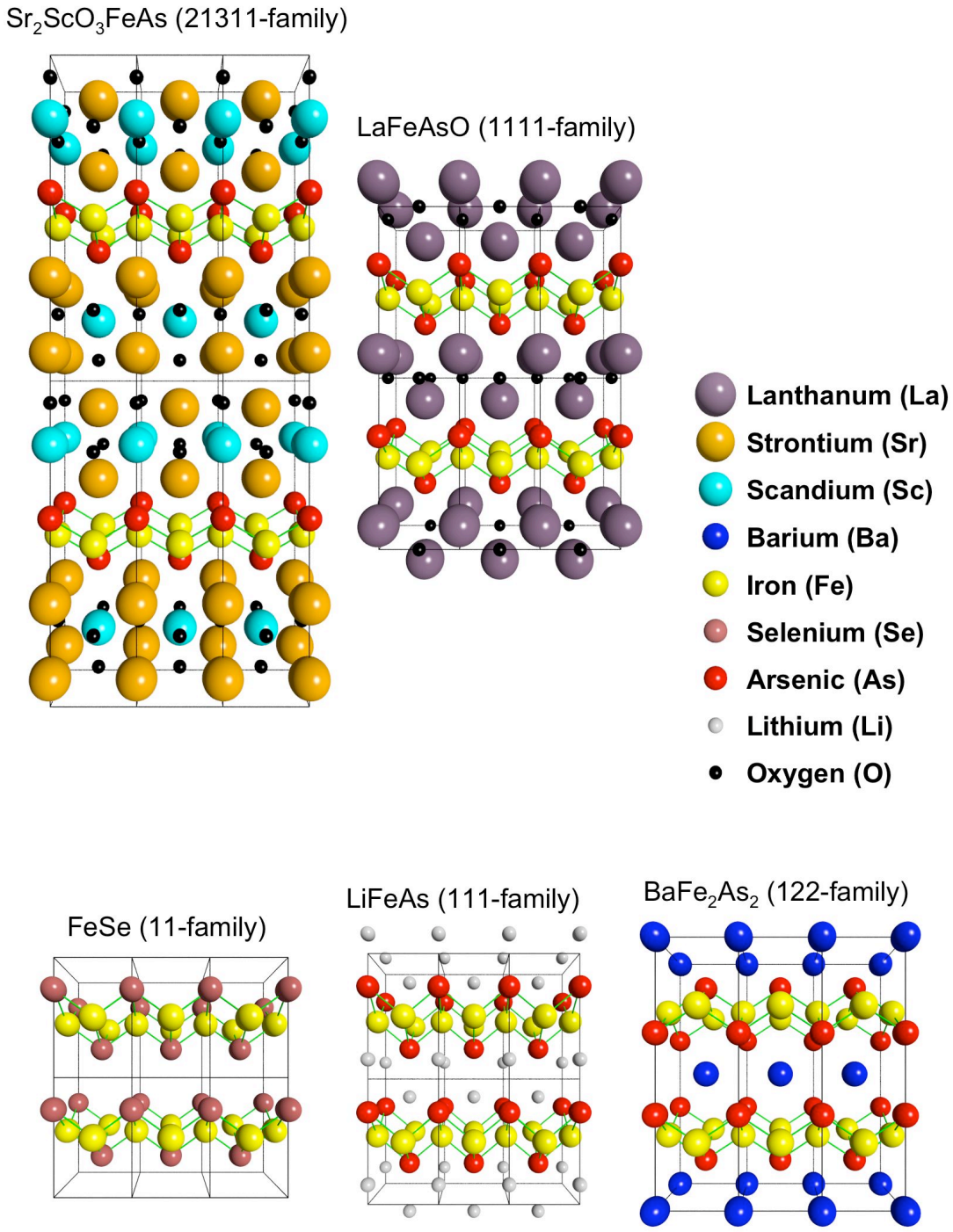

Figure 4.1: Outline of the conventional unit cells of typical parent compounds for the five families of iron-pnictide superconductors. All structures contain a similar iron-pnictide layer, where superconductivity dominantly takes place.

135, 136, 137, 138, 139, 140, 141, 142, 143, 144, 145, 146, 147, 148, 149, 150]. Various of these systems were known to exist long before the serendipitous discovery of superconductivity in the iron-pnictides [116]. The undoped parent compound LFeAsO ($L1111$) has a layered crystal structure, very similar to that of the cuprates where CuO_2 planes are separated by doped but nearly insulating sheets [21]. The compound $L1111$ consists of iron-pnictide (Fe_2As_2)-layers in which the carriers dominantly flow, sandwiched by lanthanide oxide (L_2O_2)-sheets, which act as charge reservoirs when doped with charge carriers [25]. Undoped $L1111$ is not superconducting and shows an antiferromagnetic transition at ~ 150 K. Superconductivity is induced upon doping the lanthanide oxide layers, either by partially replacing oxygen by fluorine [25], or by generating oxygen deficiency [117, 132, 151, 152], or by applying pressure [153]. It was shown that both electron doping (partially replacing L by Th [154]) and hole doping (partially replacing L by Sr [155]) in $L1111$ may also lead to superconductivity.

More recently, the discovery of superconductivity at 38 K in $Ba_{1-x}K_xFe_2As_2$ with the $ThCr_2Si_2$-type structure was reported [156]. Subsequently, superconductivity was found in various related compounds (forming the 122-family of iron-pnictides) including hole-doped $Sr_{1-x}K_xFe_2As_2$ and $Sr_{1-x}Cs_xFe_2As_2$ [157], $Ca_{1-x}Na_xFe_2As_2$ [158], $Eu_{1-x}K_xFe_2As_2$ [159], $Eu_{1-x}Na_xFe_2As_2$, [160] and $Ba_{1-x}Rb_xFe_2As_2$ [161, 162], as well as electron-doped $BaFe_{2-x}Co_xAs_2$ [163], $SrFe_{2-x}Co_xAs_2$ [164], and $BaFe_{2-x}Ni_xAs_2$ [165]. In addition, pressure induced superconductivity was discovered in the parent compounds $CaFe_2As_2$ [166, 167], $SrFe_2As_2$ [168, 169], and $BaFe_2As_2$ [169]. Similar to the superconductors of the 1111-family, several of these materials were first synthesized previously by Jeitschko *et al.* [114]. The AFe_2As_2 compounds ($A122$), have a simpler crystal structure in which (Fe_2As_2)-layers, identical to those in $L1111$, are separated by single layers containing elements like Sr, Ca, Ba, or Eu, here denoted as A-layers.

Further compounds belonging to the class of iron-pnictides are the 111-family such as LiFeAs and NaFeAs [170, 171], the dichalcogenide 11-family[3] $Fe_{1+x}Se_{1-y}Te_z$ [172, 173, 174], and the 21311-family E_2MO_3FeAs (E =Ca, Sr, Ba; M =Sc, Ti, V, Cr, Co) [175, 176, 177, 178, 179, 180, 181]. So far, five families of iron-pnictides based on a simple iron-pnictide layered structure have been identified. An overview of the crystal structures for the five families is presented in Fig. 4.1. Although all the different compounds of iron-pnictide superconductors appear to be incommensurable, there are some generic properties to be found among them. The upper critical field in all iron-pnictides is extraordinarily high. Already the first estimates of $H_{c2}^{||c}(0)$ in La1111 revealed values of the order of 100 T [37], making the iron-pnictides very interesting for applications. Also, the zero-temperature critical current density $j_c(0) \gtrsim 10^9$ A/m^2, as determined for various iron-pnictide superconductors, is at least as high as for the cuprates [161, 182]. Interestingly, the iron-pnictide superconductors have a layered crystal structure, again similar to the cuprates, suggesting these two families of high-T_c superconductors to be closely related.

The microscopic origin of superconductivity in the iron-pnictides still eludes understanding. Several experiments indicate that in this multi-band material, several gaps open in the superconducting state [37, 183, 184, 185, 186, 187, 188, 189]. Many reports point towards the so-called $s_\pm$-pairing state, which was originally proposed by Mazin *et al.* [190], and gained

[3] Although Se does not belong to the pnictide elements, FeSe and related compounds are classified among the iron-pnictides for their similar layered structure. All together belong to the class of iron-based superconductors.

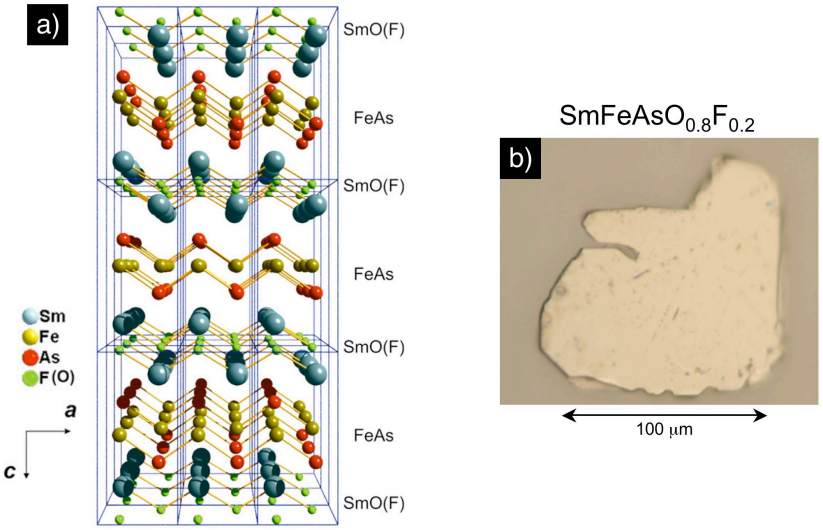

Figure 4.2: a) Crystallographic structure of the Sm1111 iron-pnictide superconductor. b) Typical Sm1111 single crystal synthesised by using the high-pressure technique. After [182].

further support by subsequent work [191, 192, 193]. This pairing mechanism incorporates multi-gap superconductivity with an additional discontinuous sign change in the amplitude of the order parameter, contrary to what is found for the two-gap superconductor MgB_2 [31]. Antiferromagnetic fluctuations, which originate from the nesting between the hole and electron Fermi surfaces, are thought to play an important role in the iron-pnictides and could be embedded into the $s_{\pm}$-pairing state. The highest T_c among iron-pnictides, however, is observed in the $L1111$-family, where the low-energy antiferromagnetic fluctuations, as probed with NMR, are suppressed in the entire electronic system [194, 195], which appears to be inconsistent with a $s_{\pm}$-pairing. On the other hand, a polaronic two-band model, involving s-wave order parameters, was proposed for the iron-pnictide superconductors [39], similar to the one for the cuprates [40, 41], where multi-gap superconductivity was suggested to occur [34, 35, 36, 196]. Since both cuprates and iron-pnictides exhibit especially high transition temperatures, a cognate pairing mechanism seems attractive.

4.2 High pressure synthesis of $SmFeAsO_{1-x}F_y$ single crystals

Singe crystals are usually required for investigating the intrinsic anisotropic properties of superconductors along the respective crystallographic orientation[4] i, such as the upper critical field $H_{c2}^{||i}$, the coherence length ξ_i, or the magnetic penetration depth λ_i. Of course, compared to polycrystalline samples, the effort to grow single crystals is substantially larger. Bulk properties, like magnetic susceptibility or specific heat, if evaluated from single crystal work, convey detailed information about the thermodynamic properties of superconductors, whereas for polycrystalline samples often only an average of the orientation dependent pa-

[4]The orientation i is either along the c-axis, or within the ab-plane for uniaxial crystal symmetries.

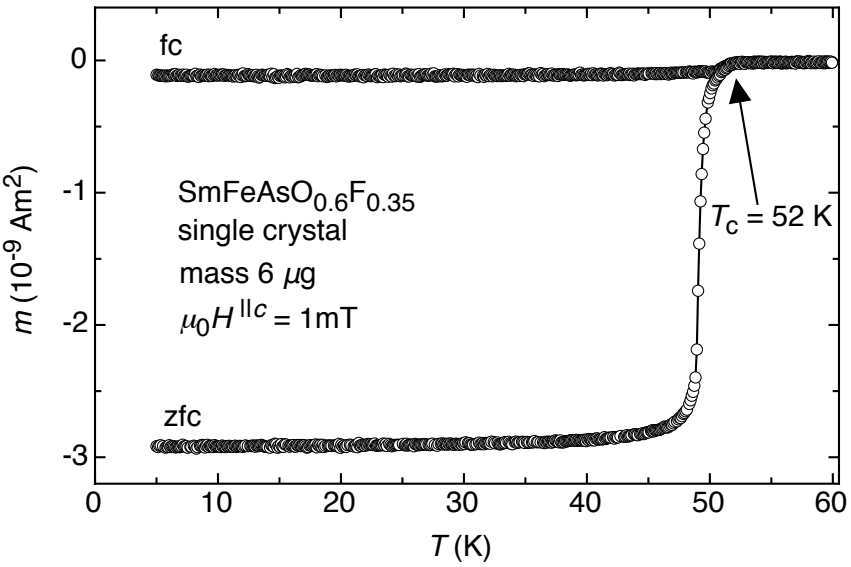

Figure 4.3: Magnetic moment m versus temperature T for a single crystal with nominal composition $SmFeAsO_{0.6}F_{0.35}$ measured in a magnetic field of 1 mT (fc: field cooled, zfc: zero-field cooled). A transition temperature $T_c \simeq 52$ K is estimated. After [162].

rameters may be probed. In addition, many surface sensitive techniques such as scanning tunneling spectroscopy (STS), angle-resolved photoemission spectroscopy (ARPES), and point contact spectroscopy (PCS) require high-quality crystalline surfaces.

The two techniques commonly used for growing $SmFeAsO_{1-x}F_y$ samples are the low-pressure quartz-ampoule method [25, 128, 129] and the more sophisticated high-pressure material synthesis technique [131, 132, 134]. In order to obtain *high-quality* single crystals, though, greater effort is needed. The successful growth of a pure crystallographic phase is highly sensitive to all the growth parameters involved. The high-pressure material synthesis is well suited for high-quality sample growing, since the wider range of the growth parameters helps to optimize the process.

For the synthesis of $SmFeAsO_{1-x}F_y$ single crystals the high-pressure cubic anvil technique was used, which has been successfully applied for growing single crystalline MgB_2 and other superconductors [97, 197]. Until the work of Zhigadlo *et al.* [182], the growth of superconducting single crystals of the Sm1111 family had not been reported. Single crystals of the nominal composition $SmFeAsO_{0.8}F_{0.2}$ were prepared using SmAs, FeAs, Fe_2O_3, Fe, and SmF_3 powders as starting materials. The plate-like $SmFeAsO_{1-x}F_y$ single crystals typically have masses not much exceeding 1 μg and dimensions of the order $100 \times 100 \times 10$ μm^3 (see Fig. 4.2).

The magnetization of $SmFeAsO_{1-x}F_y$ single crystals as measured with a *Quantum Design* SQUID magnetometer MPMS XL reveals transition temperatures up to $T_c \sim 53$ K, depending on the doping. As an example, the temperature dependence of the magnetic moment m measured in a magnetic field of 1 mT parallel to the c-axis for a $SmFeAsO_{0.6}F_{0.35}$ single crystal is shown in Fig. 4.3. The sharp transition into the superconducting state is characteristic of homogeneous doping with fluorine. The transition temperature $T_c \simeq 52$ K indicates that the crystal is almost optimally doped. The full diamagnetic response of the sample is reflected in the zero-field cooled (zfc) magnetic moment, which is typical for bulk

superconductivity. The small ratio of the field cooled (fc) to zfc magnetization suggests strong vortex pinning and a high critical current density.

4.3 Temperature dependent anisotropy parameter in the 1111-family

All known classes of high-T_c superconductors (cuprates, MgB_2, iron-pnictides) have a layered crystal structure and show pronounced anisotropic physical properties. To gain insight into the superconducting mechanism in the different classes, it is quite important to investigate the anisotropic physical properties of the various compounds, such as the effective mass anisotropy parameter, defined earlier in Eq. (2.18) as

$$\gamma = \sqrt{\frac{m_c^*}{m_{ab}^*}} = \frac{\lambda_c}{\lambda_{ab}} = \frac{H_{c2}^{||ab}}{H_{c2}^{||c}} = \frac{\xi_{ab}}{\xi_c}. \tag{4.1}$$

For the $L1111$ pnictides various estimates of γ with values ranging from 1 to 30 were reported [198, 199, 200, 201, 202, 203, 204, 205, 206, 207, 208, 209, 210]. Within the framework of classical Ginzburg-Landau theory a single, well-defined anisotropy parameter is expected to be a unique characteristic of a given compound. The situation is quite different for a two-gap superconductor, such as MgB_2 [24], for which more than one band may cross the Fermi surface, and several distinct gaps may open at T_c. Consequently, the coupling of electrons from the distinct bands determines the physical properties of a material, which may considerably differ from those of a simple one-gap superconductor. In MgB_2 the anisotropy parameter γ was found to vary from 1 to 8 depending on temperature and field [32, 211]. The temperature and field dependence of γ was interpreted to be a consequence of the complex inter- and intraband electron scattering processes taking place in the two-gap superconductor MgB_2 [33, 212, 213]. Since theoretical and experimental work in iron-pnictides revealed multi-gap superconductivity [37, 37, 187, 184, 185, 188, 189, 190, 191, 192], a detailed investigation of the temperature and field dependence of γ is crucial for understanding the mechanism of superconductivity in this novel class of material.

The angular dependent magnetic properties of $L1111$ compounds were investigated using torque magnetometry (see Sec. 2.4). For this experiment Sm1111 and Nd1111 single crystals, characterized by a well-defined transition temperature and with masses of the range of ~ 1 μg, were selected. Angle dependent measurements of the torque were performed and analyzed using Eq. (2.23) derived by Kogan *et al.* [50, 51]

$$\tau(\theta) = -\frac{V\Phi_0 H}{16\pi\lambda_{ab}^2}\left(1-\frac{1}{\gamma^2}\right)\frac{\sin(2\theta)}{\epsilon(\theta)}\ln\left(\frac{\eta H_{c2}^{||c}}{\epsilon(\theta)H}\right). \tag{4.2}$$

The raw torque data were measured with a clockwise $\tau(\theta^+)$ and a counterclockwise $\tau(\theta^-)$ angular field scan. The reversible torque τ_{rev} was calculated according to $\tau_{rev}(\theta) = (\tau(\theta^+) + \tau(\theta^-))/2$ in order to reduce vortex pinning effects (see Fig. 4.4). Examples of the reversible torque $\tau_{rev}(\theta)$ for $SmFeAsO_{0.8}F_{0.2}$ are shown in Fig. 4.5. The most important quantity that can be extracted from the torque data is the anisotropy parameter γ. According to Eq. (4.2), the anisotropy parameter γ is sensitive to the angular dependence of the torque.

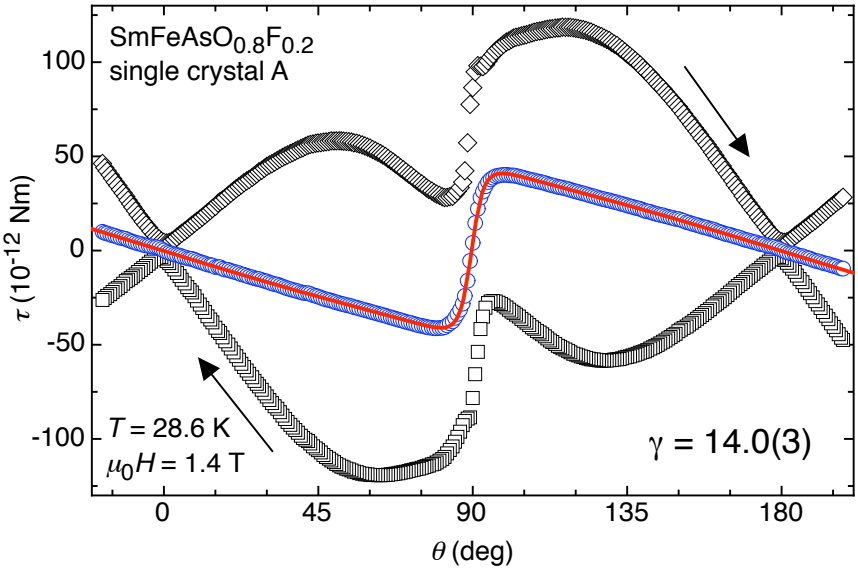

Figure 4.4: Angular dependence of the torque τ for a $SmFeAsO_{0.8}F_{0.2}$ single crystal (single crystal A) at $T = 28.6$ K and $B = 1.4$ T. The squares (diamonds) denote the measured raw torque $\tau(\theta)$ during a counterclockwise (clockwise) rotation of the magnetic field around the sample. In order to minimize pinning effects the reversible torque $\tau_{\rm rev}(\theta)$ was calculated (circles) as the average of the two branches of $\tau(\theta)$. The solid line is a fit to Eq. (4.2), resulting in an anisotropy parameter of $\gamma = 14.0(3)$. After [198].

The parameter most difficult to extract reliably from torque data[5] is the upper critical field $H_{c2}^{||c}$, since it enters logarithmically in Eq. (4.2). By fitting Eq. (4.2) to the experimental $\tau_{\rm rev}(\theta)$, the anisotropy parameter γ was determined for a $SmFeAsO_{0.8}F_{0.2}$ single crystal [198]. Figure 4.4 shows an example of such an analysis performed on torque data for a field of 1.4 T and a temperature of 28.6 K, yielding an anisotropy parameter of $\gamma = 14.0(3)$.

As it was pointed out by Kogan [214], the anisotropy parameter for the magnetic penetration depth $\gamma_\lambda = \lambda_c/\lambda_{ab}$ and for the upper critical field $\gamma_H = H_{c2}^{||ab}/H_{c2}^{||c}$, do not necessarily coincide in case of multi-gap superconductivity. A more generalized approach including the two distinct anisotropies γ_λ and γ_H leads to the generalized expression [214]

$$\begin{aligned}\tau(\theta) &= -\frac{V\Phi_0 H}{16\pi\lambda_{ab}^2}\left(1-\frac{1}{\gamma_\lambda^2}\right)\frac{\sin(2\theta)}{\epsilon_\lambda(\theta)} \\ &\times \left[\ln\left(\frac{\eta H_{c2}^{||c}}{H}\frac{4e^2\epsilon_\lambda(\theta)}{(\epsilon_\lambda(\theta)+\epsilon_H(\theta))^2}\right) - \frac{2\epsilon_\lambda(\theta)}{\epsilon_\lambda(\theta)+\epsilon_H(\theta)}\left(1+\frac{\epsilon'_\lambda(\theta)}{\epsilon'_H(\theta)}\right)\right].\end{aligned} \tag{4.3}$$

Here the scaling function $\epsilon_i(\theta) = [\cos^2(\theta)+\gamma_i^{-2}\sin^2(\theta)]^{1/2}$ with $i = \lambda, H$ is different for γ_λ and γ_H. The derivative $\partial\epsilon_i(\theta)/\partial\theta$ of the scaling function with respect to the angle θ is denoted as $\epsilon'_i(\theta)$.

To clarify the impact of the multi-band structure on the anisotropy parameter, the torque data were analyzed using an approach, involving a comparision between Eqs. (4.2) and (4.3), combined with the analysis proposed by Balicas *et al.* [206]. In this method the data are analyzed after symmetrizing the reversible torque $\tau_{\rm symm}(\theta) = \tau_{\rm rev}(\theta) + \tau_{\rm rev}(\theta+90°)$

[5] especially, in the presence of weak pinning

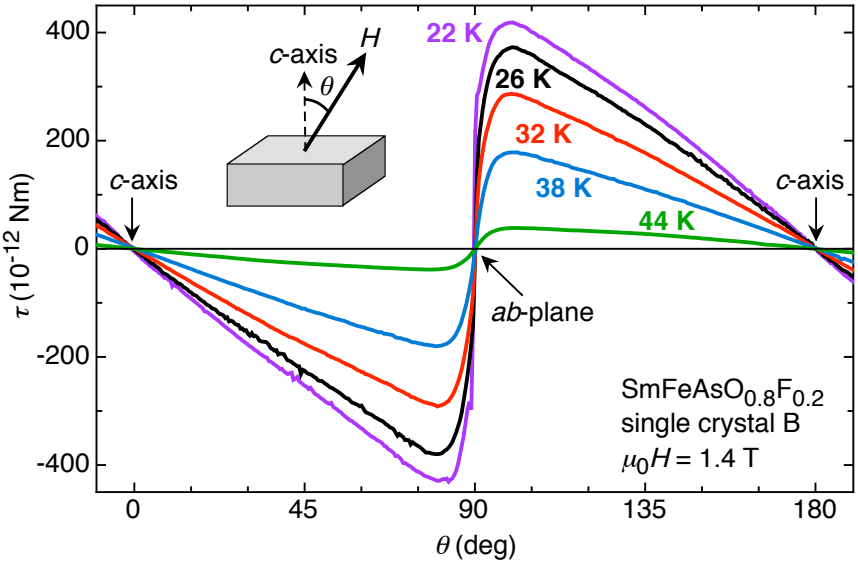

Figure 4.5: Angular dependence of the reversible torque data for $SmFeAsO_{0.8}F_{0.2}$ (single crystal B) at several temperatures derived in a magnetic field of 1.4 T. Only a small, almost temperature independent background contribution (smaller than 10^{-11} Nm) is present in the data, due to a minor anisotropic normal state magnetization contribution. For clarity, not all investigated temperatures are presented here. After [199].

in order to eliminate any anisotropic paramagnetic or diamagnetic background contribution. In the subsequent fitting procedure the upper critical field $H_{c2}^{||c}$ was always fixed, assuming a Werthamer-Helfand-Hohenberg (WHH) temperature dependence [215] with a slope of $\mu_0(\partial H_{c2}^{||c}/\partial T)|_{T_c}$=1.5 T/K, a typical value reported for similar iron-pnictide superconductors [37, 198, 199, 203, 204, 205, 209]. In this way the number of free fit parameters is reduced. Furthermore, the choice of the slope $\mu_0(\partial H_{c2}^{||c}/\partial T)|_{T_c}$=1.5 T/K does not degrade the quality of the determination of γ [198, 199, 206, 207].

Fitting the simpler expression for $\tau(\theta)$ given in Eq. (4.2) to the angular dependent torque data, yields excellent agreement as shown in Fig. 4.6a. The resulting values of γ determined for all samples investigated are shown in Fig. 4.7, where a pronounced temperature dependence of γ is observed. This result, however, is in contrast to the results obtained from resistivity data from single crystals of the similar compound $NdFeAsO_{0.7}F_{0.3}$ where $\gamma_H = H_{c2}^{||ab}/H_{c2}^{||c}$ was found to decrease with decreasing temperature [209]. It is important to explain the physical meaning of this discrepancy. In Fig. 4.6b the same data set as in Fig. 4.6a is shown, analyzed using Eq. (4.2) but now with γ fixed to linearly extrapolated values of the resistivity measurements of Jaroszynski *et al.* [209], with λ_{ab} as the only free fitting parameter. Obviously, the fit does not describe the torque data well, suggesting the presence of two distinct anisotropies, namely $\gamma_\lambda = \lambda_c/\lambda_{ab}$ and $\gamma_H = H_{c2}^{||ab}/H_{c2}^{||c}$. In order to test this hypothesis the torque data were reanalyzed using Eq. (4.3), which involves both γ_λ and γ_H as independent parameters. The result is shown in Fig. 4.6c, again with the same fixed γ_H as in Fig. 4.6b, but with γ_λ as a free parameter. It is evident that this approach describes the torque data well. Moreover, the values of γ_λ are similar to the values of γ derived from Eq. (4.2) [198, 199]. The final results from fitting γ_λ and λ_{ab} by means of Eq. (4.3) are shown in Fig. 4.7. In the temperature range $T_c \geqslant T \geqslant 25$ K the anisotropy

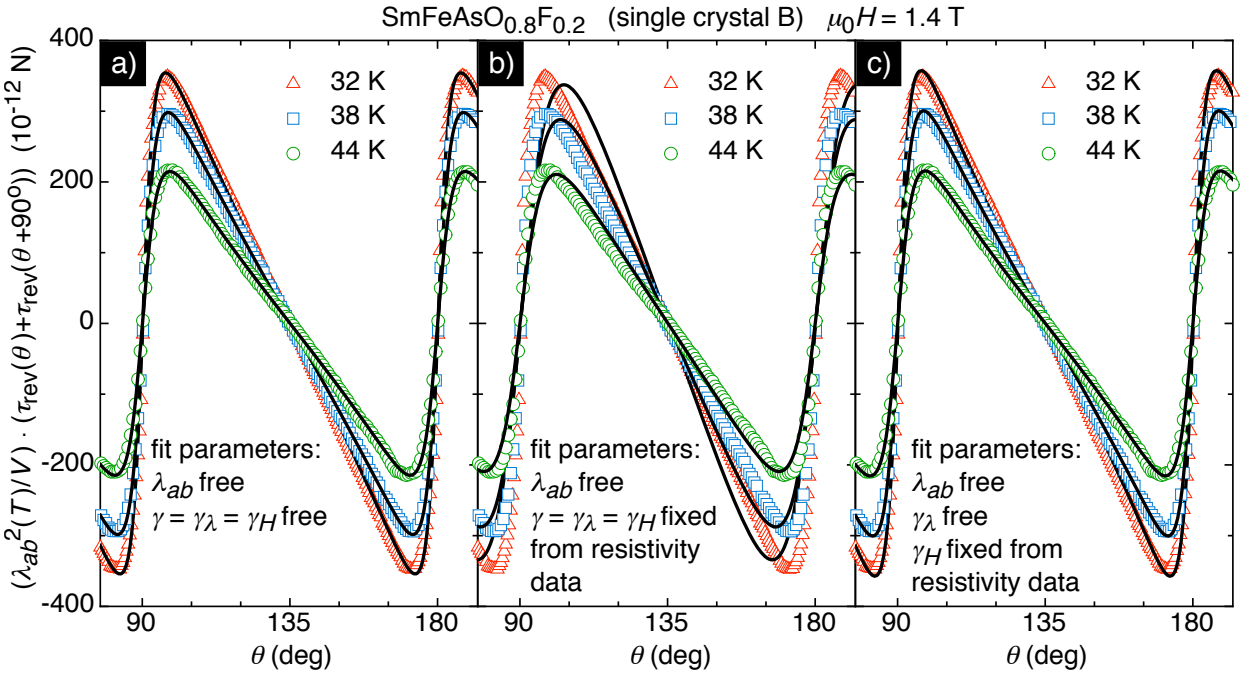

Figure 4.6: Three sets of normalized torque data, obtained at 32 K, 38 K, and 44 K in 1.4 T for $SmFeAsO_{0.8}F_{0.2}$ (single crystal B) and analyzed in terms of $\tau_{\rm symm}(\theta) = \tau_{\rm rev}(\theta) + \tau_{\rm rev}(\theta + 90°)$. a) Data analyzed using Eq. (4.2) with both γ and λ_{ab} as free parameters. b) Data analyzed using Eq. (4.2) with γ fixed to the linearly extrapolated values derived from resistivity measurements of Jaroszynski *et al.* [209] with λ_{ab} as a free parameter. c) Data analyzed using the generalized equation, Eq. (4.3), with γ_H fixed to the linearly extrapolated values from resistivity measurements [209] with γ_λ and λ_{ab} as free fit parameters. After [199].

$\gamma_\lambda(T)$ for all samples show the same temperature behavior, which appears to be a generic feature of iron-pnictide superconductors. From the trend of $\gamma_\lambda(T)$ a value of $\gamma_\lambda(0) \approx 19$ is estimated. The drastic increase of γ_λ below 25 K to values well above 20 is very likely due to a substantial pinning contribution to the torque.

It is evident from Figs. 4.6 and 4.7 that the two individual anisotropies γ_λ and γ_H describe the torque data in a consistent manner. The pronounced temperature dependence of γ_λ indicates multi-gap superconductivity, just as in MgB_2. Interestingly, Eq. (4.3) was originally proposed for analyzing experimental data of the two-gap superconductor MgB_2. Indeed, the experimental situation in both materials is quite similar. The compound MgB_2 shows two distinct anisotropies: γ_λ decreases with decreasing temperature from about 2 to 1.1, whereas γ_H increases from about 2 at T_c to values approaching 6 at low temperatures [32, 33, 212]. For the 1111 pnictides investigated here, an analogous scenario appears to prevail, but with reversed signs for the slopes of $\gamma_\lambda(T)$ and $\gamma_H(T)$. Close to T_c both anisotropy parameters have similar values of $\gamma_\lambda(T_c) \approx \gamma_H(T_c) \approx 7$, whereas at low temperatures $\gamma_\lambda(0) \approx 19$ and $\gamma_H(0) \approx 2$. The electronic origin of the temperature dependence of γ_λ observed in the iron-pnictides still needs to be clarified. In the case of MgB_2 the existence of two distinct bands of different dimensionality with characteristic inter- and intraband scattering is widely accepted to be responsible for the temperature dependence of the anisotropy parameters and the high T_c [33, 38].

In conclusion, strong evidence that two distinct anisotropies γ_λ and γ_H are involved in

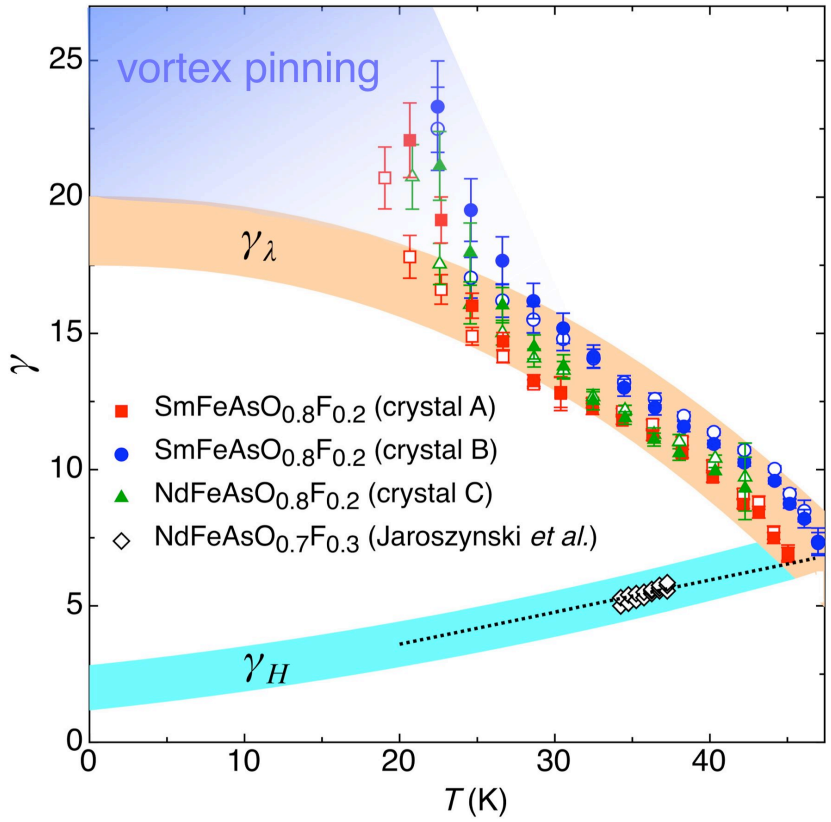

Figure 4.7: Parameters derived from the systematic analysis of the torque data of single crystals $SmFeAsO_{0.8}F_{0.2}$ (crystal A and B) and $NdFeAsO_{0.8}F_{0.2}$ (crystal C). Values for γ (open symbols) and γ_λ (closed symbols) were obtained from fits to the data with Eqs. (4.2) and (4.3), respectively. The upper broad orange band is a guide to the eye, suggesting an estimate of $\gamma_\lambda(0) \simeq 19$. The dotted line is the linear extrapolation of γ_H obtained from resistivity measurements [209] on a $NdFeAsO_{0.7}F_{0.3}$ single crystal with similar $T_c \simeq 45$ K (diamonds). The lower broad blue band is a guide to the eye, suggesting an estimate of $\gamma_H(0) \simeq 2$. Data points of γ_λ below 25 K deviate, due to considerable pinning effects. After [199].

superconductivity of the iron-pnictide superconductors was found. Torque magnetometry in low magnetic fields is very sensitive to γ_λ, which exhibits a pronounced increase with decreasing temperature. Interestingly enough, γ_H decreases with decreasing temperature as shown by resistivity measurements [209]. The temperature dependences of γ_λ and γ_H are similar to those found for the two-gap superconductor MgB_2 [33, 38, 212, 213], albeit, with reversed slopes. This suggests that multi-gap superconductivity is present in the novel class of iron-pnictide superconductors.

4.4 Low anisotropy in the 122-family

Single crystals of Rb-substituted $BaFe_2As_2$ were grown using a Sn flux method similar to that described by Ni *et al.* [216]. The single crystals of $Ba_{1-x}Rb_xFe_2As_2$ grow in a plate-like shape with typical dimensions (1-3)×(1-2)×(0.05-0.1) mm^3. Depending on the starting composition, the crystals show rather sharp transitions to the superconducting state. For

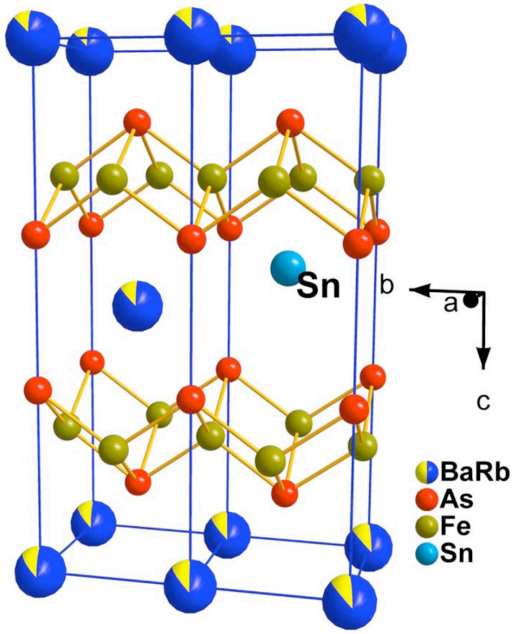

Figure 4.8: The crystallographic structure of $Ba_{1-x}Rb_xFe_2As_2$. The possible location of the Sn-atom in $Ba_{0.84}Rb_{0.10}Sn_{0.09}Fe_2As_{1.96}$ is shown. After [161].

further studies single crystals grown from the starting composition $Ba_{0.6}Rb_{0.8}Fe_2As_2$ were chosen with a $T_c \simeq 23$ K. The composition of the crystals from this batch, as determined by EDX analysis (16.79 at.% Ba, 1.94 at.% Rb, 1.74 at.% Sn, 40.19 at.% Fe, and 39.33 at.% As), leads to the chemical formula $Ba_{0.84}Rb_{0.10}Sn_{0.09}Fe_2As_{1.96}$.

As already reported, the $BaFe_2As_2$ crystals grown from a Sn flux have elementary Sn incorporated into the structure with the Sn atoms presumably located at the As sites [216]. The structure refinement, however, revealed a somewhat different picture. After several cycles of refinement the Fourier difference map showed two pronounced maxima (Sn-atoms) of electron density shifted away from the Ba/Rb site towards the (Fe_2As_2)-layers. The distances to the As site reflect the size differences between Ba and Sn, considering the covalent radius. The resulting structure is shown in Fig. 4.8. Compared to undoped $BaFe_2As_2$, the lattice parameter a is slightly shorter, whereas the lattice parameter c is longer [217]. A similar tendency was observed for other 122 compounds, when Ba or Sr is replaced by K [157, 218, 219]. The increase in the lattice parameter c in $Ba_{0.84}Rb_{0.10}Sn_{0.09}Fe_2As_{1.96}$ is caused mainly by substitution of the Ba^{2+} ions ($r = 1.42$ Å) by the larger Rb^+ ions ($r = 1.61$ Å) [220]. The marked decrease of the lattice parameter a seems to be caused by incorporation of Sn.

Torque measurements were performed in a temperature range close to T_c, where irreversibility effects lead to minor distortions of the torque signal only. In order to minimize pinning effects, the reversible torque $\tau_{rev}(\theta)$ was calculated from measurements of the raw torque $\tau(\theta)$ with counterclockwise and clockwise angular scans in the manner described in Sec. 4.3. Unfortunately, due to the small superconducting torque signal, a substantial normal state component contributes to the torque signal. This background component was accounted for by an additional sinusoidal function in the expression for $\tau(\theta)$ given in Eq. (4.2).

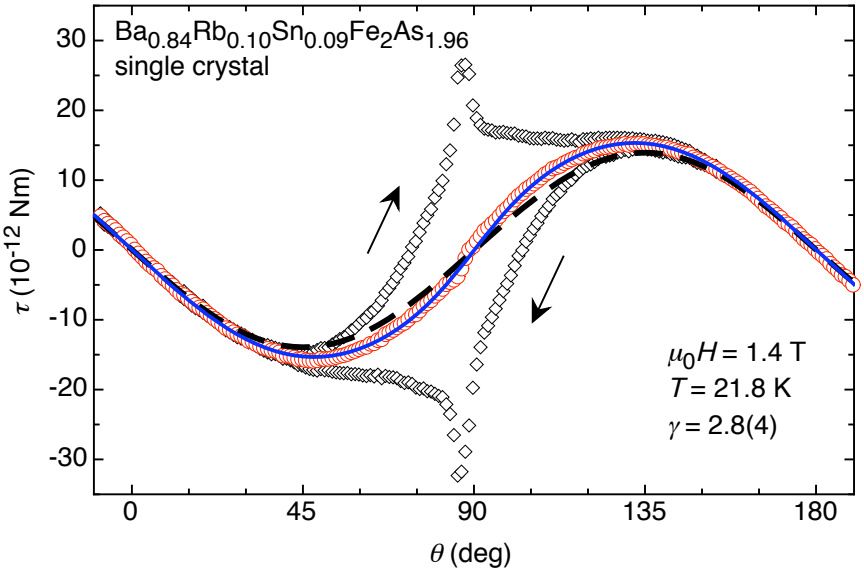

Figure 4.9: Angular dependence of the raw torque $\tau(\theta)$ (diamonds) and reversible torque $\tau_{\rm rev}(\theta)$ (circles) of the $Ba_{0.84}Rb_{0.10}Sn_{0.09}Fe_2As_{1.96}$ single crystal in the superconducting state at $T = 21.8$ K and in $\mu_0 H = 1.4$ T. The solid line is a fit of $\tau_{\rm rev}(\theta)$ to Eq. (4.2), with a substantial background component included as shown by the dashed line. After [161].

Figure 4.9 shows a torque measurement performed at $T = 21.8$ K and $\mu_0 H = 1.4$ T. The anisotropy parameter γ fitted to the mean torque data is found to be $\gamma \simeq 2.8(4)$ near T_c, in good agreement with values of γ_H from resistivity measurements in the vicinity of T_c [162]. Due to the low anisotropy parameter, the strong irreversibility, and the pronounced normal-state background, no study of the temperature dependence of the anisotropy parameter γ was made by torque magnetometry.

Obviously, superconducting $Ba_{0.84}Rb_{0.10}Sn_{0.09}Fe_2As_{1.96}$ is more isotropic than Sm1111 and Nd1111, where values of γ up to 19 are observed (see Sec. 4.3). The anisotropy parameter found for $Ba_{0.84}Rb_{0.10}Sn_{0.09}Fe_2As_{1.96}$ is smaller than those typical for high-T_c superconductors [161], but is similar to those reported for $Ba_{1-x}K_xFe_2As_2$ and $Sr_{1-x}K_xFe_2As_2$ [216, 221, 222], which indicates that the electronic coupling of the (Fe_2As_2)-layers through the intervening (Ba, Rb)-layers is more effective than through the (L_2O_2)-layers in the $L1111$ class of superconductors.

4.5 Publications related to Chapter 4

- *Single crystals of superconducting $SmFeAsO_{1-x}F_y$ grown at high pressure*
  N. D. Zhigadlo, S. Katrych, Z. Bukowski, S. Weyeneth, R. Puzniak, and J. Karpinski
  J. Phys.: Condens. Matter **20**, 342202 (2008).

- *Anisotropy of superconducting single crystal $SmFeAsO_{0.8}F_{0.2}$ studied by torque magnetometry*
  S. Weyeneth, R. Puzniak, U. Mosele, N. D. Zhigadlo, S. Katrych, Z. Bukowski, J. Karpinski, S. Kohout, J. Roos, and H. Keller
  J. Supercond. Nov. Magn. **22**, 325 (2009).

- *Evidence for two distinct anisotropies in the oxypnictide superconductors $SmFeAsO_{0.8}$-$F_{0.2}$ and $NdFeAsO_{0.8}F_{0.2}$*
  S. Weyeneth, R. Puzniak, N. D. Zhigadlo, S. Katrych, Z. Bukowski, J. Karpinski, and H. Keller
  J. Supercond. Nov. Magn. **22**, 347 (2009).

- *Superconductivity at 23 K and low anisotropy in Rb-substituted $BaFe_2As_2$ single crystals*
  Z. Bukowski, S. Weyeneth, R. Puzniak, P. Moll, S. Katrych, N. D. Zhigadlo, J. Karpinski, H. Keller, and B. Batlogg
  Phys. Rev. B **79**, 104521 (2009).

- *Single crystals of $LnFeAsO_{1-x}F_x$ (Ln=La, Pr, Nd, Sm, Gd) and $Ba_{1-x}Rb_xFe_2As_2$: Growth, structure and superconducting properties*
  J. Karpinski, N. D. Zhigadlo, S. Katrych, Z. Bukowski, P. Moll, S. Weyeneth, H. Keller, R. Puzniak, M. Tortello, D. Daghero, R. Gonnelli, I. Maggio-Aprile, Y. Fasano, Ø. Fischer, K. Rogacki, and B. Batlogg
  Physica C **469**, 370 (2009).

4.5.1 Publication IV: Single crystals of superconducting $SmFeAsO_{1-x}F_y$ grown at high pressure

N. D. Zhigadlo, S. Katrych, Z. Bukowski, S. Weyeneth, R. Puzniak, and J. Karpinski
J. Phys.: Condens. Matter **20**, 342202 (2008).

Abstract
Single crystals of $SmFeAsO_{1-x}F_y$ of a size up to 120 × 100 μm^2 have been grown from NaCl/KCl flux at a pressure of 30 kbar and temperature of 1350-1450°C using the cubic anvil high-pressure technique. The superconducting transition temperature of the obtained single crystals varies between 45 and 53 K. Obtained crystals are characterized by a full diamagnetic response in low magnetic fields and by a high critical current density in high magnetic fields. Structural refinement has been performed on the single crystals. Differential thermal analysis investigations at 1 bar Ar pressure show decomposition of $SmFeAsO_{1-x}F_y$ at 1302°C.

DOI: 10.1088/0953-8984/20/34/342202

PACS numbers: 76.62.Fj, 74.62.Bf, 74.70.Dd, 81.10.Dn, 74.25.Sv

The original publication is electronically available at:
http://www.iop.org/EJ/abstract/0953-8984/20/34/342202

Open access repositories:
http://www.zora.uzh.ch/10576
http://arxiv.org/abs/0806.0337

At completion of this thesis, according to the Thomson Reuters ISI Web of Knowledge database, this article has been cited at least 44 times.

IOP FTC

IOP Publishing Journal of Physics: Condensed Matter

J. Phys.: Condens. Matter **20** (2008) 342202 (5pp) doi:10.1088/0953-8984/20/34/342202

FAST TRACK COMMUNICATION

Single crystals of superconducting $SmFeAsO_{1-x}F_y$ grown at high pressure

N D Zhigadlo[1], S Katrych[1], Z Bukowski[1], S Weyeneth[2], R Puzniak[3] and J Karpinski[1]

[1] Laboratory for Solid State Physics, ETH, 8093 Zürich, Switzerland
[2] Physik-Institut der Universität Zürich, Winterthurerstrasse 190, 8057 Zürich, Switzerland
[3] Institute of Physics, Polish Academy of Sciences, Aleja Lotnikow 32/46, 02-668 Warsaw, Poland

E-mail: zhigadlo@phys.ethz.ch and karpinski@phys.ethz.ch

Received 3 June 2008, in final form 18 July 2008
Published 1 August 2008
Online at stacks.iop.org/JPhysCM/20/342202

Abstract

Single crystals of $SmFeAsO_{1-x}F_y$ of a size up to 120 × 100 μm^2 have been grown from NaCl/KCl flux at a pressure of 30 kbar and temperature of 1350–1450 °C using the cubic anvil high-pressure technique. The superconducting transition temperature of the obtained single crystals varies between 45 and 53 K. Obtained crystals are characterized by a full diamagnetic response in low magnetic fields and by a high critical current density in high magnetic fields. Structural refinement has been performed on the single crystal. Differential thermal analysis investigations at 1 bar Ar pressure show decomposition of $SmFeAsO_{1-x}F_y$ at 1302 °C.

(Some figures in this article are in colour only in the electronic version)

1. Introduction

The recent discovery of superconductivity in a family of quaternary oxypnictides with the general formula LnFeAsO (where Ln = La, Ce, Pr, Nd, Sm, Gd) has caused excitement in the scientific community [1–8]. The crystal structure of PrFeAsO was reported by Quebe *et al* [9]. These compounds crystallize with the tetragonal layered ZrCuSiAs structure in the space group $P4/nmm$, which has a structure of alternating LnO and FeAs layers that are electrically charged and can be represented as $(LnO)^{+\delta}(FeAs)^{-\delta}$ (figure 1). Covalent bonding is dominant in the layers, while between layers ionic bonding dominates. The charge carriers in these compounds are electrons confined to the FeAs layers. The LnO layer serves as a 'charge reservoir', when doped with electrons. This can be done by partial substitution of O^{2-} by fluorine F^- [2–5] or by generation of oxygen vacancies at a high pressure of 60 kbar [6]. The highest critical temperatures above 50 K have been observed for $LnFeAsO_{1-x}F_x$ with Ln = Sm, Gd, Pr and Nd. Both methods of doping lead to a decrease in the lattice parameters, which indicates that high pressure can promote such reactions. The presence of two structural blocks, namely conducting FeAs layers and 'charge reservoir' LnO layers, recalls the high-T_c cuprates. One can expect, similar to cuprates, strong anisotropy of superconducting properties such as upper critical field, coherence length and penetration depth. In fact investigations of penetration depth anisotropy with the torque technique show temperature dependent anisotropy varying from $\gamma = 8$ at $T \leqslant T_c$ to $\gamma = 23$ at $T = 0.4T_c$ [7]. Penetration depth investigations using a radio frequency tunnel diode oscillator technique performed on single crystals show an exponential temperature dependence, indicating a fully gapped pairing state [8]. Knowledge of the anisotropic properties is crucial for understanding the mechanism of superconductivity in this family of compounds and their potential applications.

Two techniques have been used for the synthesis of polycrystalline samples: the low-pressure quartz ampoule method [1–3] and high-pressure synthesis [4–6]. As a precursor a mixture of LnAs, FeAs, Fe_2O_3, Fe and LnF_3 is usually used. In the low-pressure method, the necessary reaction temperature range of 1150–1250 °C is at the limit of application of quartz ampoules due to reaction with the

IOP FTC
J. Phys.: Condens. Matter **20** (2008) 342202 Fast Track Communication

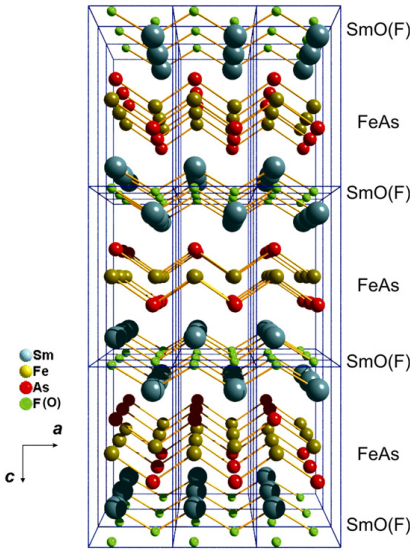

Figure 1. Schematic representation of the 3 × 3 × 3 unit cells of $SmAsFeO_{1-x}F_y$ along the a direction.

precursor, especially with fluorine vapours. In the high-pressure method the precursor mixture is placed in a BN crucible and synthesized at a pressure of 30–60 kbar at temperatures of 1250–1350 °C for several hours. Sintered polycrystalline samples with a micrometre grain size have been obtained. Until now most of the physical measurements have been performed on polycrystalline samples obtained in one of these ways. As the mechanism of superconductivity in these pnictide oxides is unknown, single crystals are necessary for the investigations of intrinsic anisotropic properties such as upper critical field, coherence length or penetration depth. Studies on single crystals are crucial for spectroscopic techniques such as scanning tunnelling spectroscopy, angle-resolved photoemission spectroscopy, point contact spectroscopy and optical investigations. In the low-pressure method for iron arsenide synthesis NaCl/KCl flux has been reported as a mineralizer, which enhances the formation of the quaternary compounds [9]. The authors emphasized that at the conditions of synthesis (800 °C) only minor amounts of the metallic component were dissolved. We decided to apply this method at high pressure, which allowed us to use a higher temperature. Up to submission of our paper, the growth of superconducting free single crystals of $LnFeAsO_{1-x}F_x$ has not been reported. The authors of [10] reported synthesis and magnetic properties of a $Nd(O_{0.9}F_{0.1})FeAs$ sintered sample containing large crystallites obtained by a similar high-pressure method. In this paper we report on the growth and properties of $SmFeAsO_{1-x}F_y$ single crystals.

2. Experimental details

For the synthesis of polycrystalline samples and single crystals of $SmFeAsO_{1-x}F_y$ we used the cubic anvil high-pressure technique which has also been used in our laboratory for the growth of MgB_2 single crystals and other superconductors. Polycrystalline samples of nominal composition $SmFeAsO_{0.8}F_{0.2}$ were prepared using SmAs, FeAs, Fe_2O_3, Fe and SmF_3 powders as starting materials. For the growth of single crystals we used the same components and NaCl/KCl flux. The precursor to flux ratio varied between 1:1 and 1:3. The mixing and grinding of precursor powders and pressing pellets were performed in a glove box due to the toxicity of arsenic. Pellets containing precursor and flux were placed in a BN crucible inside a pyrophyllite cube with a graphite heater. The six tungsten carbide anvils generated pressure on the whole assembly. In a typical run, a pressure of 3 GPa was applied at room temperature. While keeping pressure constant, the temperature was ramped up within 1 h to the maximum value of 1350–1450 °C, maintained for 4–10 h and decreased in 5–24 h to room temperature for the crystal growth. For the synthesis of polycrystalline samples the maximum temperature was maintained for 2–4 h, followed by quenching. Then pressure was released, the sample removed and in the case of single crystal growth NaCl/KCl flux was dissolved in water. One has to mention that such high-pressure experiments have to be performed very carefully, because an explosion during heating due to increased pressure in the sample container could lead to contamination of the whole apparatus with arsenide compounds. Differential thermal analysis (DTA) was carried out in a Perkin–Elmer DTA 7 analyser using Al_2O_3 crucibles in flowing Ar with a heating rate of 5 °C min^{-1} up to 1600 °C. The magnetization was measured with a Quantum Design SQUID magnetometer. Structural investigations were done using a diffractometer equipped with a charge-coupled device (CCD) detector (Xcalibur PX, Oxford Diffraction). Data reduction and analytical absorption correction were performed using the program CrysAlis [11]. The crystal structure was determined by a direct method and refined on F^2, employing the programs SHELXS-97 and SHELXL-97 [12, 13].

3. Results

In order to determine temperature limits for the crystal growth in ambient pressure, DTA investigations at 1 bar Ar pressure were performed. For this experiment a polycrystalline sample of $SmFeAsO_{1-x}F_y$ obtained at high pressure was used. The results of the run are shown in figure 2. One can notice two endothermic peaks corresponding to two reactions. The first one, with an onset at 993 °C and a maximum at 1020 °C, corresponds to melting of FeAs, which was an impurity in our $SmFeAsO_{1-x}F_y$ sample. The second one, with an onset at 1302 °C, corresponds to incongruent melting of $SmFeAsO_{1-x}F_y$. This practically excludes increasing temperature for the crystal growth at ambient pressure much above 1250 °C used usually for the synthesis of polycrystalline samples. Samples obtained at this temperature have very fine

IOP FTC
J. Phys.: Condens. Matter **20** (2008) 342202 Fast Track Communication

Table 1. Crystal data and structure refinement for the $SmFeAsO_{0.86-x}F_x$.

Empirical formula	$SmFeAsO_{0.86-x}F_x$
Temperature (K)	295(2)
Wavelength (Å)	0.71073/MoKα
Crystal system, space group, Z	Tetragonal, $P4/nmm$, 2
Unit cell dimensions (Å)	$a = 3.933\,90(10)$, $c = 8.4684(6)$,
Volume (Å^3)	131.053(10)
Calculated density (g cm^{-3})	7.49
Absorption correction type	Analytical
Absorption coefficient (mm^{-1})	39.914
$F(000)$	257
Crystal size (μm^3)	$70 \times 30 \times 10$
Theta range for data collection (deg)	4.81–37.19
Index ranges	$-5 \leqslant h \leqslant 6, -6 \leqslant k \leqslant 6, -14 \leqslant l \leqslant 13$
Reflections collected/unique	$867/235 R_{\rm int} = 0.0399$
Completeness to 2θ	97.5%
Refinement method	Full-matrix least-squares on F^2
Data/restraints/parameters	235/0/12
Goodness-of-fit on F^2	1.017
Final R indices [$I > 2\sigma(I)$]	$R_1 = 0.0323$, $wR_2 = 0.0708$
R indices (all data)	$R_1 = 0.0461$, $wR_2 = 0.0746$
$\Delta\rho_{\rm max}$ and $\Delta\rho_{\rm min}$ (e Å^{-3})	3.594 and -2.454

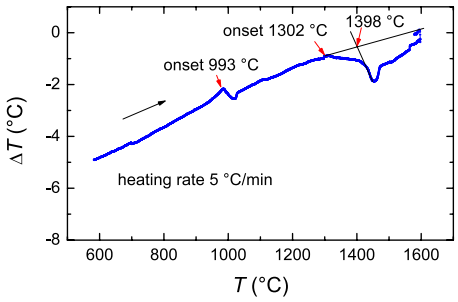

Figure 2. Differential thermal analysis performed in 1 bar Ar on a $SmAsFeO_{1-x}F_y$ polycrystalline sample showing the onset of decomposition (incongruent melting) at 1302 °C.

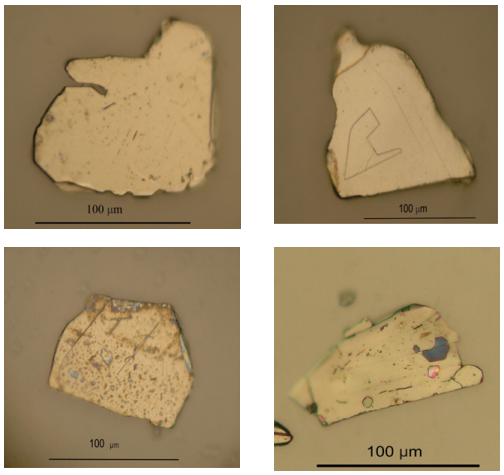

Figure 3. $SmFeAsO_{1-x}F_y$ single crystals grown from NaCl/KCl flux at high pressure. The scale is shown at the bottom.

micrometre size grains. High pressure extends the stability range of the compound to higher temperatures, which allows application of higher temperatures for the crystal growth. This increases both the size of the grains and the solubility in the flux. As a result of the crystal growth experiments $SmFeAsO_{1-x}F_y$ plate-like crystals were obtained. Crystals with a size of about $120 \times 100 \times 20$ μm^3 grown in this way are presented in figure 3. One can see remnants of the solidified flux on the surface of some crystals.

With the aim of growing single crystals suitable for physical measurements, we carried out a systematic investigation of the parameters controlling the growth of crystals, including temperature, pressure, composition, reaction time and heating/cooling rate.

One of the problems of crystal growth under high-temperature and high-pressure conditions is that the density of sites for nucleation is high and it is difficult to control nucleation to produce a small number larger single crystals and not many small crystals. This is also reflected in the quality of grown crystals; therefore many of them have irregular shapes and they form clusters of several crystals. The solubility of $SmFeAsO_{1-x}F_y$ in NaCl/KCl flux is very low, which results in a small crystal size. Unfortunately, so far no alternative solvent for this compound has been found. Several parameters which influence the quality of crystals can be specified: (i) starting composition of precursor; (ii) the precursor to flux ratio; (iii) time of dwelling and cooling, etc. For example, increase in the dwelling time at 1380 °C up to 10 h and increase in the cooling time from this temperature down to 1000 °C up to 50 h results in single crystals with a size of 120×120 μm^2. The existence of parasitic phases such as FeAs also has a significant effect on the growth mechanism and appropriate

IOP FTC
J. Phys.: Condens. Matter **20** (2008) 342202 Fast Track Communication

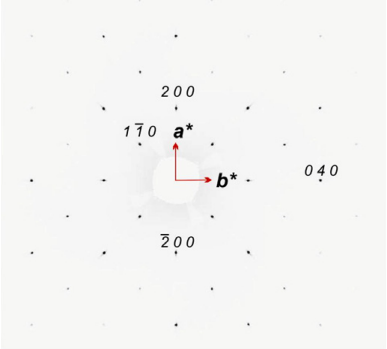

Figure 4. The reconstructed $hk0$ reciprocal space section of the $SmFeAsO_{1-x}F_y$ single crystal.

Table 2. Atomic coordinates and equivalent isotropic and anisotropic displacement parameters ($Å^2 \times 10^3$) for $SmFeAsO_{0.86-x}F_x$. (Note: U_{iso} is defined as one-third of the trace of the orthogonalized U_{ij} tensor. The anisotropic displacement factor exponent takes the form: $-2\pi^2[h^2a^2U_{11} + \cdots + 2hka^*b^*U_{12}]$. For symmetry reasons $U_{23} = U_{13} = U_{12} = 0$.)

Atom	Site	x	y	z	U_{iso}	$U_{11} = U_{22}$	U_{33}
Sm	2*c*	−1/4	−1/4	0.1411(1)	11(1)	10(1)	12(1)
Fe	2*b*	1/4	3/4	1/2	10(1)	10(1)	10(1)
As	2*c*	1/4	1/4	0.3391(2)	10(1)	9(1)	12(1)
O(F)	2*a*	1/4	3/4	0	11(3)	10(3)	15(5)

doping. A high precursor to flux ratio prevents growth of larger crystals because of a lack of space for the growth of individual grains. Further experiments with different kinds of fluxes are planned to optimize growth conditions and to grow larger and optimally doped crystals.

3.1. Crystal structure

All atomic positions were found by a direct method. The structure was refined without any restraints. Oxygen and fluorine atoms which occupy the same site are impossible to distinguish by x-ray diffraction so they were treated during refinement as one atom. The results of the structure refinement are presented in tables 1 and 2.

The results are in good agreement with the published data for PrFeAsO [9]. According to the reflection conditions for the space group $P4/nmm$ ($hk0 = 2n$) the systematic absences occur only for the $hk0$ reciprocal section (figure 4). Structural analysis revealed overall occupancy in the O(F) site to be considerably lower than 100%, equal to 0.86. Therefore, it is possible that except for F doping there is also an additional electron doping due to O vacancies. However, the accuracy of the determination of the oxygen or fluorine occupancy factor is very low because of the presence of heavy atoms like As, Fe and Sm in the unit cell. The residuals R_1 and wR_2 as well as goodness-of-fit S show small difference for the oxygen occupancy of 86% and 100% (table 3). The minimal residuals

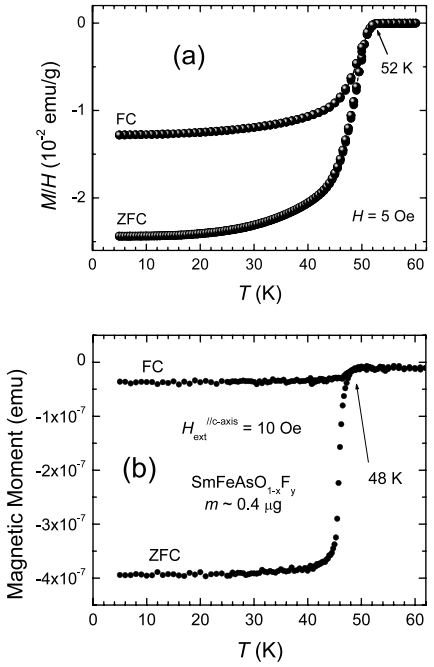

Figure 5. (a) Temperature dependence of magnetic susceptibility measured on a collection of randomly oriented $SmFeAsO_{1-x}F_y$ crystals in an applied field of 5 Oe. (b) Temperature dependence of the magnetic moment measured on one single crystal in an applied field of 10 Oe. ZFC and FC indicate zero-field cooling and field cooling curves, respectively.

Table 3. Residuals and goodness-of-fit for the different O(F) occupations in the $SmFeAsO_{1-x}F_y$.

$O(F)_{occ}$ (at.%)	R_1	wR_2	S
86	0.0461	0.0746	1.017
100	0.0474	0.0771	1.050
0	0.0849	0.1554	2.120

correspond to the $O(F)_{occ}$ of 86 ± 3 at.%. Neutron diffraction data could be helpful for clarifying this point.

3.2. Superconducting properties

Magnetic measurements of $SmFeAsO_{1-x}F_y$ crystals show that T_c varies between 45 and 53 K dependent on doping. Figure 5(a) shows the temperature dependence of magnetic susceptibility measured on a collection of single crystals from one batch. The measurements were carried out in a magnetic field of 5 Oe on heating after zero-field cooling and then on cooling in a field. The superconducting volume fraction is large enough to constitute bulk superconductivity. The maximum T_c reported for this compound is 55 K. A lower T_c indicates non-optimal doping. The relatively broad width of transition is caused by the difference in T_c between crystals from the

IOP FTC
J. Phys.: Condens. Matter **20** (2008) 342202 Fast Track Communication

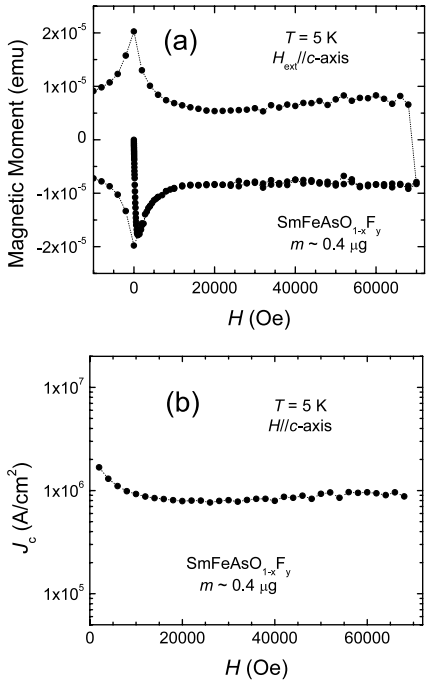

Figure 6. (a) Magnetic hysteresis loop measured on a single crystal at 5 K in a field up to 7 T parallel to the *c*-axis. (b) Critical current density calculated from the width of the hysteresis loop.

same batch. Temperature and compositional gradients in the crucible may lead to differences in the F content of crystals and differences in T_c.

The temperature dependence of magnetic moment measured in a magnetic field parallel to the *c*-axis for one single crystal from the same batch, with dimensions of about 0.09–0.12 × 0.09 × 0.006 mm^3 and a mass of about 0.41 μg, is presented in figure 5(b). A sharp transition to the superconducting state is characteristic of single crystals. A transition temperature of 48 K indicates that the crystal is underdoped. The value of the zero-field cooled magnetic moment reflects the full diamagnetic response of the crystal studied. A small ratio of field cooled to zero-field cooled magnetization is characteristic of superconductors with strong pinning. The hysteresis loop measured at 5 K in magnetic fields up to 7 T parallel to the crystal *c*-axis is presented in figure 6(a). The wide loop, with a width almost independent of the field, proves the high critical current density of the crystal. The critical current density estimated from the width of the hysteresis loop is of the order of 10^6 A cm^{-2} in the full field range investigated (see figure 6(b)). The slight increase in critical current density for higher magnetic fields may indicate an increase in the effectiveness of pinning centres with increasing magnetic field.

4. Conclusions

Single crystals of $SmFeAsO_{1-x}F_y$ superconductor have been grown using the high-pressure cubic anvil technique. The crystals have a plate-like shape with sizes up to 120 μm and are superconducting below 45–53 K. The crystal structure of $SmFeAsO_{1-x}F_y$ refined from single crystal x-ray diffraction data shows incomplete occupancy of the O(F) position. Magnetic measurements in a field up to 7 T show a relatively high critical current density of 10^6 A cm^{-2} almost independent of the field.

Acknowledgment

This work was supported by the Swiss National Science Foundation through the NCCR pool MaNEP.

References

[1] Kamihara Y, Watanabe T, Hirano M and Hosono H 2008 *J. Am. Chem. Soc.* **130** 3296
[2] Takahashi H, Igawa K, Arii K, Kamihara Y, Hirano M and Hosono H 2008 *Nature* **453** 376
[3] Chen X H, Wu T, Wu G, Liu R H, Chen H and Fang D F 2008 *Nature* **453** 761
[4] Ren Z-A *et al* 2008 *Europhys. Lett.* **82** 57002
[5] Ren Z-A *et al* 2008 *Preprint* 0803.4283 [org/abs]
[6] Ren Z-A, Che G-C, Dong X-L, Yang J, Lu W, Yi W, Shen X-L, Li Z-C, Sun L-L, Zhou F and Zhao Z-X 2008 *Europhys. Lett.* **83** 17002
[7] Weyeneth S, Mosele U, Kohout S, Roos J, Keller H, Zhigadlo N D, Katrych S, Bukowski Z and Karpinski J 2008 *Preprint* 0806.1024v1 [org/abs]
[8] Malone L, Fletcher J D, Serafin A, Carrington A, Zhigadlo N D, Katrych S, Bukowski Z and Karpinski J 2008 *Preprint* 0806.3908v1 [org/abs]
[9] Quebe P, Terbüchte L J and Jeitschko W 2000 *J. Alloys Compounds* **302** 70
[10] Prozorov R, Tillman M E, Mun E D and Canfield P C 2008 *Preprint* 0805.2783v1 [org/abs]
[11] Oxford Diffraction Ltd. XCalibur 2003 *CrysAlis Software System* Version 1.170
[12] Sheldrick G 1997 *SHELXS-97: Program for the Solution of Crystal Structures* University of Göttingen, Germany
[13] Sheldrick G 1997 *SHELXL-97: Program for the Refinement of Crystal Structures* University of Göttingen, Germany

4.5.2 Publication V: Anisotropy of superconducting single crystal $SmFeAsO_{0.8}F_{0.2}$ studied by torque magnetometry

S. Weyeneth, R. Puzniak, U. Mosele, N. D. Zhigadlo, S. Katrych, Z. Bukowski, J. Karpinski, S. Kohout, J. Roos, and H. Keller
J. Supercond. Nov. Magn. **22**, 325 (2009).

Abstract
Single crystals of the oxypnictide superconductor $SmFeAsO_{0.8}F_{0.2}$ with $T_c \simeq 45(1)$ K were investigated by torque magnetometry. The crystals of mass ≤ 0.1 μg were grown by a high-pressure cubic anvil technique. The use of a high-sensitive piezoresistive torque sensor made it possible to study the anisotropic magnetic properties of these tiny crystals. The anisotropy parameter γ was found to be field independent, but varies strongly with temperature ranging from $\gamma \simeq 8$ at $T \lesssim T_c$ to $\gamma \simeq 23$ at $T \simeq 0.4T_c$. This unusual behavior of γ signals unconventional superconductivity.

DOI: 10.1007/s10948-008-0413-1
PACS numbers: 74.70.Dd, 74.25.Ha, 74.20.De

At completion of this thesis, according to the Thomson Reuters ISI Web of Knowledge database, this article has been cited at least 22 times.

J Supercond Nov Magn (2009) 22: 325–329
DOI 10.1007/s10948-008-0413-1

LETTER

Anisotropy of Superconducting Single Crystal $SmFeAsO_{0.8}F_{0.2}$ Studied by Torque Magnetometry

S. Weyeneth · R. Puzniak · U. Mosele · N.D. Zhigadlo · S. Katrych · Z. Bukowski · J. Karpinski · S. Kohout · J. Roos · H. Keller

Received: 21 November 2008 / Accepted: 28 November 2008 / Published online: 24 December 2008

Abstract Single crystals of the oxypnictide superconductor $SmFeAsO_{0.8}F_{0.2}$ with $T_c \simeq 45(1)$ K were investigated by torque magnetometry. The crystals of mass ≤ 0.1 μg were grown by a high-pressure cubic anvil technique. The use of a high-sensitive piezoresistive torque sensor made it possible to study the anisotropic magnetic properties of these tiny crystals. The anisotropy parameter γ was found to be field independent, but varies strongly with temperature ranging from $\gamma \simeq 8$ at $T \lesssim T_c$ to $\gamma \simeq 23$ at $T \simeq 0.4T_c$. This unusual behavior of γ signals unconventional superconductivity.

Keywords Oxypnictides · Anisotropy · Multi-band superconductivity · Single crystal · Torque magnetometry

PACS 74.70.Dd · 74.25.Ha · 74.20.De

1 Introduction

The search for novel superconductors recently led to the discovery of the Fe-based oxypnictide layered superconductor $LaFeAsO_{1-x}F_x$ with a transition temperature of $T_c \simeq 26$ K [1]. By substituting La with other rare earth ions, like Sm, Ce, Nd, Pr, or Gd, a series of novel superconducting materials were synthesized with T_c up to 55 K [2–7]. These compounds have a layered crystal structure consisting of LaO and FeAs sheets, where the Fe ions are arranged on simple square lattices [1]. According to theoretical predictions, superconductivity takes place in the FeAs layers, whereas the LaO layers are charge reservoirs when doped with F ions [8, 9].

The anisotropic behavior of layered superconductors can be characterized by their effective mass anisotropy γ, which in the framework of the classical anisotropic Ginzburg–Landau theory is given by $\gamma = \sqrt{m_c^*/m_{ab}^*} = \lambda_c/\lambda_{ab} = B_{c2}^{ab}/B_{c2}^{c}$ [10]. Here m_{ab}^* and m_c^* are the effective carrier masses related to supercurrents flowing in the ab-planes and along the c-axis, respectively; λ_{ab} and λ_c are the corresponding magnetic penetration depths; and B_{c2}^{ab} and B_{c2}^{c} the corresponding upper critical fields. In order to determine reliable values of γ, high-quality single crystals are required.

An estimation of $\gamma \geq 30$ at $T = 0$ K was made for $SmFeAsO_{0.82}F_{0.18}$ from measurements of the c-axis plasma frequency using infrared ellipsometry [11]. From point-contact spectroscopy [12] and resistivity experiments [13] on $LaFeAsO_{0.9}F_{0.1-\delta}$ the anisotropy parameter was estimated to be $\gamma \simeq 10$. Recent resistivity measurements on single crystal $NdFeAsO_{0.82}F_{0.18}$ revealed a value of $\gamma \lesssim 5$ [14] close to T_c. Band structure calculations for $LaFeAsO_{1-x}F_x$ yield a resistivity anisotropy of ∼15 for isotropic scattering, corresponding to $\gamma \simeq 4$ [8]. For comparison, in MgB_2, the value of γ ranges from 1 to 8 and shows a strong temperature and field dependence [15, 16]. This unconventional behavior of γ is well described within the framework of two-band superconductivity [17, 18].

S. Weyeneth (✉) · U. Mosele · S. Kohout · J. Roos · H. Keller
Physik-Institut der Universität Zürich, Winterthurerstrasse 190, 8057 Zürich, Switzerland
e-mail: wstephen@physik.uzh.ch

R. Puzniak
Institute of Physics, Polish Academy of Sciences, Aleja Lotników 32/46, 02-668 Warsaw, Poland

N.D. Zhigadlo · S. Katrych · Z. Bukowski · J. Karpinski
Laboratory for Solid State Physics, ETH Zürich, 8093 Zürich, Switzerland

2 Experiment

Here we report magnetic torque experiments on a single crystal of $SmFeAsO_{0.8}F_{0.2}$ with a $T_c \simeq 45(1)$ K performed in the temperature range of 19 to 45 K and in magnetic fields up to 1.4 T. From these measurements the magnetic anisotropy γ was extracted in the framework of the anisotropic London model [19, 20]. Single crystals of nominal composition $SmFeAsO_{0.8}F_{0.2}$ [21] with masses of only $\approx$0.1 μg were grown from NaCl/KCl flux using a high-pressure cubic anvil technique [22, 23]. The plate-like crystals used in this work are of rectangular shape with typical dimensions of $70 \times 25 \times 3$ μm^3, corresponding to an estimated volume of $V \simeq 5 \times 10^{-15}$ m^3. The crystal structure was checked by means of X-ray diffraction revealing the c-axis to be perpendicular to the plates.

Selected crystals of $SmFeAsO_{0.8}F_{0.2}$ of the same batch with $T_c \simeq 45$ K were characterized in a commercial *Quantum Design Magnetometer* MPMS XL. As an example, Fig. 1 shows the zero-field cooled (ZFC) magnetic moment m of one of the crystals vs. temperature in 1 mT parallel to the c-axis. The rough estimate for $T_c \simeq 45(1)$ K (straight line in Fig. 1) is consistent with $T_c = 46.0(3)$ K obtained from the temperature dependence of the in-plane magnetic penetration depth λ_{ab} (see later Fig. 4). The magnetic moment m saturates in the Meissner state below 40 K and the total transition width is $\Delta T \lesssim 4$ K, demonstrating the good quality of the sample.

The magnetic torque τ of a single-crystal sample in a static magnetic field B applied under a certain angle θ with respect to the crystallographic c-axis of the crystal is given by $\vec{\tau} = \vec{m} \times \vec{B} = \mu_0(\vec{m} \times \vec{H})$, or equivalently $\tau(\theta) = m(\theta)B\sin(\phi(\theta))$. Here $\vec{m}$ denotes the magnetic moment of the sample and $\phi(\theta)$ the respective angle between $\vec{B}$ and $\vec{m}$.

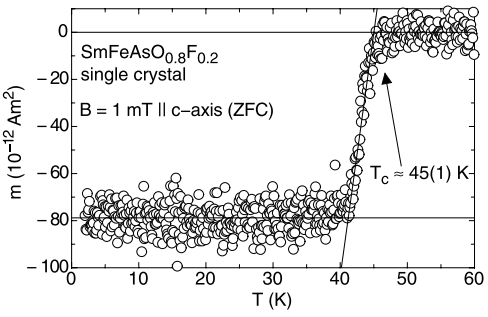

Fig. 1 Temperature dependence of the magnetic moment m of a $SmFeAsO_{0.8}F_{0.2}$ single crystal measured in 1 mT parallel to the c-axis (zero-field cooling, ZFC). The rough estimate of the transition temperature $T_c \simeq 45(1)$ K (indicated by the *arrow*) is consistent with the value of $T_c = 46.0(3)$ K determined from the temperature dependence of the in-plane magnetic penetration depth λ_{ab} (see text and Fig. 4)

Our apparatus was especially designed for measurements on micro-crystals with masses smaller than 1 μg using micro-machined sensors of high sensitivity ($\sim 10^{-14}$ N m) developed in our group [24]. To collect angular dependent torque data $\tau(\theta)$, we used a measurement system with a turnable *Bruker* NMR iron yoke magnet with a maximum magnetic field of 1.4 T, allowing a rotation of the magnetic field direction of more that 360° with respect to a crystallographic axis of the sample. Temperatures down to 10 K can be achieved with a flow cryostat between the poles of the magnet. The possibility of rotating the magnetic field around a fixed sample increases the sensitivity again because background effects to the torque are minimized.

Below T_c we observe a torque signal arising from the interaction of the applied magnetic field with vortices in the sample. Based on the 3D anisotropic London model, the free energy of an anisotropic superconductor in the mixed state was calculated by Kogan et al. [19, 20]:

$$\tau(\theta) = -\frac{V\Phi_0 B}{16\pi\mu_0\lambda_{ab}^2}\left(1-\frac{1}{\gamma^2}\right)\frac{\sin(2\theta)}{\epsilon(\theta)}\ln\left(\frac{\eta B_{c2}^c}{\epsilon(\theta)B}\right). \quad (1)$$

V is the volume of the crystal, Φ_0 is the elementary flux quantum, B_{c2}^c is the upper critical field along the c-axis of the crystal, η denotes a numerical parameter of the order unity depending on the structure of the flux-line lattice, and $\epsilon(\theta) = [\cos^2(\theta) + \gamma^{-2}\sin^2(\theta)]^{1/2}$. By measuring the angular dependence of the torque in the mixed state of a superconductor, three fundamental parameters can be extracted from the data: the in-plane magnetic penetration depth λ_{ab}, the c-axis upper critical field B_{c2}^c, and the effective mass anisotropy γ. In this work we performed angle-dependent measurements of the torque over more than 180° in order to investigate the full angular dependent magnetization in terms of (1). The torque was measured with a clockwise and a counterclockwise rotating magnetic field and then averaged according to $\tau_{\rm rev} = (\tau(\theta^+) + \tau(\theta^-))/2$ to reduce vortex pinning effects (see upper panel of Fig. 2). To further minimize the influence of pinning, we partly applied a vortex-lattice shaking technique [25]. With this technique the relaxation of the vortex-lattice towards its thermal equilibrium is strongly enhanced by using an additional small magnetic AC field perpendicular to the static external field B. The magnitude of the AC field was $\simeq$5 mT and the shaking frequency was $\simeq$200 Hz. With these parameters the best experimental conditions were obtained, including the vortex-lattice relaxation towards thermal equilibrium. Examples of the reversible torque as a function of the angle θ determined in the superconducting state are displayed in the lower panel of Fig. 2. A small temperature independent background of 10^{-12} N m was recorded well above T_c and subtracted from all measurements below T_c.

The most reliable parameter which can be extracted from the torque data is the anisotropy parameter γ because, according to (1), it only depends on the angular dependence

J Supercond Nov Magn (2009) 22: 325–329

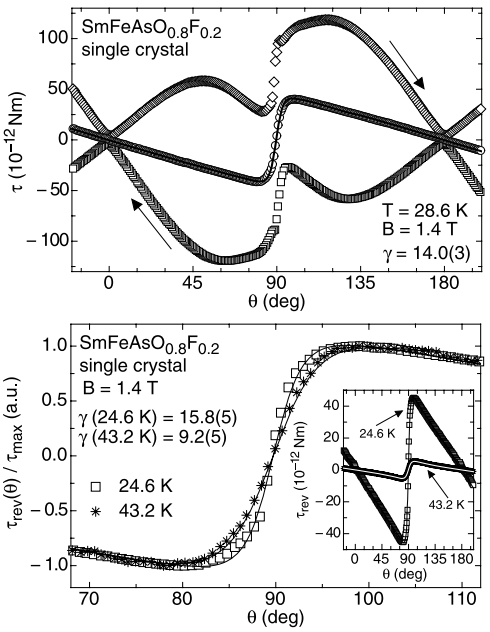

Fig. 2 *Upper panel*: Angular dependence of the reversible torque of a single crystal of $SmFeAsO_{0.8}F_{0.2}$ at $T = 28.6$ K and $B = 1.4$ T. The *squares* (*diamonds*) denote a counterclockwise (clockwise) rotating of the magnetic field around the sample. For minimizing pinning effects the mean torque $\tau_{rev} = (\tau(\theta^+) + \tau(\theta^-))/2$ was calculated (*circles*). The *solid line* denotes a fit to (1) from which the anisotropy parameter $\gamma = 14.0(3)$ was extracted. *Lower panel*: Normalized angular dependence of the torque for θ in the neighborhood of 90° (B parallel ab-plane) at 24.6 K (*squares*) and 43.2 K (*stars*). The *solid lines* represent fits to (1). The different shapes of the two torque signals reflect the temperature dependence of γ. The *inset* displays the full angular dependence of the same torque signals

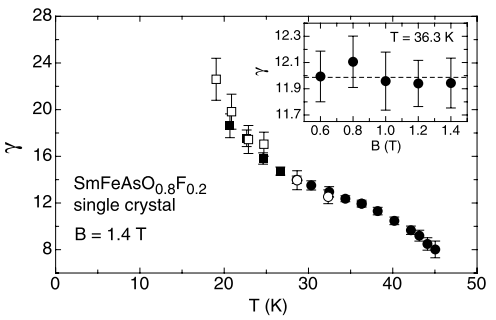

Fig. 3 Temperature dependence of the anisotropy parameter γ of a single crystal of $SmFeAsO_{0.8}F_{0.2}$ at $B = 1.4$ T obtained from a subsequent analysis of the torque data by means of (1). *Full symbols* denote values of γ extracted from simply averaged data sets, whereas *open symbols* show values of γ from shaked data sets as explained in the text. The values of γ obtained from fits to (1) with all parameters free being indicated by *circles*, whereas the *squares* represent the values of γ evaluated using extrapolated values of B^c_{c2}. The *inset* shows γ determined at 36.3 K from unshaked data at different fields. As can be seen, no field dependence of γ is observed

of the torque and not on the sample volume. Figure 2 (lower panel) displays two examples of torque measurements performed at $B = 1.4$ T and for two different temperatures, 24.6 and 43.2 K, yielding quite different values of γ, namely $\gamma(24.6\text{ K}) = 15.8(5)$ and $\gamma(43.2\text{ K}) = 9.2(5)$. This is clearly reflected in the different shapes of the torque signals for θ in the neighborhood of 90° (B almost parallel to the ab-plane). The temperature dependence of γ determined at 1.4 T is displayed in Fig. 3. As the temperature decreases, γ rises from $\gamma(45.0\text{ K}) = 8.0(7)$ to $\gamma(19.0\text{ K}) = 22.6(15)$. Note that the present values of γ are within the range of the values so far reported in the literature [8, 11–14]. At low temperatures, pinning effects give rise to the rather large errors in the anisotropy parameter, preventing a reliable determination of γ for $T < 19$ K. In order to demonstrate that the strong temperature dependence of γ is not an artefact of the increasing pinning strength at low temperatures, we compared shaked and unshaked torque data. One would expect that the shaked data are close to the reversible thermal equilibrium state. However, as indicated by the open and closed symbols in Fig. 3, there is within error bars no difference between the values of γ determined with and without shaking, attesting that the used procedure to determine γ below the irreversibility line is still reliable [25]. Furthermore, the field dependence of γ was studied at $T = 36.3$ K. As shown in the inset of Fig. 3, for $0.6\text{ T} \leq B \leq 1.4$ T no field dependence of γ could be detected, suggesting that the measured anisotropy parameter in this work is $\gamma = \lambda_c/\lambda_{ab} = B^{ab}_{c2}/B^c_{c2}$. Since γ is field-independent, its determination is not appreciably affected by weak intrinsic pinning present in the sample [26, 27].

The only parameter which is difficult to extract from (1) in the presence of weak pinning is the upper critical field B^c_{c2} as it enters only logarithmically into the formula. For this reason we fitted $B^c_{c2}(T)$ above 28 K according to $\eta B^c_{c2}(T) \approx 88\text{ T} - (1.9\text{ T/K}) \cdot T$ and extrapolated values of $B^c_{c2}(T)$ down to 19 K in order to follow the temperature dependence of γ further down in temperature (note that the fitted slope of $dB^c_{c2}/dT \approx -2$ T/K agrees well with the slope close to T_c reported in [28]). The values obtained from the extrapolated values of B^c_{c2} are displayed in Fig. 3 as squares, whereas the values evaluated by the free fits are represented by circles.

The temperature dependencies of the upper critical field B^c_{c2} and the in-plane magnetic penetration depth λ_{ab} as extracted from the torque data, are displayed in Fig. 4. B^c_{c2} follows a linear temperature dependence down to 28 K. The dashed line represents a linear fit in order to extrapolate B^c_{c2} down to 19 K. Using the WHH approximation [29],

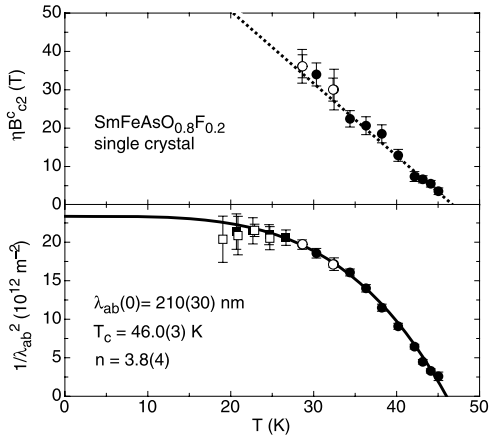

Fig. 4 *Upper panel*: Temperature dependence of the upper critical field B_{c2}^c of a single crystal of $SmFeAsO_{0.8}F_{0.2}$. The *dashed line* is a linear fit $\eta B_{c2}^c = 88\ \mathrm{T} - (1.9\ \mathrm{T/K}) \cdot T$. The meaning of the symbols is the same as in Fig. 3. *Lower panel*: In-plane magnetic penetration depth $\lambda_{ab}(T)$ obtained from the torque data and plotted as $1/\lambda_{ab}^2$ versus temperature. The *solid line* represents a fit of the data to the power law $1/\lambda_{ab}^2(T) = 1/\lambda_{ab}^2(0) \cdot 1 - (T/T_c^n)$ with all parameters free. The exponent of $n = 3.8(4)$ is close to $n = 4$ characteristic for the two-fluid model. The meaning of the symbols is the same as in Fig. 3

$B_{c2}^c(0) \simeq 60$ T. The value of λ_{ab} was also estimated from the torque data using (1). In the lower panel of Fig. 4 the temperature dependence of $1/\lambda_{ab}^2$ is displayed. As shown by the solid curve in Fig. 4 (lower panel), the data were analyzed by the power law $1/\lambda_{ab}^2(T) = 1/\lambda_{ab}^2(0) \cdot (1 - (T/T_c)^n)$ with the free parameters $\lambda_{ab}(0) \simeq 210(30)$ nm, $T_c = 46.0(3)$ K, and $n = 3.8(4)$. This value of $\lambda_{ab}(0)$ is in reasonable agreement with the values reported for polycrystalline samples: From μSR experiments Luetkens et al. extracted $\lambda_{ab}(0) = 254(2)$ nm for $LaFeAsO_{0.9}F_{0.1}$ and $\lambda_{ab}(0) = 364(8)$ nm for $LaFeAsO_{0.925}F_{0.075}$ [30], whereas Khasanov et al. obtained a value of $\lambda_{ab}(0) = 198(5)$ nm for $SmFeAsO_{0.85}$ [31]. The exponent $n = 3.8(4)$ is close to $n = 4$ for the two-fluid model, characteristic for a superconductor in the strong-coupling limit [32]. However, the present data are too limited to draw definite conclusions.

$SmFeAsO_{0.8}F_{0.2}$ exhibits a similar temperature dependence of the anisotropy parameter γ as MgB_2 for which γ varies between 1 and 8, depending on temperature and magnetic field [15, 16, 18]. Therefore, the unusual temperature dependence of γ on $SmFeAsO_{0.8}F_{0.2}$, which cannot be explained by conventional Ginzburg–Landau theory, indicates a possible two-gap scenario [18]. Note that other experiments, such as recent resistivity measurements of the upper critical field on $LaFeAsO_{0.89}F_{0.11}$ [28] and NMR studies of $PrFeAsO_{0.89}F_{0.11}$ [33], also suggest that the novel class of Fe-based oxypnictide superconductors exhibit two-band superconductivity. Nevertheless, other possibilities of a temperature dependent γ should be mentioned here [26, 27, 34].

3 Conclusions

In conclusion, the magnetic anisotropy parameter γ, and the in-plane magnetic penetration depth λ_{ab} were determined by high-sensitive magnetic torque experiments for a single crystal of $SmFeAsO_{0.8}F_{0.2}$. The parameter γ extracted from the reversible torque signals was found to be strongly temperature-dependent, ranging from $\gamma \simeq 8$ at $T \lesssim T_c$ to $\gamma \simeq 23$ at $T \simeq 0.4T_c$. However, no field dependence of γ could be detected. For the in-plane magnetic penetration depth at zero temperature a value of $\lambda_{ab}(0) \simeq 210(30)$ nm was estimated, in agreement with values reported in the literature [30, 31]. The unusual temperature dependence of γ suggests that $SmFeAsO_{0.8}F_{0.2}$ is probably a multi-band superconductor, similar to MgB_2 [18] and the cuprate superconductors [35]. However, other explanations for this unusual behavior such as e.g. the possibility of an anisotropic s-wave gap [34], cannot be ruled out. More detailed experimental work is required to clarify this point.

Acknowledgements The authors are grateful to A. Bussmann-Holder for very helpful discussions, and to S. Strässle and C. Duttwyler for the help to prepare the manuscript. This work was supported by the Swiss National Science Foundation and in part by the NCCR program MaNEP and the EU Project CoMePhS.

References

1. Kamihara, Y., Watanabe, T., Hirano, M., Hosono, H.: J. Am. Chem. Soc. **130**, 3296 (2008)
2. Chen, X.H., et al.: Nature **453**, 761 (2008)
3. Chen, G.F., et al.: Phys. Rev. Lett. **100**, 247002 (2008)
4. Ren, Z.-A., et al.: Europhys. Lett. **82**, 57002 (2008)
5. Ren, Z.-A., et al.: Mat. Res. Inn. **12**, 106 (2008)
6. Cheng, P., et al.: Sci. China G **51**, 719 (2008)
7. Ren, Z.-A., et al.: Chin. Phys. Lett. **25**, 2215 (2008)
8. Singh, D.J., Du, M.-H.: Phys. Rev. Lett. **100**, 237003 (2008)
9. Klauss, H.-H., et al.: Phys. Rev. Lett. **101**, 077005 (2008)
10. Tinkham, M.: Introduction to Superconductivity. McGraw-Hill, New York (1975)
11. Dubroka, A., et al.: Phys. Rev. Lett. **101**, 097011 (2008)
12. Shan, L., et al.: Europhys. Lett. **83**, 57004 (2008)
13. Zhu, X., et al.: Supercond. Sci. Technol. **21**, 105001 (2008)
14. Jia, Y., et al.: Appl. Phys. Lett. **93**, 032503 (2008)
15. Angst, M., et al.: Phys. Rev. Lett. **88**, 167004 (2002)
16. Lyard, L., et al.: Phys. Rev. Lett. **92**, 057001 (2004)
17. Gurevich, A.: Phys. Rev. B **67**, 184515 (2003)
18. Angst, M., Puzniak, R.: In: Martines, B.P. (ed.) Focus on Superconductivity, vol. 1, pp. 1–49. Nova Science, New York (2004). arXiv:cond-mat/0305048
19. Kogan, V.G.: Phys. Rev. B **24**, 1572 (1981)
20. Kogan, V.G., Fang, M.M., Mitra, S.: Phys. Rev. B **38**, 11958 (1988)
21. Zhigadlo, N.D., et al.: J. Phys.: Condens. Matter. **20**, 342202 (2008)

22. Karpinski, J., et al.: Supercond. Sci. Technol. **16**, 221 (2003)
23. Karpinski, J., et al.: Physica C **385**, 42 (2003)
24. Kohout, S., Roos, J., Keller, H.: Rev. Sci. Instr. **78**, 013903 (2007)
25. Willemin, M., et al.: Phys. Rev. B **58**, R5940 (1998)
26. Pugnat, P., Fillon, G., Noel, H., Barbara, B.: Europhys. Lett. **35**, 49 (1996)
27. Kawamata, S., Inoue, K., Ochida, K., Sasaki, T.: Physica B **246**, 437 (1998)
28. Hunte, F., et al.: Nature **453**, 903 (2008)
29. Werthamer, N.R., Helfand, E., Hohenberg, P.C.: Phys. Rev. **147**, 295 (1966)
30. Luetkens, H., et al.: Phys. Rev. Lett. **101**, 097009 (2008)
31. Khasanov, R., et al.: Phys. Rev. B **78**, 092506 (2008)
32. Rammer, J.: Europhys. Lett. **5**, 77 (1988)
33. Matano, K., et al.: Europhys. Lett. **83**, 57001 (2008)
34. Posazhennikova, A.I., Dahm, T., Maki, K.: Europhys. Lett. **60**, 134 (2002)
35. Khasanov, R., et al.: Phys. Rev. Lett. **99**, 237601 (2007) and Refs. therein

4.5.3 Publication VI: Evidence for two distinct anisotropies in the oxypnictide superconductors $SmFeAsO_{0.8}F_{0.2}$ and $NdFeAsO_{0.8}F_{0.2}$

S. Weyeneth, R. Puzniak, N. D. Zhigadlo, S. Katrych, Z. Bukowski, J. Karpinski, and H. Keller
J. Supercond. Nov. Magn. **22**, 347 (2009).

Abstract
Single crystals of the oxypnictide superconductors $SmFeAsO_{0.8}F_{0.2}$ and $NdFeAsO_{0.8}F_{0.2}$ with T_c in the range of 44 K to 48 K were investigated by torque magnetometry. An analysis of the data in terms of a recently proposed model for the anisotropic magnetization in the superconducting state, treating the magnetic penetration depth anisotropy γ_λ differently than the upper critical field anisotropy γ_H, provides evidence that in the oxypnictide superconductors two distinct anisotropies are present. As a result γ_λ differs significantly in magnitude and in temperature dependence from γ_H, analogous to MgB_2 but with a reversed sign of slope. This scenario strongly suggests a new multi-band mechanism in the novel class of oxypnictide high-temperature superconductors.

DOI: 10.1007/s10948-009-0445-1
PACS numbers: 74.70.Dd, 74.25.Ha, 74.20.De, 74.25.Op

At completion of this thesis, according to the Thomson Reuters ISI Web of Knowledge database, this article has been cited at least 25 times.

J Supercond Nov Magn (2009) 22: 347–351
DOI 10.1007/s10948-009-0445-1

LETTER

Evidence for Two Distinct Anisotropies in the Oxypnictide Superconductors $SmFeAsO_{0.8}F_{0.2}$ and $NdFeAsO_{0.8}F_{0.2}$

S. Weyeneth · R. Puzniak · N.D. Zhigadlo · S. Katrych · Z. Bukowski · J. Karpinski · H. Keller

Received: 29 December 2008 / Accepted: 8 January 2009 / Published online: 13 February 2009

Abstract Single crystals of the oxypnictide superconductors $SmFeAsO_{0.8}F_{0.2}$ and $NdFeAsO_{0.8}F_{0.2}$ with T_c in the range of 44 to 48 K were investigated by torque magnetometry. An analysis of the data in terms of a recently proposed model for the anisotropic magnetization in the superconducting state, treating the magnetic penetration depth anisotropy γ_λ differently than the upper critical field anisotropy γ_H, provides evidence that in the oxypnictide superconductors two distinct anisotropies are present. As a result γ_λ differs significantly in magnitude and in temperature dependence from γ_H, analogous to MgB_2 but with a reversed sign of slope. This scenario strongly suggests a new multi-band mechanism in the novel class of oxypnictide high-temperature superconductors.

Keywords Oxypnictides · Anisotropy · Multi-band superconductivity · Single crystal · Torque magnetometry · Magnetic penetration depth · Upper critical field

PACS 74.70.Dd · 74.25.Ha · 74.20.De · 74.25.Op

It is well known that all superconductors with the highest transition temperatures have a layered crystal structure, which manifests itself in pronounced anisotropic properties. In the recently discovered oxypnictide superconductors $RFeAsO_{1-x}F_x$ (R = La, Sm, Ce, Nd, Pr, Gd) with considerably high transition temperatures up to $T_c \simeq 56$ K superconductivity takes place in the FeAs layers, and the LaO sheets are charge reservoirs when doped with F ions [1–7]. Whereas the cuprates have been characterized by a well-defined effective mass anisotropy, the observation of two distinct anisotropies in MgB_2 challenged the understanding of anisotropic superconductors [8–10]. Therefore, it is important to investigate the anisotropic behavior of the oxypnictides in order to clarify the nature of superconductivity in this novel class of superconductors. In this respect a detailed knowledge of the anisotropy parameter γ is essential.

In the framework of phenomenological Ginzburg–Landau theory the anisotropic behavior of superconductors is described by means of the effective mass anisotropy parameter [11]

$$\gamma = \sqrt{m_c^*/m_{ab}^*} = \lambda_c/\lambda_{ab} = \xi_{ab}/\xi_c = H_{c2}^{\parallel ab}/H_{c2}^{\parallel c}. \quad (1)$$

Here m_{ab}^* and m_c^* are the components of the effective carrier mass related to supercurrents flowing in the ab-plane and along the c-axis, respectively; λ_{ab}, λ_c, ξ_{ab}, and ξ_c are the corresponding magnetic penetration depth and coherence length components; and $H_{c2}^{\parallel ab}$ and $H_{c2}^{\parallel c}$ are the upper critical field components. For the oxypnictides, many different estimates of the effective mass anisotropy with values ranging from 1 to 30 were reported [12–20]. The first temperature-dependent study of the anisotropy parameter γ was performed on $SmFeAsO_{0.8}F_{0.2}$ single crystals by means of torque magnetometry [12], where a strongly temperature-dependent γ was found, ranging from $\gamma \simeq 8$ at $T \lesssim T_c$ to $\gamma \simeq 23$ at $T \simeq 0.4T_c$. Other torque studies

S. Weyeneth (✉) · H. Keller
Physik-Institut der Universität Zürich, Winterthurerstrasse 190, 8057 Zürich, Switzerland
e-mail: wstephen@physik.uzh.ch

R. Puzniak
Institute of Physics, Polish Academy of Sciences, Aleja Lotników 32/46, 02-668 Warsaw, Poland

N.D. Zhigadlo · S. Katrych · Z. Bukowski · J. Karpinski
Laboratory for Solid State Physics, ETH Zurich, 8093 Zurich, Switzerland

on $SmFeAsO_{0.8}F_{0.2}$ revealed a similar temperature dependence with $\gamma \simeq 9$ saturating at lower temperatures [17], whereas surprisingly for $PrFeAsO_x$ an almost temperature-independent $\gamma \simeq 1.1$ was reported [18]. A relatively low value of $\gamma \simeq 2.5$ with a slight temperature dependence was also observed in magneto-optical studies performed on $PrFeAsO_x$ [19]. From upper critical field measurements, various investigations on oxypnictides have shown that, sufficiently below T_c, γ decreases with decreasing temperature, in sharp contrast to the magnetic torque data [12, 17] which reveal an increasing γ. A recent high magnetic field investigation [20] of the upper critical field in single crystal $NdFeAsO_{0.7}F_{0.3}$ with a $T_c = 46$ K provided an estimate of the anisotropy $H_{c2}^{\|ab}/H_{c2}^{\|c}$ with γ ranging from $\gamma \simeq 6$ at $T \simeq 38$ K to $\gamma \simeq 5$ at $T \simeq 34$ K. In summary, all these different estimates for γ seem to be very difficult to understand in a consistent way in the framework of classical Ginzburg–Landau theory by means of (1).

In order to clarify this puzzling behavior of the anisotropy parameter γ, we decided to perform further detailed torque studies on single crystals of nominal composition $SmFeAsO_{0.8}F_{0.2}$ and $NdFeAsO_{0.8}F_{0.2}$. The magnetic torque $\vec{\tau}$ of a sample with magnetic moment $\vec{m}$ in a magnetic field $\vec{H}$ is defined by

$$\vec{\tau} = \mu_0(\vec{m} \times \vec{H}). \tag{2}$$

For anisotropic superconductors in the mixed state the diamagnetic magnetization is not strictly antiparallel to the applied magnetic field due to the presence of vortices which are tilted in an arbitrary applied magnetic field. Therefore, an anisotropic superconductor in a magnetic field will exhibit a magnetic torque according to (2). In the mean-field approach of the anisotropic Ginzburg–Landau theory the torque for a superconductor with a single gap is written as [11]

$$\tau(\theta) = -\frac{V\Phi_0 H}{16\pi\lambda_{ab}^2}\left(1-\frac{1}{\gamma^2}\right)\frac{\sin(2\theta)}{\epsilon(\theta)}\ln\left(\frac{\eta H_{c2}^{\|c}}{\epsilon(\theta)H}\right). \tag{3}$$

V is the volume of the crystal, Φ_0 is the elementary flux quantum, $H_{c2}^{\|c}$ is the upper critical field along the c-axis of the crystal, η denotes a numerical parameter of the order unity, depending on the structure of the flux-line lattice, and $\epsilon(\theta) = [\cos^2(\theta) + \gamma^{-2}\sin^2(\theta)]^{1/2}$. Three fundamental thermodynamic parameters can be extracted from the angular dependence of the torque in the mixed state of a superconductor: the in-plane magnetic penetration depth λ_{ab}, the c-axis upper critical field $H_{c2}^{\|c}$, and the effective mass anisotropy γ. As has been pointed out by Kogan [21], the anisotropies for the magnetic penetration depth $\gamma_\lambda = \lambda_c/\lambda_{ab}$ and for the upper critical field $\gamma_H = H_{c2}^{\|ab}/H_{c2}^{\|c}$ do not necessarily coincide for unconventional Ginzburg–Landau superconductors, as described in (1) where $\gamma = \gamma_\lambda = \gamma_H$. A more generalized approach, including the two distinct anisotropies γ_λ and γ_H, leads to the more general expression [21]

$$\tau(\theta) = -\frac{V\Phi_0 H}{16\pi\lambda_{ab}^2}\left(1-\frac{1}{\gamma_\lambda^2}\right)\frac{\sin(2\theta)}{\epsilon_\lambda(\theta)} \times\left[\ln\left(\frac{\eta H_{c2}^{\|c}}{H}\frac{4e^2\epsilon_\lambda(\theta)}{(\epsilon_\lambda(\theta)+\epsilon_H(\theta))^2}\right) - \frac{2\epsilon_\lambda(\theta)}{\epsilon_\lambda(\theta)+\epsilon_H(\theta)}\left(1+\frac{\epsilon'_\lambda(\theta)}{\epsilon'_H(\theta)}\right)\right]. \tag{4}$$

Here the scaling function $\epsilon_i(\theta) = [\cos^2(\theta)+\gamma_i^{-2}\sin^2(\theta)]^{1/2}$ with $i = \lambda, H$ is different for γ_λ and γ_H. $\epsilon'_i(\theta)$ denotes its derivative with respect to the angle θ.

The method of crystal growth and the basic superconducting properties of the $SmFeAsO_{1-x}F_y$ single crystals investigated here were already reported [22]. The same procedure was used to grow single crystals of $NdFeAsO_{1-x}F_y$. The plate-like crystals used in this work were of rectangular shape with typical masses of the order of 100 ng. The crystal structure was checked by means of X-ray diffraction revealing the c-axis to be perpendicular to the plates. The magnetization curves shown in Fig. 1 were measured in the Meissner state using a commercial Quantum Design SQUID magnetometer MPMS XL with installed Reciprocating Sample Option. Small variation of the transition temperature of the various samples may be due to oxygen and

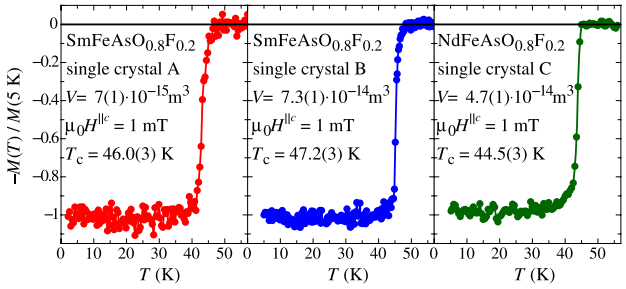

Fig. 1 (Color online) Normalized magnetization for the three single crystals studied in this work. The magnetic moment was measured in the zero field cooling mode with an applied field of 1 mT parallel to the c-axis. Below T_c all samples show full diamagnetic response with a narrow and well-defined transition temperature

J Supercond Nov Magn (2009) 22: 347–351

fluorine deficiency. The volume of the crystals given in Fig. 1 was estimated from magnetization measurements in low magnetic fields applied along the samples' ab-plane. The c-axis dimension is much smaller than the a- and b-dimensions, and therefore demagnetizing effects can be neglected. Good agreement was found with optical microscope measurements of the dimensions of the sample.

To perform most accurate measurements of the superconducting anisotropy parameter, we have chosen high sensitivity torque magnetometry. For the low field torque measurements we used an experimental setup described in detail elsewhere [12]. It is worth pointing out that the anisotropy data published several years ago for single-crystal MgB_2 were also obtained with this torque setup [8]. In order to derive the reversible torque from the raw data, recorded in the irreversible regime by clockwise (θ^+) and counterclockwise (θ^-) rotating of the magnetic field with respect to the c-axis, we used the standard approximation $\tau(\theta) = (\tau_{\rm raw}(\theta^+) + \tau_{\rm raw}(\theta^-))/2$ described elsewhere [12]. Some of the reversible torque data for $SmFeAsO_{0.8}F_{0.2}$ (single crystal B) are shown in Fig. 2.

The torque data in the superconducting state were analyzed using the approach proposed by Balicas et al. [17] in order to eliminate any anisotropic paramagnetic or diamagnetic background contribution. In this approach the torque data were first symmetrized according to $\tau_{\rm symm}(\theta) = \tau(\theta) + \tau(\theta + 90°)$ and subsequently analyzed. In the fitting procedure we always kept the upper critical field fixed, assuming a WHH dependence [23] with a slope at T_c of $\mu_0(dH_{c2}^{\|c}/dT)|_{T_c} = 1.5$ T/K, which is a typical value reported for oxypnictide superconductors [12, 15, 16, 20, 24]. This approach reduces the number of free fit parameters, so that both γ and λ_{ab} can be reliably determined in a simultaneous fit. By fitting the simple Kogan expression in (3) to the angular-dependent torque data, we get excellent agreement as shown in Fig. 3a. The resulting values of γ determined for all samples are shown in Fig. 4. It is important to stress that the choice of the actual slope $\mu_0(dH_{c2}^{\|c}/dT)|_{T_c} = 1.5$ T/K does not much influence the determination of γ, since γ is mostly sensitive to the angular dependence of the torque close to the ab-plane. We tested the influence of a variation of $H_{c2}^{\|c}(T)$ on the error in γ by altering the slope $\mu_0(dH_{c2}^{\|c}/dT)|_{T_c}$ from 1 to 2 T/K. As a result, γ varies only within a few percent as depicted in Fig. 5. All of the

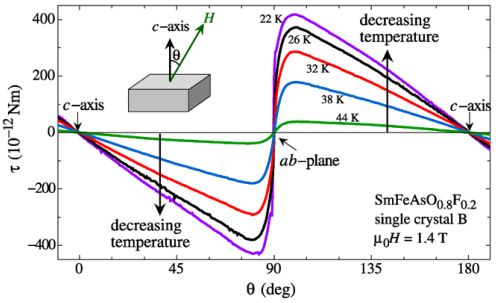

Fig. 2 (Color online) Angular dependence of the reversible torque data for $SmFeAsO_{0.8}F_{0.2}$ (single crystal B) at several temperatures derived in a magnetic field of 1.4 T. Only a small almost temperature-independent background contribution (smaller than 10^{-11} Nm) is present in the data, stemming from a minor anisotropic normal state magnetization. For clarity, not all investigated temperatures are presented

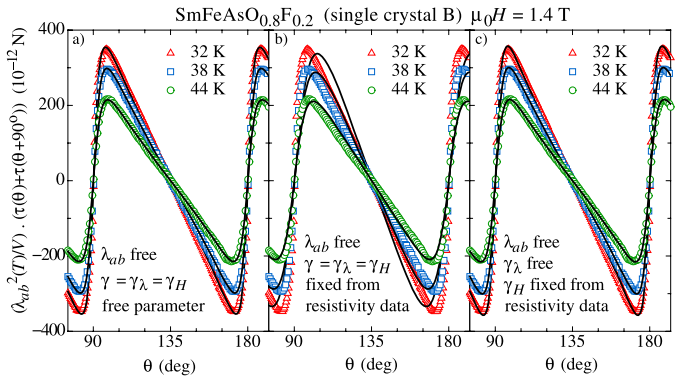

Fig. 3 (Color online) Three sets of normalized torque data, obtained at 32 K, 38 K, and 44 K in 1.4 T for $SmFeAsO_{0.8}F_{0.2}$ (single crystal B) and analyzed in terms of $\tau(\theta) + \tau(\theta + 90°)$. **a** Data described by (3) with both γ and λ_{ab} as free parameters. **b** Data described by (3) with γ fixed to the linearly extrapolated values of the resistivity measurements [20] and with λ_{ab} as a free parameter. **c** Data described in the generalized equation, (4), with γ_H fixed to the linearly extrapolated values of the resistivity measurements [20] and with γ_λ and λ_{ab} as free parameters

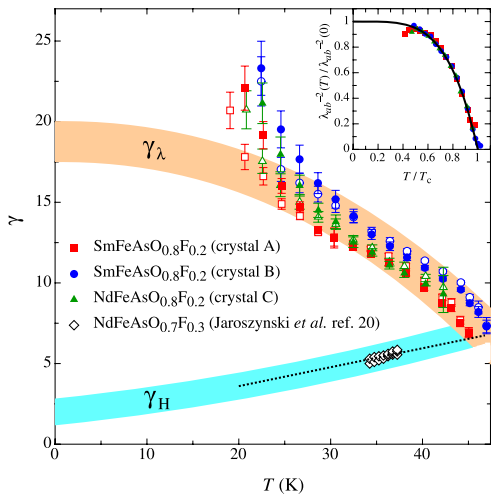

Fig. 4 (Color online) Summary of all the parameters derived from the systematic analysis of the torque data of single crystals $SmFeAsO_{0.8}F_{0.2}$ (crystal A and B) and $NdFeAsO_{0.8}F_{0.2}$ (crystal C). Values of γ (*open symbols*) and γ_λ (*closed symbols*) were obtained from fits to the data with (3) and (4), respectively. The upper *broad orange band* is a guide to the eye, suggesting an estimate of $\gamma_\lambda(0) \approx 19$. The *dotted line* is the linear extrapolation of γ_H obtained from resistivity measurements [20] on a $NdFeAsO_{0.7}F_{0.3}$ single crystal with similar $T_c = 45$ K (*diamonds*). The lower *broad blue band* is a guide to the eye, suggesting an estimate of $\gamma_H(0) \approx 2$. The *inset* shows the normalized superfluid density as obtained from fits of (4) to the torque data. The *solid line* denotes the best fit to the data using the power law in (5) as explained in the text

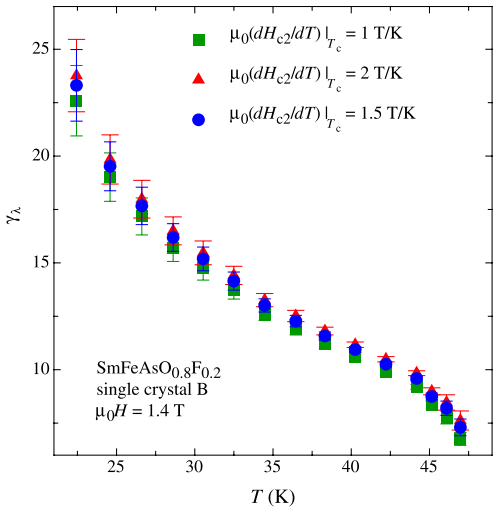

Fig. 5 (Color online) Values of γ_λ for $SmFeAsO_{0.8}F_{0.2}$ (crystal B) obtained from fits to the data in (4). The used WHH relation for $H_{c2}^{\|c}(T)$ was varied assuming three different slopes $\mu_0(dH_{c2}^{\|c}/dT)|_{T_c} = 1$, 1.5 and 2 T/K, as explained in the text. The resulting temperature dependencies of γ_λ are within experimental errors the same, and therefore do not depend significantly on the slope. The anisotropy can be reliably determined by fixing the slope to 1.5 T/K, which is a typical value reported for oxypnictide superconductors

anisotropy data obtained with different slopes are the same within the experimental errors given in Fig. 4. With $H_{c2}^{\|c}$ as a free parameter the scattering of all fitted parameters is strongly enhanced, and unphysical values for the upper critical field are obtained, which was already noted in earlier torque studies [12, 17, 18].

The analysis of the torque data presented so far leads to a pronounced temperature-dependent γ with values of $\gamma \geqslant 20$ for $T \lesssim 20$ K [12]. However, this result is in strong contrast to the results obtained from resistivity data on single crystals of the similar compound $NdFeAsO_{0.7}F_{0.3}$ where the anisotropy $H_{c2}^{\|ab}/H_{c2}^{\|c}$ was found to decrease with decreasing temperature [20]. Different techniques should lead to similar values for the same quantity, and therefore it is important to explain the physical meaning of this discrepancy. In Fig. 3b we depict the same data set as shown in Fig. 3a, analyzed according to (3) with γ fixed to linearly extrapolated values of the resistivity measurements of Jaroszynski et al. [20] and only with λ_{ab} as a free parameter. Obviously, the fit does not describe the torque data well. This discrepancy suggests the presence of two distinct anisotropies, namely $\gamma_\lambda = \lambda_c/\lambda_{ab}$ and $\gamma_H = H_{c2}^{\|ab}/H_{c2}^{\|c}$. In order to test this hypothesis we analyzed the torque data with the generalized expression in (4), including both γ_λ and γ_H. The result is shown in Fig. 3c, again with the same fixed γ_H as in Fig. 3b, but with γ_λ as a free parameter. Note that this approach describes all torque data very well. Moreover, the values of γ_λ are very similar to those previously obtained by means of (3) [12]. The final results of fitting γ_λ and λ_{ab} by means of (4) are shown in Fig. 4. In the temperature range $T_c \geqslant T \geqslant 25$ K, all values for γ_λ show the same temperature behavior, which appears to be generic for oxypnictide superconductors. From this trend, a value of $\gamma_\lambda(0) \approx 19$ can be estimated. The drastic increase of γ_λ below 25 K to values well above 20 is very likely due to a substantial pinning contribution to the torque, which makes it impossible to derive reversible torque data from measurements in the irreversible region. Moreover, in this regime the fit parameters deviate from each other and depend even on the used fitting expression, further supporting the presence of non-equilibrium effects, such as strong pinning. The pronounced temperature dependence of γ_λ between 25 K and T_c strongly signals multi-band superconductivity, like in e.g. MgB_2. However, in order to clarify its origin, more systematic experimental work is required.

Further support for the proposed scenario stems from the temperature dependence of the in-plane magnetic penetration depth λ_{ab}. In the inset to Fig. 4 the normalized superfluid density $\lambda_{ab}^{-2}(T)/\lambda_{ab}^{-2}(0)$ as obtained from fits to (4) is shown for the three single crystals (A, B, C). It is well described by the power law

$$\lambda_{ab}^{-2}(T)/\lambda_{ab}^{-2}(0) = 1 - (T/T_c)^n \quad (5)$$

with $n = 4.2(3)$, which is close to $n = 4$ characteristic for a superconductor in the very strong coupling limit [25]. The zero temperature value of $\lambda_{ab}(0) \approx 250(50)$ nm obtained for all samples is in reasonable agreement with other values reported [12, 26–28].

It is evident from Fig. 4 that two distinct anisotropies, γ_λ and γ_H, describe the torque data consistently. Equation (4) was originally proposed for the two-band superconductor MgB_2. Indeed the experimental situations in both materials are quite similar. MgB_2 shows two distinct anisotropies: γ_λ decreases with decreasing temperature from about 2 to 1.1, whereas γ_H increases from about 2 at T_c to values of up to 6 at low temperatures [8–10]. For the oxypnictide superconductors investigated here, a similar situation appears to be present, but with reversed signs of the slopes of $\gamma_\lambda(T)$ and $\gamma_H(T)$. In MgB_2 the existence of two distinct bands of different dimensionality, and with strong interband and intraband scattering, was suggested to be responsible for the high T_c's [9, 29].

In conclusion, we found strong evidence that two distinct anisotropies, γ_λ and γ_H, are involved in the superconductivity of the oxypnictide superconductors. Torque magnetometry in low magnetic fields is very sensitive to γ_λ which exhibits a pronounced increase with decreasing temperature. This is in contrast to the behavior of γ_H which, according to recent resistivity measurements, decreases with decreasing temperature [20]. Close to T_c both anisotropies have very similar values of $\gamma_\lambda(T_c) \approx \gamma_H(T_c) \approx 7$, whereas at low temperatures the magnetic penetration depth anisotropy $\gamma_\lambda(0) \approx 19$ and the upper critical field anisotropy $\gamma_H(0) \approx 2$. This behavior is similar to the situation in the two-band superconductor MgB_2 where the temperature dependencies of the two anisotropies are well understood [9, 10, 29]. This result strongly suggests multi-band superconductivity in the novel class of oxypnictide superconductors, as already suggested in previous investigations [12, 17, 24, 28].

Acknowledgements The authors are grateful to B. Graneli for the help to prepare the manuscript. This work was supported by the Swiss National Science Foundation and in part by the NCCR program MaNEP, the Polish Ministry of Science and Higher Education, within the research project for the years 2007–2009 (No. N N202 4132 33), and the EU Project CoMePhS.

References

1. Kamihara, Y., Watanabe, T., Hirano, M., Hosono, H.: J. Am. Chem. Soc. **130**, 3296 (2008)
2. Chen, X.H., Wu, T., Wu, G., Liu, R.H., Chen, H., Fang, D.F.: Nature **453**, 761 (2008)
3. Chen, G.F., et al.: Phys. Rev. Lett. **100**, 247002 (2008)
4. Ren, Z.-A., et al.: Europhys. Lett. **82**, 57002 (2008)
5. Ren, Z.-A., et al.: Mat. Res. Inn. **12**, 106 (2008)
6. Cheng, P., et al.: Sci. China G **51**, 719 (2008)
7. Ren, Z.-A., et al.: Chin. Phys. Lett. **25**, 2215 (2008)
8. Angst, M., et al.: Phys. Rev. Lett. **88**, 167004 (2002)
9. Angst, M., Puzniak, R.: In: Martines, B.P. (ed.) Focus on Superconductivity, vol. 1, pp. 1–49. Nova Science, New York (2004). arXiv:cond-mat/0305048v1
10. Fletcher, J.D., Carrington, A., Taylor, O.J., Kazakov, S.M., Karpinski, J.: Phys. Rev. Lett. **95**, 097005 (2005)
11. Kogan, V.G.: Phys. Rev. B **24**, 1572 (1981)
12. Weyeneth, S., et al.: J. Supercond. Nov. Magn. (2008). doi:10.1007/s10948-008-0413-1
13. Dubroka, A., et al.: Phys. Rev. Lett. **101**, 097011 (2008)
14. Martin, C., et al.: arXiv:cond-mat/0807.0876v1
15. Jia, Y., et al.: Supercond. Sci. Technol. **21**, 105018 (2008)
16. Welp, U., et al.: Phys. Rev. B **78**, 140510 (2008)
17. Balicas, L., et al.: arXiv:cond-mat/0809.4223v2
18. Kubota, D., et al.: arXiv:cond-mat/0810.5623v1
19. Okazaki, R., et al.: arXiv:cond-mat/0809.4223v2, accepted for publication in Phys. Rev. B
20. Jaroszynski, J., et al.: Phys. Rev. B **78**, 174523 (2008)
21. Kogan, V.G.: Phys. Rev. Lett. **89**, 237005 (2002)
22. Zhigadlo, N.D., Katrych, S., Bukowski, Z., Weyeneth, S., Puzniak, R., Karpinski, J.: J. Phys.: Condens. Matter **20**, 342202 (2008)
23. Werthamer, N.R., Helfand, E., Hohenberg, P.C.: Phys. Rev. **147**, 295 (1966)
24. Hunte, F., et al.: Nature **453**, 903 (2008)
25. Rammer, J.: Europhys. Lett. **5**, 77 (1988)
26. Luetkens, H., et al.: Phys. Rev. Lett. **101**, 097009 (2008)
27. Khasanov, R., et al.: Phys. Rev. B **78**, 092506 (2008)
28. Malone, L., et al.: arXiv:cond-mat/0806.3908v1
29. Bussmann-Holder, A., Micnas, R., Bishop, A.R.: Eur. Phys. J. B **37**, 345 (2004)

4.5.4 Publication VII: Superconductivity at 23 K and low anisotropy in Rb-substituted $BaFe_2As_2$ single crystals

Z. Bukowski, S. Weyeneth, R. Puzniak, P. Moll, S. Katrych, N. D. Zhigadlo, J. Karpinski, H. Keller, and B. Batlogg
Phys. Rev. B **79**, 104521 (2009).

Abstract
Single crystals of $Ba_{1-x}Rb_xFe_2As_2$ with $x = 0.05 - 0.1$ have been grown from Sn flux and are bulk superconductors with T_c up to 23 K. The crystal structure was determined by x-ray diffraction analysis, and Sn is found to be incorporated for $\sim 9\%$ Ba, shifted by ~ 1.1 Å away from the Ba site toward the (Fe_2As_2) layers. The upper critical field deduced from resistance measurements is anisotropic with slopes of 7.1(3) T/K ($H||ab$-plane) and 4.2(2) T/K ($H||c$-axis), sufficiently far below T_c. The extracted upper critical field anisotropy $\gamma_H \sim 3$ close to T_c is in good agreement with the estimate from magnetic torque measurements. This indicates that the electronic properties in the doped $BaFe_2As_2$ compound are significantly more isotropic than those in the $L1111$ family. The in-plane critical current density at 5 K exceeds 10^6 A/cm^2, making $Ba_{1-x}Rb_xFe_2As_2$ a promising candidate for technical applications.

DOI: 10.1103/PhysRevB.79.104521
PACS numbers: 74.70.Dd, 74.25.Op, 61.05.cp

PHYSICAL REVIEW B **79**, 104521 (2009)

Superconductivity at 23 K and low anisotropy in Rb-substituted $BaFe_2As_2$ single crystals

Z. Bukowski*
Laboratory for Solid State Physics, ETH Zurich, CH-8093 Zurich, Switzerland

S. Weyeneth
Physik-Institut der Universität Zürich, Winterthurerstrasse 190, CH-8057 Zürich, Switzerland

R. Puzniak
Institute of Physics, Polish Academy of Sciences, Aleja Lotników 32/46, PL-02-668 Warsaw, Poland

P. Moll, S. Katrych, N. D. Zhigadlo, and J. Karpinski
Laboratory for Solid State Physics, ETH Zurich, CH-8093 Zurich, Switzerland

H. Keller
Physik-Institut der Universität Zürich, Winterthurerstrasse 190, CH-8057 Zürich, Switzerland

B. Batlogg
Laboratory for Solid State Physics, ETH Zurich, CH-8093 Zurich, Switzerland

(Received 12 December 2008; revised manuscript received 20 February 2009; published 30 March 2009)

Single crystals of $Ba_{1-x}Rb_xFe_2As_2$ with $x=0.05-0.1$ have been grown from Sn flux and are bulk superconductors with T_c up to 23 K. The crystal structure was determined by x-ray diffraction analysis, and Sn is found to be incorporated for ~9% Ba, shifted by ~1.1 Å away from the Ba site toward the (Fe_2As_2) layers. The upper critical field deduced from resistance measurements is anisotropic with slopes of 7.1(3) T/K ($H\|ab$ plane) and 4.2(2) T/K ($H\|c$ axis), sufficiently far below T_c. The extracted upper critical field anisotropy γ_H ~3 close to T_c is in good agreement with the estimate from magnetic torque measurements. This indicates that the electronic properties in the doped $BaFe_2As_2$ compound are significantly more isotropic than those in the *Ln*FeAsO family. The in-plane critical current density at 5 K exceeds 1×10^6 A/cm^2, making $Ba_{1-x}Rb_xFe_2As_2$ a promising candidate for technical applications.

DOI: 10.1103/PhysRevB.79.104521 PACS number(s): 74.70.Dd, 74.25.Op, 61.05.cp

I. INTRODUCTION

The report on superconductivity at 5 K in LaFePO with the ZrCuSiAs-type structure by Kamihara *et al.*[1] was almost overlooked for two years until the discovery of superconductivity at $T_c\simeq26$ K in F-substituted LaFeAsO.[2] This finding initiated an intensive search for new FeAs-based superconductors, and in the few following months superconductivity has been discovered in a number of analogs, primarily by substituting other rare-earth ions for La, yielding its current maximum $T_c\simeq55$ K for $SmFeAsO_{1-x}F_x$.[3] The crystal structure of *Ln*FeAsO (abbreviated as 1111) consists of (Fe_2As_2) layers sandwiched by (Ln_2O_2) layers, where *Ln* denotes any lanthanide element. The parent compound *Ln*FeAsO is antiferromagnetic, but may become superconducting upon electron doping by either partially replacing oxygen by fluorine, by generating oxygen deficiency, or by applying pressure.[4] Superconductivity can be also induced in *Ln*FeAsO through electron doping [partially replacing *Ln* by Th (Ref. 5)] or hole doping [partially replacing *Ln* by Sr (Ref. 6)].

More recently, the discovery of superconductivity at 38 K in $Ba_{1-x}K_xFe_2As_2$ with the $ThCr_2Si_2$-type structure has been reported.[7] The AFe_2As_2 (A=Ca, Sr, Ba) compounds (called 122) have a more simple crystal structure in which (Fe_2As_2) layers, identical to those in *Ln*FeAsO, are separated by single elemental *A* layers. Thus, a new class of superconductors was established by the subsequent reports on superconductivity in isostructural hole-doped $Sr_{1-x}K_xFe_2As_2$ and $Sr_{1-x}Cs_xFe_2As_2$,[8] $Ca_{1-x}Na_xFe_2As_2$,[9] $Eu_{1-x}K_xFe_2As_2$, and $Eu_{1-x}Na_xFe_2As_2$,[10,11] and in electron-doped Co-substituted $BaFe_2As_2$ and $SrFe_2As_2$,[12,13] and Ni-substituted $BaFe_2As_2$.[14] Furthermore, pressure-induced superconductivity has been discovered in the parent compounds $CaFe_2As_2$,[15,16] $SrFe_2As_2$,[17,18] and $BaFe_2As_2$.[18]

Besides KFe_2As_2 and $CsFe_2As_2$, which are superconductors with T_c's of 3.8 and 2.6 K,[8] respectively, $RbFe_2As_2$ is known to exist as well.[19] Therefore, it seemed natural to us using Rb as a chemical substitute in order to extend the number of elements which can effectively induce superconductivity in AFe_2As_2 compounds. In this paper, we report on the superconductivity induced in $BaFe_2As_2$ by partial substitution of Rb for Ba, and present its basic superconducting properties, including estimates of the electronic anisotropy.

II. EXPERIMENTAL DETAILS

Single crystals of Rb-substituted $BaFe_2As_2$ [(Ba,Rb)122] were grown using a Sn flux method similar to that described by Ni *et al.*[20] The Fe:Sn ratio (1:24) in a starting composition was kept constant in all runs while the Rb:Ba ratio was varied between 0.7 and 2.0. The appropriate amounts of Ba, Rb, Fe_2As, As, and Sn were placed in alumina crucibles and sealed in silica tubes under 1/3 atmosphere of Ar gas. Next,

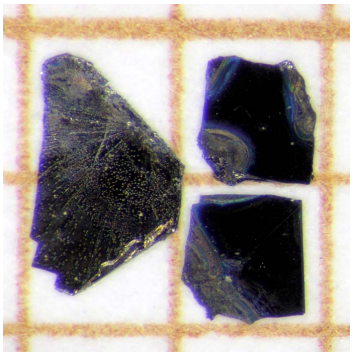

FIG. 1. (Color online) Photograph of three single crystals of $Ba_{0.84}Rb_{0.10}Sn_{0.09}Fe_2As_{1.96}$ on a millimeter grid.

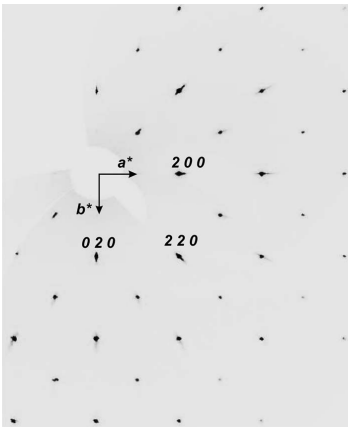

FIG. 2. The *hk*0 reciprocal space section determined by XRD of the single crystal $Ba_{0.84}Rb_{0.10}Sn_{0.09}Fe_2As_{1.96}$.

the ampoules were heated at 850 °C for 3 h until all components were completely melted, and cooled to 500 °C in 50 h. At this temperature the ampoule was turned upside down inside a furnace and liquid Sn was decanted from the crystals. The remaining thin film of Sn at the crystal surfaces was subsequently dissolved at room temperature by soaking crystals for a few days in liquid Hg. Finally, the crystals were heated for one hour at 190 °C in vacuum to evaporate the remaining traces of Hg. No signs of superconducting Hg are seen in the magnetic measurements.

The phase purity was checked on crushed crystals by means of powder x-ray diffraction (XRD) measurements carried out on a STOE diffractometer using Cu $K\alpha$ radiation and a graphite monochromator.

Single-crystal x-ray diffraction data were collected on a four-circle diffractometer equipped with a charge-coupled device (CCD) detector (Oxford Diffraction Ltd, Mo $K\alpha$, 60 mm sample to detector distance). Data reduction and analytical absorption correction were applied using the CRYSALIS RED software package.[21] The crystal structure was refined on F^2 employing the SHELXL program.[22] The starting model for the refinement was taken from Ref. 23. The elemental analysis of the crystals was performed by means of energy dispersive x-ray (EDX) spectrometry.

Magnetic measurements were performed in a Quantum Design Magnetic Property Measurement System (MPMS XL) with the Reciprocating Sample Option (RSO) installed. Transport measurements were performed in a 14 Tesla Quantum Design Physical Property Measurement System (PPMS). Magnetic torque measurements were carried out by using a highly sensitive miniaturized piezoresistive torque sensor within a home-made experimental setup described elsewhere.[24,25]

III. RESULTS AND DISCUSSION

The single crystals of $Ba_{1-x}Rb_xFe_2As_2$ grow in a platelike shape with typical dimensions $(1-3)\times(1-2)\times(0.05-0.1)$ mm^3 (see Fig. 1). Depending on the starting composition, the crystals displayed a broad variety of properties from nonsuperconducting to superconducting with rather sharp transitions to the superconducting state. For further studies we chose single crystals grown from the starting composition $Ba_{0.6}Rb_{0.8}Fe_2As_2$. The composition of the crystals from this batch determined by EDX analysis (16.79 at. % Ba, 1.94 at. % Rb, 1.74 at. % Sn, 40.19 at. % Fe, and 39.33 at. % As) leads to the chemical formula $Ba_{0.84}Rb_{0.10}Sn_{0.09}Fe_2As_{1.96}$. Crystals from the selected batch exhibit a T_c around 23 K but compared to the crystals with higher T_c their superconducting transition is relatively sharp, suggesting superior quality.

A. Crystal structure

The crystals studied by XRD are of good quality, and no additional phases (impurities, twins, or intergrowing crystals) were detected by examining the reconstructed reciprocal space sections (see Fig. 2). The average mosaic spread of 1.45° was estimated using the XCALIBUR, CRYSALIS Software System by analyzing all frames.[21]

We assumed that Rb atoms substitute for Ba atoms and the Rb/Ba occupations have been refined simultaneously. The content of these elements was found to be 1.0 at. % Rb and 17.8 at. % Ba, in acceptable agreement with the EDX analysis (1.9 at. % Rb and 16.8 at. % Ba).

It has been reported that the $BaFe_2As_2$ crystals grown from a Sn flux have approximately 1 at. % of Sn incorporated into the structure with the Sn atoms most likely located on the As sites.[20] However, our structure refinement reveals a somewhat different picture. After several cycles of refinement the Fourier difference map shows two pronounced maxima of the electron density away from the Ba/Rb site. We located the Sn atoms on these sites, shifted toward the (Fe_2As_2) layers (Fig. 3). This interpretation is supported by the considerable reduction in the R factor from 5.41% to 3.89% when Sn atoms are allowed to occupy these "off-center" sites. The resulting distances to the As site reflect

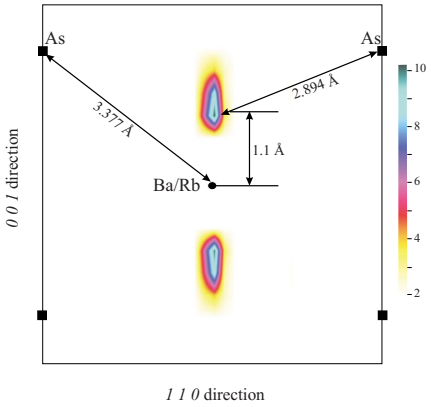

FIG. 3. (Color online) 110 section of the F_0-F_c difference Fourier map. The enhanced electron density reveals the location of Sn atoms, shifted by 1.1 Å toward the (Fe_2As_2) layers. The black dot shows the Ba/Rb position and black squares mark the As positions.

very well the size difference between Ba and Sn, considering the covalent radius.

We assumed the overall occupation of Ba, Rb, and Sn to be 100%. The Sn occupation was also refined and found to be ~6% of the Ba/Rb/Sn sites. The Sn content of 1.2 ± 0.3 at. % agrees with the EDX data (1.7 at. %). The results of structure refinement are presented in the Tables I and II. The resulting structure is shown in Fig. 4. Compared to unsubstituted $BaFe_2As_2$ the lattice parameter a is slightly shorter, the c parameter is longer, and the volume of the unit cell is smaller too.[23] A similar tendency has been observed for other 122 compounds, when Ba or Sr is replaced by K.[8,26,27] The increase in the c parameter in the studied crystals $Ba_{0.84}Rb_{0.10}Sn_{0.09}Fe_2As_{1.96}$ is caused mainly by substitution of Ba^{2+} ions ($r=1.42$ Å) by larger Rb^+ ions ($r=1.61$ Å).[28] The relatively marked shortening of the a parameter (larger than expected from Vegard's law) seems to be caused by Sn incorporation.

B. Critical current density and irreversibility line

A platelike single crystal from the same batch and therefore identical lattice parameters with approximate dimensions of $125\times125\times10$ μm^3 was chosen for dc magnetization and for magnetic torque studies. In Fig. 5 we show the susceptibility measured in a magnetic field of 1 mT parallel to the crystallographic c axis, showing a narrow transition with an effective transition temperature around 22 K and with an onset to superconductivity at 22.6 K.

The low-temperature signal recorded in the zero-field-cooled mode corresponds to a full diamagnetic response. The observed extremely small magnetic moment in the field-cooled mode is due to the pronounced magnetic irreversibility, possibly due to the local lattice distortions caused by the substitution with relatively big Rb ions, introducing effective pinning centers.

TABLE I. Crystal data and structure refinement for Rb and Sn substituted $BaFe_2As_2$.

Crystallographic formula (XRD)	$Ba_{0.89}Rb_{0.05}Sn_{0.06}Fe_2As_2$
Temperature (K)	295(2)
Wavelength (Å)	0.71073/Mo $K\alpha$
Crystal system, space group, Z	Tetragonal, $I4/mmm$, 2
Unit cell dimensions (Å)	$a=3.9250(2)$, $c=13.2096(5)$
Volume (Å^3)	203.502(3)
Calculated density (g/cm^3)	6.449
Absorption correction type	Analytical
Absorption coefficient (mm^{-1})	32.413
$F(000)$	345
Crystal size (μm^3)	$117\times77\times18$
θ range for data collection	5.42°–42.81°
Index ranges	$-6\le h\le7$, $-7\le k\le6$, $-26\le l\le7$
Reflections collected/unique	1626/291 $R_{int}=0.0458$
Completeness to 2θ	96.4%
Refinement method	Full-matrix least squares on F^2
Data/restraints/parameters	291/0/13
Goodness of fit on F^2	1.052
Final R indices [$I>2\sigma(I)$]	$R_1=0.0389$, $wR_2=0.1106$
R indices (all data)	$R_1=0.0414$, $wR_2=0.1122$
$\Delta\rho_{max}$ and $\Delta\rho_{min}$ (e/Å^3)	5.848 and −3.457
Bond lengths (Å)	
Ba/Rb-As	$3.3774(3)\times8$
Fe-As	$2.3979(3)\times4$
Fe-Fe	$2.7754(1)\times4$
As-Sn	$2.894(3)\times4$
Fe-Sn	$2.945(7)\times4$
Bond angles (deg)	
As-Fe-As	109.86(2)
	109.28(1)

A relatively strong pinning was confirmed in magnetic hysteresis loop measurements [see Figs. 6(a), 6(b), and 7] and by magnetic torque, as discussed later. The critical current density at 2, 5, and 10 K, estimated from the field dependence of the magnetic moment using Bean's model,[29,30] reaches values of the order of 10^6 A/cm^2 [see Fig. 6(b)], which is very promising for applications. Similar values for the critical current were reported for $BaFe_2As_2$ substituted with K.[31] The slight increase in the critical current density with increasing field in Fig. 6(b) is most likely due to the peak effect, which results in an effective increase in the irreversibility in the $M(H)$ curves [see Fig. 6(a)]. Numerous explanations have been proposed, relying the effect to an increase in the microscopic pinning force, matching effects, field-induced granularity or pinning site activation, crossover of pinning regimes, or a phase transition in vortex matter. All models include a field-dependent flux-creep rate and a critical current density that decreases monotonically with increasing magnetic field.[32]

TABLE II. Atomic coordinates, occupancy factors, and equivalent isotropic and anisotropic displacement parameters [$Å^2 \times 10^3$] for Rb- and Sn-substituted $BaFe_2As_2$. U_{iso} is defined as one third of the trace of the orthogonalized U_{ij} tensor. The anisotropic displacement factor exponent takes the form: $-2\pi^2 \cdot (h^2a^2 \cdot U_{11} + \cdots + 2hkab \cdot U_{12})$. For symmetry reasons $U_{23}=U_{13}=U_{12}=0$.

Atom	Site	x	y	z	Occupancy	U_{iso}	$U_{11}=U_{22}$	U_{33}
Ba(Rb)	2*a*	0	0	0	0.89(0.05)	17(1)	17(1)	17(1)
Sn	4*e*	0	0	0.0837(7)	0.06	10(3)	13(4)	5(3)
As	4*e*	0	0	0.3543(1)	1	12(1)	11(1)	15(1)
Fe	4*d*	0.5	0	0.25	1	12(1)	9(1)	17(1)

From temperature-dependent magnetization measurements at various magnetic fields we deduced the irreversibility line $H_{irr}(T)$ by following the temperatures for which the zero-field-cooled and field-cooled branches merge. The results are plotted in Fig. 7, where the upper inset to the figure illustrates the derivation in a magnetic field of 0.75 T. The irreversibility line is located in relatively high magnetic fields. A similar behavior has been reported for K-substituted $BaFe_2As_2$.[31]

The irreversibility line for $Ba_{0.84}Rb_{0.10}Sn_{0.09}Fe_2As_{1.96}$ is very well described by a power-law temperature dependence according to $(1-T/T_c)^n$ with fitted parameters $T_c = 22.6(2)$ K and $n=1.47(5)$ [see the straight line in the log-log H_{irr} vs $(1-T/T_c)$ dependence in Fig. 8]. The value of $n=1.47(5)$ is very close to $n=3/2$, typical for high-T_c superconductors characterized by an unusually small coherence length and an exceptionally high thermal activation at high temperatures.[33] A comparison of the irreversibility lines is presented in Fig. 8: single crystal of $Ba_{0.84}Rb_{0.10}Sn_{0.09}Fe_2As_{1.96}$, high-$T_c$ $YBa_2Cu_3O_{7-\delta}$,[34] $La_{1.86}Sr_{0.14}CuO_4$,[35] $Bi_2Sr_2CaCu_2O_{8+\delta}$ single crystals,[36] and $HgBa_2Ca_2Cu_3O_{8+\delta}$ single crystal with strong pinning centers intentionally introduced by neutron irradiation.[37] The irreversibility line for $Ba_{0.84}Rb_{0.10}Sn_{0.09}Fe_2As_{1.96}$ is located in significantly higher magnetic fields and temperatures than those of $La_{1.86}Sr_{0.14}CuO_4$, $Bi_2Sr_2CaCu_2O_{8+\delta}$, and $HgBa_2Ca_2Cu_3O_{8+\delta}$. Its position in the reduced temperature phase diagram is comparable only with that one for $YBa_2Cu_3O_{7-\delta}$, i.e., with the position of the irreversibility line for the high-T_c superconductor characterized by the lowest anisotropy value among the compounds compared here ($\gamma \sim 6$). Furthermore, the power-law exponents describing the irreversibility lines for both $Ba_{0.84}Rb_{0.10}Sn_{0.09}Fe_2As_{1.96}$ and $YBa_2Cu_3O_{7-\delta}$ are essentially identical (see the parallel lines in Fig. 8).

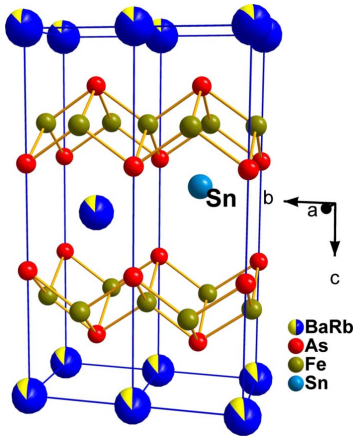

FIG. 4. (Color online) Schematic illustration of two unit cells of Rb and Sn substituted $BaFe_2As_2$. The possible Sn location is shown, for clarity, on one site only.

C. Upper critical field and superconducting state anisotropy

The electronic anisotropy is a determining factor for the behavior of a superconductor in an applied magnetic field, and thus is also of importance when possible applications are considered. We have estimated the anisotropy from the shift of the resistive transition as well as from magnetic torque measurements, leading to consistent results.

The resistance has been measured with the magnetic field applied parallel to the (Fe_2As_2) layers ($H \| ab$, $I \| H$) and perpendicular to them ($H \| c$, $I \| ab$). Examples of $\rho(T,H)$ are shown in Fig. 9. Particularly notable is the well-defined shift of the resistance drop with increasing field, without a significant broadening due to flux flow dissipation. In several of the larger crystals used for resistance measurements, the resistance drop proceeds in two or three steps, indicative of the presence of two or more distinct parts of the crystal with distinct transition temperatures. Yet, each of the steps can be

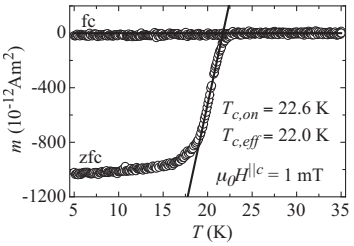

FIG. 5. Temperature dependence (field-cooled and zero-field-cooled) of the magnetic moment in a magnetic field of 1 mT applied parallel to the c axis on the $Ba_{0.84}Rb_{0.10}Sn_{0.09}Fe_2As_{1.96}$ crystal with a volume of about 1.56×10^{-13} m^3.

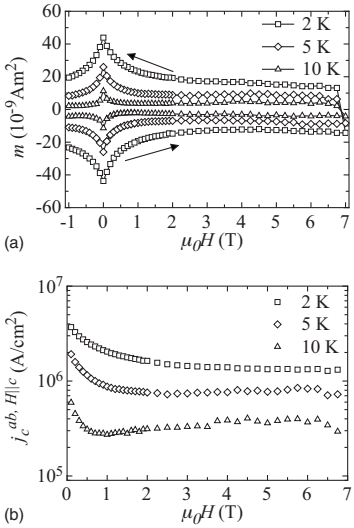

FIG. 6. (a) Magnetic hysteresis loops measured at 2, 5, and 10 K in a field up to 7 T parallel to the c axis on the $Ba_{0.84}Rb_{0.10}Sn_{0.09}Fe_2As_{1.96}$ crystal with a volume of about 1.56×10^{-13} m^3 and with dimensions of 125×125 μm^2 in the plane perpendicular to the applied magnetic field. (b) The critical current density calculated from the hysteresis loops.

followed as a function of field yielding very similar and consistent slopes of the upper critical field.

As the resistive transitions are not markedly broadened, we define $T_c(H)$ as the temperature where the resistance has decreased to 50% (see Fig. 10). For $H\|ab$ the upper critical field $H_{c2}^{\|ab}$ increases with a slope of 7.1(3) T/K with a clearly visible rounding near T_c, whereas $H_{c2}^{\|c}$ increases with a slope of 4.2(2) T/K again exhibiting an upturn near T_c where thermal phase fluctuations are expected to influence its determination. The upper critical slope $\mu_0 dH_{c2}^{\|c}/dT$ is considerably higher than in $YBa_2Cu_3O_{7-\delta}$ (1.9 T/K),[38] in

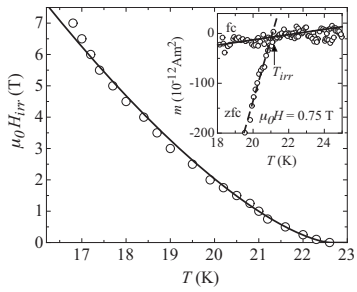

FIG. 7. Temperature dependence of the irreversibility field H_{irr} for $Ba_{0.84}Rb_{0.10}Sn_{0.09}Fe_2As_{1.96}$ for $H\|c$. The inset illustrates how the quantity was determined. The irreversibility line is approximated very well by a power-law temperature dependence with an exponent 3/2 (solid line), as discussed in the text.

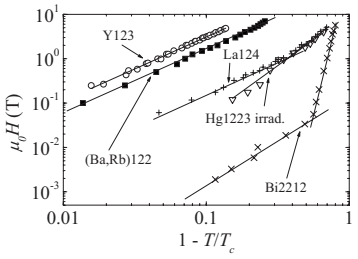

FIG. 8. Comparison of the irreversibility line for the $Ba_{0.84}Rb_{0.10}Sn_{0.09}Fe_2As_{1.96}$ single crystal for $H\|c$ axis [(Ba,Rb)122] with those for $YBa_2Cu_3O_{7-\delta}$ [Y123] (Ref. 34), $La_{1.86}Sr_{0.14}CuO_4$ [La214] (Ref. 35), $Bi_2Sr_2CaCu_2O_{8+\delta}$ single crystals [Bi2212] (Ref. 36) and with $HgBa_2Ca_2Cu_3O_{8+\delta}$ single crystal with strong pinning centers intentionally introduced by neutron irradiation [Hg1223 irrad.] (Ref. 37). The solid lines are fits to a power-law dependence as explained in the text.

$HgBa_2Ca_2Cu_3O_{8+\delta}$ (2 T/K),[39] in unsubstituted MgB_2 (0.12 T/K),[40] and in $LaFeAsO_{0.89}F_{0.11}$ (2 T/K).[41] This steep slope also points to a very high $H_{c2}^{\|c}(T=0)$. The upper critical field anisotropy in the vicinity of T_c, defined as $\gamma_H = H_{c2}^{\|ab}/H_{c2}^{\|c}$ (inset to the Fig. 10), decreases with decreasing temperature, a similar trend as observed in the 1111 pnictides.[42] This suggests similar temperature dependences of the anisotropic parameters among different classes of pnictides.[43] However, it should be noted that the values for the upper critical field anisotropy are significantly smaller in the 122 class

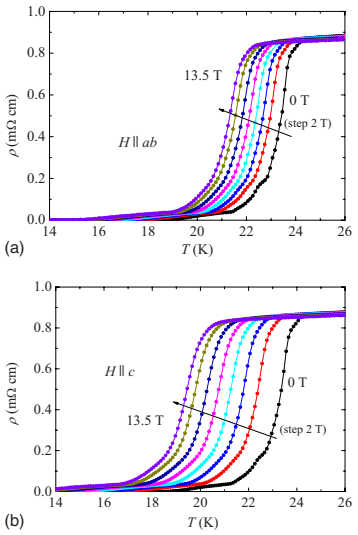

FIG. 9. (Color online) Examples of $\rho(T,H)$ dependences measured on the $Ba_{0.84}Rb_{0.10}Sn_{0.09}Fe_2As_{1.96}$ crystal with the field applied parallel to the (Fe_2As_2) layers ($H\|ab$) (a) and perpendicular to them ($H\|c$) (b) in magnetic fields of 0, 2, 4, 6, 8, 10, 12, and 13.5 T. The solid lines are guides to the eye.

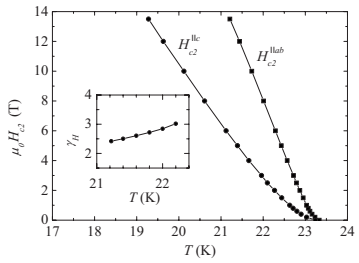

FIG. 10. Temperature dependence of the upper critical field with $H\|ab$ and with $H\|c$ for $Ba_{0.84}Rb_{0.10}Sn_{0.09}Fe_2As_{1.96}$. The solid lines are guides to the eye. Inset: The upper critical field anisotropy $\gamma_H = H_{c2}^{\|ab}/H_{c2}^{\|c}$ in the vicinity of T_c.

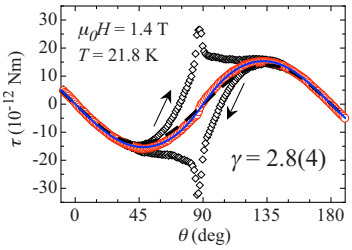

FIG. 11. (Color online) Angular dependence of the raw (black open diamonds) and the reversible (open circles) torque of the $Ba_{0.84}Rb_{0.10}Sn_{0.09}Fe_2As_{1.96}$ single crystal in the superconducting state at $T=21.8$ K and in $\mu_0 H=1.4$ T. The solid line is given by the Kogan model [Eq. (1)] with the parameters fitted to the reversible torque data (open circles). A very big background component contributes a pronounced signal to the torque and is shown by dashed line.

(~2.5–3) than in the 1111 group of superconductors (~5–6), with a T_c of ~45 K.[42]

A very important difference between the behavior of the 122 and 1111 iron-pnictide superconductors should be pointed out. While (Ba,Rb)122 shows a sharp transition and a clear onset of superconductivity, there is no sharp transition for 1111 superconductors.[42] Therefore, $T_c(H)$ for 1111 superconductors is less clearly defined and the determination of $H_{c2}(T)$ and its anisotropy $\gamma_H(T)$ in the vicinity of T_c is criterion dependent. The results of high-field resistivity measurements by Jaroszynski *et al.*[42] indicate that the upper critical-field anisotropy becomes criterion independent for temperatures of about 10 K below T_c only, providing convincing evidence for the temperature-dependent anisotropy in 1111 superconductors for the limited temperature range of ~10–17 K below T_c. In contrast, the resistance drop at T_c in the (Ba,Rb)122 crystals remains essentially unaffected by high magnetic fields and, therefore, provides for a reliable determination of $H_{c2}(T)$. Accordingly, the upper critical field anisotropy $\gamma_H(T)$ is well defined too (see Figs. 9 and 10).

Estimating $H_{c2}(0)$ from extrapolations of the present data, covering a limited temperature range, is inappropriate not only due to the curvature of $H_{c2}(T)$, but more importantly because of the two-band nature of superconductivity. Nevertheless, if one would disregard these considerations, the simple Werthamer-Helfand-Hohenberg (WHH) extrapolation[44] would give values of $\mu_0 H_{c2}^{\|c}(0) \simeq 70(5)$ T and $\mu_0 H_{c2}^{\|ab}(0) \simeq 120(6)$ T.

Torque measurements were performed in the temperature range close to T_c, where the pronounced irreversibility leads to only minor distortions of the torque. For minimizing pinning effects, the mean (reversible) torque, $\tau_{rev} = [\tau(\theta^+) + \tau(\theta^-)]/2$ was calculated from measurements with counterclockwise and clockwise rotating of the magnetic field around the sample, as indicated by the black open diamonds in Fig. 11. Unfortunately, due to the small superconducting torque signal a big background component is contributing a pronounced additional signal to the torque. This sinusoidal component has been included by an additional sinusoidal function in the fitting model after Kogan *et al.*[45,46]

$$\tau(\theta) = -\frac{V\Phi_0 H}{16\pi\lambda_{ab}^2}\left(1-\frac{1}{\gamma^2}\right)\frac{\sin(2\theta)}{\epsilon(\theta)}\ln\left(\frac{\eta H_{c2}^{\|c}}{\epsilon(\theta)H}\right) + A\sin(2\theta), \quad (1)$$

where V is the volume of the crystal, Φ_0 is the elementary flux quantum, γ denotes the superconducting state anisotropy parameter, λ_{ab} is the in-plane component of the magnetic penetration depth, $H_{c2}^{\|c}$ is the upper critical field along the c axis of the crystal, η denotes a numerical parameter of the order of unity depending on the structure of the flux-line lattice, A is the amplitude of the background torque, and $\epsilon(\theta) = [\cos^2(\theta) + \gamma^{-2}\sin^2(\theta)]^{1/2}$.

The superconducting state anisotropy parameter γ fitted to the mean torque data is found to be 2.8(4) near T_c in very good agreement with the estimate of γ_H from resistivity measurements shown in Fig. 10. Due to the low anisotropy, the strong irreversibility, and the pronounced normal-state background, no temperature-dependent study of the anisotropy parameter was performed. It is highly gratifying to find excellent agreement among the two ways for estimating the electronic anisotropy in the vicinity of T_c, where independently of the predictions for the detailed electronic structure, all of the electronic anisotropies should coincide. Obviously, superconducting $Ba_{0.84}Rb_{0.10}Sn_{0.09}Fe_2As_{1.96}$ is much more isotropic than $SmFeAsO_{0.8}F_{0.2}$ and $NdFeAsO_{0.8}F_{0.2}$, where reliable anisotropy parameter values up to 20 can be derived.[25,43] The anisotropy parameter measured for $Ba_{0.84}Rb_{0.10}Sn_{0.09}Fe_2As_{1.96}$ is much smaller than those typical for high-T_c superconductors, but it is quite similar to those reported for $Ba_{1-x}K_xFe_2As_2$ and $Sr_{1-x}K_xFe_2As_2$.[20,47,48] The electronic coupling of the Fe_2As_2 layers through the intervening (Ba, Rb) layers is more effective than through the *Ln*O layers in the 1111 class of superconductors.

D. Effect of Sn incorporation

The effect of Sn incorporation on the properties of AFe_2As_2 has not been studied in detail. Single crystals of $BaFe_2As_2$ grown from Sn flux reveal the structural and mag-

netic phase transition at significantly lower temperature (85 K)[20] than Sn-free material (140 K) although the magnetic structure is virtually the same.[49] The electrical resistivity (below the tetragonal-orthorombic transition) for $BaFe_2As_2$ with 1% Sn increases upon decreasing temperature[20] while for pure $BaFe_2As_2$ crystals $\rho(T)$ is typical for metals.[50] It is worth noting that although Sn incorporation lowers the structural transition temperature in $BaFe_2As_2$, it does not lead to superconductivity. The effect of Sn incorporation in superconducting alkali-metal-substituted $BaFe_2As_2$ seems to be fully masked by the much stronger effect of the alkali metal doping.

IV. SUMMARY

Single crystals of $Ba_{1-x}Rb_xFe_2As_2$ ($x=0.05-0.1$) have been grown and their crystallographic and basic superconducting state properties were presented. This is the first example of superconductivity induced by Rb substitution in this family of materials. It was found that the irreversibility line is located in relatively high magnetic fields comparable to the one for $YBa_2Cu_3O_{7-\delta}$ only, i.e., for the high-T_c superconductor with the lowest anisotropy. The electronic anisotropy, derived consistently from resistance and from magnetic torque measurements, ranges from ~ 3 near T_c to lower values at lower temperatures, and indicates that $Ba_{1-x}Rb_xFe_2As_2$ is electronically much more isotropic than $SmFeAsO_{0.8}F_{0.2}$ and $NdFeAsO_{0.8}F_{0.2}$. The critical current density at 5 K exceeds 10^6 A/cm^2, which together with the high upper critical fields, is very promising for applications.

ACKNOWLEDGMENTS

We would like to thank P. Wägli for the EDX analysis. This work was supported by the Swiss National Science Foundation, by the NCCR program MaNEP, and partially by the Polish Ministry of Science and Higher Education within the research project for the years 2007–2009 (Grant No. N N202 4132 33).

*bukowski@phys.ethz.ch

[1] Y. Kamihara, H. Hiramatsu, M. Hirano, R. Kawamura, H. Yangi, T. Kamiya, and H. Hosono, J. Am. Chem. Soc. **128**, 10012 (2006).
[2] Y. Kamihara, T. Watanabe, M. Hirano, and H. Hosono, J. Am. Chem. Soc. **130**, 3296 (2008).
[3] Z.-A. Ren, W. Lu, J. Yang, W. Yi, X.-L. Shen, Z.-C. Li, G.-C. Che, X.-L. Dong, L.-L. Sun, F. Zhou, and Z.-X. Zhao, Chin. Phys. Lett. **25**, 2215 (2008).
[4] H. Okada, K. Igawa, H. Takahashi, Y. Kamihara, M. Hirano, H. Hosono, K. Matsubayashi, and Y. Uwatoko, J. Phys. Soc. Jpn. **77**, 113712 (2008).
[5] C. Wang, L. Li, S. Chi, Z. Zhu, Z. Ren, Y. Li, Y. Wang, X. Lin, Y. Luo, S. Jiang, X. Xu, G. Cao, and Z. Xu, EPL **83**, 67006 (2008).
[6] H.-H. Wen, G. Mu, L. Fang, H. Yang, and X. Zhu, EPL **82**, 17009 (2008).
[7] M. Rotter, M. Tegel, and D. Johrendt, Phys. Rev. Lett. **101**, 107006 (2008).
[8] K. Sasmal, B. Lv, B. Lorenz, A. M. Guloy, F. Chen, Y.-Y. Xue, and C.-W. Chu, Phys. Rev. Lett. **101**, 107007 (2008).
[9] G. Wu, H. Chen, T. Wu, Y. L. Xie, Y. J. Yan, R. H. Liu, X. F. Wang, J. J. Ying, and X. H. Chen, J. Phys.: Condens. Matter **20**, 422201 (2008).
[10] H. S. Jeevan, Z. Hossain, D. Kasinathan, H. Rosner, C. Geibel, and P. Gegenwart, Phys. Rev. B **78**, 092406 (2008).
[11] Y. Qi, Z. Gao, L. Wang, D. Wang, X. Zhang, and Y. Ma, New J. Phys. **10**, 123003 (2008).
[12] A. S. Sefat, R. Jin, M. A. McGuire, B. C. Sales, D. J. Singh, and D. Mandrus, Phys. Rev. Lett. **101**, 117004 (2008).
[13] A. Leithe-Jasper, W. Schnelle, C. Geibel, and H. Rosner, Phys. Rev. Lett. **101**, 207004 (2008).
[14] L. J. Li, Q. B. Wang, Y. K. Luo, H. Chen, Q. Tao, Y. K. Li, X. Lin, M. He, Z. W. Zhu, G. H. Cao, and Z. A. Xu, New J. Phys. **11**, 025008 (2009).
[15] T. Park, E. Park, H. Lee, T. Klimczuk, E. D. Bauer, F. Ronning, and J. D. Thompson, J. Phys.: Condens. Matter **20**, 322204 (2008).
[16] M. S. Torikachvili, S. L. Budko, N. Ni, and P. C. Canfield, Phys. Rev. Lett. **101**, 057006 (2008).
[17] K. Igawa, H. Okada, H. Takahashi, S. Matsuishi, Y. Kamihara, M. Hirano, H. Hosono, K. Matsubayashi, and Y. Uwatoko, J. Phys. Soc. Jpn. **78**, 025001 (2009).
[18] P. L. Alireza, Y. T. C. Ko, J. Gillett, C. M. Petrone, J. M. Cole, S. E. Sebastian, and G. G. Lonzarich, J. Phys.: Condens. Matter **21**, 012208 (2009).
[19] P. Wenz and H. U. Schuster, Z. Naturforsch. B **39**, 1816 (1984).
[20] N. Ni, S. L. Budko, A. Kreyssig, S. Nandi, G. E. Rustan, A. I. Goldman, S. Gupta, J. D. Corbett, A. Kracher, and P. C. Canfield, Phys. Rev. B **78**, 014507 (2008).
[21] Oxford Diffraction Ltd., XCALIBUR, CRYSALIS Software System, Version 1.171.32.15, 2008.
[22] G. Sheldrick, *SHELXL-97: Program for the Refinement of Crystal Structures* (University of Göttingen, Germany, 1997).
[23] M. Rotter, M. Tegel, D. Johrendt, I. Schellenberg, W. Hermes, and R. Pöttgen, Phys. Rev. B **78**, 020503(R) (2008).
[24] S. Kohout, J. Roos, and H. Keller, Rev. Sci. Instrum. **78**, 013903 (2007).
[25] S. Weyeneth, R. Puzniak, U. Mosele, N. D. Zhigadlo, S. Katrych, Z. Bukowski, J. Karpinski, S. Kohout, J. Roos, and H. Keller, J. Supercond. Novel Magn. **22**, 325 (2009).
[26] H. Chen, Y. Ren, Y. Qiu, W. Bao, R. H. Liu, G. Wu, T. Wu, Y. L. Xie, X. F. Wang, Q. Huang, and X. H. Chen, EPL **85**, 17006 (2009).
[27] M. Rotter, M. Pangerl, M. Tegel, and D. Johrendt, Angew. Chem. Int. Ed. **47**, 7949 (2008).
[28] R. D. Shannon, Acta Crystallogr., Sect. A: Cryst. Phys., Diff., Theor. Gen. Crystallogr. **32**, 751 (1976).
[29] C. P. Bean, Phys. Rev. Lett. **8**, 250 (1962).
[30] C. P. Bean, Rev. Mod. Phys. **36**, 31 (1964).

[31] H. Yang, H. Luo, Z. Wang, and H.-H. Wen, Appl. Phys. Lett. **93**, 142506 (2008).
[32] M. Werner, F. M. Sauerzopf, H. W. Weber, and A. Wisniewski, Phys. Rev. B **61**, 14795 (2000).
[33] Y. Yeshurun and A. P. Malozemoff, Phys. Rev. Lett. **60**, 2202 (1988).
[34] A. Schilling, H. R. Ott, and Th. Wolf, Phys. Rev. B **46**, 14253 (1992).
[35] A. Schilling, R. Jin, J. D. Guo, H. R. Ott, I. Tanaka, and H. Kojima, Physica B **194-196**, 1555 (1994).
[36] J. Ricketts, R. Puzniak, C.-J. Liu, G. D. Gu, N. Koshizuka, and H. Yamauchi, Appl. Phys. Lett. **65**, 3284 (1994).
[37] A. Wisniewski, R. Puzniak, J. Karpinski, J. Hofer, R. Szymczak, M. Baran, F. M. Sauerzopf, R. Molinski, E. M. Kopnin, and J. R. Thompson, Phys. Rev. B **61**, 791 (2000).
[38] U. Welp, W. K. Kwok, G. W. Crabtree, K. G. Vandervoort, and J. Z. Liu, Phys. Rev. Lett. **62**, 1908 (1989).
[39] A. Schilling, O. Jeandupeux, S. Büchi, H. R. Ott, and C. Rossel, Physica C **235-240**, 229 (1994).
[40] M. Angst, R. Puzniak, A. Wisniewski, J. Jun, S. M. Kazakov, J. Karpinski, J. Roos, and H. Keller, Phys. Rev. Lett. **88**, 167004 (2002).
[41] F. Hunte, J. Jaroszynski, A. Gurevich, D. C. Larbalestier, R. Jin, A. S. Sefat, M. A. McGuire, B. C. Sales, D. K. Christen, and D. Mandrus, Nature (London) **453**, 903 (2008).
[42] J. Jaroszynski, F. Hunte, L. Balicas, Y.-J. Jo, I. Raicevic, A. Gurevich, D. C. Larbalestier, F. F. Balakirev, L. Fang, P. Cheng, Y. Jia, and H.-H. Wen, Phys. Rev. B **78**, 174523 (2008).
[43] S. Weyeneth, R. Puzniak, N. D. Zhigadlo, S. Katrych, Z. Bukowski, J. Karpinski, and H. Keller, J. Supercond. Novel Magn. **22**, 347 (2009).
[44] N. R. Werthamer, E. Helfand, and P. C. Hohenberg, Phys. Rev. **147**, 295 (1966).
[45] V. G. Kogan, Phys. Rev. B **24**, 1572 (1981).
[46] V. G. Kogan, M. M. Fang, and S. Mitra, Phys. Rev. B **38**, 11958 (1988).
[47] H. Q. Yuan, J. Singleton, F. F. Balakirev, S. A. Baily, G. F. Chen, J. L. Luo, and N. L. Wang, Nature (London) **457**, 565 (2009).
[48] G. F. Chen, Z. Li, J. Dong, G. Li, W. Z. Hu, X. D. Zhang, X. H. Song, P. Zheng, N. L. Wang, and J. L. Luo, Phys. Rev. B **78**, 224512 (2008).
[49] Y. Su, P. Link, A. Schneidewind, Th. Wolf, P. Adelmann, Y. Xiao, M. Meven, R. Mittal, M. Rotter, D. Johrendt, Th. Brueckel, and M. Loewenhaupt, Phys. Rev. B **79**, 064504 (2009).
[50] X. F. Wang, T. Wu, G. Wu, H. Chen, Y. L. Xie, J. J. Ying, Y. J. Yan, R. H. Liu, and X. H. Chen, Phys. Rev. Lett. **102**, 117005 (2009).

4.5.5 Publication VIII: Single crystals of $LnFeAsO_{1-x}F_x$ (Ln = La, Pr, Nd, Sm, Gd) and $Ba_{1-x}Rb_xFe_2As_2$: Growth, structure and superconducting properties

J. Karpinski, N. D. Zhigadlo, S. Katrych, Z. Bukowski, P. Moll, S. Weyeneth, H. Keller, R. Puzniak, M. Tortello, D. Daghero, R. Gonnelli, I. Maggio-Aprile, Y. Fasano, Ø. Fischer, K. Rogacki, and B. Batlogg
Physica C **469**, 370 (2009).

Abstract
A review of our investigations on single crystals of $LnFeAsO_{1-x}F_x$ (Ln=La, Pr, Nd, Sm, Gd) and $Ba_{1-x}Rb_xFe_2As_2$ is presented. A high-pressure technique has been applied for the growth of $LnFeAsO_{1-x}F_x$ crystals, while $Ba_{1-x}Rb_xFe_2As_2$ crystals were grown using a quartz ampoule method. Single crystals were used for electrical transport, structure, magnetic torque and spectroscopic studies. Investigations of the crystal structure confirmed high structural perfection and show incomplete occupation of the (O, F) position in superconducting $LnFeAsO_{1-x}F_x$ crystals. Resistivity measurements on $LnFeAsO_{1-x}F_x$ crystals show a significant broadening of the transition in high magnetic fields, whereas the resistive transition in $Ba_{1-x}Rb_xFe_2As_2$ simply shifts to lower temperature. The critical current density for both compounds is relatively high and exceeds 2×10^9 A/m^2 at 15 K in 7 T. The anisotropy of magnetic penetration depth, measured on $LnFeAsO_{1-x}F_x$ crystals by torque magnetometry is temperature dependent and apparently larger than the anisotropy of the upper critical field. $Ba_{1-x}Rb_xFe_2As_2$ crystals are electronically significantly less anisotropic. Point-Contact Andreev-Reflection spectroscopy indicates the existence of two energy gaps in $LnFeAsO_{1-x}F_x$. Scanning Tunneling Spectroscopy reveals in addition to a superconducting gap, also some feature at high energy ($\sim$ 20 meV).

DOI: 10.1016/j.physc.2009.03.048
PACS numbers: 81.10.-h; 74.62.Bf; 74.70.Dd; 74.25.-q

The original publication is electronically available at:
http://dx.doi.org/10.1016/j.physc.2009.03.048

Open access repositories:
http://www.zora.uzh.ch/20073
http://arxiv.org/abs/0902.0224

At completion of this thesis, according to the Thomson Reuters ISI Web of Knowledge database, this article has been cited at least 30 time.

Physica C 469 (2009) 370–380

Contents lists available at ScienceDirect

Physica C

journal homepage: www.elsevier.com/locate/physc

Single crystals of $LnFeAsO_{1-x}F_x$ (Ln = La, Pr, Nd, Sm, Gd) and $Ba_{1-x}Rb_xFe_2As_2$: Growth, structure and superconducting properties

J. Karpinski [a,*], N.D. Zhigadlo [a], S. Katrych [a], Z. Bukowski [a], P. Moll [a], S. Weyeneth [b], H. Keller [b], R. Puzniak [c], M. Tortello [d], D. Daghero [d], R. Gonnelli [d], I. Maggio-Aprile [e], Y. Fasano [e,f], Ø. Fischer [e], K. Rogacki [g], B. Batlogg [a]

[a] Laboratory for Solid State Physics, ETH Zurich, 8093 Zurich, Switzerland
[b] Physik-Institut der Universität Zürich, 8057 Zürich, Switzerland
[c] Institute of Physics, Polish Academy of Sciences, Aleja Lotników 32/46, 02-668 Warsaw, Poland
[d] Dipartimento di Fisica, Politecnico di Torino, 10129 Torino, Italy
[e] DPMC-MaNEP, University of Geneva, Geneva, Switzerland
[f] Low Temperatures Laboratory and Instituto Balseiro, Bariloche, Argentina
[g] Institute of Low Temperature and Structure Research, Polish Academy of Sciences, 50-950 Wroclaw, P.O. Box 1410, Poland

ARTICLE INFO

Article history:
Available online 20 March 2009

PACS:
81.10.-h
74.62.Bf
74.70.Dd
74.25.-q

Keywords:
Crystal growth
Superconductivity
Anisotropy
Pnictides
High-pressure

ABSTRACT

A review of our investigations on single crystals of $LnFeAsO_{1-x}F_x$ (Ln = La, Pr, Nd, Sm, Gd) and $Ba_{1-x}Rb_xFe_2As_2$ is presented. A high-pressure technique has been applied for the growth of $LnFeAsO_{1-x}F_x$ crystals, while $Ba_{1-x}Rb_xFe_2As_2$ crystals were grown using a quartz ampoule method. Single crystals were used for electrical transport, structure, magnetic torque and spectroscopic studies. Investigations of the crystal structure confirmed high structural perfection and show incomplete occupation of the (O, F) position in superconducting $LnFeAsO_{1-x}F_x$ crystals. Resistivity measurements on $LnFeAsO_{1-x}F_x$ crystals show a significant broadening of the transition in high magnetic fields, whereas the resistive transition in $Ba_{1-x}Rb_xFe_2As_2$ simply shifts to lower temperature. The critical current density for both compounds is relatively high and exceeds 2×10^9 A/m^2 at 15 K in 7 T. The anisotropy of magnetic penetration depth, measured on $LnFeAsO_{1-x}F_x$ crystals by torque magnetometry is temperature dependent and apparently larger than the anisotropy of the upper critical field. $Ba_{1-x}Rb_xFe_2As_2$ crystals are electronically significantly less anisotropic. Point-Contact Andreev-Reflection spectroscopy indicates the existence of two energy gaps in $LnFeAsO_{1-x}F_x$. Scanning Tunneling Spectroscopy reveals in addition to a superconducting gap, also some feature at high energy (~20 meV).

1. Introduction

Since the first report on superconductivity at 26 K in F-doped LaFeAsO at the end of February 2008, the superconducting transition temperature has been quickly raised to about 55 K and several new superconductors of a general formula $LnFeAsO_{1-x}F_x$ (Ln = La, Ce, Pr, Nd, Sm, Gd, Tb, Dy), abbreviated as Ln1111, have been synthesized [1–8]. These compounds crystallize with the tetragonal layered ZrCuSiAs structure, in the space group *P*4/nmm. The structure consists of alternating LnO and FeAs layers, which are electrically charged represented as $(LnO)^{+\delta}(FeAs)^{-\delta}$ (Fig. 1). Covalent bonding is dominant in the layers, while ionic bonding dominates between layers. Electron carriers can be introduced by substituting F for O or by oxygen deficiency [1–8]. By substituting Sr^{2+} for La^{3+} in La1111, holes are introduced [9].

More recently, superconductivity in AFe_2As_2 (A = Ca, Sr, Ba) (called A122) with $ThCr_2Si_2$-type structure and maximum T_c = 38 K has been reported [10]. These compounds have a more simple crystal structure in which (Fe_2As_2)-layers, identical to those in Ln1111 are separated by single elemental A layers (Fig. 2). Up to date superconductivity has been found in hole-doped $Sr_{1-x}K_xFe_2As_2$ and $Sr_{1-x}Cs_xFe_2As_2$ [11], $Ca_{1-x}Na_xFe_2As_2$ [12], $Eu_{1-x}K_xFe_2As_2$ [13], and $Eu_{1-x}Na_xFe_2As_2$ [14], as well as in electron-doped Co-substituted $BaFe_2As_2$ [15] and $SrFe_2As_2$ [16], and Ni-substituted $BaFe_2As_2$ [17]. Furthermore, pressure induced superconductivity has been also discovered in the parent compounds $CaFe_2As_2$ [18,19], $SrFe_2As_2$ [20,21], and $BaFe_2As_2$ [21].

Besides KFe_2As_2 and $CsFe_2As_2$, which are superconductors with T_c's of 3.8 K and 2.6 K [11] respectively, $RbFe_2As_2$ is known to exist as well [22]. Therefore, it seemed natural to us to explore the $BaFe_2As_2$–$RbFe_2As_2$ system in order to search for superconductivity.

It is interesting to explore the important parameters which govern the superconducting properties of new superconductors. In the case of high-T_c cuprates it is the number of carriers doped into the

* Corresponding author.
E-mail address: karpinski@phys.ethz.ch (J. Karpinski).

0921-4534/$ - see front matter © 2009 Elsevier B.V. All rights reserved.
doi:10.1016/j.physc.2009.03.048

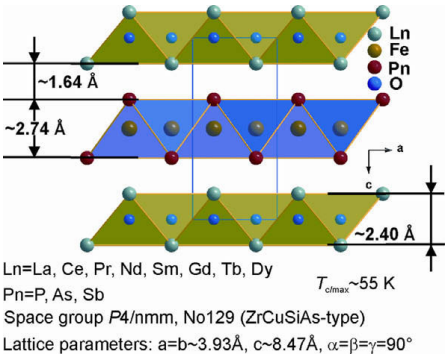

Fig. 1. Structure projection of Ln1111 along the *b* direction.

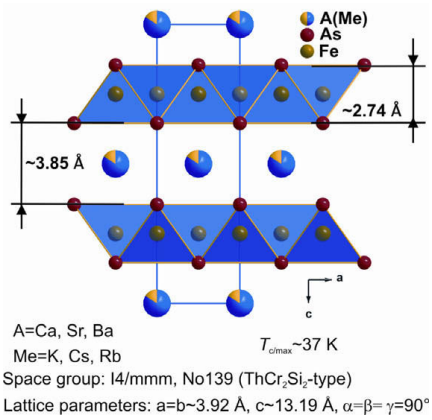

Fig. 2. Structure projection of A122 along the *b* direction.

CuO_2 layers. In analogy in the pnictides it is the number of carriers doped into the FeAs layers. There are some similarities between the new pnictide superconductors and the cuprate superconductors due to the layered structure and the fact that both Fe and Cu are 3*d*-elements. However, there are important differences. First, doping on the Fe site in Sr122 or Ba122 by substitution of Fe by Co leads also to the appearance of superconductivity [15,16] in contrast to cuprates, where substitution for Cu suppresses superconductivity. Second, in cuprates, introducing of one oxygen atom is equivalent to introducing of two fluorine atoms [23]. In Ln1111 there is a significant difference in carrier doping between oxygen deficiency and fluorine substitution. One expects that one oxygen atom deficiency provides two electrons while substitution of F^- for O^{2-} provides one electron. However, according to [24,25] oxygen deficiency is much less effective as a source of electrons than F-substitution. Structural parameters play also an important role for obtaining high T_c's. There is dependence between T_c and the As–Fe–As bond angle of the $FeAs_4$ tetrahedron: maximum T_c is achieved when As–Fe–As bond angle is close to 109.47° corresponding to an ideal tetrahedron [25].

Despite all these differences, the similarities due to the layered crystal structure are important as well. So far, all high-T_c superconductors have a layered crystal structure leading to pronounced anisotropic physical properties. All cuprate superconductors have been characterized by a well-defined effective mass anisotropy parameter γ [26]

$$\gamma = \sqrt{m_c^*/m_{ab}^*} = \lambda_c/\lambda_{ab} = \xi_{ab}/\xi_c = H_{c2}^{\parallel ab}/H_{c2}^{\parallel c}, \quad (1)$$

where m_i^* denote the effective mass, λ_i the magnetic penetration depth, ξ_i the coherence length and $H_{c2}^{\parallel i}$ the upper critical field in the magnetic field direction *i*. Nevertheless, the understanding of high-temperature superconductivity was challenged by the observation of two distinctly different and temperature dependent anisotropies in MgB_2 single crystals [27–29]:

$$\gamma_\lambda = \lambda_c/\lambda_{ab}, \quad (2)$$

$$\gamma_H = H_{c2}^{\parallel ab}/H_{c2}^{\parallel c}. \quad (3)$$

A straight forward interpretation based on a two-band model was quickly developed, which also lead to a further understanding of the temperature and field dependence of the anisotropy parameters in MgB_2, mirroring the complex inter- and intraband mechanism of the two superconducting gaps [30]. For having an overall comparison with the other high-temperature superconductors (e.g. cuprates and MgB_2) a detailed knowledge of γ in the oxypnictides is required. Various attempts were made to estimate anisotropy in the oxypnictide superconductors [31–42], leading to a wide range of results. Nevertheless, from both experimental and theoretical sides there is clear evidence that superconductivity in the pnictides involves more than one-band [31–33,43–48] and therefore it is expected that anisotropy is temperature dependent.

Not only the anisotropic properties are, obviously, best investigated on single crystals. Single crystals are also required for spectroscopic techniques such as Scanning Tunneling Spectroscopy (STS), Angle-Resolved Photoemission Spectroscopy (ARPES), Point-Contact Andreev-Reflection (PCAR) spectroscopy, optical spectroscopy, etc. A number of recent investigations of oxypnictides have focused on the multi-band superconductivity [31–33,43–48]. Answering the question of whether the different Fermi surface sheets are associated with different gaps is of crucial importance in order to identify the mechanism of superconductivity in these compounds. In this regard, experimental techniques such as ARPES, PCAR, and STS are very powerful methods since they allow a direct determination of the energy gap(s). STS is a suitable technique to study this issue since it probes the quasiparticle excitation spectrum in the superconducting state, a direct measure of the local density of states and therefore of the fundamental properties of the superconducting order parameter. This technique was successfully applied to MgB_2, where multi-band superconductivity was unambiguously demonstrated through directional STS measurements [49].

We succeeded in growing of the first free standing FeAs-oxypnictide crystals ($SmFeAsO_{1-x}F_x$) using a high pressure technique and NaCl/KCl flux [50]. The NaCl/KCl flux has very low solubility at temperatures below 1000 °C used for processes in quartz ampoules, therefore crystal growth at this temperature is extremely slow [51]. In order to increase the solubility in NaCl/KCl flux for more efficient crystal growth higher temperature should be used, but Ln1111 becomes unstable. This trend can be counteracted by applying high pressure, which then tends to stabilize the structure of Ln1111 at high temperature.

Single crystals of AFe_2As_2 can be grown from Sn flux, similar to many other intermetallic compounds [52,53]. Tin is practically the only metal that dissolves iron reasonably well and does not form stable unwanted compounds. Due to high solubility in Sn flux at temperatures compatible with quartz ampoules, large, millimeter-sized crystals of A122 have been grown, which allowed extensive measurements of their physical properties. The disadvantage

of the Sn-flux technique is that crystals usually contain ~1 at.% Sn. Another method of growing AFe_2As_2 crystals is the high-temperature growth from FeAs flux [54].

Here, we report on the crystal growth using both the high-pressure, high-temperature method with NaCl/KCl flux for Ln1111 and the quartz ampoule method with Sn flux for A122 [55]. The results of structure investigations on series of Ln1111 crystals (Ln = Sm, Nd, Pr, La, Gd) and $Ba_{1-x}Rb_xFe_2As_2$ are presented. Electrical resistivity measurements, investigations of the anisotropy parameter and spectroscopic studies are also summarized.

2. Experimental

2.1. Crystal growth

For the synthesis of $LnFeAsO_{1-x}F_x$ (Ln = La, Pr, Nd, Sm, Gd) polycrystalline samples and single crystals we used a cubic anvil high-pressure technique which has been successfully applied in our laboratory at ETH Zurich also for the single crystal growth of MgB_2 and other superconductors. The mixture of LnAs, FeAs, Fe_2O_3, Fe, and LnF_3 powders was used as a precursor. For the growth of single crystals we used additionally NaCl/KCl flux. The precursor-to-flux ratio was varied between 1:1 and 1:3. By variation of nominal oxygen and fluorine content between 0.6–0.8 and 0.4–0.2, respectively, different doping levels were achieved. The precursor powders were ground mixed and pressed into pellets in a glove box due to toxicity of arsenic. Pellets containing precursor and flux were placed in a BN crucible inside a pyrophyllite cube with a graphite heater. Six tungsten carbide anvils generated pressure on the whole assembly. In a typical run, a pressure of 3 GPa was applied at room temperature. For the crystal growth the temperature was increased within 1 h to the maximum value of 1350–1450 °C, kept for 4–85 h and decreased in 1–24 h to room temperature. For the synthesis of polycrystalline samples the maximum temperature of 1300–1350 °C was kept for 2–6 h followed by quenching. Then the pressure was released, the sample removed and in the case of single crystal growth the NaCl/KCl flux dissolved in water. After drying, the shiny single crystals could be selected easily. One has to mention that such high-pressure experiments have to be performed very carefully, because an explosion during heating due to increased pressure in the sample container can lead to a contamination of the whole apparatus with arsenide compounds.

With the aim of growing single crystals suitable for physical measurements, we carried out systematic investigations of the parameters controlling the growth of crystals, including growth temperature, applied pressure, starting composition, dwelling time and heating/cooling rate. Most of our exploratory crystal growth experiments were performed on the SmFeAs(O, F) system. Fig. 3 shows typical single crystals of SmFeAs(O, F), obtained in the growth experiment at 30 kbar and 1380 °C for 60–85 h. Their size is much smaller than the size of single crystals of $Ba_{1-x}Rb_xFe_2As_2$ (Fig. 4). By optimization of the growth conditions SmFeAs(O, F) single crystals with the sizes in the *ab*-plane in the range of 150–300 μm and $T_c \approx 53$ K have been obtained. In general, extending the soak time leads to larger crystals, but parasitic phases such as FeAs balls are formed simultaneously. One of the problems of crystal growth at high-temperature and high-pressure conditions is that the density of sites for nucleation is high and it is difficult to control nucleation so that fewer, but larger crystals would grow. This is also reflected on the quality of the grown crystals, therefore many of them have irregular shapes and they form clusters of several crystals. The solubility of SmFeAs(O, F) in NaCl/KCl flux is very low, which results in small crystals. In order to obtain larger and high quality crystals, it is important to choose the growth condition where crystals grow from only limited number of nuclei at a reasonable growth rate. It is necessary to search for a new solvent system with higher solubility and in which the kinetic barrier for nucleation of the Ln1111-phase is large. The existence of parasitic phases also has a significant effect on the growth mechanism and appropriate doping. Too high precursor-to-flux ratio prevents growth of larger crystals because of insufficient space for growth

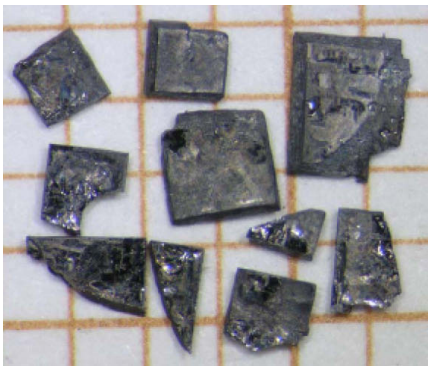

Fig. 4. Single crystals of (Ba, Rb) 122 on a millimeter grid.

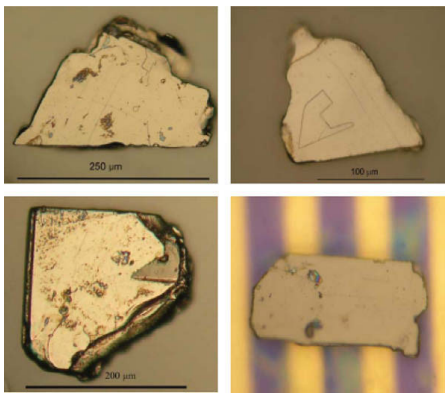

Fig. 3. Single crystals of $SmFeAsO_{1-x}F_x$.

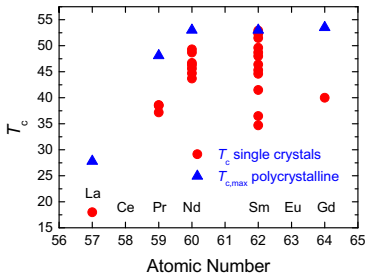

Fig. 5. T_c measured on single crystals from various growth experiments with different doping level, compared with $T_{c,max}$ for polycrystalline samples from literature [1–8] vs. the atomic number.

of individual grains. The crystal growth conditions which were optimized for the growth of optimally doped and relatively large SmFeAs(O, F) crystals have been applied to other systems, such as Nd-, La-, Gd-, and PrFeAs(O, F). For all these system we were able to grow single crystals. For each of these compounds, however the growth conditions and composition of the precursor need to be optimized. X-ray diffraction analysis of high-pressure crystal growth products indicate that several parasitic reactions proceeded in the crucible together with the single crystal growth of the Ln1111-type phase. For example, in the case of the LaFeAs(O, F) system, we observed several impurity phases, such as FeAs, LaOF, LaOCl, etc. T_c's measured with a SQUID magnetometer on Ln1111 (Ln = La, Pr, Nd, Sm, Gd) single crystals with various F doping are presented in Fig. 5.

Single crystals of $Ba_{1-x}Rb_xFe_2As_2$ were grown using a Sn flux method similar to that described in Ref. [54]. The Fe:Sn ratio (1:24) in a starting composition was kept constant in all runs while the Rb:Ba ratio was varied between 0.7 and 2.0. The appropriate amounts of Ba, Rb, Fe_2As, As, and Sn were placed in alumina crucibles and sealed in silica tubes under 1/3 atmosphere of Ar gas. Next, the ampoules were kept at 850 °C for 3 h until all components were completely melted, and cooled over 50 h to 500 °C. At this temperature the liquid Sn was decanted from the crystals. The remaining thin film of Sn at the crystal surfaces was subsequently dissolved at room temperature using liquid Hg, and finally the crystals were heated to 190 °C in vacuum to evaporate the remaining traces of Hg. No signs of superconducting Hg are seen in the magnetic measurements.

The single crystals of $Ba_{1-x}Rb_xFe_2As_2$ grow in a plate-like shape with typical dimensions $(1–3)\times(1–2)\times(0.05–0.1)\,mm^3$ (Fig. 4). Depending on the starting composition, the crystals displayed a broad variety of properties from nonsuperconducting to superconducting with sharp transitions to the superconducting state. For further studies we chose single crystals grown from initial composition $Ba_{0.6}Rb_{0.8}Fe_2As_2$. The composition of the crystals from this batch determined by EDX analysis (16.79 at.% Ba, 1.94 at.% Rb, 1.74 at.% Sn, 40.19 at.% Fe, and 39.33 at.% As) leads to the chemical formula $Ba_{0.84}Rb_{0.10}Sn_{0.09}Fe_2As_{1.96}$. Crystals from the selected batch exhibit a moderate T_c (around 22–24 K) but compared to the crystals with higher T_c their superconducting transition is relatively sharp, with more than one step in the resistance curve, however.

2.2. Experimental details of structure and superconducting properties studies

Single crystals were studied on a four-circle diffractometer equipped with CCD detector (X-calibur PX, Oxford Diffraction) using Mo Kα radiation. The single crystals of various batches have been characterized by X-ray diffraction showing well-resolved reflection patterns indicating a high quality of the crystallographic structure. Data reduction and analytical absorption correction were done using the program CrysAlis [56]. The crystal structure was determined by a direct method and refined on F^2 employing the programs SHELXS-97 and SHELXL-97 [57,58].

Magnetic measurements were performed using a Quantum Design SQUID Magnetometer MPMS XL with a standard Reciprocating Sample Option installed. Low field susceptibility measurements revealed a narrow and well-defined transition from the normal to the superconducting state.

Torque magnetometry has been applied to determine γ, a technique which allows to measure the angular dependent superconducting magnetization by detecting the torque of a single crystal in a magnetic field along a certain orientation with respect to the crystallographic *c*-axis. A home-made piezoresistive torque sensor was used [59]. The crystal was mounted in an Oxford flow cryostat allowing stabilization of temperatures between 10 K and 300 K. A turnable Bruker NMR magnet with a maximum field of 1.4 T was used to vary the field magnitude and its orientation with respect to the crystallographic axes allowing for a full rotation through 360 deg. For this experiment several single crystals have been chosen with the nominal composition $SmFeAsO_{0.8}F_{0.2}$ and $NdFeAsO_{0.8}F_{0.2}$ with masses of ~100 ng and T_c of the order of 45 K.

Direct four-point resistivity measurements were performed on SmFeAs(O, F) (Sm1111) and (Ba, Rb)Fe_2As_2 ((Ba, Rb)122) crystals using a Quantum Design Physical Property Measurement System (PPMS) in magnetic fields up to 14 T. To minimize the broadening of the transition due to material inhomogeneities, Sm1111 crystals smaller than 200 μm were selected and contacted using a Focused Ion Beam. This technique produces precisely deposited micrometer-sized Pt leads onto the crystal and was found not to alter the bulk superconducting properties. The diameter of typical (Ba, Rb)122 crystals was well above 1 mm and allowed for standard manual contacting.

PCAR spectroscopy measurements were performed in SmFeAs(O, F) crystals in order to study the superconducting energy gap(s). The relatively small size of the crystals prevents the use of the standard point-contact technique which consists in pressing a sharp metallic tip against the material under study and also of the "soft" PCAR technique [60] where the contact is achieved by means of a small drop of Ag conductive paste. Instead the current was therefore injected in the crystals through a very small (10 μm diameter) Au-wire which acts as the tip. The crystals were vertically mounted by contacting the lateral edges by means of In. The Au-wire was leant transversely on the thin lateral side of the crystal. In this way, the current is mainly injected along the *ab*-plane (*ab*-plane contact) and it is possible to measure the differential conductance curves, d*I*/d*V* vs. *V*, across the Au/crystal junction.

STS measurements have been performed on a single crystal of $SmFeAsO_{0.86-x}F_x$. Due to the small sizes of the samples ($\sim 50\times 50\,\mu m^2$), in situ cleaving or fracturing was not feasible, and therefore all measurements were made on as-grown surfaces. Before being introduced into the UHV chamber, a batch of single crystals was glued on the sample holder, and rinsed in pure deionized water and isopropyl alcohol. Tunneling topographic and spectroscopic measurements were performed with a home-made low-temperature scanning tunneling microscope, at 4.2 K in 10^{-3} mbar He exchange gas pressure. Electrochemically etched Iridium tips served as the ground electrode and were positioned perpendicular to the (0 0 1) face of the crystal. The tunneling resistance was adjusted in the 500 MΩ range (0.1 V sample bias voltage, and 200 pA tunnel current) to ensure a true tunneling regime.

3. Results and discussion

3.1. Crystal structure

3.1.1. Crystal structure of LnFeAs(O, F)

All atomic positions were found using the direct method. The refinement was performed without any constraints. The oxygen and fluorine atoms occupy the same position and were treated as one atom because it is impossible to distinguish between them by X-ray diffraction. The results of the structure refinement are presented in the Table 1. The lanthanide contraction reflects itself in a systematic lattice parameters reduction across the series (Figs. 6 and 7). The only two variable atomic coordinates *z* for As and Ln also vary regularly across lanthanides series (Fig. 8). All samples reveal more than 10% vacancies on the O(F) site (Table 1). However, the accuracy of the determination of the oxygen/fluorine occupancy is low due to the presence of the heavy As, Fe and Sm elements. The bonding in the layers LnO and FeAs for the

Table 1
Details of the structure refinement for the LnFeAs(O, F) (Ln = La, Pr, Nd, Sm, Gd) crystals. The diffraction study is performed at 295(2) *K* using Mo K_α radiation with $\lambda = 0.71073$ Å, The lattice is tetragonal, *P*4/nmm space group with $Z = 2$. The absorption correction was done analytically. A full-matrix least-squares method was employed to optimize F^2.

Empirical formula	$LaFeAsO_{0.88-x}F_x$	$PrFeAsO_{0.80-x}F_x$	$NdFeAsO_{0.89-x}F_x$	$SmFeAsO_{0.86-x}F_x$	$GdFeAsO_{0.76-x}F_x$
$T_c/\Delta T_c$ (K)	non-superconducting	38.8/3	46.3/3	47.9/2.5	22.7/5
Unit cell dimensions (Å)	$a = 4.02690(10)$, $c = 8.7010(3)$	$a = 3.97820(10)$, $c = 8.5810(4)$	$a = 3.95940(10)$, $c = 8.5443(2)$	$a = 3.93110(10)$, $c = 8.4655(5)$	$a = 3.91610(10)$, $c = 8.4486(6)$
Volume ($Å^3$)	141.095(7)	135.804(8)	133.948(6)	130.822(9)	129.566(10)
Calculated density (g/cm^3)	6.741	7.016	7.238	7.551	7.753
Absorption coefficient (mm^{-1})	31.405	34.831	36.516	39.985	43.3
Crystal size (μm^3)	$163 \times 115 \times 24$	$137 \times 111 \times 12$	$91 \times 72 \times 10$	$86 \times 96 \times 14$	$117 \times 77 \times 18$
Θ Range for data collection	4.69–42.32 (deg)	4.75–45.78 (deg)	4.77–53.87 (deg)	4.82–40.78 (deg)	5.74–40.65 (deg)
Index ranges	$-7 = h \leqslant 3$, $-2 \leqslant k \leqslant 7$, $-16 \leqslant l \leqslant 10$	$-6 = h \leqslant 7$, $-7 \leqslant k \leqslant 7$, $-17 \leqslant l \leqslant 16$	$-8 = h \leqslant 7$, $-5 \leqslant k \leqslant 8$, $-19 \leqslant l \leqslant 10$	$-5 = h \leqslant 6$, $-6 \leqslant k \leqslant 7$, $-13 \leqslant l \leqslant 15$	$-6 = h \leqslant 7$, $-5 \leqslant k \leqslant 7$, $-15 \leqslant l \leqslant 14$
Reflections collected/ unique	1212/330 $R_{int} = 0.0293$	1612/384 $R_{int.} = 0.0242$	1859/474 $R_{int.} = 0.0264$	1163/285 $R_{int.} = 0.0370$	975/281 $R_{int.} = 0.0396$
Data/restraints/ parameters	330/0/12	384/0/12	474/0/12	285/0/12	281/0/12
Goodness-of-fit on F^2	1.118	1.173	0.996	1.149	1.104
Final *R* indices [$I > 2\Omega(I)$]	$R_1 = 0.0408$, $wR_2 = 0.1145$	$R_1 = 0.0323$, $wR_2 = 0.0786$	$R_1 = 0.0286$, $wR_2 = 0.0681$	$R_1 = 0.0424$, $wR_2 = 0.1172$	$R_1 = 0.0497$, $wR_2 = 0.1157$
R Indices (all data)	$R_1 = 0.0494$, $wR_2 = 0.1190$	$R_1 = 0.0385$, $wR_2 = 0.0800$	$R_1 = 0.0393$, $wR_2 = 0.0708$	$R_1 = 0.0479$, $wR_2 = 0.1199$	$R_1 = 0.0593$, $wR_2 = 0.1195$
Fractional atomic coordinates, O(F) occupation and atomic displacement parameters ($Å^2$)					
Fe $x = ¼$; $y = ¾$; $z = ½$					
Ln $x = -¼$; $y = -¼$; z	0.1468(1)	0.1435(1)	0.1440(1)	0.1419(1)	0.1382(1)
As $x = ¼$; $y = ¼$; z	0.3474(1)	0.3435(1)	0.3414(1)	0.3388(2)	0.3375(2)
O(F) $x = ¼$; $y = ¾$; $z = 0$					
O(F) occupation	0.88	0.80	0.89	0.86	0.76
Interatomic distances (Å)					
Ln-O	2.3844(5)	2.3392(2)	2.3309(1)	2.3035(4)	2.2797(5)
Ln-As	3.3398(6)	3.2952(5)	3.2686(4)	3.2411(1)	3.241(1)
FeAs	2.4118(5)	2.4002(5)	2.3989(4)	2.393(1)	2.391(2)

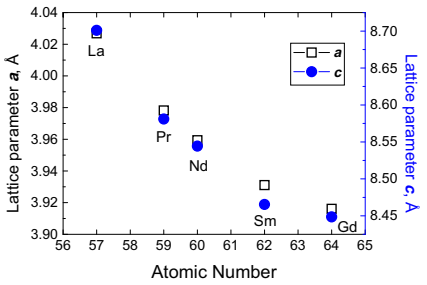

Fig. 6. Cell parameters as a function of the atomic number for LnFeAs(O, F) (Ln = La, Pr, Nd, Sm, Gd). Squares show the *a* and circles represent the *c* lattice parameters.

LnFeAs(O, F) is covalent. The absolute values of these distances ($d_{Ln\text{-}O} \sim 2.28$–$2.34$ Å) are close to the sum of covalent radii of the elements $r_{Ln}^{cov} + r_O^{cov} \sim 2.27$–$2.35$ Å for Gd–La series). The sum of the covalent radii of the Ln and As atoms ($r_{Ln}^{cov} + r_{As}^{cov} \sim 2.82$–$2.90$ Å for Gd–La series) is smaller than the distances between these atoms ($d_{Ln\text{–}As} \sim 3.24$–$3.34$ Å (Table 1). Between the layers ionic bonding is dominant.

3.1.2. Crystal structure of (Ba, Rb)Fe_2As_2

A structure analysis was performed on Rb-substituted $BaFe_2As_2$. We assumed that Rb substitute for Ba atoms, and the Rb/Ba occupation was refined simultaneously. Anisotropic displacement parameters as well as atomic coordinates for both elements were restrained to the same value. After several cycles of refinement we found in the Fourier difference map a pronounced maximum close to but displaced from the Ba/Rb site. According to EDX anal-

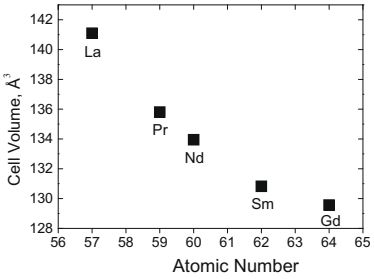

Fig. 7. Cell volume as a function of the atomic number for LnFeAs(O, F) (Ln = La, Pr, Nd, Sm, Gd).

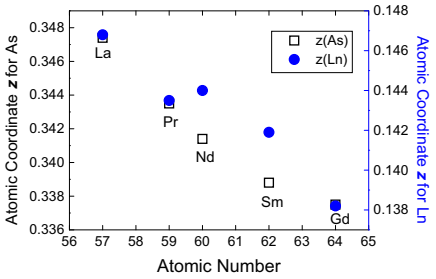

Fig. 8. Atomic coordinates *z* as a function of atomic number. Squares show *z* for As and circles represent *z* for LnFeAs(O, F) (Ln = La, Pr, Nd, Sm, Gd).

Table 2
Crystal data for the Rb substituted $BaFe_2As_2$ Single crystals.

Crystal system, space group, Z	Tetragonal, $I4/mmm$, 2
Unit cell dimensions (Å)	a = 3.9250(2), c = 13.2096(5)
Volume (Å^3)	203.502(3)
Fractional atomic coordinates	
Ba/Rb: $x = y = z = 0$, Sn: $x = y = 0$; $z = 0.0837(7)$, As: $x = y = 0$; $z = 0.3543(1)$, Fe: $x = 1/2$; $y = 0$; $z = 1/4$	
Bond lengths (Å)	
Ba/Rb-As	3.3774(3) × 8
Fe–As	2.3979(3) × 4
Fe–Fe	2.7754(1) × 4
As–Sn	2.894(3) × 4
Fe–Sn	2.945(7) × 4
Bond angles (deg)	
As–Fe–As	109.86(2)
	109.28(1)

ysis a small amounts of Sn (from the flux) are present in the crystal. We assume that the maximum off the Ba/Rb site corresponds to the location of Sn in the structure. The next step of the refinement was performed with Sn located in the position of maxima, and the occupation parameter of Sn was refined. Inserting Sn in the refinement decreased the R factor considerably (from 5.41% to 3.89%). We assumed the overall occupation of Ba, Rb and Sn to be 100%. The overall occupation of the Rb/Ba site was decreased by the amount of Sn and fixed while the ratio Ba/Rb was refined. After several refinement cycles the absorption correction for the correct crystallographic composition was performed. The occupation parameters for the Rb/Ba and Sn sites were found to be 0.89/0.05 and 0.06, respectively. Therefore, according to crystallographic data, the more appropriate chemical formula is $Ba_{0.89}Rb_{0.05}Sn_{0.06}Fe_2As_2$. The results of the final structure refinement are presented in Table 2 and the resulting structure in Fig. 9. Compared to unsubstituted $BaAs_2Fe_2$ the lattice parameter a is slightly shorter, the c parameter is longer and the volume of the unit cell is smaller. A similar tendency has been observed for other A122 compounds, when Ba or Sr is replaced by K. The increase of the c parameter in (Ba, Rb) 122 is caused mainly by substitution of Ba^{2+} ions (r = 1.42 Å) by larger Rb^+ ions (r = 1.61 Å). The relatively large contraction of the a parameter (larger than expected from Vegard's law) seems to be the effect of Sn incorporation.

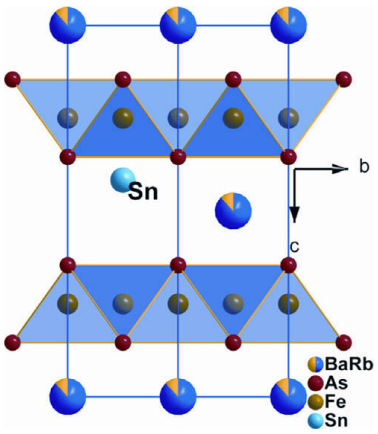

Fig. 9. Crystal structure of (Ba, Rb) 122.

3.2. Upper critical fields, critical current and superconducting state anisotropy

3.2.1. Resistivity measurements

Resistivity measurements $\rho(T, H)$ near T_c for magnetic fields parallel ($H||ab$) and perpendicular ($H||c$) to the FeAs-planes show remarkably different behavior for Sm1111 and (Ba, Rb)122 (Fig. 10). In (Ba, Rb)122 the presence of magnetic fields shift the onset of superconductivity to lower temperatures, but do not cause any broadening. This shift of T_c is linear in the applied magnetic field and therefore the upper critical fields $H_{c2}^{\|ab}$ and $H_{c2}^{\|c}$ do not show any significant curvature. Sm1111, however, shows a distinctly different behavior. Magnetic fields cause only a slight shift of the onset of superconductivity, but a significant broadening of the transition, indicating weaker pinning and accordingly larger flux flow dissipation. The resistivity in our Sm1111 crystals shows typically two or three steps at low fields. These steps vanish at magnetic fields higher than 1 T.

The diamagnetic signal does not show any steps, thus they may be associated with surface imperfections. While (Ba, Rb)122 shows a sharp transition and a clear onset of superconductivity, there is no sharp transition in Sm1111 and T_c is therefore less clearly defined. We chose three different criteria: 90% ρ_n, 50% ρ_n and 10% ρ_n, where $\rho_n(T)$ is the linear extrapolation of the normal state resistivity. Due to the absence of field-induced broadening in (Ba, Rb)122, all definitions of T_c lead to the same results for the H_{c2} slopes and we chose the 50% ρ_n criterion. The upper critical fields $H_{c2}^{\|ab}$ and $H_{c2}^{\|c}$ extracted from resistivity measurements of both materials are shown in Fig. 11. The upper critical fields H_{c2} in (Ba, Rb)122 increase linearly with decreasing temperature ~0.5 K below T_c, with a slope of 4.2 T/K ($H||c$) and 7.1 T/K ($H||ab$). The slopes dH_{c2}/dT in Sm1111 depend strongly on the choice of the criterion due to the pronounced broadening. We found 3.3–1.2 T/K for $H||c$ and 8.0–5.5 T/K for $H||ab$. All these large slopes indicate very high values of $H_{c2}(0)$.

The (Ba, Rb)122 structure is more isotropic than the structure of Sm1111, which is already manifested in the upper critical field anisotropy $\gamma_H = H_{c2}^{\|ab}/H_{c2}^{\|c}$ (insets Fig. 11). The anisotropy γ_H in Sm1111 ranges between 7 and 7.5 using the 50% ρ_n criterion, while it was found to be between 2.5 and 3.2 in (Ba, Rb)122. This reflects a stronger coupling of the FeAs layers and therefore more electronic coupling in the A122 compounds compared to the Ln1111 compounds. The anisotropy γ_H is temperature dependent and decreases with decreasing temperature for both (Ba, Rb)122 and Sm1111. This is in very good agreement with previous experiments and seems to be a general feature in all different classes of pnictide superconductors.

3.2.2. Magnetic measurements and critical current density

Temperature dependence of the magnetic moment, measured in a magnetic field of 1 mT parallel to the c-axis for a single crystal of $SmFeAsO_{0.6}F_{0.35}$ with a mass of about 6 μg, is presented in Fig. 12. The sharp transition to the superconducting state is characteristic for a high-quality single crystal. A transition temperature of 52 K indicates that the crystal is close to optimal doping. The value of the zero-field cooled magnetic moment reflects the full diamagnetic response of the crystal studied. The small ratio of field cooled to zero-field cooled magnetization is characteristic for a superconductor with relatively strong pinning, which was confirmed in the magnetic hysteresis loop measurements reported previously [50]. A wide loop measured at 5 K in a magnetic field up to 7 T revealed a hysteresis width almost independent on the field. A high critical current density of the crystal was deduced, reaching values of about 10^{10} A/m^2 at 5 K. It was suggested that a slight increase of the critical current density for higher magnetic field may indicate the increase of the effectiveness of pinning centers with increasing

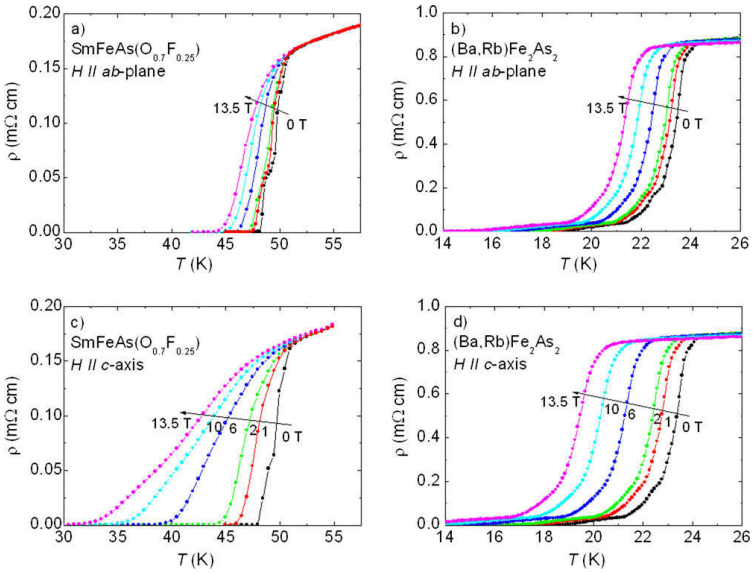

Fig. 10. Examples of resistivity $\rho(T,H)$ for SmFeAs ($O_{0.7}$ $F_{0.25}$) and for (Ba, Rb) Fe_2As_2 single crystals measured in fields applied parallel to the (Fe_2As_2)-layers ($H||ab$) (a and b) and perpendicular to them ($H||c$) (c and d), at magnetic field strengths of 0, 1, 2, 6, 10 and 13.5 T.

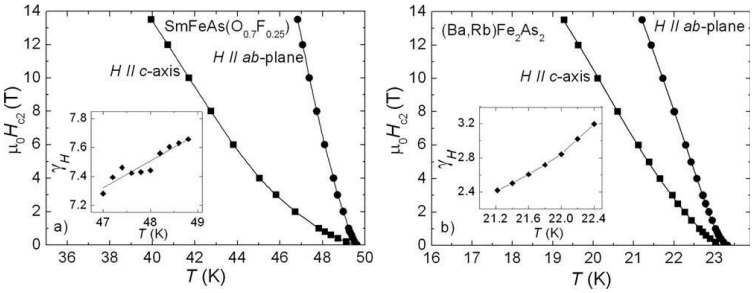

Fig. 11. Temperature dependence of the upper critical field with $H_{c2}^{||ab}$ and $H_{c2}^{||c}$ for the SmFeAs ($O_{0.7}$ $F_{0.25}$) and the (Ba, Rb)Fe_2As_2 system. Inset: the upper critical field anisotropy $\gamma_H = H_{c2}^{||ab}/H_{c2}^{||c}$ in the vicinity of T_c. To determine H_{c2} the 50% p_n criterion was used.

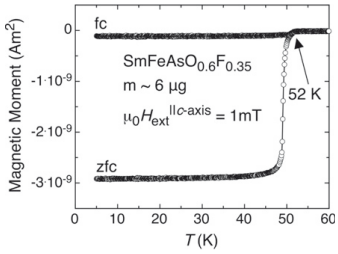

Fig. 12. Temperature dependence of the magnetic moment measured on a $SmFeAsO_{0.6}F_{0.35}$ (nominal content) single crystal with T_c of 52 K in an applied field of 1 m T parallel to its c-axis. ZFC and FC denote zero-field cooling and field cooling curves, respectively.

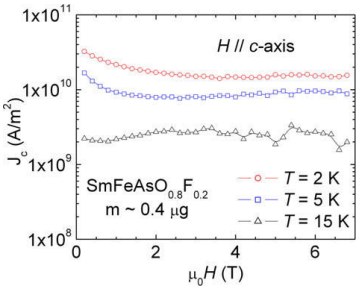

Fig. 13. Critical current density calculated from the width of the hysteresis loop measurements up to 7 T at 2 K, 5 K and 15 K.

magnetic field [45]. The critical current density at 2 K, 5 K and 15 K, estimated from the field dependence of the magnetic moment for $SmFeAsO_{0.8}F_{0.2}$, are higher than 10^9 A/m^2 (Fig. 13), what is promising for having applications in mind. Very similar results were obtained for single crystals of (Ba, Rb) 122. The observed extremely small Meissner fraction is due to the pronounced magnetic irreversibility, stemming most likely from the lattice mismatch caused by the substitution with relatively big Rb ions, introducing effective pinning centers. Again, a relatively strong pinning was confirmed in magnetic hysteresis loop measurements [55]. The critical current density at 2 K and 5 K reaches values of the order of 10^{10} A/m^2, similar like the Sm1111 results. The slight increase of the critical current density with increasing field was observed and it is most likely due to the occurrence of the peak effect.

3.2.3. Magnetic torque investigations

First, the analysis of the measured torque data was done with the simple one-anisotropy model [26]. The anisotropy parameter was found to be up to 1.4 T almost field independent, but varies strongly in temperature between 8 at $T \approx T_c$ and 23 at $T \approx 0.4T_c$ for a $SmFeAsO_{0.8}F_{0.2}$ crystal with T_c of 45 K [31]. This disagrees with the temperature dependence of γ_H determined from H_{c2} by resistivity measurements as shown above, and with recent values of γ_H of NdFeAs(O, F) crystals obtained from high field resistivity measurements [33]. It is evident that γ_H decreases with decreasing temperature and with temperature dependent values γ_H all much smaller than the torque results.

Nevertheless, a temperature dependent γ would imply an unconventional (non-Ginzburg–Landau) behavior of the thermodynamic parameters. A possible and natural explanation would be multi-band superconductivity, where different parts of the Fermi surface sheet develop distinct gaps in the superconducting state. The complex interband and intraband scattering of charge carriers will rule the physics and therefore influence strongly the superconducting state anisotropy. In this framework a temperature and even field dependent anisotropy can be well understood, since interband and intraband scattering processes will lead to modifications in the simple one-gap Ginzburg–Landau relation.

Since for multi-band superconductors the magnetic penetration depth anisotropy γ_λ might be different from the upper critical field anisotropy γ_H a more general two-anisotropy model for the angular dependent torque was proposed by Kogan [26,61]. We performed a detailed analysis of several $SmFeAsO_{0.8}F_{0.2}$ and $NdFeAsO_{0.8}F_{0.2}$ single crystals by torque experiments using the two-anisotropy model. Details of the calculations have been published elsewhere [62].

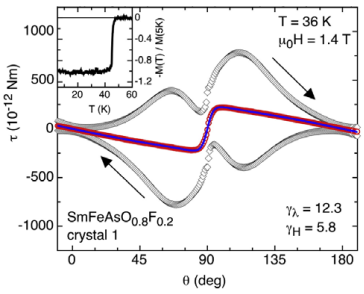

Fig. 14. Angle dependent raw torque measured for a $SmFeAsO_{0.8}F_{0.2}$ single crystal at 36 K in 1.4 T. The squares denote the raw (irreversible) torque, which was subsequently averaged in order to obtain the reversible component (circles). The line is a fit with the parameters $\gamma_\lambda = 12.3$ and $\gamma_H = 5.8$. The inset displays the low field magnetic moment with a sharp superconducting transition measured in a SQUID experiment, suggestive for the excellent quality of the single crystal.

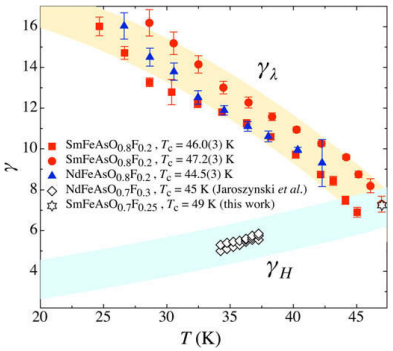

Fig. 15. Summary of the anisotropies γ_λ deduced from the torque data, using fixed values for γ_H after Jaroszynski et al. [33]✡ – γ_H determined from Fig. 11a. All data plotted in this figure are described in more detail in [62].

By fixing the upper critical field anisotropy γ_H to the values obtained by Jaroszynski et al. [33] the magnetic penetration depth anisotropy γ_λ was found to be strongly temperature dependent in a very similar way as the single anisotropy model predicted. Fig. 14 shows exemplarity one sketch of angular dependent magnetic torque experiment. Fig. 15 shows the extracted γ_λ and γ_H as a function of temperature, derived by systematic fitting of the torque data.

As a result, the low field torque is mostly sensitive to the magnetic penetration depth anisotropy γ_λ and is almost insensitive on the upper critical field anisotropy γ_H. This might be different in higher fields close to the phase transition, where the effective anisotropy of the system would correspond much more to the upper critical field anisotropy, which should lead to a reduction of γ in higher fields [32]. For the temperature dependence of the magnetic penetration depth a good agreement was found with the two-fluid model [63] and the value of $\lambda_{ab}(0) = 250$ nm extracted from the data is in good agreement with other estimates [64–66]. The upper critical field was estimated according to the WHH relation [67] to be $\mu_0 H_{c2} = 70$ T.

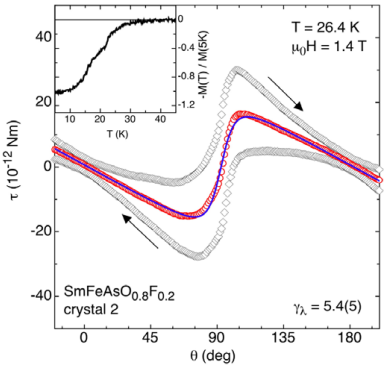

Fig. 16. data derived on a $SmFeAsO_{0.8}F_{0.2}$ crystal of inferior quality. The usually sharply featured angular torque is distorted in the *ab*-plane (90 deg), just where the fitting curve is mostly sensitive to the anisotropy parameter γ_λ. The fitted γ_λ is found to be strongly reduced 5.4(5). The inset shows the broad transition of the low field magnetic moment, measured in a SQUID experiment.

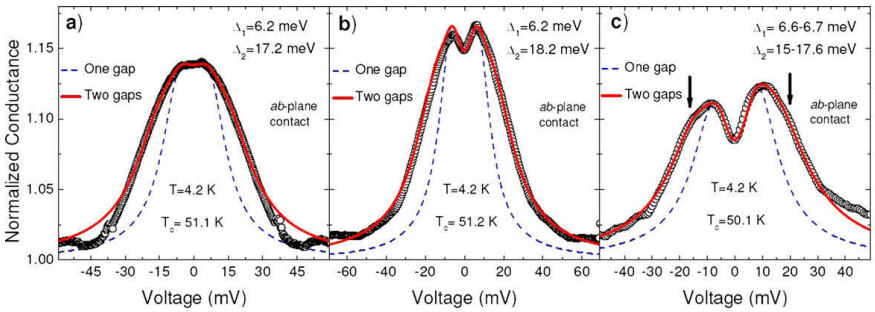

Fig. 17. (a–c) Examples of normalized conductance curves measured at 4.2 K in Au/SmFeAsO$_{0.8}$F$_{0.2}$ point-contact junctions (symbols). The main direction of current injection is along the *ab*-planes of the crystals (*ab*-plane contacts). Dash lines: single-band BTK fit. Solid lines: two-band BTK fit.

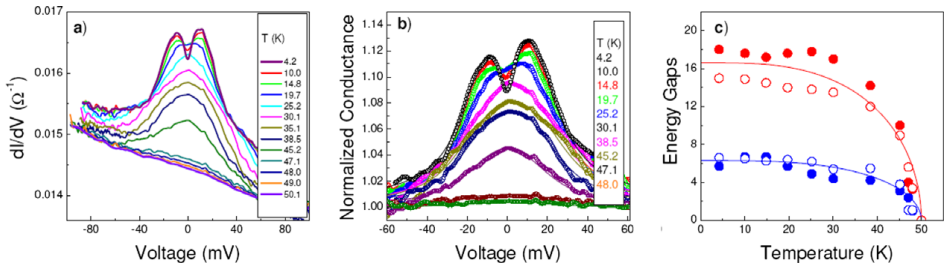

Fig. 18. (a) Temperature dependence of the raw conductance curves for a Au/SmFeAsO$_{0.8}$F$_{0.2}$ single crystal point-contact junction with the current mainly injected along the *ab*-planes. (b) Temperature dependence of the normalized conductance curves shown in (a) (symbols) together with their relevant two-gap BTK fits (lines). (c) Gap values obtained by fitting the curves shown in (b). Due to the asymmetry of the conductance curves, the extracted gap values differ slightly between the negative (open symbols) and the positive bias part (full symbols).

We would like to stress, that crystals of a bad quality, containing domains with different crystallographic orientation show a much lower and temperature independent anisotropy. This might be a reason for the various results on the magnetic penetration depth anisotropy published recently by several groups. To illustrate this, Fig. 16 presents torque measurements performed on a crystal which shows a broad superconducting transition and slight disorder in the structure observed by X-ray diffraction. The anisotropy is strongly reduced. Therefore, well characterized single crystals of high quality are better suited to study anisotropic properties.

3.3. Point-Contact Andreev-Reflection spectroscopy measurements

Fig. 17a–c shows some examples of low-temperature normalized conductance curves (symbols) measured on various Au/SmFeAsO$_{1-x}$F$_x$ junctions. The enhancement of the conductance around zero bias and the presence of peaks clearly reveal the occurrence of the Andreev-reflection phenomenon at the N/S junction. The peaks in the conductance curves indicate the presence of a superconducting gap while higher-bias features (such as a widening of the Andreev feature) in Fig. 17a and b and small humps (indicated by arrows) in the curve shown in Fig. 17c suggest the presence of a second gap. In order to confirm this observation a comparison has been carried out between the one-gap and two-gap models for Andreev reflection at the N/S interface. Since no zero bias conductance peaks (ZBCP) are present, the fitting has been performed using nodeless gaps. The modified [68] Blonder–Tinkham–Klapwijk (BTK) model [69] generalized to take into account the angular distribution of the current injection at the interface [70] was adopted. In the two-band case the conductance is the weighed sum of two BTK contributions: $G = w_1G_1 + (1 - w_1)G_2$ [71].

The result of the comparison is also shown in Fig. 17a–c: the one-band model (dash lines) reproduces only a small central portion of the curves while the two-band model (solid lines) is remarkably better, indicating the presence of two superconducting gaps whose values, as determined by the fitting procedure, are $\Delta_1 = 6.45 \pm 0.25$ meV and $\Delta_2 = 16.6 \pm 1.6$ meV, with ratios $2\Delta_1/k_BT_c = 2.8–3.1$ and $2\Delta_2/k_BT_c = 6.8–8.5$, in good agreement with PCAR spectroscopy results on polycrystalline samples [47]. Fig. 18a shows the temperature dependence of the raw conductance curves of the same Au/SmFeAsO$_{0.8}$F$_{0.2}$ point-contact junction whose low-temperature curve is shown in Fig. 17c. The overall appearance of the conductance curves is asymmetric, being higher at negative bias voltages, as it has also been observed in several other PCAR spectroscopy measurements in iron pnictides. Furthermore, the Andreev peaks in the low-temperature conductance usually are of opposite asymmetry (i.e. they are higher at positive bias voltage). This asymmetry is more or less pronounced. When this feature is significant, a separate fit of negative and of the positive bias part has been performed (Fig. 17c and Fig. 18b), but further studies have to be carried out in order to clarify its origin.

As a further confirmation of the presence of two gaps in SmFeAsO$_{1-x}$F$_x$, a fit of the temperature dependence of the conductance curves has been carried out. Fig. 18b shows the temperature dependence of the normalized conductance curves (symbols)

shown in panel (a) together with their relevant two-band BTK fitting curves (lines). Since the asymmetry is rather pronounced in this case, the left and the right part of the curves are fitted with slightly different parameters. The gap values obtained by this procedure are reported in Fig. 18c. As far as the small gap, Δ_1 is concerned, the values are almost identical in the two cases (open and full circles, respectively) while a small difference is derived for the larger one (open and full circles, respectively). Both Δ_1 and Δ_2 follow a BCS-like behavior (dash and dash-dot lines, respectively) and close at the critical temperature of the junction.

3.4. Scanning Tunneling Spectroscopy measurements

The surfaces of $SmFeAsO_{0.8}F_{0.2}$ crystals imaged by scanning tunneling microscopy present plateaus of irregular shape, with an rms roughness of less than 0.1 nm. These terraces have a height difference of 0.8 or 1.6 nm steps, roughly a single or double crystal c-axis lattice constant for $SmFeAsO_{0.8}F_{0.2}$ (c = 0.847 nm).

Low temperature tunneling conductance spectra are shown in Fig. 19. These data (a and b) have been acquired at two different locations of the sample surface, using the same tunneling conditions. At energies close to the Fermi level (low bias voltage), the dI/dV spectra present a conductance depletion. At the edge of this depletion, conductance kinks or faint peaks are detected, indicated in the figure by the dotted lines. Following common practice [72], we consider half the peak-to-peak energy separation as a measure of the superconducting gap. Considering thousands of spectra acquired within regions of tens of nanometer wide, we find a mean gap value of 7(1) meV. The variation in Δ (~14%) is relatively small compared to the gap distributions usually measured in Bi-based high-T_c cuprates [72]. The average critical temperature of several samples of the same batch is T_c = 45 K, yielding $2\Delta/k_BT_c$ = 3.6, a ratio close to that expected for a weak-coupling s-wave superconductivity.

A second gap-like feature is detected at voltages around 20 meV (see arrows in Fig. 19a and b). In contrast to the low energy feature, the peaks at higher energy vary in height, are much wider, and are located over a broader energy scale. Remarkably, they are often not detected simultaneously for occupied and empty states, and when they are, their energy locations are not symmetric with respect to the Fermi level. The last fact questions the interpretation of the high-voltage feature as a second superconducting gap.

A tunneling conductance spectrum over a wider voltage range is shown in Fig. 19c. The conductance at high-bias voltages is voltage-dependent (V-shaped) with a strong particle-hole asymmetry, the conductance measured at negative sample bias (occupied states) being systematically higher than the conductance at positive sample bias (empty states). This asymmetry is strikingly similar to the one measured in a number of high-T_c cuprates [72], possibly indicating strong electronic correlations in this compound.

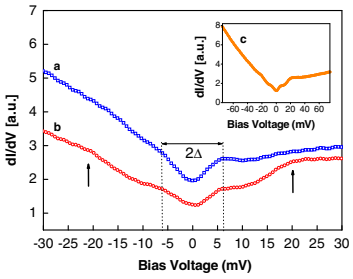

Fig. 19. (a and b) Scanning tunneling spectra measured on a $SmFeAsO_{0.8}F_{0.2}$ single crystal at 4.2 K, at two different locations of the sample. The dotted lines are set at the position of the peaks or kinks used for determining the value of the superconducting gap 2Δ. The arrows indicate the position of the gap-like features detected at higher-bias. (c) Local tunneling spectrum displayed over a wide energy range: the voltage-dependent conductance at high bias and the particle-hole asymmetry can be interpreted as indications of strong electronic correlations.

The 7 meV value found for the low energy gap is in agreement with the values measured in point contact spectroscopy studies on similar compounds and on polycrystalline samples [47,73]. Moreover, the value of the $2\Delta/k_BT_c$ ratio suggests that this spectroscopic feature is the signature of a superconducting gap. However, caution imposes on the interpretation of the high-energy feature observed in SmFeAs(O, F) as a second superconducting gap. Although the energy scale of this feature is of the order of the one reported in point contact spectroscopy [47,73], it is not systematically detected for empty and occupied states and it is particle-hole asymmetric. Moreover, it is not systematically detected in a recent STS study of $BaFe_{1.8}Co_{0.2}As_2$ single crystals [74]. Therefore, the STS measurements rather cast doubts on this feature being a manifestation of a second superconducting gap. In order to elucidate this discrepancy on the interpretation of the data, detailed studies of the temperature dependence of the spectral features, vortex core spectroscopy and/or tunneling along different crystallographic directions are needed.

4. Conclusions

Single crystals of $LnFeAsO_{1-x}F_x$ (Ln = La, Pr, Nd, Sm, Gd) have been grown using a cubic anvil high-pressure technique, and $Ba_{1-x}Rb_xFe_2As_2$ crystals have been grown in quartz ampoules. Superconductivity in the Ba122 compound has been induced by Rb substitution for the first time. The availability of Ln1111 single crystals made it possible to determine several basic superconducting parameters, such as upper critical fields and their anisotropy γ_H and magnetic penetration depth anisotropy γ_λ. The anisotropy γ_λ is temperature dependent and increases with decreasing temperature from $\gamma_\lambda(T_c) = \gamma_H(T_c) = 7$ towards $\gamma_\lambda(0) = 19$, while the anisotropy γ_H varies much less and decreases towards $\gamma_H(0) = 2$ with decreasing temperature [62]. This is suggestive of two superconducting gaps. PCAR studies support this scenario and show the existence of two-gaps, $\Delta_1 = 6.45 \pm 0.25$ meV and $\Delta_2 = 16.6 \pm 1.6$ meV, in good agreement with results on polycrystalline samples [47]. STM investigations reveal a superconducting gap at the energy scale of 7(1) meV and a high-energy feature around 20 meV whose connection to a second superconducting gap has to be further explored. The critical current is relatively high, with J_c values of 2×10^9 A/m^2 at 15 K in field up to 7 T. $Ba_{1-x}Rb_xFe_2As_2$ crystals are electronically more isotropic, indicative of better coupling of the FeAs layers by the (Ba, Rb) layers than by the Sm(O, F) layers.

Acknowledgements

This work was supported by the Swiss National Science Foundation, by the NCCR program MaNEP, and partially supported by the Polish Ministry of Science and Higher Education under Research Project for the years 2007–2009 (No. N N202 4132 33). This work was a part of the research program of the Polish National Scientific Network "Materials with strongly correlated electrons".

References

[1] Y. Kamihara, T. Watanabe, M. Hirano, H. Hosono, J. Am. Chem. Soc. 130 (2008) 3296.
[2] H. Takahashi, K. Igawa, K. Arii, Y. Kamihara, M. Hirano, H. Hosono, Nature 453 (2008) 376.

[3] X.H. Chen, T. Wu, G. Wu, R.H. Liu, H. Chen, D.F. Fang, Nature 453 (2008) 761.
[4] G.F. Chen, Z. Li, D. Wu, G. Li, W.Z. Hu, J. Dong, P. Zheng, J.L. Luo, N.L. Wang, Phys. Rev. Lett. 100 (2008) 247002.
[5] Z.-A. Ren, J. Yang, W. Lu, W. Yi, X.-L. Shen, Z.-C. Li, G.-C. Che, X.-L. Dong, L.-L. Sun, F. Zhou, Z.-X. Zha, Europhys. Lett. 82 (2008) 57002.
[6] Z.-A. Ren, G.-C. Che, X.-L. Dong, J. Yang, W. Lu, W. Yi, X.-L. Shen, Z.-C. Li, L.-L. Sun, F. Zhou, Z.-X. Zhao, Europhys. Lett. 83 (2008) 17002.
[7] P. Cheng, L. Fang, H. Yang, X.-Y. Zhu, G. Mu, H.Q. Luo, Z.S. Wang, H.H. Wen, Sci. China, Ser. G51 (2008) 719.
[8] Z.-A. Ren, J. Yang, W. Lu, W. Yi, G.-C. Che, X.-L. Dong, L.-L. Sun, Z.-X. Zhao, Mater. Res. Innov. 12 (2008) 105.
[9] J.-W.G. Bos, G.B.S. Penny, J.A. Rodgers, D.A. Sokolov, A.D. Huxley, J.P. Attfield, Chem. Commun. (2008) 3634.
[10] M. Rotter, M. Tegel, D. Johrendt, Phys. Rev. Lett. 101 (2008) 107006.
[11] K. Sasmal, B. Lv, B. Lorenz, A.M. Guloy, F. Chen, Y.-Y. Xue, C.-W. Chu, Phys. Rev. Lett. 101 (2008) 107007.
[12] G. Wu, H. Chen, T. Wu, Y.L. Xie, Y.J. Yan, R.H. Liu, X.F. Wang, J.J. Ying, X.H. Chen, J. Phys. Condens. Matter 20 (2008) 422201.
[13] H.S. Jeevan, Z. Hossain, D. Kasinathan, H. Rosner, C. Geibel, P. Gegenwart, Phys. Rev. B 78 (2008) 092406.
[14] Y. Qi, Z. Gao, L. Wang, D. Wang, X. Zhang, Y. Ma, New J. Phys. 10 (2008) 123003.
[15] A.S. Sefat, R. Jin, M.A. McGuire, B.C. Sales, D.J. Singh, D. Mandrus, Phys. Rev. Lett. 101 (2008) 117004.
[16] A. Leithe-Jasper, W. Schnelle, C. Geibel, H. Rosner, Phys. Rev. Lett. 101 (2008) 207004.
[17] L.J. Li, Q.B. Wang, Y.K. Luo, H. Chen, Q. Tao, Y.K. Li, X. Lin, M. He, Z.W. Zhu, G.H. Cao, Z.A. Xu, New J. Phys. 11 (2009) 025008.
[18] T. Park, E. Park, H. Lee, T. Klimczuk, E.D. Bauer, F. Ronning, J.D. Thompson, J. Phys. Condens. Matter 20 (2008) 322204.
[19] M.S. Torikachvili, S.L. Bud'ko, N. Ni, P.C. Canfield, Phys. Rev. Lett. 101 (2008) 057006.
[20] K. Igawa, H. Okada, H. Takahashi, S. Matsuishi, Y. Kamihara, M. Hirano, H. Hosono, K. Matsubayashi, Y. Uwatoko, J. Phys. Soc. Jpn. 78 (2009) 025001.
[21] P.L. Alireza, Y.T.C. Ko, J. Gillett, C.M. Petrone, J.M. Cole, S.E. Sebastian, G.G. Lonzarich, J. Phys.: Condens. Matter. 21 (2008) 012208.
[22] P. Wenz, H.J. Schuster, Z. Naturforsch, B Anorg. Chem. Org. Chem. 39 (1984) 1816.
[23] A.M. Abakumov, V.L. Aksenov, V.A. Alyoshin, E.V. Antipov, A.M. Balagurov, D.A. Mikhailova, S.N. Putilin, M.G. Rozova, Phys. Rev. Lett. 80 (1998) 385.
[24] C.-H. Lee, A. Iyo, H. Eisaki, H. Kito, M.T. Fernandez-Diaz, T. Ito, K. Kihou, H. Matsuhata, M. Braden, K. Yamada, J. Phys. Soc. Jpn. 77 (2008) 083704.
[25] H. Eisaki, A. Iyo, H. Kito, K. Miyazawa, P.M. Shirage, H. Matsuhata, K. Kihou, C.-H. Lee, N. Takeshita, R. Kumai, Y. Tomioka, T. Ito, J. Phys. Soc. Jpn. 77 (Suppl. C) (2008) 36.
[26] V.G. Kogan, Phys. Rev. B 24 (1981) 1572.
[27] M. Angst, R. Puzniak, A. Wisniewski, J. Jun, S.M. Kazakov, J. Karpinski, J. Roos, H. Keller, Phys. Rev. Lett. 88 (2002) 167004.
[28] M. Angst, R. Puzniak, in: B.P. Martines (Ed.), Focus on Superconductivity, vol. 1, Nova Science Publishers, New York, 2004, pp. 1–49. arXiv:0305048.
[29] J.D. Fletcher, A. Carrington, O.J. Taylor, S.M. Kazakov, J. Karpinski, Phys. Rev. Lett. 95 (2005) 097005.
[30] A. Gurevich, Phys. Rev. B 67 (2003) 184515.
[31] S. Weyeneth, R. Puzniak, U. Mosele, N.D. Zhigadlo, S. Katrych, Z. Bukowski, J. Karpinski, S. Kohout, J. Roos, H. Keller, J. Supercond. Nov. Magn. 22 (2009) 325.
[32] L. Balicas, A. Gurevich, Y.-J. Jo, J. Jaroszynski, D.C. Larbalestier, R. H. Liu, H. Chen, X.H. Chen, N.D. Zhigadlo, S. Katrych, Z. Bukowski, J. Karpinski, arXiv:0809.4223.
[33] J. Jaroszynski, F. Hunte, L. Balicas, Y.-J. Jo, I. Raicevic, A. Gurevich, D.C. Larbalestier, F.F. Balakirev, L. Fang, P. Cheng, Y. Jia, H.-H. Wen, Phys. Rev. B 78 (2008) 174523.
[34] A. Dubroka, K.W. Kim, M. Rössle, V.K. Malik, A.J. Drew, R.H. Liu, G. Wu, X.H. Chen, C. Bernhard, Phys. Rev. Lett. 101 (2008) 097011.
[35] L. Shan, Y. Wang, X. Zhu, G. Mu, L. Fang, C. Ren, H.-H. Wen, Europhys. Lett. 83 (2008) 57004.
[36] X. Zhu, H. Yang, L. Fang, G. Mu, H.-H. Wen, Supercond. Sci. Technol. 21 (2008) 105001.
[37] Y. Jia, P. Cheng, L. Fang, H.Q. Luo, H. Yang, C. Ren, L. Shan, C.-Z. Gu, H.-H. Wen, Appl. Phys. Lett. 93 (2008) 032503.
[38] C. Martin, R.T. Gordon, M.A. Tanatar, M.D. Vannette, M.E. Tillman, E.D. Mun, P.C. Canfield, V.G. Kogan, G.D. Samolyuk, J. Schmalian, R. Prozorov, arXiv:0807.0876.
[39] Y. Jia, P. Cheng, L. Fang, H. Yang, C. Ren, L. Shan, C.-Z. Gu, H.-H. Wen, Supercond. Sci. Technol. 21 (2008) 105018.
[40] U. Welp, R. Xie, A.E. Koshelev, W.K. Kwok, P. Cheng, L. Fang, H.-H. Wen, Phys. Rev. B 78 (2008) 140510.
[41] D. Kubota, T. Ishida, M. Ishikado, S. Shamoto, H. Kito, A. Iyo, H. Eisaki, arXiv:0810.5623.
[42] R. Okazaki, M. Konczykowski, C.J. van der Beek, T. Kato, K. Hashimoto, M. Shimozawa, H. Shishido, M. Yamashita, M. Ishikado, H. Kito, A. Iyo, H. Eisaki, S. Shamoto, T. Shibauchi, Y. Matsuda, Phys. Rev. B 79 (2009) 064520.
[43] F. Hunte, J. Jaroszynski, A. Gurevich, D.C. Larbalestier, R. Jin, A.S. Sefat, M.A. McGuire, B.C. Sales, D.K. Christen, D. Mandrus, Nature 453 (2008) 903.
[44] K. Matano, Z.A. Ren, X.L. Dong, L.L. Sun, Z.X. Zhao, G.-Q. Zheng, Europhys. Lett. 83 (2008) 57001.
[45] H. Ding, P. Richard, K. Nakayama, K. Sugawara, T. Arakane, Y. Sekiba, A. Takayama, S. Souma, T. Sato, T. Takahashi, Z. Wang, X. Dai, Z. Fang, G.F. Chen, J.L. Luo, N.L. Wang, Europhys. Lett. 83 (2008) 47001.
[46] D.V. Evtushinsky, D.S. Inosov, V.B. Zabolotnyy, A. Koitzsch, M. Knupfer, B. Buchner, M.S. Viazovska, G.L. Sun, V. Hinkov, A.V. Boris, C.T. Lin, B. Keimer, A. Varykhalov, A.A. Kordyuk, S.V. Borisenko, Phys. Rev. B 79 (2009) 054517.
[47] D. Daghero, M. Tortello, R.S. Gonnelli, V.A. Stepanov, N.D. Zhigadlo, J. Karpinski, arXiv:0812.1141.
[48] R.S. Gonnelli, D. Daghero, M. Tortello, G.A. Ummarino, V.A. Stepanov, J.S. Kim, R.K. Kremer, arXiv: 0807.3149.
[49] M.R. Eskildsen, M. Kugler, G. Levy, S. Tanaka, J. Jun, S.M. Kazakov, J. Karpinski, Ø. Fischer, Physica C 385 (2003) 169.
[50] N.D. Zhigadlo, S. Katrych, Z. Bukowski, S. Weyeneth, R. Puzniak, J. Karpinski, J. Phys. Condens. Matter 20 (2008) 342202.
[51] L. Fang, P. Cheng, Y. Jia, X.Y. Zhu, H.Q. Luo, G. Mu, C.-Z. Gu, H.-H. Wen, J. Cryst. Growth 311 (2009) 358.
[52] P.C. Canfield, Z. Fisk, Philos. Mag. B 65 (1992) 1117.
[53] N. Ni, S.L. Bud'ko, A. Kreyssig, S. Nandi, G.E. Rustan, A.I. Goldman, S. Gupta, J.D. Corbett, A. Kracher, P.C. Canfield, Phys. Rev. B 78 (2008) 014507.
[54] X.F. Wang, T. Wu, G. Wu, H. Chen, Y.L. Xie, J.J. Ying, Y.J. Yan, R.H. Liu, X.H. Chen, Phys. Rev. Lett. 102 (2009) 117005.
[55] Z. Bukowski, S. Weyeneth, R. Puzniak, P. Moll, S. Katrych, N.D. Zhigadlo, J. Karpinski, H. Keller, B. Batlogg, Phys. Rev. B 79 (2009) 104521.
[56] Oxford Diffraction Ltd. XCalibur 2003 *CrysAlis Software System* Version 1.170.
[57] Sheldrick G 1997 SHELXS-97: *Program for the Solution of Crystal Structures*, University of Göttingen, Germany.
[58] Sheldrick G 1997 *SHELXL-97: Program for the Refinement of Crystal Structures*, University of Göttingen, Germany.
[59] S. Kohout, J. Roos, H. Keller, Rev. Sci. Instrum. 78 (2007) 013903.
[60] R.S. Gonnelli, D. Daghero, D. Delaude, M. Tortello, G.A. Ummarino, V.A. Stepanov, J.S. Kim, R.K. Kremer, A. Sanna, G. Profeta, S. Massidda, Phys. Rev. Lett. 100 (2008) 207004.
[61] V.G. Kogan, Phys. Rev. Lett. 89 (2002) 237005.
[62] S. Weyeneth, R. Puzniak, N.D. Zhigadlo, S. Katrych, Z. Bukowski, J. Karpinski, H. Keller, J. Supercond. Nov. Magn. 22 (2009) 347.
[63] J. Rammer, Europhys. Lett. 5 (1988) 77.
[64] H. Luetkens, H.-H. Klauss, R. Khasanov, A. Amato, R. Klingeler, I. Hellmann, N. Leps, A. Kondrat, C. Hess, A. Köhler, G. Behr, J. Werner, B. Büchner, Phys. Rev. Lett. 101 (2008) 097009.
[65] R. Khasanov, H. Luetkens, A. Amato, H.-H. Klauss, Z.-A. Ren, J. Yang, W. Lu, Z.-X. Zhao, Phys. Rev. B 78 (2008) 092506.
[66] L. Malone, J.D. Fletcher, A. Serafin, A. Carrington, N.D. Zhigadlo, Z. Bukowski, S. Katrych, J. Karpinski, Phys. Rev. B, in press, arXiv:0806.3908.
[67] N.R. Werthamer, E. Helfand, P.C. Hohenberg, Phys. Rev. 147 (1966) 295.
[68] A. Plecenik, M. Grajcar, Š. Beňačka, A. Seidel, A. Pfuch, Phys. Rev. B 49 (1994) 10016.
[69] G.E. Blonder, M. Tinkham, T.M. Klapwijk, Phys. Rev. B 25 (1982) 4515.
[70] S. Kashiwaya, Y. Tanaka, M. Koyanagi, K. Kajimura, Phys. Rev. B 53 (1996) 2667.
[71] R.S. Gonnelli, D. Daghero, G.A. Ummarino, V.A. Stepanov, J. Jun, S.M. Kazakov, J. Karpinski, Phys. Rev. Lett. 89 (2002) 247004.
[72] Ø. Fischer, M. Kugler, I. Maggio-Aprile, C. Berthod, C. Renner, Rev. Mod. Phys. 79 (2007) 353.
[73] P. Samuely, P. Szabo, Z. Pribulova, M.E. Tillman, S. Bud'ko, P.C. Canfield, Supercond. Sci. Tech. 22 (2009) 014003.
[74] Y. Yin, M. Zech, T.L. Williams, X.F. Wang, G. Wu, X.H. Chen, J.E. Hoffman, Phys. Rev. Lett. 102 (2009) 097002.

5 Concluding Remarks

High-temperature superconductivity is an exciting and fascinating field in modern condensed matter physics research, incorporating a tremendous amount of physics within a variety of systems. To find a pathway to superconducting systems with higher transition temperatures is for technical and academic reasons of great interest.

In this thesis critical fluctuation effects of the order parameter were investigated in the three different high-T_c superconductors MgB_2, $YBa_2Cu_4O_8$, and $Bi_2Sr_2CaCu_2O_{8+\delta}$ [83, 84, 85]. The magnetization data close to T_c reveal remarkable consistency with 3D-xy critical behavior. It was shown that the universal scaling properties are essentially the same in comparison with those of superfluid ^{4}He. The parameter H_{c2} is affirmed to be an artefact of the mean-field approach, since finite size effects, induced either by inhomogeneity or an applied magnetic field dominate at the phase boundary, resulting in a rounded transition. The data evidence a dimensional crossover of the macroscopic superconducting state, from an effective 3D to a quasi 1D behavior. In addition, a vortex-lattice melting transition is observed, consistent with the predictions of the 3D-xy model. Whereas the anisotropy parameter for both, MgB_2 and $YBa_2Cu_4O_8$ is well below 10, the quasi two-dimensional system $Bi_2Sr_2CaCu_2O_{8+\delta}$ exhibits a more complex fluctuation behavior close to T_c. Here the relatively high anisotropy parameter leads to a 2D-xy behavior sufficiently below T_c. The fluctuating magnetization data are well described within the Kosterlitz-Thouless theory applied to stacked superconductors, whereas close to T_c the system shows 3D-xy critical behavior. Consequently, an additional 2D to 3D crossover takes place which is reflected in the magnetic behavior.

Magnetization experiments were performed on novel iron-pnictide superconductors [161, 162, 182, 198, 199]. The availability of $SmFeAsO_{1-x}F_y$ and $NdFeAsO_{1-x}F_y$ single crystals made it possible to determine the anisotropy parameter in the $L1111$ family of iron-pnictides. Interestingly enough, the magnetic penetration depth anisotropy γ_λ is temperature dependent and increases from $\gamma_\lambda(T_c) \simeq 7$ towards $\gamma_\lambda(0) \simeq 19$, while the upper critical field anisotropy γ_H decreases from $\gamma_H(T_c) \simeq 7$ towards $\gamma_H(0) \simeq 2$. Such an unconventional behavior of the anisotropy parameter is strikingly similar to that observed in the two-gap superconductor MgB_2, where both, γ_λ and γ_H are found to be temperature dependent as well, but with reversed slopes as compared to the iron-pnictide superconductors. Although the direct origin of the temperature dependent anisotropy parameters in the iron-pnictides is so far not clarified, such a temperature dependence is characteristic for an anisotropic pairing mechanism involving multiple energy gaps. A two-band model involving a pairing mechanism based on polaron formation has been proposed for the iron-pnictides by Bussmann-Holder *et al.* [39], similar to that reported for cuprates [40, 41]. This appears to be a plausible scenario for the iron-pnictides.

Apparently, all superconductors known with $T_c > 30$ K, have striking features in common, although the chemical composition is quite different (cuprates, diborides, pnictides). It is evident that all high-T_c superconductors have a characteristic anisotropy, in connection

with a layered structure, which seems to be an essential ingredient to achieve high temperature superconductivity. In addition, the multi-band structure of these materials, makes it plausible that multi-gap superconductivity must be involved in the superconducting mechanism. This scenario is strongly evidenced for the cuprates [34, 35, 36], well-established for MgB_2 [29, 31, 32, 33], highly supported for the iron-pnictides [37, 162, 183, 184, 185, 186, 187, 188, 189, 198, 199], and presumably essential for high-T_c superconductivity in general. Obviously high-T_c superconductivity is based on universal ingredients, which must not be disregarded in a unified theoretical description.

To find further conclusion, it will be important to determine the anisotropy parameter for all the different types of iron-pnictide superconductors in order to clarify the relation between the band structure and the anisotropic properties. This may help to understand the multi-band structure for identifying the origin of the multiple superconducting gaps. Of further interest will be to verify the fluctuation phenomena in the recently discovered iron-based superconductors with T_c up to 56 K. The rather short coherence lengths and extremely high "upper critical fields" make these materials highly interesting for investigations of the magnetic field induced finite size effect. Lastly, since the anisotropy parameter is known to be strongly doping dependent in the cuprates, a similar scenario is expected in the pnictides. Such a doping dependence is well expected for a polaronic pairing mechanism, since the anisotropic effects are strongly related to the amount of polaronic carriers. In order to draw definite conclusions on multi-band superconductivity in the high-T_c's, an extended torque study on various cuprate superconductors is desired, in order to investigate how the anisotropy parameter depends on external parameters.

Bibliography

[1] H. Kamerlingh Onnes, *The liquefaction of helium*, Proc. K. Akad. Amsterdam **11**, 168 (1908).

[2] H. Kamerlingh Onnes, *Further experiments with liquid helium D - On the change of the electrical resistance of pure metals at very low temperatures, etc. V The disappearance of the resistance of mercury*, Proc. K. Akad. Amsterdam **14**, 113 (1911).

[3] H. Kamerlingh Onnes, *The resistance of pure mercury at helium temperatures*, Comm. Phys. Lab. Leiden **120b** (1911).

[4] H. Kamerlingh Onnes, *The disappearance of the resistance of mercury*, Comm. Phys. Lab. Leiden **122b** (1911).

[5] H. Kamerlingh Onnes, *On the sudden change in the rate at which the resistance of mercury disappears*, Comm. Phys. Lab. Leiden **124c** (1911).

[6] W. Buckel and R. Kleiner, *Supraleitung: Grundlagen und Anwendungen*, Wiley-VCH, Wernheim, 2004.

[7] W. Meissner and R. Ochsenfeld, *Short initial announcements*, Naturwissenschaften **21**, 787 (1933).

[8] F. London and H. London, *Supra conduction and diamagnetism*, Physica (Amsterdam) **2**, 341 (1935).

[9] F. London and H. London, *The electromagnetic equations of the supraconductor*, Proc. R. Soc. A **149**, 71 (1935).

[10] V. L. Ginzburg and L. D. Landau, *On the theory of superconductivity*, Zh. Eksp. Theor. Fiz. **20**, 1064 (1950).

[11] C. A. Reynolds, B. Serin, W. H. Wright, and L. B. Nesbitt, *Superconductivity of isotopes of mercury*, Phys. Rev. **78**, 487 (1950).

[12] E. Maxwell, *Isotope effect in the superconductivity of mercury*, Phys. Rev. **78**, 477 (1950).

[13] H. Fröhlich, *Theory of the superconducting state I. The ground state at the absolute zero of temperature*, Phys. Rev. **79**, 845 (1950).

[14] H. Fröhlich, *Isotope effect in superconductivity*, Proc. R. Soc. A **63**, 778 (1950).

[15] J. G. Daunt and K. Mendelssohn, *An experiment on the mechanism of superconductivity*, Proc. R. Soc. A **185**, 225 (1946).

[16] J. Bardeen, L. N. Cooper, and J. R. Schrieffer, *Microscopic theory of superconductivity*, Phys. Rev. **106**, 162 (1957).

[17] J. Bardeen, L. N. Cooper, and J. R. Schrieffer, *Theory of superconductivity*, Phys. Rev. **108**, 1175 (1957).

[18] L. N. Cooper, *Bound electron pairs in a degenerate Fermi gas*, Phys. Rev. **104**, 1189 (1956).

[19] B. T. Matthias, T. H. Geballe, R. H. Willens, E. Corenzwit, and G. W. Hull, *Superconductivity of Nb_3Ge*, Phys. Rev. **139**, A1501 (1965).

[20] J. R. Gavaler, *Superconductivity in Nb-Ge Films above 22 K*, Appl. Phys. Lett. **23**, 480 (1973).

[21] J. G. Bednorz and K. A. Müller, *Possible high-T_c superconductivity in the Ba-La-Cu-O system*, Z. Phys. B - Condens. Matter **64**, 189 (1986).

[22] P. Dai, B. C. Chakoumakos, G. F. Sun, K. W. Wong, Y. Xin, and D. F. Lu, *Synthesis and neutron powder diffraction study of the superconductor $HgBa_2Ca_2Cu_3O_{8+\delta}$ by Tl substitution*, Physica C **243**, 201 (1995).

[23] A. Schilling, M. Cantoni, J. D. Guo, and H. R. Ott, *Superconductivity above 130 K in the Hg-Ba-Ca-Cu-O system*, Nature (London) **363**, 56 (1993).

[24] J. Nagamatsu, N. Nakagawa, T. Muranaka, Y. Zenitani, and J. Akimitsu, *Superconductivity at 39 K in magnesium diboride*, Nature (London) **410**, 63 (2001).

[25] Y. Kamihara, T. Watanabe, M. Hirano, and H. Hosono, *Iron-based layered superconductor $La[O_{1-x}F_x]FeAs$ (x=0.05-0.12) with T_c=26 K*, J. Am. Chem. Soc. **130**, 3296 (2008).

[26] D. Zech, *A magnetization study of cuprate superconductors*, Ph.D. thesis, University of Zurich, 1995.

[27] M. Willemin, *Ultrasensitive torque magnetometry on high-T_c superconductors*, Ph.D. thesis, University of Zurich, 1999.

[28] J. Hofer, *Studies of intrinsic magnetic properties of high temperature superconductors by means of torque magnetometry*, Ph.D. thesis, University of Zurich, 2000.

[29] M. Angst, *Studies of magnetic properties of novel superconductors by means of SQUID and torque magnetometry*, Ph.D. thesis, ETH Zurich, 2003.

[30] S. Kohout, *Torque magnetometry in novel superconductors*, Ph.D. thesis, University of Zurich, 2005.

[31] A. Y. Liu, I. I. Mazin, and J. Kortus, *Beyond Eliashberg superconductivity in MgB_2: Anharmonicity, two-phonon scattering, and multiple gaps*, Phys. Rev. Lett. **87**, 087005 (2001).

[32] M. Angst, R. Puzniak, A. Wisniewski, J. Jun, S. M. Kazakov, J. Karpinski, J. Roos, and H. Keller, *Temperature and field dependence of the anisotropy of MgB_2*, Phys. Rev. Lett. **88**, 167004 (2002).

[33] M. Angst and R. Puzniak, *Focus on superconductivity*, edited by B. P. Martines, Nova Science, New York, 2004.

[34] R. Khasanov, A. Shengelaya, A. Maisuradze, F. La Mattina, A. Bussmann-Holder, H. Keller, and K. A. Müller, *Experimental evidence for two gaps in the high-temperature $La_{1.83}Sr_{0.17}CuO_4$ superconductor*, Phys. Rev. Lett. **98**, 057007 (2007).

[35] R. Khasanov, S. Strässle, D. D. Castro, T. Masui, S. Miyasaka, S. Tajima, A. Bussmann-Holder, and H. Keller, *Multiple gap symmetries for the order parameter of cuprate superconductors from penetration depth measurements*, Phys. Rev. Lett. **99**, 237601 (2007).

[36] A. Bussmann-Holder, R. Khasanov, A. Shengelaya, A. Maisuradze, F. La Mattina, H. Keller, and K. A. Müller, *Mixed order parameter symmetries in cuprate superconductors*, EPL **77**, 27002 (2007).

[37] F. Hunte, J. Jaroszynski, A. Gurevich, D. C. Larbalestier, R. Jin, A. S. Sefat, M. A. McGuire, B. C. Sales, D. K. Christen, and D. Mandrus, *Two-band superconductivity in $LaFeAsO_{0.89}F_{0.11}$ at very high magnetic fields*, Nature (London) **453**, 903 (2008).

[38] A. Bussmann-Holder, R. Micnas, and A. R. Bishop, *Enhancements of the superconducting transition temperature within the two-band model*, Eur. Phys. J. B **37**, 345 (2004).

[39] A. Bussmann-Holder, A. Simon, H. Keller, and A. R. Bishop, *Identifying the pairing mechanism in Fe-As based superconductors: Gaps and isotope effects*, arXiv:cond-mat/0906.2283v1 (2009).

[40] A. Bussmann-Holder and H. Keller, *Polaron formation as origin of unconventional isotope effects in cuprate superconductors*, Eur. Phys. J. B **44**, 487 (2005).

[41] A. Bussmann-Holder, H. Keller, A. R. Bishop, A. Simon, R. Micnas, and K. A. Müller, *Unconventional isotope effects as evidence for polaron formation in cuprates*, EPL **72**, 423 (2005).

[42] H. Keller, A. Bussmann-Holder, and K. A. Müller, *Jahn-Teller physics and high-T_c superconductivity*, Materials Today **11**, 38 (2008).

[43] L. D. Landau, *The theory of phase transitions*, Nature (London) **138**, 840 (1936).

[44] M. Tinkham, *Introduction to superconductivity*, McGraw-Hill, New York, 1996.

[45] P. de Gennes, *Superconductivity of metals and alloys*, Addison-Wesley, 1965.

[46] V. G. Kogan, A. Gurevich, J. H. Cho, D. C. Johnston, M. Xu, J. R. Thompson, and A. Martynovich, *Nonlocal electrodynamics and low-temperature magnetization of clean high-κ superconductors*, Phys. Rev. B **54**, 12386 (1996).

[47] D. E. Farrell, J. P. Rice, D. M. Ginsberg, and J. Z. Liu, *Experimental evidence of a dimensional crossover in $Y_1 Ba_2 Cu_3 O_{7-\delta}$*, Phys. Rev. Lett. **64**, 1573 (1990).

[48] D. E. Farrell, R. G. Beck, M. F. Booth, C. J. Allen, E. D. Bukowski, and D. M. Ginsberg, *Superconducting effective-mass anisotropy in $Tl_2 Ba_2 CaCu_2 O_x$*, Phys. Rev. B **42**, 6758 (1990).

[49] G. Blatter, M. V. Feigel'mann, V. B. Geshkenbein, A. I. Larkin, and V. M. Vinokur, *Vortices in high-temperature superconductors*, Rev. Mod. Phys. **66**, 4 (1994).

[50] V. G. Kogan, *London approach to anisotropic type-II superconductors*, Phys. Rev. B **24**, 1572 (1981).

[51] V. G. Kogan, M. M. Fang, and S. Mitra, *Reversible magnetization of high-T_c materials in intermediate fields*, Phys. Rev. B **38**, 11958 (1988).

[52] Quantum Design, Inc., 11578 Sorrento Valley Road, San Diego, CA 92121-1311, USA. http://www.qdusa.com.

[53] T. P. Papageorgiou, L. Bauernfeind, and H. F. Braun, *Possible pitfalls in SQUID magnetometry of superconducting samples: The case of $RuSr_2 GdCu_2 O_8$*, J. Low Temp. Phys. **131**, 129 (2003).

[54] C. Rossel, P. Bauer, D. Zech, J. Hofer, M. Willemin, and H. Keller, *Active microlevers as miniature torque magnetometers*, J. Appl. Phys. **79**, 8166 (1996).

[55] M. Willemin, C. Rossel, J. Brugger, M. H. Despont, H. Rothuizen, P. Vettiger, J. Hofer, and H. Keller, *Piezoresistive cantilever designed for torque magnetometry*, J. Appl. Phys. **83**, 1163 (1998).

[56] C. Rossel, M. Willemin, A. Gasser, H. Bothuizen, G. I. Meijer, and H. Keller, *Torsion cantilever as magnetic torque sensor*, Rev. Sci. Instrum. **69**, 3199 (1998).

[57] S. Kohout, J. Roos, and H. Keller, *Novel sensor design for torque magnetometry*, Rev. Sci. Instrum. **78**, 013903 (2007).

[58] K. G. Wilson and J. B. Kogut, *The renormalization group and the ϵ-expansion*, Phys. Rept. **12**, 75 (1974).

[59] M. E. Fisher, *The renormalization group in the theory of critical behavior*, Rev. Mod. Phys. **46**, 597 (1974).

[60] P. C. Hohenberg, A. Aharony, B. I. Halperin, and E. D. Siggia, *Two-scale-factor universality and the renormalization group*, Phys. Rev. B **13**, 2986 (1976).

[61] T. Schneider and J. M. Singer, *Phase transition approach to high temperature superconductivity*, Imperial College Press, London, 2000.

[62] T. Schneider and D. Ariosa, *Thermal fluctuations in high-temperature superconductors*, Z. Phys. B - Condens. Matter **89**, 267 (1992).

[63] T. Schneider, *The physics of superconductors*, edited by K. Bennemann and J. B. Ketterson, Springer, Berlin, 2004.

[64] T. Schneider, J. Hofer, M. Willemin, J. M. Singer, and H. Keller, *Universal scaling properties of extreme type-II superconductors in magnetic fields*, Eur. Phys. J. B **3**, 413 (1998).

[65] R. Lortz, C. Meingast, A. I. Rykov, and S. Tajima, *Magnetic-field-induced finite-size effect in the high-temperature superconductor $YBa_2Cu_3O_{7-\delta}$: A comparison with rotating superfluid ^4He*, Phys. Rev. Lett. **91**, 207001 (2003).

[66] T. Schneider, *Magnetic field induced 3D-1D crossover in type-II superconductors*, J. Phys.: Condens. Matter **20**, 423201 (2008).

[67] J. Hofer, T. Schneider, J. M. Singer, M. Willemin, H. Keller, C. Rossel, and J. Karpinski, *Angular-dependent torque magnetometry on single-crystal $HgBa_2CuO_{4+y}$ near the critical temperature*, Phys. Rev. B **60**, 1332 (1999).

[68] A. Pelissetto and E. Vicari, *Critical phenomena and renormalization-group theory*, Phys. Rept. **368**, 549 (2002).

[69] T. Schneider and H. Keller, *Extreme type-II superconductors - Universal properties and trends*, Int. J. Mod. Phys. B **8**, 487 (1994).

[70] N. Overend, M. A. Howson, and I. D. Lawrie, *3D $X-Y$ scaling of the specific heat of $YBa_2Cu_3O_{7-\delta}$ single crystals*, Phys. Rev. Lett. **72**, 3238 (1994).

[71] S. Kamal, D. A. Bonn, N. Goldenfeld, P. J. Hirschfeld, R. Liang, and W. N. Hardy, *Penetration depth measurements of 3D XY critical behavior in $YBa_2Cu_3O_{6.95}$ crystals*, Phys. Rev. Lett. **73**, 1845 (1994).

[72] M. A. Hubbard, M. B. Salamon, and B. W. Veal, *Fluctuation diamagnetism and mass anisotropy of $YBa_2Cu_3O_{6+x}$*, Physica C **259**, 309 (1996).

[73] Y. Jaccard, T. Schneider, J.-P. Looquet, E. J. Williams, P. Martinoli, and O. Fischer, *Evidence of 3D-XY critical behaviour in $La_{2-x}Sr_xCuO_4$ Films*, EPL **34**, 281 (1996).

[74] S. Kamal, R. Liang, A. Hosseini, D. A. Bonn, and W. N. Hardy, *Magnetic penetration depth and surface resistance in ultrahigh-purity $YBa_2Cu_3O_{7-\delta}$ crystals*, Phys. Rev. B **58**, R8933 (1998).

[75] V. Pasler, P. Schweiss, C. Meingast, B. Obst, H. Wühl, A. I. Rykov, and S. Tajima, *3D-XY critical fluctuations of the thermal expansivity in detwinned $YBa_2Cu_3O_{7-\delta}$ single crystals near optimal doping*, Phys. Rev. Lett. **81**, 1094 (1998).

[76] M. Roulin, A. Junod, and E. Walker, *Observation of second-order transitions below T_c in the specific heat of $YBa_2Cu_3O_x$: Case for the melting of a vortex glass*, Physica C **296**, 137 (1998).

[77] D. Babić, J. R. Cooper, J. W. Hodby, and C. Changkang, *Changes in irreversibility line, anisotropy, and condensation energy by oxygen depletion of $YBa_2Cu_3O_{7-\delta}$*, Phys. Rev. B **60**, 698 (1999).

[78] T. Schneider, *Probing thermal fluctuations and inhomogeneities in type II superconductors by means of applied magnetic fields*, arXiv:cond-mat/0210702v1 (2002).

[79] T. Schneider, *Probing inhomogeneities in type II superconductors by means of thermal fluctuations, magnetic fields, and isotope effects*, J. Supercond. Nov. Magn. **17**, 41 (2004).

[80] T. Plackowski, Y. Wang, R. Lortz, A. Junod, and T. Wolf, *Reversible and irreversible magnetocaloric effect in the $NdBa_2Cu_3O_7$ superconductor in relation to specific heat and magnetization*, J. Phys.: Condens. Matter **17**, 6871 (2005).

[81] T. Schneider, *Evidence for three-dimensional XY critical properties in underdoped $YBa_2Cu_3O_{7-\delta}$*, Phys. Rev. B **75**, 174517 (2007).

[82] T. Schneider, *Magnetic-field-induced 3D-to-1D crossover in $Sr_{0.9}La_{0.1}CuO_2$*, EPL **79**, 57005 (2007).

[83] S. Weyeneth, T. Schneider, N. D. Zhigadlo, J. Karpinski, and H. Keller, *Probing superconductivity in MgB_2 confined to magnetic field tuned cylinders by means of critical fluctuations*, J. Phys.: Condens. Matter **20**, 135208 (2008).

[84] S. Weyeneth, T. Schneider, Z. Bukowski, J. Karpinski, and H. Keller, *3D-xy critical properties of $YBa_2Cu_4O_8$ and magnetic-field-induced 3D to 1D crossover*, J. Phys.: Condens. Matter **20**, 345210 (2008).

[85] S. Weyeneth, T. Schneider, and E. Giannini, *Evidence for Kosterlitz-Thouless and 3D-xy critical behavior in $Bi_2Sr_2CaCu_2O_{8+\delta}$*, Phys. Rev. B **79**, 214504 (2009).

[86] A. B. Harris, *Effect of random defects on the critical behaviour of Ising models*, J. Phys. C: Solid State Phys. **7**, 1671 (1974).

[87] *Finite-size scaling*, edited by J. L. Cardy, Amsterdam: North-Holland, 1988.

[88] V. Privman, *Finite size scaling and numerical simulations of statistical systems*, Singapore: World Scientific, 1990.

[89] A. Abrikosov, *On the magnetic properties of superconductors of the second group*, Sov. Phys. JETP **5**, 1174 (1957).

[90] R. E. Prange, *Diamagnetic susceptibility at the transition to the superconducting state*, Phys. Rev. B **1**, 2349 (1970).

[91] S. L. Lee, P. Zimmermann, H. Keller, M. Warden, I. M. Savić, R. Schauwecker, D. Zech, R. Cubitt, E. M. Forgan, P. H. Kes, T. W. Li, A. A. Menovski, and Z. Tarnawski, *Evidence for flux-lattice melting and a dimensional crossover in single-crystal $Bi_{2.15}Sr_{1.85}CaCu_2O_{8+\delta}$ from muon spin rotation studies*, Phys. Rev. Lett. **71**, 3862 (1993).

[92] A. Schilling, R. A. Fisher, N. E. Phillips, U. Welp, D. Dasgupta, W. K. Kwok, and G. W. Crabtree, *Calorimetric measurement of the latent heat of vortex-lattice melting in untwinned $YBa_2Cu_3O_{7-\delta}$*, Nature (London) **382**, 791 (1996).

[93] M. Willemin, A. Schilling, H. Keller, C. Rossel, J. Hofer, U. Welp, W. K. Kwok, R. J. Olsson, and G. W. Crabtree, *First-order vortex-lattice melting transition in $YBa_2Cu_3O_{7-\delta}$ near the critical temperature detected by magnetic torque*, Phys. Rev. Lett. **81**, 4236 (1998).

[94] W. N. Kang, K. H. P. Kim, H.-J. Kim, E.-M. Choi, M.-S. Park, M.-S. Kim, Z.-L. Du, C. U. Jung, K. H. Kim, S.-I. Lee, and M.-O. Mun, *Fluctuation of superconductivity in MgB_2*, J. Korean Phys. Soc. **40**, 949 (2002).

[95] T. Park, M. B. Salamon, C. U. Jung, M.-S. Park, K. Kim, and S.-I. Lee, *Fluctuation study of the specific heat of $Mg^{11}B_2$*, Phys. Rev. B **66**, 134515 (2002).

[96] A. Lascialfari, T. Mishonov, A. Rigamonti, P. Tedesco, and A. Varlamov, *Superconducting diamagnetic fluctuations in MgB_2*, Phys. Rev. B **65**, 180501(R) (2002).

[97] J. Karpinski, M. Angst, J. Jun, S. M. Kazakov, R. Puzniak, A. Wisniewski, J. Roos, H. Keller, A. Perucchi, L. Degiorgi, M. R. Eskildsen, P. Bordet, L. Vinnikov, and A. Mironov, *MgB_2 single crystals: High pressure growth and physical properties*, Supercond. Sci. Technol. **16**, 221 (2003).

[98] A. Larkin and A. Varlamov, *Theory of fluctuations in superconductors*, Oxford: Oxford University Press, 2005.

[99] A. Lascialfari, P. Tedesco, and I. Zucca, *Superconducting fluctuations and related fluctuating diamagnetism in YBCO124*, Int. J. Mod. Phys. B **17**, 805 (2003).

[100] C. Baraduc, A. Buzdin, J.-Y. Henry, J.-P. Brison, and L. Puech, *Fluctuations in quasi-2D superconductors under magnetic field: The case of $YBa_2Cu_3O_{7-\delta}$*, Physica C **248**, 138 (1995).

[101] B. Rosenstein, B. Y. Shapiro, R. Prozorov, A. Shaulov, and Y. Yesherun, *Fluctuations in single-crystal $YBa_2Cu_3O_{6.5}$: Evidence for crossover from two-dimensional to three-dimensional behavior*, Phys. Rev. B **63**, 134501 (2001).

[102] A. Rigamonti, A. Lascialfari, L. Romanó, A. Varlamov, and I. Zucca, *Superconducting fluctuating diamagnetism versus precursor diamagnetism in heterogeneous superconductors*, J. Supercond. **18**, 763 (2005).

[103] J. Karpinski, E. Kaldis, E. Jilek, S. Rusiecki, and B. Bucher, *Bulk synthesis of the 81-K superconductor $YBa_2Cu_4O_8$ at high oxygen pressure*, Nature (London) **336**, 660 (1988).

[104] J. Karpinski, G. I. Meijer, H. Schwer, R. Molinski, E. Kopnin, K. Conder, M. Angst, J. Jun, S. Kazakov, A. Wisniewski, R. Puzniak, J. Hofer, V. Alyoshin, and A. Sin, *High-pressure synthesis, crystal growth, phase diagrams, structural and magnetic properties*

of $Y_2Ba_4Cu_nO_{2n+x}$, $HgBa_2Ca_{n-1}Cu_nO_{2n+2+\delta}$ *and quasi-one-dimensional cuprates*, Supercond. Sci. Technol. **12**, R153 (1999).

[105] V. L. Berezinskii, *Destruction of long-range order in one-dimensional and two-dimensional systems possessing a continuous symmetry group 2. Quantum systems*, Sov. Phys. JETP **34**, 610 (1972).

[106] J. M. Kosterlitz and D. J. Thouless, *Ordering, metastability and phase transitions in two-dimensional systems*, J. Phys. C **6**, 1181 (1973).

[107] V. Oganesyan, D. A. Huse, and S. L. Sondhi, *Theory of diamagnetic response of the vortex liquid phase of two-dimensional superconductors*, Phys. Rev. B **73**, 094503 (2006).

[108] A. Revcolevschi and J. Jegoudez, *Growth of large high-T_c single crystals by the floating zone method: A review*, Prog. Mat. Sci. **42**, 321 (1997).

[109] G. Triscone, A. Junod, and R. E. Gladyshevskii, *Magnetic and thermal properties of the 116 K superconductor Tl-1223*, Physica C **264**, 233 (1996).

[110] G. Triscone, M. S. Chae, M. C. de Andrade, and M. B. Maple, *Magnetic properties of the* $Bi_{1.95}Sr_{2.05-x}La_xCuO_y$ *(Bi-2201) superconducting phase*, Physica C **290**, 188 (1997).

[111] H. Iwasaki, F. Matsuoka, and K. Tanigawa, *Magnetization peak around $H||a$ axis in* $La_{2-x}Sr_xCuO_4$ *single crystals with different anisotropy*, Phys. Rev. B **59**, 14624 (1999).

[112] A. Junod, A. Erb, and C. Renner, *Specific heat of high temperature superconductors in high fields at T_c: From BCS to the Bose-Einstein condensation*, Physica C **317**, 333 (1999).

[113] V. Johnson and W. Jeitschko, *ZrCiSiAs - Filled PbFCl-type*, J. Solid State Chem. **11**, 161 (1974).

[114] M. Reehuis and W. Jeitschko, *Structure and magnetic-properties of the phosphides* $CaCo_2P_2$ *and* LnT_2P_2 *with* $ThCr_2Si_2$ *structure and lanthanoids FeP, lanthanoids CoP, lanthanoids NiP with PbFCl structure*, J. Phys. Chem. Solids **51**, 961 (1990).

[115] B. I. Zimmer, W. Jeitschko, J. H. Albering, R. Glaum, and M. Reehuis, *The rare earth transition metal phosphide oxides LnFePO, LnRuPO and LnCoPO with ZrCuSiAs type structure*, J. Alloys Comp. **229**, 238 (1995).

[116] P. Quebe, L. J. Terbuchte, and W. Jeitschko, *Quaternary rare earth transition metal arsenide oxides RTAsO (T = Fe, Ru, Co) with ZrCuSiAs type structure*, J. Alloys Comp. **302**, 70 (2000).

[117] Y. Kamihara, H. Hiramatsu, M. Hirano, R. Kawamura, H. Yanagi, T. Kamiya, and H. Hosono, *Iron-based layered superconductor: LaOFeP*, J. Am. Chem. Soc. **128**, 10012 (2006).

[118] Y. Maeno, H. Hashimoto, K. Yoshida, S. Nishizaki, T. Fujita, J. G. Bednorz, and F. Lichtenberg, *Superconductivity in a layered perovskite without Copper*, Nature (London) **372**, 532 (1994).

[119] S. Yonezawa, Y. Muraoka, Y. Matsushita, and Z. Hiroi, *Superconductivity in a pyrochlore-related oxide* KOs_2O_6, J. Phys.: Condens. Matter **16**, L9 (2004).

[120] T. Yamauchi, Y. Ueda, and N. Mori, *Pressure-induced superconductivity in* $\beta-Na_{0.33}V_2O_5$ *beyond charge ordering*, Phys. Rev. Lett. **89**, 057002 (2002).

[121] K. Takada, H. Sakurai, E. Takayama-Muromachi, F. Izumi, R. A. Dilanian, and T. Sasaki, *Superconductivity in two-dimensional* CoO_2 *layers*, Nature (London) **422**, 53 (2003).

[122] B. S. Chandrasekhar and J. K. Hulm, *The electrical resistivity and superconductivity of some uranium alloys and compounds*, J. Phys. Chem. Solids **7**, 259 (1958).

[123] B. T. Matthias, V. B. Compton, and E. Corenzwit, *Some new superconducting compounds*, J. Phys. Chem. Solids **19**, 130 (1961).

[124] H. F. Braun, *Superconductivity of rare earth-iron silicides*, Phys. Lett. A **75**, 386 (1980).

[125] C. U. Segre and H. F. Braun, *Reentrant superconductivity in* $Tm_2Fe_3Si_5$, Phys. Lett. A **85**, 372 (1981).

[126] G. P. Meisner, *Superconductivity and magnetic order in ternary rare-earth transition metal phosphides*, Physica B & C **108**, 763 (1981).

[127] I. Shirotani, Y. Shimaya, K. Kihou, C. Sekine, N. Takeda, M. Ishikawa, and T. Yagi, *Superconductivity of new filled skutterudite* YFe_4P_{12} *prepared at high pressure*, J. Phys.: Condens. Matter **15**, S2201 (2003).

[128] H. Takahashi, K. Igawa, K. Arii, Y. Kamihara, M. Hirano, and H. Hosono, *Superconductivity at 43 K in an iron-based layered compound* $LaO_{1-x}F_xFeAs$, Nature (London) **453**, 376 (2008).

[129] X. H. Chen, T. Wu, G. Wu, R. H. Liu, H. Chen, and D. F. Fang, *Superconductivity at 43 K in* $SmFeAsO_{1-x}F_x$, Nature (London) **453**, 761 (2008).

[130] G. F. Chen, Z. Li, D. Wu, G. Li, W. Z. Hu, J. Dong, P. Zheng, J. L. Luo, and N. L. Wang, *Superconductivity at 41 K and its competition with spin-density-wave instability in layered* $CeO_{1-x}F_xFeAs$, Phys. Rev. Lett. **100**, 247002 (2008).

[131] Z.-A. Ren, J. Yang, W. Lu, W. Yi, X.-L. Shen, Z.-C. Li, G.-C. Che, X.-L. Dong, L.-L. Sun, F. Zhou, and Z.-X. Zhao, *Superconductivity in the iron-based F-doped layered quaternary compound* $Nd[O_{1-x}F_x]FeAs$, EPL **82**, 57002 (2008).

[132] Z.-A. Ren, G.-C. Che, X.-L. Dong, J. Yang, W. Lu, W. Yi, X.-L. Shen, Z.-C. Li, L.-L. Sun, F. Zhou, and Z.-X. Zhao, *Superconductivity and phase diagram in iron-based arsenic-oxides $ReFeAsO_{1-\delta}$ (Re = rare-earth metal) without fluorine doping*, EPL **83**, 17002 (2008).

[133] P. Cheng, L. Fang, H. Yang, X. Y. Zhu, G. Mu, H. Q. Luo, Z. S. Wang, and H.-H. Wen, *Superconductivity at 36 K in gadolinium-arsenide oxides $GdO_{1-x}F_xFeAs$*, Sci. China, Ser. G **51**, 719 (2008).

[134] Z.-A. Ren, J. Yang, W. Lu, W. Yi, G.-C. Che, X.-L. Dong, L.-L. Sun, and Z.-X. Zhao, *Superconductivity at 52 K in iron based F doped layered quaternary compound $Pr[O_{1-x}F_x]FeAs$*, Mat. Res. Inn. **12**, 105 (2008).

[135] J.-W. G. Bos, G. B. S. Penny, J. A. Rodgers, D. A. Sokolov, A. D. Huxley, and J. P. Attfield, *High pressure synthesis of late rare earth RFeAs(O,F) superconductors; R = Tb and Dy*, Chem. Comm. , 3634 (2008).

[136] Z.-A. Ren, W. Lu, J. Yang, W. Yi, X.-L. Shen, Z.-C. Li, G.-C. Che, X.-L. Dong, L.-L. Sun, F. Zhou, and Z.-X. Zhao, *Superconductivity at 55 K in iron-based F-doped layered quaternary compound $Sm[O_{1-x}F_x]FeAs$*, Chin. Phys. Lett. **25**, 2215 (2008).

[137] W. Lu, X.-L. Shen, J. Yang, Z.-C. Li, W. Yi, Z.-A. Ren, X.-L. Dong, G.-C. Che, L.-L. Sun, F. Zhou, and Z.-X. Zhao, *Superconductivity at 41.0 K in the F-doped $LaFeAsO_{1-x}F_x$*, Supercond. Sci. Technol. **148**, 168 (2008).

[138] W. Yi, C. Zhang, L.-L. Sun, Z.-A. Ren, W. Lu, X.-L. Dong, Z.-C. Li, G.-C. Che, J. Yang, X.-L. Shen, X. Dai, Z. Fang, F. Zhou, and Z.-X. Zhao, *High-pressure study on $LaFeAs(O_{1-x}F_x)$ and LaFeAsO with different T_c*, EPL **84**, 67009 (2008).

[139] H. Kito, H. Eisaki, and A. Iyo, *Superconductivity at 54 K in F-free $NdFeAsO_{1-y}$*, J. Phys. Soc. Jap. **77**, 063707 (2008).

[140] J. Yang, Z.-C. Li, W. Lu, W. Yi, X.-L. Shen, Z.-A. Ren, G.-C. Che, X.-L. Dong, L.-L. Sun, F. Zhou, and Z.-X. Zhao, *Superconductivity at 53.5 K in $GdFeAsO_{1-\delta}$*, Supercond. Sci. Technol. **21**, 082001 (2008).

[141] J. Yang, X.-L. Shen, W. Lu, W. Yi, Z.-C. Li, Z.-A. Ren, G.-C. Che, X.-L. Dong, L.-L. Sun, F. Zhou, and Z.-X. Zhao, *Superconductivity in some heavy rare-earth iron arsenide $REFeAsO_{1-\delta}$ (RE = Ho, Y, Dy and Tb) compounds*, New J. Phys. **11**, 025005 (2008).

[142] Y. Kamihara, M. Hirano, H. Yanagi, T. Kamiya, Y. Saitoh, E. Ikenaga, K. Kobayashi, and H. Hosono, *Electromagnetic properties and electronic structure of the iron-based layered superconductor LaFePO*, Phys. Rev. B **77**, 214515 (2008).

[143] Y. Kamihara, H. Hiramatsu, M. Hirano, H. Yanagi, T. Kamiya, and H. Hosono, *Electronic and magnetic properties of layered LnFePO (Ln = La und Ce)*, J. Phys. Chem. Solids **69**, 2916 (2008).

[144] J. J. Hamlin, R. E. Baumbach, D. A. Zocco, T. A. Sayles, and M. B. Maple, *Superconductivity in single crystals of LaFePO*, J. Phys.: Condens. Matter **20**, 365220 (2008).

[145] R. E. Baumbach, J. J. Hamlin, L. Shu, D. A. Zocco, N. M. Crisosto, and M. B. Maple, *Superconductivity in LnFePO (Ln = La, Pr and Nd) single crystals*, New J. Phys. **11**, 025019 (2009).

[146] K. Igawa, H. Okada, K. Arii, H. Takahashi, Y. Kamihara, M. Hirano, H. Hosono, S. Nakano, and T. Kikegawa, *Pressure study of superconducting oxypnictide LaFePO*, J. Phys. Soc. Jap. **78**, 023701 (2009).

[147] R. Pöttgen and D. Johrendt, *Materials with ZrCuSiAs-type structure*, Z. Naturforsch. **63b**, 1135 (2008).

[148] Y.-P. Qi, L. Wang, Z.-S. Gao, D.-L. Wang, X.-P. Zhang, Z.-Y. Zhang, and Y.-W. Ma, *Superconductivity in Ir-doped $LaFe_{1-x}Ir_xAsO$*, Phys. Rev. B **80**, 054502 (2009).

[149] Y.-P. Qi, L. Wang, Z.-S. Gao, D.-L. Wang, X.-P. Zhang, Z.-Y. Zhang, and Y.-W. Ma, *Superconductivity in $SmFe_{1-x}M_xAsO$ (M = Co, Rh, Ir)*, EPL **89**, 67007 (2010).

[150] X.-Y. Zhu, F. Han, P. Cheng, G. Mu, B. Shen, and H.-H. Wen, *Superconductivity in fluorine-arsenide $Sr_{1-x}La_xFeAsF$*, EPL **85**, 17011 (2009).

[151] T. M. McQueen, M. Regulacio, A. J. Williams, Q. Huang, J. W. Lynn, Y. S. Hor, D. V. West, M. A. Green, and R. J. Cava, *Intrinsic properties of stoichiometric LaFePO*, Phys. Rev. B **78**, 024521 (2008).

[152] R. C. Che, R. J. Xiao, C. Y. Liang, H. X. Yang, C. Ma, H. Shi, and J. Q. Li, *Electron energy-loss spectroscopy and ab initio electronic structure of the LaOFeP superconductor*, Phys. Rev. B **77**, 184518 (2008).

[153] H. Okada, K. Igawa, H. Takahashi, Y. Kamihara, M. Hirano, H. Hosono, K. Matsubayashi, and Y. Uwatoko, *Superconductivity under high pressure in LaFeAsO*, J. Phys. Soc. Jap. **77**, 113712 (2008).

[154] C. Wang, L. Li, S. Chi, Z. Zhu, Z. Ren, Y. Li, Y. Wang, X. Lin, Y. Luo, S. Jiang, X. Xu, G. Cao, and Z. Xu, *Thorium-doping induced superconductivity up to 56 K in $Gd_{1-x}Th_xFeAsO$*, EPL **83**, 67006 (2008).

[155] H.-H. Wen, G. Mu, L. Fang, H. Yang, and X. Zhu, *Superconductivity at 25 K in hole-doped $(La_{1-x}Sr_x)OFeAs$*, EPL **82**, 17009 (2008).

[156] M. Rotter, M. Tegel, and D. Johrendt, *Superconductivity at 38 K in the iron arsenide $(Ba_{1-x}K_x)Fe_2As_2$*, Phys. Rev. Lett. **101**, 107006 (2008).

[157] K. Sasmal, B. Lv, B. Lorenz, A. M. Guloy, F. Chen, Y.-Y. Xue, and C.-W. Chu, *Superconducting Fe-based compounds $(A_{1-x}Sr_x)Fe_2As_2$ with A = K and Cs with transition temperatures up to 37 K*, Phys. Rev. Lett. **101**, 107007 (2008).

[158] G. Wu, H. Chen, T. Wu, Y. L. Xie, Y. J. Yan, R. H. Liu, X. F. Wang, J. J. Ying, and X. H. Chen, *Different resistivity response to spin-density wave and superconductivity at 20 K in $Ca_{1-x}Na_xFe_2As_2$*, J. Phys.: Condens. Matter **20**, 422201 (2008).

[159] H. S. Jeevan, Z. Hossain, D. Kasinathan, H. Rosner, C. Geibel, and P. Gegenwart, *High-temperature superconductivity in $Eu_{0.5}K_{0.5}Fe_2As_2$*, Phys. Rev. B **78**, 092406 (2008).

[160] Y. Qi, Z. Gao, L. Wang, D. Wang, X. Zhang, and Y. Ma, *Superconductivity at 34.7 K in the iron arsenide $Eu_{0.7}Na_{0.3}Fe_2As_2$*, New J. Phys. **10**, 123003 (2008).

[161] Z. Bukowski, S. Weyeneth, R. Puzniak, P. Moll, S. Katrych, N. D. Zhigadlo, J. Karpinski, H. Keller, and B. Batlogg, *Superconductivity at 23 K and low anisotropy in Rb-substituted $BaFe_2As_2$ single crystals*, Phys. Rev. B **79**, 104521 (2009).

[162] J. Karpinski et al., *Single crystals of $LnFeAsO_{1-x}F_x$ (Ln = La, Pr, Nd, Sm, Gd) and $Ba_{1-x}Rb_xFe_2As_2$: Growth, structure and superconducting properties*, Physica C **469**, 370 (2009).

[163] A. S. Sefat, R. Jin, M. A. McGuire, B. C. Sales, D. J. Singh, and D. Mandrus, *Superconductivity at 22 K in Co-doped $BaFe_2As_2$ crystals*, Phys. Rev. Lett. **101**, 117004 (2008).

[164] A. Leithe-Jasper, W. Schnelle, C. Geibel, and H. Rosner, *Superconducting state in $SrFe_{2-x}Co_xAs_2$ by internal doping of the iron arsenide layers*, Phys. Rev. Lett. **101**, 207004 (2008).

[165] L. J. Li, Y. K. Luo, Q. B. Wang, H. Chen, Z. Ren, Q. Tao, Y. K. Li, X. Lin, M. He, Z. W. Zhu, G. H. Cao, and Z. A. Xu, *Superconductivity induced by Ni doping in $BaFe_2As_2$ single crystals*, New J. Phys. **11**, 025008 (2009).

[166] T. Park, E. Park, H. Lee, T. Klimczuk, E. D. Bauer, F. Ronning, and J. D. Thompson, *Pressure-induced superconductivity in $CaFe_2As_2$*, J. Phys.: Condens. Matter **20**, 322204 (2008).

[167] M. S. Torikachvili, S. L. Bud'ko, N. Ni, and P. C. Canfield, *Pressure induced superconductivity in $CaFe_2As_2$*, Phys. Rev. Lett. **101**, 057006 (2008).

[168] K. Igawa, H. Okada, H. Takahashi, S. Matsuishi, Y. Kamihara, M. Hirano, H. Hosono, K. Matsubayashi, and Y. Uwatoko, *Pressure-induced superconductivity in iron pnictide compound $SrFe_2As_2$*, J. Phys. Soc. Jap. **78**, 025001 (2009).

[169] P. L. Alireza, Y. T. C. Ko, J. Gillett, C. M. Petrone, J. M. Cole, S. E. Sebastian, and G. G. Lonzarich, *Superconductivity up to 29 K in $SrFe_2As_2$ and $BaFe_2As_2$ at high pressures*, J. Phys.: Condens. Matter **21**, 012208 (2009).

[170] X. C. Wang, Q. Q. Liu, Y. X. Lv, W. B. Gao, L. X. Yang, R. C. Yu, F. Y. Li, and C. Q. Jin, *The superconductivity at 18 K in LiFeAs system*, Solid State Comm. **148**, 538 (2008).

[171] D. R. Parker, M. J. Pitcher, P. J. Baker, I. Franke, T. Lancaster, S. J. Blundell, and S. J. Clarke, *Structure, antiferromagnetism and superconductivity of the layered iron arsenide NaFeAs*, Chem. Comm. **16**, 2189 (2009).

[172] F.-C. Hsu, J.-Y. Luo, K.-W. Yeh, T.-K. Chen, T.-W. Huang, P. M. Wu, Y.-C. Lee, Y.-L. Huang, Y.-Y. Chu, D.-C. Yan, and M.-K. Wu, *Superconductivity in the PbO-type structure α-FeSe*, Proc. Nat. Acad. Sci. USA **105**, 14262 (2008).

[173] B. C. Sales, A. S. Sefat, M. A. McGuire, R. Y. Jin, D. Mandrus, and Y. Mozharivskyj, *Bulk superconductivity at 14 K in single crystals of $Fe_{1+y}Te_xSe_{1-x}$*, Phys. Rev. B **79**, 094521 (2009).

[174] R. Khasanov, M. Bendele, A. Amato, P. Babkevich, A. T. Boothroyd, A. Cervellino, K. Conder, S. N. Gvasaliya, H. Keller, H.-H. Klauss, H. Luetkens, E. Pomjakushina, and B. Roessli, *Coexistence of incommensurate magnetism and superconductivity in $Fe_{1+y}Se_xTe_{1-x}$*, Phys. Rev. B **80**, 140511(R) (2009).

[175] H. Ogino, Y. Matsumura, Y. Katsura, K. Ushiyama, S. Horii, K. Kishio, and J. Shimoyama, *Superconductivity at 17 K in $(Fe_2P_2)(Sr_4Sc_2O_6)$: A new superconducting layered pnictide oxide with a thick perovskite oxide layer*, Supercond. Sci. Technol. **22**, 075008 (2009).

[176] H. Ogino, Y. Katsura, S. Horii, K. Kishio, and J.-I. Shimoyama, *New iron-based arsenide oxides $(Fe_2As_2)(Sr_4M_2O_6)(M = Sc, Cr)$*, Supercond. Sci. Technol. **22**, 085001 (2009).

[177] G. F. Chen, T. L. Xia, H. X. Yang, J. Q. Li, P. Zheng, J. L. Luo, and N. L. Wang, *Possible high temperature superconductivity in a Ti-doped A-Sc-Fe-As-O (A = Ca, Sr) system*, Supercond. Sci. Technol. **22**, 072001 (2009).

[178] X. Y. Zhu, F. Han, G. Mu, B. Zeng, P. Cheng, B. Shen, and H.-H. Wen, *$Sr_3Sc_2Fe_2As_2O_5$ as a possible parent compound for FeAs-based superconductors*, Phys. Rev. B **79**, 024516 (2009).

[179] X. Y. Zhu, F. Han, G. Mu, P. Cheng, B. Shen, B. Zeng, and H.-H. Wen, *Transition of stoichiometric Sr_2VO_3FeAs to a superconducting state at 37.2 K*, Phys. Rev. B **79**, 220512 (2009).

[180] X. Y. Zhu, F. Han, G. Mu, P. Cheng, B. Shen, B. Zeng, and H.-H. Wen, *Superconductivity in Ti-doped iron-arsenide compound $Sr_4Cr_{0.8}Ti_{1.2}O_6Fe_2As_2$*, arXiv:cond-mat/0904.0972v3 (2009).

[181] M. Tegel, F. Hummel, S. Lackner, I. Schellenberg, R. Pöttgen, and D. Johrendt, *The layered iron arsenides Sr_2CrO_3FeAs and Ba_2ScO_3FeAs*, Zeitschrift für Anorganische und Allgemeine Chemie **635**, 2242 (2009).

[182] N. D. Zhigadlo, S. Katrych, Z. Bukowski, S. Weyeneth, R. Puzniak, and J. Karpinski, *Single crystals of superconducting $SmFeAsO_{1-x}F_y$ grown at high pressure*, J. Phys.: Condens. Matter **20**, 342202 (2008).

[183] H. Ding et al., *Observation of Fermi-surface-dependent nodeless superconducting gaps in $Ba_{0.6}K_{0.4}Fe_2As_2$*, EPL **83**, 47001 (2008).

[184] K. Matano, Z. A. Ren, X. L. Dong, L. L. Sun, Z. X. Zhao, and G.-Q. Zheng, *Spin-singlet superconductivity with multiple gaps in $PrFeAsO_{0.89}F_{0.11}$*, EPL **83**, 57001 (2008).

[185] A. J. Drew, F. L. Pratt, T. Lancaster, S. J. Blundell, P. J. Baker, R. H. Liu, G. Wu, X. H. Chen, I. Watanabe, V. K. Malik, A. Dubroka, K. W. Kim, M. Rössle, , and C. Bernhard, *Coexistence of magnetic fluctuations and superconductivity in the pnictide high temperature superconductor $SmFeAsO_{1-x}F_x$ measured by muon spin rotation*, Phys. Rev. Lett. **101**, 097010 (2008).

[186] K. Nakayama, T. Sato, P. Richard, Y.-M. Xu, Y. Sekiba, S. Souma, G. F. Chen, J. L. Luo, N. L. Wang, H. Ding, and T. Takahashi, *Superconducting gap symmetry of $Ba_{0.6}K_{0.4}Fe_2As_2$ studied by angle-resolved photoemission spectroscopy*, EPL **85**, 67002 (2009).

[187] Y.-L. Wang, L. Shan, L. Fang, P. Cheng, C. Ren, and H.-H. Wen, *Nodal superconductivity with multiple gaps in $SmFeAsO_{0.9}F_{0.1}$*, Supercond. Sci. Technol. **22**, 015018 (2009).

[188] L. Malone, J. D. Fletcher, A. Serafin, A. Carrington, N. D. Zhigadlo, Z. Bukowski, S. Katrych, and J. Karpinski, *Magnetic penetration depth of single-crystalline $SmFeAsO_{1-x}F_y$*, Phys. Rev. B **79**, 140501 (2009).

[189] I. Felner, I. Nowik, M. I. Tsindlekht, Z.-A. Ren, X.-L. Shen, G.-C. Che, and Z.-X. Zhao, *Magnetic measurements and ^{57}Fe Mossbauer spectroscopy in oxygen deficient $SmFeAsO_{0.85}$*, arXiv:cond-mat/0805.2794v2 (2008).

[190] I. I. Mazin, D. J. Singh, M. D. Johannes, and M. H. Du, *Unconventional superconductivity with a sign reversal in the order parameter of $LaFeAsO_{1-x}F_x$*, Phys. Rev. Lett. **101**, 057003 (2008).

[191] A. V. Chubukov, D. V. Efremov, and I. Eremin, *Magnetism, superconductivity, and pairing symmetry in iron-based superconductors*, Phys. Rev. B **78**, 134512 (2008).

[192] D. Parker, O. V. Dolgov, M. M. Korshunov, A. A. Golubov, and I. I. Mazin, *Extended s(+/-) scenario for the nuclear spin-lattice relaxation rate in superconducting pnictides*, Phys. Rev. B **78**, 134524 (2008).

[193] M. M. Korshunov and I. Eremin, *Theory of magnetic excitations in iron-based layered superconductors*, Phys. Rev. B **78**, 140509 (2008).

[194] N. Terasaki, H. Mukuda, M. Yashima, Y. Kitaoka, K. Miyazawa, P. M. Shirage, H. Kito, H. Eisaki, and A. Iyo, *Spin fluctuations and unconventional superconductivity in the Fe-based oxypnictide superconductor $LaFeAsO_{0.7}$ probed by Fe-57-NMR*, J. Phys. Soc. Jap. **78**, 013701 (2009).

[195] K. Ishida, Y. Nakai, and H. Hosono, *To what extent iron-pnictide new superconductors have been clarified: A progress report*, J. Phys. Soc. Jap. **78**, 062001 (2009).

[196] R. Khasanov, A. Shengelaya, J. Karpinski, A. Bussmann-Holder, H. Keller, and K. A. Müller, *s-wave symmetry along the c-axis and $s + d$ in-plane superconductivity in bulk $YBa_2Cu_4O_8$*, J. Supercond. Nov. Magn. **21**, 81 (2008).

[197] N. D. Zhigadlo, J. Karpinski, S. Weyeneth, R. Khasanov, S. Katrych, P. Wägli, and H. Keller, *Synthesis and bulk properties of oxychloride superconductor $Ca_{2-x}Na_xCuO_2Cl_2$*, J. Phys.: Conf. Ser. **97**, 012121 (2008).

[198] S. Weyeneth, R. Puzniak, U. Mosele, N. D. Zhigadlo, S. Katrych, Z. Bukowski, J. Karpinski, S. Kohout, J. Roos, and H. Keller, *Anisotropy of superconducting single crystal $SmFeAsO_{0.8}F_{0.2}$ studied by torque magnetometry*, J. Supercond. Nov. Magn. **22**, 325 (2009).

[199] S. Weyeneth, R. Puzniak, N. D. Zhigadlo, S. Katrych, Z. Bukowski, J. Karpinski, and H. Keller, *Evidence for two distinct anisotropies in the oxypnictide superconductors $SmFeAsO_{0.8}F_{0.2}$ and $NdFeAsO_{0.8}F_{0.2}$*, J. Supercond. Nov. Magn. **22**, 347 (2009).

[200] A. Dubroka, K. W. Kim, M. Rössle, V. K. Malik, A. J. Drew, R. H. Liu, G. Wu, X. H. Chen, and C. Bernhard, *Superconducting energy gap and c-axis plasma frequency of (Nd,Sm)$FeAsO_{0.82}F_{0.18}$ superconductors from infrared ellipsometry*, Phys. Rev. Lett. **101**, 097011 (2008).

[201] C. Martin, R. T. Gordon, M. A. Tanatar, M. D. Vannette, M. E. Tillman, E. D. Mun, P. C. Canfield, V. G. Kogan, G. D. Samolyuk, J. Schmalian, and R. Prozorov, *Nodeless superconducting gap in $NdFeAsO_{0.9}F_{0.1}$ single crystals from anisotropic penetration depth studies*, arXiv:cond-mat/0807.0876v1 (2008).

[202] C. Martin, M. E. Tillman, H. Kim, M. A. Tanatar, S. K. Kim, A. Kreyssig, R. T. Gordon, M. D. Vannette, S. Nandi, V. G. Kogan, S. L. Bud'ko, P. C. Canfield, A. I. Goldman, and R. Prozorov, *Non-exponential London penetration depth of FeAs-based superconducting $RFeAsO_{0.9}F_{0.1}$ (R = La, Nd) single crystals*, Phys. Rev. Lett. **102**, 247002 (2009).

[203] Y. Jia, P. Cheng, L. Fang, H. Luo, H. Yang, C. Ren, L. Shan, C. Gu, and H.-H. Wen, *Critical fields and anisotropy of $NdO_{0.82}F_{0.18}FeAs$ single crystals*, Appl. Phys. Lett. **93**, 032503 (2008).

[204] Y. Jia, P. Cheng, L. Fang, H. Yang, C. Ren, L. Shan, C.-Z. Gu, and H.-H. Wen, *Angular dependence of resistivity in the superconducting state of $NdFeAsO_{0.82}F_{0.18}$ single crystals*, Supercond. Sci. Technol. **21**, 105018 (2008).

[205] U. Welp, R. Xie, A. E. Koshelev, W. K. Kwok, P. Cheng, L. Fang, and H.-H. Wen, *Calorimetric determination of the upper critical fields and anisotropy of $NdFeAsO_{1-x}F_x$ single crystals*, Phys. Rev. B **78**, 140510(R) (2008).

[206] L. Balicas, A. Gurevich, Y.-J. Jo, J. Jaroszynski, D. C. Larbalestier, R. H. Liu, H. Chen, X. H. Chen, N. D. Zhigadlo, S. Katrych, Z. Bukowski, and J. Karpinski, *Probing multi-band superconductivity and magnetism in $SmFeAsO_{0.8}F_{0.2}$ single crystals by high-field vortex torque magnetometry*, arXiv:cond-mat/0809.4223v2 (2008).

[207] D. Kubota, T. Ishida, M. Ishikado, S. Shamoto, H. Kito, A. Iyo, and H. Eisaki, *Diminishing superconducting anisotropy in a layered iron arsenic $PrFeAsO_{1-y}$ single crystal*, arXiv:cond-mat/0810.5623v1 (2008).

[208] R. Okazaki, M. Konczykowski, C. J. van der Beek, T. Kato, K. Hashimoto, M. Shimozawa, H. Shishido, M. Yamashita, M. Ishikado, H. Kito, A. Iyo, H. Eisaki, S. Shamoto, T. Shibauchi, and Y. Matsuda, *Lower critical fields of superconducting $PrFeAsO_{1-y}$ single crystals*, Phys. Rev. B **79**, 064520 (2009).

[209] J. Jaroszynski, F. Hunte, L. Balicas, Y.-J. Jo, I. Raičević, A. Gurevich, D. C. Larbalestier, F. F. Balakirev, L. Fang, P. Cheng, Y. Jia, and H.-H. Wen, *Upper critical fields and thermally-activated transport of $NdFeAsO_{0.7}F_{0.3}$ Single Crystal*, Phys. Rev. B **78**, 174523 (2008).

[210] R. Prozorov, M. A. Tanatar, R. T. Gordon, C. Martin, H. Kim, V. G. Kogan, N. Ni, M. E. Tillman, S. L. Budko, and P. C. Canfield, *Anisotropic London penetration depth and superfluid density in single crystals of iron-based pnictide superconductors*, Physica C **469**, 582 (2009).

[211] L. Lyard, P. Szabó, T. Klein, J. Marcus, C. Marcenat, K. H. Kim, B. W. Kang, H. S. Lee, and S. I. Lee, *Anisotropies of the lower and upper critical fields in MgB_2 single crystals*, Phys. Rev. Lett. **92**, 057001 (2004).

[212] J. D. Fletcher, A. Carrington, O. J. Taylor, S. M. Kazakov, and J. Karpinski, *Temperature-dependent anisotropy of the penetration depth and coherence length of MgB_2*, Phys. Rev. Lett. **95**, 097005 (2005).

[213] A. Gurevich, *Enhancement of the upper critical field by nonmagnetic impurities in dirty two-gap superconductors*, Phys. Rev. B **67**, 184515 (2003).

[214] V. G. Kogan, *Free energy and torque for superconductors with different anisotropies of H_{c2} and λ*, Phys. Rev. Lett. **89**, 237005 (2002).

[215] N. R. Werthamer, E. Helfand, and P. C. Hohenberg, *Temperature and purity dependence of the superconducting critical field, H_{c2}. III. Electron spin and spin-orbit effects*, Phys. Rev. **147**, 295 (1966).

[216] N. Ni, S. L. Bud'ko, A. Kreyssig, S. Nandi, G. E. Rustan, A. I. Goldman, S. Gupta, J. D. Corbett, A. Kracher, and P. C. Canfield, *Anisotropic thermodynamic and transport properties of single-crystalline $Ba_{1-x}K_xFe_2As_2$ ($x = 0$ and 0.45)*, Phys. Rev. B **78**, 014507 (2008).

[217] M. Rotter, M. Tegel, D. Johrendt, I. Schellenberg, W. Hermes, and R. Pöttgen, *Spin-density-wave anomaly at 140 K in the ternary iron arsenide $BaFe_2As_2$*, Phys. Rev. B **78**, 020503(R) (2008).

[218] H. Chen, Y. Ren, Y. Qiu, W. Bao, R. H. Liu, G. Wu, T. Wu, Y. L. Xie, X. F. Wang, Q. Huang, and X. H. Chen, *Coexistence of the spin-density wave and superconductivity in $Ba_{1-x}K_xFe_2As_2$*, EPL **85**, 17006 (2009).

[219] M. Rotter, M. Pangerl, M. Tegel, and D. Johrendt, *Superconductivity and crystal structures of $Ba_{1-x}K_xFe_2As_2$ $(x = 0 - 1)$*, Angew. Chem. Int. Ed. **47**, 7949 (2008).

[220] R. D. Shannon, *Revised effective ionic-radii and systematic studies of interatomic distances in halides and chalcogenides*, Acta Crystallogr., Sect. A **32**, 751 (1976).

[221] H. Q. Yuan, J. Singleton, F. F. Balakirev, S. A. Baily, G. F. Chen, J. L. Luo, and N. L. Wang, *Nearly isotropic superconductivity in (Ba,K)Fe_2As_2*, Nature (London) **457**, 565 (2009).

[222] G. F. Chen, Z. Li, J. Dong, G. Li, W. Z. Hu, X. D. Zhang, X. H. Song, P. Zheng, N. L. Wang, and J. L. Luo, *Transport and anisotropy in single-crystalline $SrFe_2As_2$ and $A_{0.6}K_{0.4}Fe_2As_2$ (A = Sr, Ba) superconductors*, Phys. Rev. B **78**, 224512 (2008).

Acknowledgements

All jenen die zum Gelingen dieser Dissertation beigetragen haben sei an dieser Stelle ein grosses *DANKE* gewidmet. Insbesondere möchte ich speziell den untenstehenden Menschen für ihre vielfältige Unterstützung persönlich danken.

Grosser Dank gebührt an dieser Stelle Prof. Dr. Hugo Keller, der mir die Möglichkeit gab in seiner Forschungsgruppe diese Arbeit zu realisieren. Seine Unterstützung in wissenschaftlicher, als auch finanzieller Hinsicht haben wesentlich zum Erfolg dieses Projekts beigetragen.

I would like to thank Prof. Dr. Roman Puzniak for introducing me into SQUID and torque magnetometry, for all the fruitful discussions, and for his valuable and everlasting support in scientific research. Dziękuję za wszystko Roman.

Ich möchte Prof. Dr. Toni Schneider danken, einerseits für die essentielle Unterstützung in der wissenschaftlichen Forschung, andererseits für sein grossen Engagement, mit welchem er mich in die vielfältige Physik der kritischen Phänomene eingeführt hat.

An Dr. Josef Roos geht ein ganz herzlicher Dank für seine wesentliche Unterstützung in technischer und beratender Seite. Egal ob Reparaturen an Messinstrumenten oder Probleme physikalischer Art anstanden; er ist immer mit Tat und Rat zur Stelle.

Ich möchte ebenso Dr. Björn Graneli für seine unermüdliche Hilfe danken, diese Arbeit in ein leicht verständliches und grammatikalisch korrektes Englisch zu bringen. Tack för allt Björn.

Dr. Simon Strässle gebührt Dank für die kollegiale Atmosphäre während des gesamten Projektdauer und der guten Freundschaft.

Ich danke Dr. Janusz Karpinski, Dr. Nikolai Zhigadlo, Dr. Zbigniew Bukowski, Dr. Sergiy Katrych, Dr. Enrico Giannini, Dr. Kazimierz Conder und Dr. Ekaterina Pomjakushina für das Bereitstellen von Proben ausschliesslich hervorragender Qualität.

Im Labor wurde ich von drei begabten Studenten tatkräftig unterstützt. Besten Dank an Urs Mosele, Clemens Duttwyler und Jeanette Schmidlin.

Im administrativen als auch im technischen Bereich hat es an keiner Hilfeleistung gemangelt. Vielen Dank hierzu an Martin Klöckner, Walter Fässler, Tiziano Crudeli, Roland Bernet sowie dem gesamten Werkstatt-Team um Kurt Bösiger.

Vielen Dank auch all jenen die in kollegialer Weise zu einem angenehmen Arbeitsklima beigetragen haben. Speziell erwähnt seien: Dr. Raffaele Dell'Amore, Dr. Andreas Engel, Dr. Dmitry Eshchenko, Dr. Petra Häfliger, Dr. Rustem Khasanov, Dr. Stefan Kohout, Dr. Fabio La Mattina, Dr. Alexander Maiszuradze, Dr. Ferenc Muranyi, Holger Bartolf, Markus Bendele, Alexander Gafner, Mark Reibelt, Stefan Siegrist, Bastian Wojek.

Zu guter Letzt möchte ich herzlichst meinen Eltern, Stephan und Ursula Weyeneth, als auch meiner langjährigen Partnerin Nicole Ruf für die stetige und liebevolle Unterstüztung im privaten Umfeld danken.

Curriculum Vitae

Name	Weyeneth
Prename	Stephen Michael
Date of birth	November 4th, 1979
Place of birth	Chicago (USA)
Citizenship	Lüterkofen-Ichertswil (SO), Switzerland

Education

Aug 1996−Jul 2000	- Maturity at the *Alte Kantonsschule*, Aarau
Jul 2000	- **Matura Typus C**
Oct 2000−Oct 2004	- Undergraduate Sudies of Physics, ETH Zurich - Main focus: Condensed Matter Physics
Oct 2004−Mar 2005	- Diploma Work in the *Condensed Matter at Low Temperatures* group of Prof. Dr. H. R. Ott, ETH Zurich
Mar 2005	- **Diploma-thesis** *Kernresonanz-Untersuchungen an CeTe bei tiefen Temperaturen* - Supervisors: Dr. J. L. Gavilano, Dr. J. Hinderer, Dr. M. Weller
Aug 2005	- **Graduation: Dipl. Phys. ETH**
Sep 2005	- **Certificate of Teaching Ability, ETH**
since Sep 2005	- Ph.D. student in the *Superconductivity and Magnetism* group of Prof. Dr. H. Keller, University of Zurich
Sep 2009	- **Ph.D. thesis** *Anisotropic Properties and Critical Behavior of High-Temperature Superconductors* Supervisor: Prof. Dr. H. Keller

Publication List

issued 1.11.2010

- *Field-dependent superfluid density in the optimally doped $SmFeAsO_{1-x}F_y$ superconductor*
  S. Weyeneth, M. Bendele, R. Puzniak, F. Murániy, A. Bussmann-Holder, N. D. Zhigadlo, S. Katrych, Z. Bukowski, J. Karpinski, A. Shengelaya, R. Khasanov, and H. Keller
  Europhys. Lett. **91**, 47005 (2010).

- *Th-substituted SmFeAsO: Structural details and superconductivity with T_c above 50 K*
  N. D. Zhigadlo, S. Katrych, S. Weyeneth, R. Puzniak, P. J. W. Moll, Z. Bukowski, J. Karpinski, H. Keller, and B. Batlogg
  Phys. Rev. B **82**, 064517 (2010).

- *Anisotropic superconducting properties of single-crystalline $FeSe_{0.5}Te_{0.5}$*
  M. Bendele, S. Weyeneth, R. Puzniak, A. Maisuradze, E. Pomjakushina, K. Conder, V. Pomjakushin, H. Luetkens, S. Katrych, A. Wiesniewski, R. Khasanov, and H. Keller
  Phys. Rev. B **81**, 224520 (2010).

- *Quasiparticle relaxation dynamics in spin-density-wave and superconducting $SmFeAsO_{1-x}F_x$ single crystals*
  T. Mertelj, P. Kusar, V. V. Kabanov, L. Stojchevska, N. D. Zhigadlo, S. Katrych, Z. Bukowski, J. Karpinski, S. Weyeneth, and D. Mihailovic
  Phys. Rev. B **81**, 224504 (2010).

- *Microwave-hydrothermal synthesis of nanostructured zinc-copper gallates*
  F. Conrad, Y. Zhou, M. Yulikov, K. Hametner, S. Weyeneth, G. Jeschke, D. Gunther, J. D. Grunwaldt, and G. R. Patzke
  Eur. J. Inorg. Chem. **2010**, 2036 (2010).

- *Novel carboxymethyl chitin nanoparticles for cancer drug delivery applications*
  A. Dev, J. C. Mohan, V. Sreeja, H. Tamura, G. R. Patzke, F. Hussain, S. Weyeneth, N. V. Nair, and R. Jayakumar
  Carbohydrate Polymers **79**, 1073 (2010).

- *Evidence for Kosterlitz-Thouless and three-dimensional XY critical behavior in $Bi_2Sr_2CaCu_2O_{8+\delta}$*
  S. Weyeneth, T. Schneider, and E. Giannini
  Phys. Rev. B **79**, 214504 (2009).

- *Single crystals of $LnFeAsO_{1-x}F_x$ (Ln=La, Pr, Nd, Sm, Gd) and $Ba_{1-x}Rb_xFe_2As_2$: Growth, structure and superconducting properties*
  J. Karpinski, N. D. Zhigadlo, S. Katrych, Z. Bukowski, P. Moll, S. Weyeneth, H. Keller, R. Puzniak, M. Tortello, D. Daghero, R. Gonnelli, I. Maggio-Aprile, Y. Fasano, Ø. Fischer, K. Rogacki, and B. Batlogg
  Physica C **469**, 370 (2009).

- *Superconductivity at 23 K and low anisotropy in Rb-substituted $BaFe_2As_2$ single crystals*
  Z. Bukowski, S. Weyeneth, R. Puzniak, P. Moll, S. Katrych, N. D. Zhigadlo, J. Karpinski, H. Keller, and B. Batlogg
  Phys. Rev. B **79**, 104521 (2009).

- *Evidence for two distinct anisotropies in the oxypnictide superconductors $SmFeAsO_{0.8}F_{0.2}$ and $NdFeAsO_{0.8}F_{0.2}$*
  S. Weyeneth, R. Puzniak, N. D. Zhigadlo, S. Katrych, Z. Bukowski, J. Karpinski, and H. Keller
  J. Supercond. Nov. Magn. **22**, 347 (2009).

- *Anisotropy of superconducting single crystal $SmFeAsO_{0.8}F_{0.2}$ studied by torque magnetometry*
  S. Weyeneth, R. Puzniak, U. Mosele, N. D. Zhigadlo, S. Katrych, Z. Bukowski, J. Karpinski, S. Kohout, J. Roos, and H. Keller
  J. Supercond. Nov. Magn. **22**, 325 (2009).

- *Single crystals of superconducting $SmFeAsO_{1-x}F_y$ grown at high pressure*
  N. D. Zhigadlo, S. Katrych, Z. Bukowski, S. Weyeneth, R. Puzniak, and J. Karpinski
  J. Phys.: Condens. Matter **20**, 342202 (2008).

- *3D-xy critical properties of $YBa_2Cu_4O_8$ and magnetic-field-induced 3D to 1D crossover*
  S. Weyeneth, T. Schneider, Z. Bukowski, J. Karpinski, and H. Keller
  J. Phys.: Condens. Matter **20**, 345210 (2008).

- *Nodeless superconductivity in the infinite-layer electron-doped $Sr_{0.9}La_{0.1}CuO_2$ cuprate superconductor*
  R. Khasanov, A. Shengelaya, A. Maisuradze, D. Di Castro, I. M. Savi¸, S. Weyeneth, M. S. Park, D. J. Jang, S.-I. Lee, and H. Keller
  Phys. Rev. B **77**, 184512 (2008).

- *Probing superconductivity in MgB_2 confined to magnetic field tuned cylinders by means of critical fluctuations*
  S. Weyeneth, T. Schneider, N. D. Zhigadlo, J. Karpinski, and H. Keller
  J. Phys.: Condens. Matter **20**, 135208 (2008).

- *Resonant soft X-ray powder diffraction study to determine the orbital ordering in A-Site-ordered $SmBaMn_2O_6$*
  M. Garcia-Fernandez, U. Staub, Y. Bodenthin, S. M. Lawrence, A. M. Mulders, C. E. Buckley, S. Weyeneth, E. Pomjakushina, and K. Conder
  Phys. Rev. B **77**, 060402 (2008).

- *Synthesis and bulk properties of oxychloride superconductor $Ca_{2-x}Na_xCuO_2Cl_2$*
  N. D. Zhigadlo, J. Karpinski, S. Weyeneth, R. Khasanov, S. Katrych, P. Wägli, and H. Keller
  J. Phys.: Conf. Ser. **97**, 012121 (2008).

- *Magnetic transition in $Na_{0.5}CoO_2$ at 88 K*
  B. Pedrini, S. Weyeneth, J. L. Gavilano, J. Hinderer, M. Weller, H. R. Ott, S. M. Kazakov, and J. Karpinski
  Physica B **378**, 861 (2006).

- *NMR study of CeTe at low temperatures*
  J. Hinderer, S. M. Weyeneth, M. Weller, J. L. Gavilano, E. Felder, F. Hulliger, and H. R. Ott
  Physica B **378**, 765 (2006).

- *Magnetic phase transition at 88 K in $Na_{0.5}CoO_2$ revealed by Na-23 NMR investigations*
  B. Pedrini, J. L. Gavilano, S. Weyeneth, E. Felder, J. Hinderer, M. Weller, H. R. Ott, S. M. Kazakov, and J. Karpinski
  Phys. Rev. B **72**, 214407 (2005).

- *Kondo behavior of U in CaB_6*
  G. A. Wigger, E. Felder, S. Weyeneth, H. R. Ott, and Z. Fisk
  Physica C **359**, 938 (2005).

- *Kondo behavior of U in CaB_6*
  G. A. Wigger, E. Felder, S. Weyeneth, H. R. Ott, and Z. Fisk
  Europhys. Lett. **68**, 685 (2004).